FRONT-END CONSIDERATIONS FOR NEXT GENERATION COMMUNICATION RECEIVERS

A thesis submitted to the University of Manchester
for the degree of Doctor of Philosophy
in the Faculty of Engineering and Physical Sciences

2011

By
Mousumi Roy
School of Electrical and Electronic Engineering

Contents

On CD-ROM:

'Appendices' file containing Appendices A, B and C

Word Count: 57,295

List of Tables

List of Figures

Abstract

The ever increasing diversity in communication systems has created a demand for constant improvements in receiver components. This thesis describes the design and characterisation of front-end receiver components for various challenging applications, including characterisation of low noise foundry processes, LNA design and multi-band antenna design. It also includes a new theoretical analysis of noise coupling in low noise phased array receivers.

In LNA design much depends on the choice of the optimum active devices. A comprehensive survey of the performance of low noise transistors is therefore extremely beneficial. To this end a comparison of the DC, small-signal and noise behaviours of 10 state-of-the-art GaAs and InP based pHEMT and mHEMT low noise processes has been carried out. Their suitability in LNA designs has been determined, with emphasis on the SKA project. This work is part of the first known detailed investigation of this kind. Results indicate the superiority of mature GaAs-based pHEMT processes, and highlight problems associated with the studied mHEMT processes. Two of the more promising processes have then been used to design C-band and UHF-band MMIC LNAs.

A new theoretical analysis of coupled noise between antenna elements of a low noise phased array receiver has been carried out. Results of the noise wave analysis, based on fundamental principles of noisy networks, suggest that the coupled noise contribution to system noise temperatures should be smaller than had previously been suggested for systems like the SKA. The principles are applicable to any phased array receiver.

Finally, a multi-band antenna has been designed and fabricated for a severe operating environment, covering the three extremely crowded frequency bands, the 2.1 GHz UMTS, the 2.4 GHz ISM and the 5.8 GHz ISM bands. Measurements have demonstrated excellent performance, exceeding that of equivalent commercial antennas aimed at similar applications.

Declaration

No portion of the work referred to in this thesis has been submitted in support of an application for another degree or qualification of this or any other university or other institute of learning.

Copyright

Acknowledgements

I am grateful to Dr. Danielle George for her efficient and friendly supervision and guidance, and for providing me with an opportunity to work on different aspects of receiver front-ends. I am immensely thankful to UK-India Education and Research Initiative (UKIERI) and ASTRON (The Netherlands) for their help and support. I would also like to take this opportunity to express my gratitude towards Mr. Neil Roddis of the Square Kilometer Array Program Development Office (SPDO) for his technical insights and his unconditional help and guidance, Mr. Peter Green of the University of Manchester for technical feedback in the multi-band antenna design work, Mr. Keith Williams (former employee of the University of Manchester) for his guidance in the laboratory, Dr. Graham Parkinson, Ms. Mina Panahi and Dr. Saswata Bhaumik for their support.

Glossary

3G	3rd Generation
ADS	Advanced Design System
AlGaAs	Aluminium Gallium Arsenide
ASTRON	ASTRonomisch Onderzoek in Nederland
ATS	Automated Tuner System
AUT	Antenna Under Test
CAD	Computer Aided Design
COTS	Commercially available Off-The-Shelf
CST	Computer Simulation Technology
DBS	Direct Broadcast Satellite
DC	Direct Current
DRC	Design Rule Check
DUT	Device Under Test
EIRP	Effective Isotropically Radiated Power
ENA	Electronic Network Analyzer
ENR	Excess Noise Ratio
FET	Field Effect Transistor
FNBW	First Null Beam Width
GaAs	Gallium Arsenide
GPRS	General Packet Radio Service
HEMT	High Electron Mobility Transistor
HPBW	Half Power Beam Width
InAlAs	Indium Aluminium Arsenide
InGaAs	Indium Gallium Arsenide
InP	Indium Phosphide
ISM	Industrial, Scientific and Medical

LNA	Low Noise Amplifier
LNB	Low Noise Block
LRRM	Line-Reflect-Reflect-Match
MATLAB	Matrix Laboratory
mHEMT	metamorphic HEMT
MESFET	Metal Semiconductor FET
MIC	Microwave Integrated Circuit
MMIC	Monolithic Microwave Integrated Circuit
MPA	Microstrip Patch Antenna
MS	Microstrip
MWS	Microwave Studio
NFA	Noise Figure Analyzer
NFM	Noise Figure Meter
PA	Power Amplifier
pHEMT	pseudomorphic HEMT
PIFA	Planar Inverted-F Antenna
PSU	Power Supply Unit
QoS	Quality of Service
RF	Radio Frequency
SiGe	Silicon Germanium
SKA	Square Kilometer Array
SNR	Signal-to-Noise Ratio
TL	Transmission Line
UMTS	Universal Mobile Telecommunications System
VNA	Vector Network Analyzer
WLAN	Wireless Local Area Network
WPAN	Wireless Personal Area Network
WSN	Wireless Sensor Network

Publication List

1. M. Roy and D. George, "Estimation of Coupled Noise in Low Noise Phased Array Antennas", *IEEE Trans. Antennas Propag.*, Special Edition Antennas for Next Generation Radio Telescopes, vol. 59, no. 6, pp. 1846-1854, Jun. 2011.

2. S. Bhaumik, M. Roy and D. George, "Comprehensive Comparative Study of Low Noise HEMT processes for LNAs in the Square Kilometre Array Telescope", submitted to *IEEE Trans. Microw. Theory Tech.*, Jul. 2011.

3. S. Bhaumik, M. Roy and D. George, "pHEMT and mHEMT considerations for ultra Low Noise Amplifiers for SKA", in *IEEE MTT-S Int. Microwave Symp. Digest (MTT)*, Jun. 2011, pp. 1-4.

4. M. Roy, S. Bhaumik and D. George, "Study of Dependence of Noise Parameters of HEMTs on Gate Periphery in the C-band", submitted to *IEEE MTT-S Int. Microwave Symp.*, Jun. 2012.

5. A. Prasad, M. Roy, A. Biswas and D. George, "Application of Genetic Algorithm to multi-objective optimization in LNA design", in *Asia-Pacific Microwave Conf. Proc. (APMC)*, Dec. 2010, pp. 362.

to Parents, Family, Friends and Saswata

Chapter 1

Introduction

1.1 Introduction

Wireless communication technologies are being utilised in an increasingly diverse range of applications in the commercial, military and industrial sectors in the recent decades. The commercial sector has perhaps seen the greatest uptake of this technology with mobile devices offering wireless and cellular network communications as standard. Whilst less publicised, there has also been a rapid growth in the use of wireless technologies in the industrial sector, most notably with the use of Wireless Sensor Networks (WSNs) in the process industries. The requirements of these applications range from very short range communication links (paths) of a few metres or less to those with low power requirements. This proliferation of wireless communication technologies has benefited greatly from standardisation, especially from the IEEE 802 family of standards. Whilst the 802.11a/b/g/n Wireless Local Area Networks (WLANs) [1], 802.15.1 Bluetooth [2] and 802.15.4 low-rate Wireless Personal Area Networks (WPANs) [2] standards deliver solutions for a wide range of applications, the harsh environments found in the process industries demand improved receiver front-end designs. These harsh conditions may include reduced space for placement of receiver components such as antennas, requirement of conformability to surfaces of varying curvatures, presence of large metallic structures in close proximity, lack of direct line-of-sight transmission path, possible contamination of exposed receiver components, harsh chemical conditions and exposure to significant variations of temperature and humidity. The specific challenges are the design of efficient Low Noise Amplifier (LNA) blocks, and the design of multi-band, low-profile antennas capable of

conformal mounting on metallic structures.

Although such stringent requirements in receiver front-end design is comparatively new to these industrial, commercial and consumer applications, such high performance and high sensitivity receivers have already been researched and implemented in science-driven applications like radio astronomy. A radio telescope, although not strictly a 'communication' system, represents an extreme application of this type of technology. Looking to detect sources of radio energy coming from the edge of the universe, this requires extremely high receiver sensitivity. The requirements of the radio-receiver front-ends are different from those of ground-based applications. The minimum detectable signal ΔT for radio receivers is determined from the following equation [3]:

$$\Delta T \propto \frac{T}{\sqrt{B \times \tau}} \tag{1.1}$$

where T is the system noise temperature, B is the bandwidth and τ is the integration time. Lower ΔT imply higher sensitivity. The importance of low system noise temperature T in increasing the sensitivity for a given bandwidth and integration time is evident from equation 1.1. Therefore the component of a radio receiver front-end which plays a much more important role than in ground-based receivers is the Low Noise Block (LNB). It determines the sensitivity and hence the quality of reception to a large extent. In-depth mathematical analysis of the need for ultra low noise performance in radio receivers is provided in [3].

One project which has captured the attention of radio astronomers around the World in the past 2 decades is the Square Kilometre Array (SKA), first conceived in 1991 [4]. This project involves the development of a radio telescope which is unprecedented in scale in radio astronomy [5, 6]. The primary objectives of the telescope are to gain insights into the formation of cosmos after the Big Bang, the discovery of extra terrestrial life, the nature of gravity and the role of cosmic magnetism. It will also aid the discovery of new cosmic bodies and in enhancing the understanding of theoretical physics [7]. This objective can only be achieved if the telescope is capable of high dynamic range, high sensitivity and novel supercomputing [8]. With a collecting area of more than 1 km^2, the SKA will require front-end receiver systems with temperatures below 40 K [7]. Since the sensitivity of a telescope is directly proportional to its total collecting area and inversely proportional to the receiver system noise temperature [9], the overall

telescope sensitivity of the SKA will ultimately reach 10,000 m^2/K, at least 50 times than that of existing radio telescopes at comparable frequencies [6]. The design and development of this telescope have therefore provided a significant motivation to innovations in radio astronomy instrumentation, and an excellent opportunity for researchers to gain insights into the various aspects of receiver system designs, including receiver front-ends.

The crucial role of the LNB in a radio receiver front-end in determining the system sensitivity has been stated earlier. One aspect of the present work concentrates on the LNA component of the LNB, and its effect in a low noise phased array environment such as the SKA. In achieving efficient LNA designs, the choice of the semiconductor technology assumes paramount importance. The first objective of the research presented in this thesis was to characterise transistors of state-of-the-art low noise semiconductor processes to investigate their applicability in room temperature SKA LNA designs. The second objective was to validate the transistor characterisation work by designing LNAs using the more promising processes. Two LNAs, in the C and Ultra High Frequency (UHF) bands have been designed for this purpose. Both of these frequency bands are covered by the SKA, as detailed in subsection 1.2.1. The third objective of this work was to determine how the LNB in a receiver system affects the system level noise temperature in low noise phased array receivers. All these objectives are detailed in subsection 1.2.1.

Although the SKA project has provided the primary motivation for these objectives, the applicability of the work is much broader. For example, the designed C-band LNA can be used in applications such as satellite communications, the IEEE 802.15.4 Wireless Sensor Networks (WSNs) and the IEEE 802.11a Wireless Local Area Networks (WLANs) [10, 11]. Potential applications of the UHF band LNA are the Global System for Mobile Communications (GSM) applications or the mobile digital TV systems. In this context, in the second year of research, the author identified one specific application with increasing requirements of efficient LNA designs - WSNs in the process industry.

The School of Electrical and Electronic Engineering in the University of Manchester has a number of collaborative research projects with the process industries. Discussions with academic staff involved in some of these projects helped in identifying this requirement of efficient LNAs in the wireless technology-based

systems being deployed in the process industries. The usage of wireless communication and sensor network technologies in process monitoring and control in these industries is a rapidly growing application. Practical systems are being deployed in the agri-science, food processing, nuclear, pharmaceutical, and petrochemical sectors [12, 13]. These serve to collect process data such as temperature, humidity, density and flow through sensing units and transfer these to a control system for operation and management [14].

These WSNs generally operate in the 2.4 GHz Industrial, Scientific and Medical (ISM) band and are based on the IEEE 802.15.4 standards [2] or the higher-layer protocols such as Zigbee [15]. Few WSNs requiring higher data rates implement the IEEE 802.11b/g/n WLAN standard [1]. The use of the 5.8 GHz ISM band used by IEEE 802.11a WLAN application [1] is also increasing. Quite a few of the process industries also employ some form of mobile data communication using the General Packet Radio Service (GPRS), 3rd Generation (3G) or the Universal Mobile Telecommunications System (UMTS) technologies. One challenging aspect of communication in all these bands is to achieve operation over increased range or with marginal received signal levels. In Europe, the regulations for the maximum transmit power levels are specified in terms of the Effective Isotropically Radiated Power (EIRP). These are specified at 10 mW for the IEEE 802.15.4 standard and 100 mW for the IEEE 802.11 standard (in indoor applications) [1, 2]. Use of power amplifies (PAs) or directional antennas offers no benefit in terms of link budget since the transmit power limit is exceeded. The path losses for an application are determined by the range and environment and cannot be modified. These systems would therefore benefit from the increased sensitivities offered by LNAs in the front-end. An example of a 2.4 GHz receiver front-end (which also serves as a range extender) incorporating an LNA is the CC2590 component from Texas Instruments [16].

From this discussion, it is evident that efficiently designed LNAs could be commercially viable products in these wireless sensor based applications in the process industry. However, many of these applications require mounting of wireless communication antennas on process and storage vessels. These metallic vessels are cylindrical or spherical in shape and their diameters ranging from 1 m to 20 m [17]. An appreciation of the diversity in a process industry environment is obtained from the pictures in Figure 1.1. These vessels are typically surrounded by pipework and access platforms, and there are severe restrictions on both the

(a) Example 1

(b) Example 2

Figure 1.1: Typical structures in a process industry environment [17, 18]

size and placement of the antennas. In addition, vessel mounted antennas may be subject to wide temperature and humidity variations, and surface fouling from contaminants such as oils. The need for mechanical robustness and retrofitting only adds to the challenges of producing an efficient antenna design.

These challenges have provided the motivation for the fourth objective of the author's research - a novel antenna design for use in front-end receiver systems in such environments. One objective of initiating this work was to gain a better understanding of passive front-end components. Details of the design objectives are presented in subsection 1.2.2. Section 1.3 presents the structure in which this thesis is organised, and section 1.4 highlights the contributions of this research work to the subject.

1.2 Research objectives

This section describes the four research objectives outlined in the discussion in section 1.1 in greater detail. These have been categorised on the basis of active or passive components.

1.2.1 Objectives relevant to active front-end components

The research objectives relevant to LNAs and their effect on the system noise levels are detailed as follows:

Objective 1. Transistor characterisation

As stated in section 1.1, the characterisation of state-of-the-art low noise transistors was commenced as part of research to determine suitable processes for development of SKA room temperature LNAs. The frequency of operation of the SKA extends from 70 MHz to 10 GHz [4]. A variety of technologies is expected to be employed for the SKA:

1. Low frequency aperture array (AA-lo) covering 70 to 450 MHz
2. Mid-frequency aperture array (AA-mid) covering 400 MHz to 1.4 GHz
3. Dish Array covering 450 MHz to 10 GHz

The technical requirements of the AA-lo system are significantly different from that of the AA-mid system. In the AA-lo operational frequency range, the receiver sensitivity will be heavily influenced by the high sky noise. Above 450 MHz the sky noise reduces significantly making the receiver system noise critically important. This distribution of sky noise therefore presents a challenge at selecting the most suitable semiconductor technologies for LNA designs in the above 3 frequency bands. Furthermore, the semiconductor technologies chosen should not only provide excellent noise performance but also must be very repeatable, reliable and robust with very high yields and low costs. There is also the probability that different technologies are adopted for different frequency bands depending on the defining requirements.

From the literature review, it is evident that the transistor which has established its supremacy in LNA design at room temperature is the High Electron

Mobility Transistor (HEMT) [19]. The HEMT and its variants have excellent gain and noise performance and have been extensively used in recent years for ultra low noise applications for frequencies up to W-band [20]. Hence, the present transistor characterisation work focuses on different HEMT processes. The DC, RF and noise performance of 10 different HEMT processes of various technologies and topologies have been measured, and a comparative analysis has been performed. This characterisation work also serves to determine the best low noise processes for other applications.

Objective 2. MMIC LNA design

The second research objective was to validate the transistor characterisation work (detailed in Objective 1) by designing a C-band and a UHF-band LNA based on the more promising processes. The implementation of LNAs has evolved considerably over the decades. A historical review of the pre-1970s evolution of low noise techniques was carried out by Okwit [21]. The early 1980s saw the emergence of the Microwave Integrated Circuit (MIC) technology in low noise receiver designs. Also called hybrid technology, this technique uses packaged transistors in conjunction with lumped passive components. These components are then integrated using solder, conductive epoxy adhesive and gold bondwires. This method has produced very low noise figures [19], and still continues to be in widespread use. In spite of this, it has some severe shortcomings such as increased costs for large-scale productions, large circuit dimensions and lack of repeatability of performance. The key to solving these problems lies in the Monolithic MIC (or MMIC technology).

The word 'monolithic' in Greek means 'as a single stone'. The active and passive components of a circuit are all fabricated on the same semiconductor substrate in a MMIC, with the necessary interconnections in place [22]. MMICs achieve high performance with significantly reduced circuit dimensions and therefore have found widespread use in various commercial, military and space applications. Base station transceiver systems, satellite transceiver systems, phased array systems and electronic warfare are representative examples [22]. Owing to the superior performance of MMICs, namely size and weight reduction, significantly improved repeatability and reliability, reduced costs for bulk production, the present LNAs in the C and UHF bands have been designed by implementing this technology.

Objective 3. Noise estimation in low noise phased array systems

The third research objective was to estimate the degradation in system noise performance, if any, due to noise coupling between adjacent antenna elements in low noise phased array receiver systems, which have been very popular for radio astronomy applications [23, 24]. In the SKA, several thousand dishes will be equipped with wideband single-pixel feeds. Apart from the wide bandwidth, these systems will be similar to the traditional radio astronomy receivers in use today, and their noise performance can be analysed in a straightforward manner using well-known techniques. However, a proportion of the dishes are expected to be equipped with phased array feeds, each comprising of order 100 close-coupled antenna elements.

The design of these feeds will draw on the development experience of the APERTIF programme in the Netherlands [23], the Australian Square Kilometer Array Pathfinder (ASKAP) programme in Australia [24] and the Phased Array Demonstrator (PHAD) programme in Canada [25]. Additionally, a large part of the SKA is expected to consist of multiple ground-mounted dense aperture arrays. Other radio astronomy projects already using aperture arrays on the ground include the Low Frequency Array (LOFAR) [26], the Murchison Widefield Array (MWA) [27] and the PAPER [28]. The SKA aperture arrays are expected to be approximately 60 m in diameter, each consisting of hundreds of thousands of close-coupled antenna elements. As stated in Objective 1, at frequencies above a few hundred MHz, where the sky noise rapidly decreases with increasing frequency, it will be vital to obtain very low noise temperature performance from these arrays in order for them to be practical as radio astronomy receivers. As such, there is a demand for noise analysis in these low noise phased array systems.

Receiver noise coupled between antenna elements has been thought to be a significant contributor to overall system noise in such low noise phased arrays [29]. In the present work, the fundamental principles of linear noisy networks have been used to estimate the noise waves emanating from the input of each LNA towards the antenna element. The theory has been implemented using the Matrix Laboratory (MATLAB) software [30], and successfully used to predict the noise levels emanating from the input ports of 2 packaged amplifiers. The theory has then been applied to an example 2-antenna array model previously used by SKA engineers, and the potential coupled noise contribution has been estimated. The applicability of this noise analysis work, although primarily undertaken for

the SKA, extends to any phased array system.

In summary, the author's research on active front-end components extends from transistor characterisation to LNA design to determining the effect of the LNB on the system level noise temperatures in a low noise phased array system.

1.2.2 Objectives relevant to passive front-end components

Objective 4 describes the research objective relevant to the passive component (antenna) design:

Objective 4. Multi-band microstrip patch antenna design

The typical problems encountered in process industry environments have been discussed in section 1.1. The need for efficient antennas in such environments, as well as the increasing use of different frequency bands for wireless transmission within these environments have also been highlighted. One technique of improving the communication link in such systems is to achieve diversity through the use of different frequency bands and services. The same data may be transmitted through different frequency bands simultaneously, such that any loss of information can be remedied. Alternatively, weighting of the Quality of Service (QoS) in the different bands may be considered. Implementation of these concepts requires efficient multi-band antenna designs. In fact, research on multi-band antennas has received extensive interest in recent years, especially with the impetus provided by mobile communications [31].

In an effort to utilise diversity, a worst case antenna design requirement can be created from a study of the typical problems encountered in the process industry: a tri-band antenna to be conformally mounted on a cylindrical metallic vessel just beneath a large metallic access platform. This forms the basis of the fourth objective of the present research - to develop a prototype multi-band Microstrip Patch Antenna (MPA) structure, operational in such harsh environments, and covering three popular frequency bands, the 2.14 GHz UMTS band, the 2.4 GHz ISM band and the 5.8 GHz ISM band.

Some of these frequency bands are either extremely congested (for UMTS) or have severe interference from other users in the band using the WLAN, Zigbee or Bluetooth applications (for 2.4 GHz). Leakage from other ISM applications such as microwave ovens and ultrasonic equipment can also degrade performance.

Moreover, the fact that these ISM frequency bands are unlicensed with minimum regulatory mechanism in place leads to rapid unstructured deployment of ISM applications. This implies that new users can appear in the band in a random manner, and there is a requirement to cope with rapidly changing band occupancy levels. These factors indicate that system designs for the ISM bands need to be robust [12].

The choice of implementing the multi-band antenna design using microstrip technology is based on the fact that MPAs are inexpensive to fabricate, light-weight, low-profile and can be made conformable with planar and non-planar surfaces [31]. Such antennas have in fact found widespread use in communications systems in the last few decades.

It is evident from this discussion that the rather stringent requirements naturally make this particular tri-band antenna design very challenging. The advantage is that the robustness of an antenna structure satisfying these requirements would render it suitable for a broader range of applications.

Based on the 4 objectives described above, in summary, the research work presented in this thesis encompasses aspects of both active and passive components of receiver front-ends. The motivations behind the different aspects of the work have arisen from 2 applications of different natures, both of which have attained increasing importance in recent years and have resulted on increasing demands in receiver front-end designs. This thesis provides the reader with a better insight into some aspects of design and characterisation of the different front-end components in these applications.

1.3 Thesis structure

The thesis consists of 13 chapters. The block diagrams shown in Figure 1.2 will be used to identify the aspects of the receiver front-end addressed in each chapter. In this Introduction chapter, the context, relevance and objectives of the current research have been outlined. Chapters 2 to 5 review the literature relevant to this research. Specifically, chapter 2 provides an overview of the structure and working principle of HEMTs. Their DC and small-signal behaviour are briefly discussed, and their noise characterisation (and associated techniques) is discussed in detail. Chapter 3 discusses the principles of MMIC multi-stage LNA designs, and includes a section on the benefits of MMIC technology. Chapter

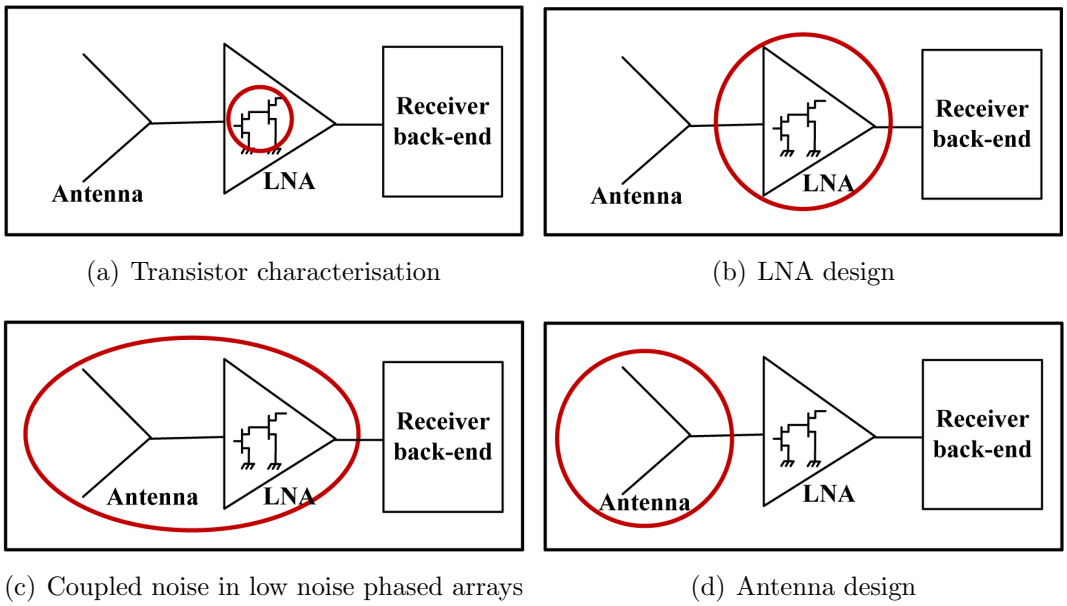

(a) Transistor characterisation

(b) LNA design

(c) Coupled noise in low noise phased arrays

(d) Antenna design

Figure 1.2: Diagrams showing the focuses of the different chapters

4 presents the theoretical principles which underpin the noise analysis in low noise phased array systems. Chapter 5 presents the fundamental principles of antenna design, with special emphasis on MPAs. An analysis of the effect of the design parameters on the performance is also included.

Chapter 6 combines the transistor characterisation work and the LNA design work, because they both relate to the front-end LNB. It includes the details of the characterised low noise processes. A step-by-step discussion of the LNA design work is presented, starting from transistor selection to final layout generation. In chapter 7, the design of a multi-band MPA is detailed. It provides the design requirements, choices in design approaches and feed considerations.

Accurate characterisation of HEMTs and MMIC LNAs requires high performance measurement equipment. The measurement of the low levels of noise emanating from the input of an LNA (in context of the low noise phased array noise analysis) requires a special purpose experimental arrangement. Antenna measurements are conducted in specially designed RF anechoic chambers. Chapter 8 presents an overview of these different experimental arrangements used in this work.

Chapters 9 to 12 present the simulation and measurement results and relevant analyses. Specifically, chapter 9 presents an analysis of the measured performances of the low noise transistors of various processes, and is followed by the results of the LNA designs in chapter 10. Some aspects of the transistor characterisation work have been conducted in collaboration with a colleague working in the same team. References to this colleague's thesis have been made wherever relevant. Chapter 11 presents the results of measurements to validate the theory used in the phased array noise analysis. The relevance of the principles in the SKA project have been analysed as well. Chapter 12 provides the results and analysis of the multi-band MPA design work.

Chapter 13 summarises the important inferences that can be drawn from this research work. Based on the accomplishments and limitations of the present work, this chapter also explores the potential future development work that can be undertaken.

1.4 Contributions to the subject

This research has contributed to the knowledge and practical understanding of the subject in the following areas:

- State-of-the-art low noise transistors of different technologies and topologies have been characterised to determine their applicability in various applications, with special emphasis on the SKA. Comparison between available transistor processes for LNA design is a usual practice in LNA design work. However, in this work, 10 processes from different foundries around the world with widely varying gate lengths and gate widths have been measured and characterised using the same experimental arrangement. This work forms part of the first known detailed investigation of this kind [19, 32].

- Two MMIC LNAs operating in the C and UHF bands have been designed. Simulations indicate noise figures of 0.62 dB and 0.45 dB for the 2 LNAs, respectively, with peak gains exceeding 30 dB. Maximum input and output return loss values of 23 dB and 11 dB, respectively, have been reached. The specifications for the design were determined from knowledge of current LNA capabilities in the C and UHF bands, and the results compare well with available LNA designs in these bands. The novelty of these designs

lies in the wide bandwidths that have been achieved. The 0.1 dB noise bandwidth and the 1 dB gain bandwidth for the C-band LNA are both 4 GHz and therefore extend to the entire C-band. The 0.1 dB noise bandwidth and the 3 dB gain bandwidth for the UHF band MMIC LNA are 450 MHz and 600 MHz, respectively.

- A new theoretical analysis of coupled noise between antenna elements of a low noise phased array receiver has been carried out. This work offers interesting insights into the importance of noise parameters such as the noise resistance in phased array system designs. The principles are applicable to any phased array receiver and provide a simple and effective tool for LNA and phased array system designers. Results of this noise analysis and applications in systems like the SKA are reported in [33].

- A novel multi-band microstrip MPA structure to be implemented under the severe spatial and environmental constraints imposed by process industry environments has been designed, fabricated and characterised.

Chapter 2

Low noise transistors - technologies, topologies and characterisation

2.1 Introduction

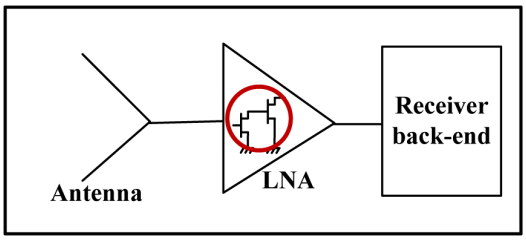

Figure 2.1: Focus of the chapter - low noise transistor processes

This chapter provides a synopsis of the various technologies and topologies of HEMT-based low noise transistors. HEMTs are generally implemented using III-V semiconductor compounds such as Gallium Arsenide (GaAs) and Indium Phosphide (InP). The idea of the HEMT was first conceived by T. Mimura [34]. Their excellent noise and gain performance ushered in rapid advances in low noise applications. By 1985 HEMTs had attained supremacy as the lowest noise transistors, and implementation in most satellite communication applications worldwide had begun. An account of the evolution of low noise technology till late 1980s is available in [21, 35]. Later developments have been highlighted in [20].

The substrate which has been most widely used for development of HEMTs in the past 3 decades is GaAs [36]. It is presently a stable and mature technology, and has completely revolutionised LNA design. LNAs fabricated on InP substrates have also shown superior performances [37]. The important properties of the III-V compounds GaAs and InP which enhance their suitability in low noise applications are discussed in section 2.2. Section 2.3 describes the operating principle of HEMTs. The DC and small-signal behaviours are outlined in sections 2.4 and 2.5, respectively. Finally, the noise characterisation of HEMTs is discussed in greater detail in section 2.6. It includes the fundamental aspects of noise in linear 2-ports and noise parameter extraction techniques as well.

2.2 HEMT Technologies

Table 2.1 lists the basic properties of conventional substrates Si, GaAs and InP, at an ambient temperature of 300 K [38]. The important parameters that determine the speed and low noise performance of a substrate are the electron mobility and the electron drift velocity. In small gate length devices, higher electron drift velocities decrease the electron transit times and hence increase the cut-off frequencies. Higher mobilities and drift velocities also lead to lower parasitic resistances and larger transconductances. Due to the enhanced conduction properties of GaAs compounds in comparison to Si, GaAs FETs achieve significant improvements in performance for low noise applications at microwave and millimetre-wave frequencies [36]. InP based HEMTs have also exhibited superior low noise characteristics, with high cut-off frequencies (>115 GHz) [38]. However, the InP substrate suffers from some inherent drawbacks - they are expensive, unavailable in large scale, mechanically fragile (brittle) and more difficult to handle than GaAs [22].

Table 2.1: Properties of common substrate materials [19, 38]

Parameters	Units	GaAs	InP	Si
Peak Electron Velocity	$\times 10^7$ cms^{-1}	1.6-2.3	2.5-3.5	0.3-0.7
Electron Mobility	cm$^2V^{-1}s^{-1}$	5500-7000	10000-12000	900-1100
Saturated Drift Velocity	$\times 10^6$ cm^{-2}	5	6	8.5
Band Gap	eV	1.4	1.3	1.1
Intrinsic Resistivity	Ωcm	3.3×10^8	8.6×10^7	3.2×10^5

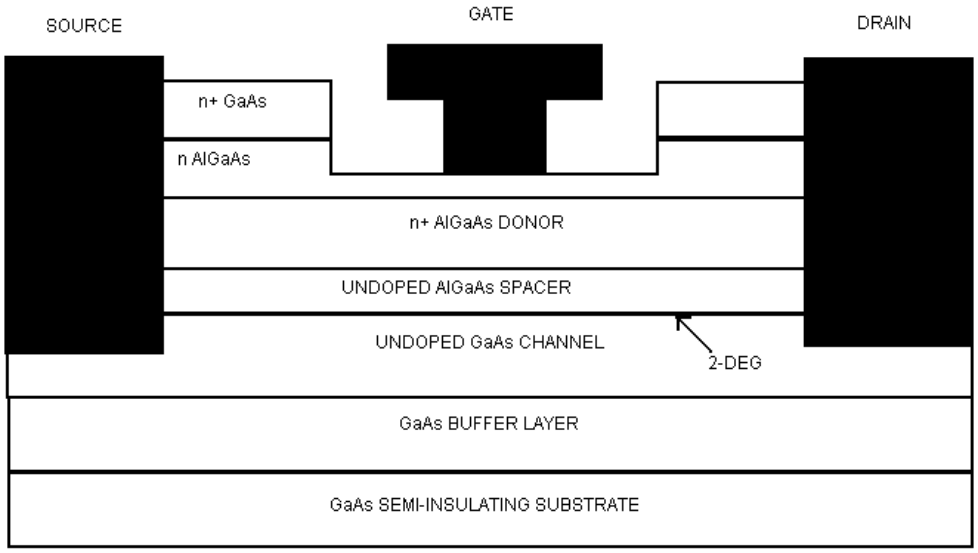

Figure 2.2: Structure of an AlGaAs/GaAs HEMT [19]

2.3 HEMT Topologies

This section provides a brief description of the topology and operating principle of the traditional HEMT, and the evolution of its variants. Unlike in a conventional MESFET, the design of a HEMT is such that the mobility of the electrons in the transistor is enhanced significantly [36]. It utilises the hetero-junction principle to create a 2-dimensional high concentration of carriers at the interface of a higher band gap material like AlGaAs and a lower band gap material like GaAs. Separation of the doping layer from the channel helps in achieving high carrier concentration and high mobility simultaneously. The product of these two quantities determines the current and the transconductance of transistors, and hence the performances are enhanced. The noise performance is also significantly enhanced due to the same reason. Addition of an un-doped spacer layer improves performance. Figure 2.2 shows the structure of a typical n-AlGaAs/GaAs HEMT [39, 40].

pHEMTs

Despite the excellent gain, noise and power performance obtained from HEMTs at microwave frequencies, the conventional AlGaAs/GaAs structure has some severe shortcomings, inherent to the AlGaAs material [39]. Structures grown with slightly different lattice constants called pseudomorphic HEMTs or pHEMTs provide the solutions. For the AlGaAs/GaAs system, the compound InGaAs forms the pseudomorphic layer. It is also the channel layer. Hence the structure benefits from the enhanced transport properties of InGaAs, but is still fabricated on a GaAs substrate. This allows even higher current densities, higher transconductances, lower noise figures and higher operating frequencies than conventional HEMTs [36, 39]. Delta doping technology has enhanced the performance of pHEMTs even more [40].

mHEMTs

In the comparatively new technology of metamorphic HEMT, a buffer layer is placed between lattice-mismatched channel layer InGaAs and the substrate GaAs. InAlAs forms the buffer layer, and the In concentration is graded to match the lattice constants of GaAs on one side and InGaAs on the other side. This is referred to as 'metamorphism'. The advantage is that the In content in the InGaAs channel layer can be independently varied to enhance device properties [19]. The mHEMT technology has not yet reached a matured state and there are rising concerns about their repeatabilities.

2.4 DC behaviour [39]

The DC behaviour of HEMTs is similar to that of MESFETs. The devices are classified as either depletion mode or enhancement mode. For depletion mode devices, current can flow between the drain and source electrodes at zero gate bias. For enhancement mode devices, there is no current conduction unless a positive gate bias is applied. The static characteristics are obtained by studying the increase in current levels with application of the drain-source bias voltage V_{ds}.

The transconductance g_m is one of the most important device parameters, and an important indicator of the device quality for microwave and the millimetre-wave applications. It is defined as the slope of the I_{ds} - V_{gs} characteristics, at

constant V_{ds}. It is mathematically expressed as:

$$g_m = \frac{dI_{ds}}{dV_{gs}} \text{ at constant } V_{ds} \tag{2.1}$$

g_m is a strong function of the device dimensions and channel material properties. It is proportional to the device gate width and is often expressed as transconductance per unit gate width as 'mS/mm'. As stated earlier in section 2.3, the superior electron transport properties and the excellent carrier confinement obtained in a HEMT lead to high values of g_m in a HEMT.

2.5 Small-signal behaviour

Modern day CAD tools for active microwave circuits rely heavily on models of active devices [39]. An understanding of the small-signal and noise models of HEMTs is essential in LNA design. Small-signal models offer the designer the ability to predict device performance without performing measurements and determine parameters such as the transconductance g_m and the cut-off frequency f_T. Small-signal models can also be used to extrapolate measured data to extended frequency ranges.

Over the years, many different modelling techniques have been proposed to represent the small-signal equivalent circuit of a HEMT. Figure 2.3 shows the model proposed by Dambrine [41]. The various equivalent circuit elements that can be uniquely extracted from this model can be segregated into 2 categories [39]:

- Intrinsic elements: These elements are intrinsic to the device and are bias-dependent. The transconductance g_m, the output conductance g_{ds}, the capacitances between the 3 electrodes C_{gs}, C_{ds} and C_{gd}, the gate-to-source resistance R_i, and the delay time τ constitute the intrinsic elements.

- Extrinsic elements: These are linear parasitic elements, and exhibit no bias dependence. These consists of the parasitic inductances L_s, L_d, and L_g, the parasitic resistance R_s, R_d and R_g, and the parasitic pad capacitances C_{pg} and C_{pd}.

The equivalent circuit elements are determined from accurate measurements of the S-parameters of the device. The simulated response derived from the

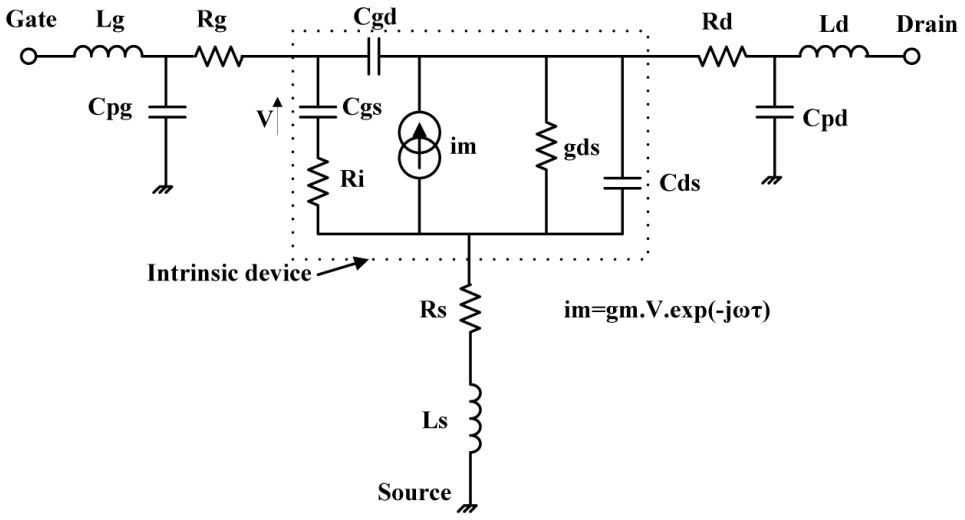

Figure 2.3: Small-signal model of a HEMT [41]

modelled small-signal circuit should match the measured response closely [42].

2.6 Noise characterisation of HEMTs

In LNA design work, knowledge of the small-signal equivalent circuit of HEMTs needs to be supplemented by knowledge of the noise sources within HEMTs. Complete characterisation of this noise behaviour in HEMTs is also very important. Topics related to the noise behaviour of HEMTs are discussed in this section.

2.6.1 Noise sources in a HEMT

In semiconductors, various types of noise sources are present, generated by different mechanisms. The conduction band carriers undergo random changes in their motions due to temperature, and experience collisions with each other, or with the vibrating atoms. This leads to what is referred to as thermal noise. A second type of noise, called shot noise, is generated by sudden bursts of carriers in a conducting channel (which may occur due to various reasons) and consequent fluctuations in the current levels [19, 43]. Another possibility is that a free electron combines with a free hole to move to a more stable valence band, and in the process releases energy. These random trapping and de-trapping of carriers

occur due to traps and recombination centres in semiconductors. This leads to a fluctuation in the number of free charge carriers per unit time, creating a noise voltage in effect. This is termed as generation-recombination noise [43].

The type of noise dominant at low frequencies is called flicker noise. It is inversely proportional to the frequency (raised to a specific order depending on channel properties), and is therefore also called the $(1/f)$ noise. Flicker noise is ubiquitous but the definite cause is not proved yet. It can be modelled empirically, but cannot be predicted *a priori*. An empirical expression is provided for flicker noise in [3]. All these sources of noise are present in HEMTs, but their contributions to the overall noise performance may vary depending on the substrate properties and the quality of fabrication [43].

2.6.2 Noise representation of linear 2-ports

The intrinsic noise sources of any linear noisy 2-port can be represented in various ways, such as the open circuit impedance $[Z]$ representation, the short-circuit admittance $[Y]$ representation and the chain $[ABCD]$ representation (also called the Rothe-Dahlke representation [44]). Figure 2.4 depicts these representations. One representation not depicted in this figure is the noise wave representation. It is discussed in greater detail, along with the chain representation, in chapter 4, where these have been utilised in noise analysis of low noise phased array systems.

Irrespective of the adopted representation, the active noise sources within the 2-port are represented by 2 lumped noise sources placed outside the 2-port. The 2-port then consists of passive noiseless components only [45]. For instance, in the impedance representation, there are 2 noise voltage sources at the input and the output ports. The impedance matrix of a noisy 2-port is modified to:

$$\begin{pmatrix} V_1 \\ V_2 \end{pmatrix} = \begin{pmatrix} Z_{11} & Z_{12} \\ Z_{21} & Z_{22} \end{pmatrix} \begin{pmatrix} I_1 \\ I_2 \end{pmatrix} + \begin{pmatrix} e_{n1} \\ e_{n2} \end{pmatrix} \tag{2.2}$$

Equation 2.2 depicts that a noisy 2-port would generate voltages e_{n1} and e_{n2} across both ports if they are simultaneously open-circuited. Similar relations can be developed for the other representations [45].

In general, the internal noise sources within the 2-port which contribute to the noise voltage or current generators have some degree of correlation between them. This leads to a complex correlation component for all representations.

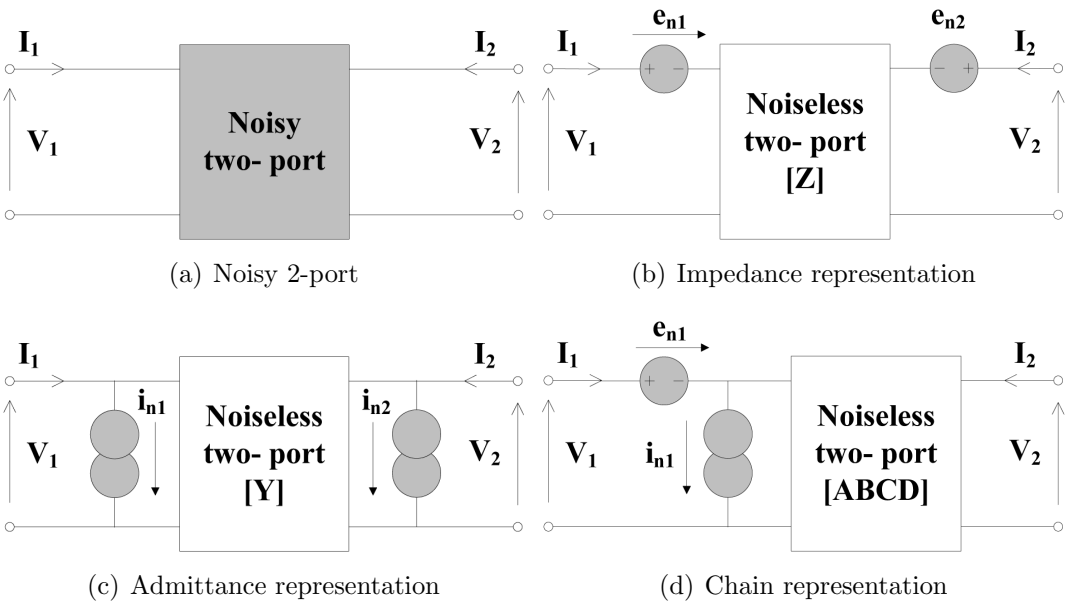

(a) Noisy 2-port (b) Impedance representation

(c) Admittance representation (d) Chain representation

Figure 2.4: Noise representations of linear 2-ports [45]

Hence, 4 real quantities are required in total to completely characterise the noise behaviour of a linear noisy 2-port - the values assigned to the 2 noise generators, and the real and imaginary components of the complex correlation coefficient relating them [45].

2.6.3 Fundamental definitions

The most widely used figure-of-merit in noise analysis is the noise factor F. At a specific frequency, it is defined as the available signal-to-noise ratio (SNR) at the input of any noisy 2-port to that available at the output, when the temperature of the input termination is at the standard temperature T_0=290 K and the bandwidth is limited by the receiver [45]. It thereby quantifies the SNR degradation caused by the 2-port. It is dependent both on the source impedance at the input port and the noise sources within the 2-port. The noise factor F expressed in dB is called the noise figure NF. The mathematical expressions of these quantities are:

$$F = \frac{S_i/N_i}{S_o/N_o} \tag{2.3}$$

$$NF = 10\log F \tag{2.4}$$

The noise figure in a 50 Ω system is denoted as NF_{50}.

Often it is preferable to represent the noise in a 2-port in terms of thermal noise. This leads to the concept of equivalent noise temperature, T_e. It is defined as "that temperature of the signal source which, when connected to a noise-free equivalent of the 2-port, produces the same available noise power per unit bandwidth at the output as that produced by the noisy 2-port, excited by a noise-free identical source" [45].

For a linear noisy 2-port, F is a function of the source impedance presented to it, and hence is not sufficient to fully characterise its noise performance. In order to achieve complete characterisation, knowledge of 'noise parameters' is essential [46]. The value of F at an arbitrary source impedance can be determined using noise parameters. These help in predicting noise behaviour under mismatch conditions and in optimising match condition for a particular device [47]. In terms of the 4 noise parameters, F is given by [46]:

$$\begin{aligned} F &= F_{min} + \frac{R_n}{G_s}\left\{(G_s - G_{opt})^2 + (B_s - B_{opt})^2\right\} \\ &= F_{min} + \frac{R_n}{G_s}|Y_s - Y_{opt}|^2 \end{aligned} \tag{2.5}$$

where F_{min} is the minimum noise factor (expressed in dB scale as NF_{min}, the minimum noise figure), R_n is the noise resistance, $Y_s = G_s + iB_s$ is the source admittance and $Y_{opt} = G_{opt} + iB_{opt}$ is the optimum admittance for noise match. F_{min}, R_n, G_{opt} and B_{opt} constitute the 4 noise parameters. In terms of the source and optimum noise reflection coefficients, Γ_s and Γ_{opt}, F is expressed as [46]:

$$F = F_{min} + \frac{4R_n}{Z_0}\left(\frac{|\Gamma_s - \Gamma_{opt}|^2}{|1 + \Gamma_{opt}|^2\,(1 - |\Gamma_s|^2)}\right) \tag{2.6}$$

Equation 2.6 depicts that the minimum noise factor F_{min} is obtained only when the optimum noise match condition is achieved, that is, when $\Gamma_s = \Gamma_{opt}$. The noise resistance R_n is a sensitivity term that determines the rate at which the noise factor degrades as the source impedance varies from this condition [46].

2.6.4 Noise parameter extraction

There are various methods of determining noise parameters. Until 3 decades ago, the procedures were very much trial dependent, and several measurements of noise factor were performed at different source impedances to experimentally

search for the minimum noise figure [19]. More systematic procedures have been developed over the years, and are briefly discussed in the next subsections.

Curve-fitting techniques

The classical method of noise parameter extraction, also termed the 'multiple impedance' method, is most suitable for automatic characterisation, and as such is most commonly employed. A least-squares-fit technique to minimise errors in this method was first outlined by Lane in 1969 [48]. The noise figure is measured at multiple source impedances, using a manual or automated tuner. In theory, 4 sets of data generating 4 simultaneous equations should be sufficient to provide solutions of the 4 noise parameters. In practice, since noise measurements are sensitive to small errors, it is a standard practice to perform measurements at more than 4 values of source impedance, and then apply a least-mean-squares algorithm to reduce the over-determined data [48, 49].

Lane's technique reduces the derivation of noise parameters to the solution of a set of 4 linear equations, with an evaluation based on minimising a specific estimated error [48]. However, minute data perturbations are entailed due to unavoidable measurement uncertainties and these produce strong variations of computed noise parameters, leading to inaccuracy [50]. Furthermore, since measured datasets are assigned weights based on 'perceived' measurement accuracy, this technique may sometimes be impractical [50].

To improve accuracy, Davidson introduced switching the tuner to a set of 'predetermined' impedance points instead of employing random source impedance variation [50]. Mitama and Katoh [51] proposed a method which took into account measured source impedance errors along with measured noise factor errors, and entailed minimising the distance between the estimated data and the measured data [52]. Subsequent works in this technique of noise parameter extraction have generally involved generating different impedance patterns in the Smith Chart, since the constellation of impedance points plays a significant role in determining accuracy [53].

Analytical Computation from measured data

Vasilescu *et al.* proposed an analytical approach of noise parameter extraction in 1988 [45]. Instead of linearising the error-sensitive noise equation, he proposed direct solution of the 4 non-linear equation system. All possible M combinations

of 4 data sets among N measured data sets are employed in computation, and the noise parameter set which reduces a specific error function is retained. This technique provides satisfactory results, however in some cases, 50% of the data is meaningless [52].

Boudiaf proposed an algorithm in which the noise parameter equation is transformed into a straight line with F_{min} as the intercept and R_n as the slope, and equation 2.6 is translated to [54]:

$$y_i = F_{min} + R_n x_i \tag{2.7}$$

where $y_i = F_i$ and $x_i = \left[(G_{si} - G_{opt})^2 + (B_{si} - B_{opt})^2\right] / G_{si}$.

In this technique, initial estimates of the noise parameters are necessary, and the weighted distances between the adjusted values (x_i, y_i) and the measured values (X_i, Y_i) are minimised using an error function to obtain the noise parameters.

Computer and measurement based comparisons of some of these extraction methods were performed in a significant work by Escotte [52]. It concluded that, overall, the technique proposed by Boudiaf was least sensitive to the selected source impedance constellation and provided the best accuracy levels, while at the same time being less time-consuming [52]. Other methods involving optimising algorithms have been proposed as well [55] but different constraints limit their suitability for automated measurements [52].

2.6.5 Noise modelling using drain temperature

In 1989, Pospieszalski [35] established that the intrinsic noise of a transistor can be predicted by associating temperatures T_g and T_d (the subscripts relating to the gate and drain) to the intrinsic resistive components R_i and R_{ds}, respectively, in the small-signal equivalent circuit model [19]. The noise behaviour in the input side is modelled by a noise equivalent circuit consisting of a noiseless resistor in series with an input noise voltage source, the noise power of which is determined by R_i and T_g. The noise behaviour of the output side is modelled, in a similar manner, by a noiseless resistor and an uncorrelated output noise current source (with noise power determined by the value of the R_{ds} and T_d). The gate temperature T_g is generally set to the ambient temperature T_a [19, 35].

Expressions of the 4 noise parameters in terms of the intrinsic elements and the temperatures T_g and T_d are obtained by comparison of this model to the Rothe

and Dahlke model (the chain representation) [44]. This method is very easily implementable in Computer Aided Design (CAD) softwares and has been widely used in recent years [19]. The drain temperature T_d can be derived from device equations [35]. A trial and error procedure can also be employed to find T_d by matching simulated and measured noise factors, thereby making this a simple and cost-effective approach. However, this technique of noise modelling also requires precision noise factor measurements and accurate small-signal modelling.

2.7 Summary

In this chapter, the various technologies and topologies of high performance low noise transistors used in LNA design work have been highlighted. A brief discussion on the different semiconductor technologies used in HEMTs has been presented. The operating principles of the different variants of HEMTs have been discussed. This study brings forth the reasons why HEMTs are in widespread use in microwave LNA designs.

A brief overview of the DC and small-signal response of HEMTs has been followed by an elaborate discussion on their noise behaviour. A portrayal of the conventional noise parameter extraction techniques has been presented. These topics form the foundation of the transistor characterisation work detailed in chapter 6.

Chapter 3

LNA design using MMIC techniques

3.1 Introduction

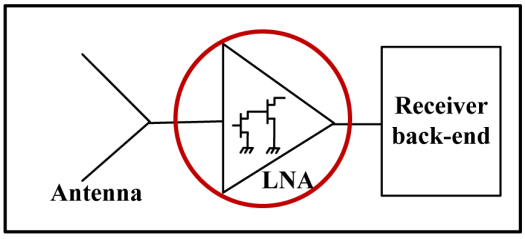

Figure 3.1: Focus of the chapter - Techniques of LNA design

This chapter focuses on the various aspects of MMIC LNA design. The primary objective of an LNA design is to retain a high SNR value at the output by minimising the noise contribution from the LNA. This is accomplished in multi-stage designs by aiming for a low noise figure and a high gain to minimise the noise contributions of subsequent stages. Other essential performance parameters are the input and output return losses, the bandwidth and the power consumption. These aspects of LNA design are discussed in section 3.2, and the conventional matching techniques are described in section 3.3.

Section 3.4 presents an overview of the MMIC technology. The primary difference between a MMIC and a MIC is that, in the former, both active and passive microwave components are fabricated on the same substrate. MMICs have found

widespread use in recent years in applications involving transmitting and receiving microwave signals because they allow many complex circuitries to be fabricated in a significantly reduced chip area. This enhances repeatability and decreases production costs [38]. Cellular systems, Global Positioning Systems (GPS) and satellite systems are representative examples of applications where MMICs are extensively used.

3.2 Design principles of LNAs

Modern day CAD softwares have considerably simplified circuit design procedures, and this applies to LNA design as well. However, an understanding of the fundamental principles of LNA design is a pre-requisite for developing an efficient design. Some of these aspects are discussed in the next subsections.

3.2.1 Noise Figure

The concepts of noise factor F, noise figure NF and noise parameters of linear noisy 2-ports have been discussed in section 2.6.3. The expression of F in terms of the 4 noise parameters and the source reflection coefficient Γ_s is:

$$F = F_{min} + \frac{4R_n}{Z_0}\left(\frac{|\Gamma_s - \Gamma_{opt}|^2}{|1+\Gamma_{opt}|^2\,(1-|\Gamma_s|^2)}\right) \tag{3.1}$$

At a specific bias, the locus of Γ_{opt} as a function of frequency can be plotted on the Smith Chart [42]. At a spot frequency, 'noise circles' are traced when Γ_{opt} is plotted on the Smith Chart for a set of constant noise factors. Noise circles display the complex relationship between Γ_s and F (or NF) in a convenient format, as shown in Figure 3.2. At a single frequency, the Γ_{opt} point is encircled by several noise circles which represent constant NFs for corresponding impedance mismatch from Γ_{opt} [42]. The rate at which the circles move away from Γ_{opt} is determined by the noise resistance R_n, implying that selecting transistors with a low R_n value comprises an essential criterion to achieve broadband designs. The equations for the centres and radii of the noise circles are provided in [42].

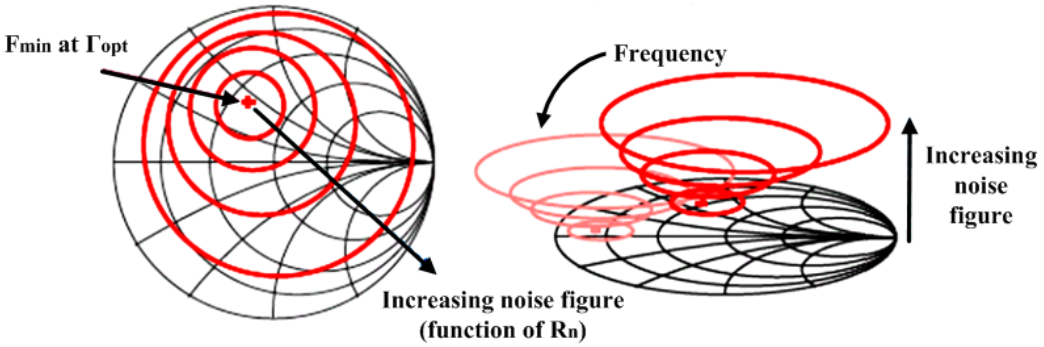

Figure 3.2: Noise circles on the Smith Chart and variation with frequency [47]

3.2.2 Gain

The gain of an LNA is one of its most important parameters. The gain of a 2-port network can be defined in 3 ways, the transducer gain G_T, the power gain G_p, and the available gain G_a, defined by equations 3.2 to 3.4 [42].

$$G_T = \frac{power\ delivered\ to\ the\ load}{power\ available\ from\ the\ source} \tag{3.2}$$

$$G_p = \frac{power\ delivered\ to\ the\ load}{power\ input\ to\ the\ network} \tag{3.3}$$

$$G_a = \frac{power\ available\ from\ the\ network}{power\ available\ from\ the\ source} \tag{3.4}$$

The gain of a LNA is commonly referred to the transducer gain G_T. However, in order to maximise G_T, a study of G_a and G_p of the transistors during intermediate-stage matching is essential. This helps a designer select appropriate transistor sizes for the different stages of the amplifier to generate the required gain in the frequency band of interest. Depending on the available gain G_a and the maximum available gain, MAG of the transistors, the number of stages required to achieve the desired gain from the LNA can be determined [42].

One figure-of-merit used by some design engineers, which takes into account both the noise and the gain performance, is the noise measure M, defined as [42]:

$$M = \frac{F - 1}{1 - 1/G} \tag{3.5}$$

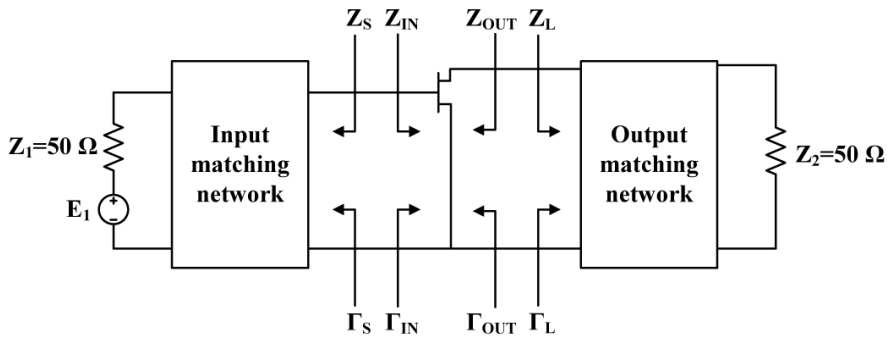

Figure 3.3: A single-stage microwave amplifier with matching networks [42]

Lower noise measure values indicate lower noise and higher gain.

3.2.3 Return Loss

High input and output return loss values ensure less loss of signal power and improvement in the design efficiency. A good input return loss is also required to decrease the noise coupling levels between adjacent elements in an antenna array system, as detailed later in chapter 12. In reality, obtaining good input return loss value while achieving good noise performance is more challenging in LNA design because of the separated positions of the noise and gain circles in the Smith Chart. An isolator prior to the LNA input can improve the input return loss. However, the system loss is increased, and the increased isolator dimensions at lower frequencies make them impractical to accommodate [19].

A standard technique of improving the return loss of an LNA is incorporating an inductive element in series with the source terminal. This is referred to as the source inductive feedback technique. This increases the real part of the transistor's input impedance and brings S_{11}^* and Γ_{opt} much closer, with only slight degradation in noise performance. This reduces the gain of the amplifier, and enhances the low-frequency stability [38, 56, 57]. In the present work, source inductive feedback has been used in both the C-band and the UHF-band MMIC LNA designs.

In terms of the 2-port S-parameters, and the source and load reflection coefficients Γ_s and Γ_l, the input and output reflection coefficients Γ_{IN} and Γ_{OUT},

indicated in Figure 3.3 are [42]:

$$\Gamma_{IN} = S_{11} + \frac{S_{21}S_{12}\Gamma_l}{1 - S_{22}\Gamma_l} \tag{3.6}$$

$$\Gamma_{OUT} = S_{22} + \frac{S_{21}S_{12}\Gamma_s}{1 - S_{11}\Gamma_s} \tag{3.7}$$

This is a bilinear transformation relation. As such, constant Voltage Standing Wave Ratio (VSWR) circles, which can be drawn on both the Γ_s and the Γ_l planes in the Smith Chart, can be mapped to the Γ_{OUT} and Γ_{IN} planes, respectively [42].

3.2.4 Bandwidth

The operating bandwidth of an amplifier is defined as the frequency band in which the amplifier exhibits the required gain. Over this frequency range, the gain remains within a specified peak-to-peak ripple [42]. However, for an LNA, the bandwidth can be viewed in 2 ways – the gain bandwidth (as defined above), and the noise bandwidth. The noise bandwidth implies the frequency band over which the noise matching remains within an acceptable level. For example, this may be defined in terms of 1 dB variation in NF.

One method of obtaining flatness in the gain curve is employing feedback techniques. Use of effective biasing networks in the design or adopting a passive filtering approach can also improve the gain response. The out-of-band gain curve is required to have good roll-off to diminish the possibilities of outside band oscillations [19]. One technique to achieve wider noise bandwidths is to select the optimum transistors with low R_n values for the designs.

3.2.5 Stability

The stability of an amplifier can be determined from the S-parameters, the matching networks and the terminations. In a 2-port network, the possibility of oscillations arises when a negative resistance is presented by either the input or output port, which occurs when $|\Gamma_{IN}|>1$ or $|\Gamma_{OUT}|>1$. The 2-port network is then said to be potentially unstable or not unconditionally stable, and this indicates that certain source and load terminations may produce oscillations. For a unilateral device (S_{12}=0), this occurs when $|S_{11}|>1$ or $|S_{22}|>1$ [42]. In terms of reflection

coefficients, the conditions for unconditional stability are [42]:

$$|\Gamma_s| < 1 \tag{3.8}$$

$$|\Gamma_l| < 1 \tag{3.9}$$

$$|\Gamma_{IN}| < 1 \tag{3.10}$$

$$|\Gamma_{OUT}| < 1 \tag{3.11}$$

Using equations 3.6 and 3.10 for the input side, and equations 3.7 and 3.11 for the output side, it can be deduced that the solutions to the boundary conditions $|\Gamma_{IN}| = 1$ and $|\Gamma_{OUT}| = 1$ produce a set of circles in the Γ_l and Γ_s planes, respectively. The circles on the 2 planes are called the source and load stability circles, respectively, and their centres and radii are provided by equations 3.12 and 3.13, and equations 3.14 and 3.15, respectively [42]:

$$C_s = \frac{S_{11} - \Delta S_{22}^*}{|S_{11}|^2 - \Delta^2} \tag{3.12}$$

$$R_s = \left| \frac{S_{12}S_{21}}{|S_{11}|^2 - \Delta^2} \right| \tag{3.13}$$

$$C_l = \frac{S_{22} - \Delta S_{11}^*}{|S_{22}|^2 - \Delta^2} \tag{3.14}$$

$$R_l = \left| \frac{S_{12}S_{21}}{|S_{22}|^2 - \Delta^2} \right| \tag{3.15}$$

where $\Delta = S_{11}S_{22} - S_{12}S_{21}$. With some calculations, it is also revealed that the necessary and sufficient conditions for an LNA to be unconditionally stable are the following [42]:

$$|\Delta| < 1 \tag{3.16}$$

$$K = \frac{1 - |S_{11}^2 - |S_{22}|^2 + \Delta^2}{2|S_{12}S_{21}|} > 1 \tag{3.17}$$

where K is another important and very frequently used parameter to inspect stability and is called the Rollet factor. In most microwave transistors produced by manufacturers, practical values of K lie in the range $0 < K < 1$. The source and load stability circles of these potentially unstable transistors intersect with the boundary of the Smith Chart. Unconditional stability can be achieved by resistive loading or incorporating negative feedback in the design, or by selecting

suitable Γ_s and Γ_l in narrowband designs [42].

The S-parameters of a device, and hence its stability, are both frequency and bias dependent. An LNA is unconditionally stable if equations 3.8 to 3.11, and 3.16 to 3.17 are satisfied across all frequencies for all bias conditions [42].

3.2.6 Power consumption

In applications requiring LNAs in large numbers, or in systems with limited power availability to drive the LNA, the power consumption becomes a crucial parameter. Examples include cryogenic applications with limited cooling capacity, antenna arrays with several receiver chains such as the SKA [4], ground-based communication receivers with limited access to power supply and satellite applications. Power consumption in an LNA perspective generally refers to the DC power consumption, because the RF power dissipation is negligible in comparison [19]. The power efficiency of the design is generally governed by that of the active devices, and is primarily determined by the process. For instance, GaAs based processes are generally more power hungry than InP based processes. Selecting an InP process will therefore provide an edge to applications where power efficiency is crucial. Implementing power efficient designs and allowing trade-offs with gain can also reduce the power dissipation.

3.3 Matching techniques in Multi-stage LNA design

The overall noise factor for a multi-stage LNA is given by the formula developed by Friis for receiver systems [58]:

$$F = F_1 + \frac{F_2 - 1}{G_1} + \frac{F_3 - 1}{G_1 G_2} + \frac{F_4 - 1}{G_1 G_2 G_3} + ... \tag{3.18}$$

where F_n and G_n are the noise factor and the available gain of component n in the chain. From equation 3.18, it is evident that in the LNA design context, the first stage noise factor, F_1, plays a crucial role in determining the F of the overall design. Additionally, a sufficiently high gain in the first stage is necessary to reduce the noise contribution of the second and subsequent stages. Hence, for the first stage, the primary design focus is on reducing the F while at the same

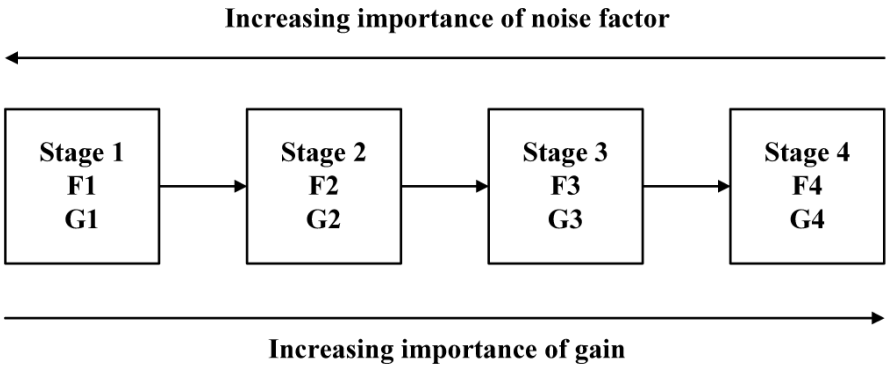

Figure 3.4: Implementation of Friis formula in LNA design

time obtaining a high gain value. In the latter stages, the gain assumes increasing importance, as illustrated in Figure 3.4.

3.3.1 Noise Matching

Noise matching is generally employed in the LNA first stage input, although some compromise may be required to simultaneously meet the input impedance specification. Noise matching is performed by incorporating suitable networks to transform the source impedance Z_s to the optimum noise impedance Z_{opt} of the transistor, so that F becomes equal to F_{min}. On some occasions, the transistor could be matched to impedances in close proximity to Z_{opt} to achieve, for example, a better input match [19]. Since R_n dictates the gradient of F away from Z_{opt}, it is a good practice to select a transistor with the lowest F_{min} and a low value of R_n, and then perform the noise matching.

3.3.2 Conjugate Matching

Inter-stage matching is generally a compromise between noise matching and power (or conjugate) matching to obtain the required gain response. The LNA output is usually conjugate matched to the characteristic impedance of the following stage in the receiver chain.

For a practical LNA, in which the unilateral condition may not be completely satisfied (that is, the reverse gain $S_{12} \neq 0$), an estimate of the gain is obtained from the available gain of the transistors [42]. It is mathematically expressed as

[42]:

$$G_a = \frac{|S_{21}|^2(1-|\Gamma_s|^2)}{|1-S_{11}\Gamma_s|^2(1-|\Gamma_{OUT}|^2)} \tag{3.19}$$

The objective of conjugate matching is to obtain the maximum available gain. This is a function of the Rollet stability factor K and is defined as [42]:

$$MAG = \frac{|S_{21}|}{|S_{12}|}\left(K - \sqrt{K^2-1}\right) \text{ for } K > 1 \tag{3.20}$$

Using equation 3.19, at a spot frequency, Γ_s can be plotted on the Smith Chart for constant values of gain, to obtain source gain circles, in a similar manner to noise circles. Similarly Γ_l can be plotted for constant values of gain to obtain load gain circles [42]. These facilitate suitable matching network designs. In practice, both noise and gain circles are plotted in the same Smith Chart over the desired frequencies to provide the designer with a better perspective.

3.3.3 Importance of passive components

The active components in an LNA design provide the required gain. The passive components constitute the matching circuit and the DC bias circuits, and thus form a crucial aspect of the design. The losses in the passive circuitry can degrade the NF, especially in the noise matching network. As such, in MIC LNA designs, low-loss passive components should be selected after wide investigation. The self resonance frequencies of the passive components also need to be considered to diminish the possibility of oscillations [19]. In MMIC LNA designs, the passive components are fabricated on the same substrate as the active components, using the process layers, and the library models incorporate the losses.

3.4 MMIC technology

The first MMICs were reported in 1968 [59, 60]. The first GaAs MMIC was demonstrated in 1976 [61]; it had a gate length of 1 μm and exhibited gain in the X-band. In the early 1980s MMICs were primarily used for niche applications such as satellite and military applications, but the development of mobile and wireless communications in the early 1990s ushered in the mass production of GaAs MMICs. Since then MMIC research and development has gained a high impetus. GaAs MMIC technology is presently a mature one and have a dominant

presence in power, low noise and passive applications from a few GHz to 100 GHz [20]. Research has also been focused on InP-based MMICs, and in recent years, on Silicon Germanium (SiGe) MMICs.

3.4.1 Comparison with MICs

A comparative analysis of the advantages and disadvantages of MMICs, with respect to MICs, are outlined below [22, 38]:

1. **Size and weight** - MMICs are smaller, and hence lighter, than their MIC counterparts. Both these features provide them a commercial advantage, as they can be more easily incorporated into mobile applications.

2. **Cost** - Fabrication costs for MMICs are much less compared to MICs, but only for larger quantities or complex circuits. A single wafer can produce 1000 or more amplifiers, with very similar characteristics and performance. However, due to the high running costs of fabrication facilities, production of smaller number of units is expensive.

3. **Reliability** - Reliability in MIC designs may suffer due to the separate assembly of components. This is not relevant to MMICs, and they are increasingly being used for space-borne applications because of their high reliabilities.

4. **Reproducibility** - MMICs have excellent reproducibility, because the active and passive components are produced through the same fabrication steps. MIC reproducibility is worse due to the need for device placement, soldering and bond-wiring.

5. **Choice of components** - MMICs suffer from a limited choice of components, and devices such as Gunn diodes and tunable filters are rarely incorporated in MMICs, either due to poor performance or increased design complexity. MICs do not exhibit these problems and a wide choice of devices and components is available.

6. **Turnaround time** - The MMIC fabrication process is significantly more time-consuming than that of MICs.

Although the advantages of MMIC outweigh the disadvantages, the passive component sizes (especially of inductors) offer a challenge in circuit size reduction. The resistive losses in MMIC passive components such as spiral inductors are also higher than their MIC counterparts, since they are created using high impedance transmission lines. These losses increase for low-resistivity substrates. When used in the input noise matching network, they significantly affect the LNA noise figure, especially at lower frequencies [38]. This is not a hindrance in MIC designs, and very low noise figure values have been obtained using MIC techniques. For instance, L-band and S-band MIC LNAs with 0.25 dB noise figures and over 14 dB gain have been reported [62]. However, the assembly of components using MICs becomes increasingly difficult at higher frequencies. This factor, coupled with the advantages offered by MMIC technology (namely, significantly improved reliability, repeatability and cost-effectiveness for high volume productions) render MMIC technology a natural choice in LNA designs for application at higher frequencies and/or requiring bulk production. Often, in an effort to minimise chip area (and hence cost) and improve noise figure especially at low frequencies, designers use off-chip components in conjunction with the MMIC chips. In spite of the degraded reproducibility, this method provides a compromise when necessary.

3.5 Summary

In this chapter a portrayal of various aspects of LNA design has been presented. Techniques of LNA design have been depicted with suitable reasoning. The principles of multi-stage design have been discussed and the primary objectives of each stage have been outlined. The main aim of LNA design is to attain the minimum noise figure, while optimising the gain and also the return loss. The various trade-offs in performance occurring between the different parameters have been discussed. A comparison has also been made between the MIC and MMIC technologies, both of which are used by LNA designers. The relatively small dimensions of MMICs enable significant miniaturization of RF and microwave circuits. MMIC technology has ushered in a new era in the LNA design technology. These principles underpin the design of 2 MMIC LNAs working in the C and UHF bands that has been undertaken in this research, and is discussed in chapter 6.

Chapter 4

Noise in low noise phased array systems

4.1 Introduction

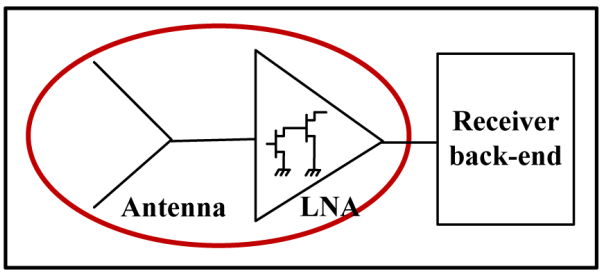

Figure 4.1: Focus of the chapter - coupled noise in phased array systems

Principles of LNA design have been outlined in chapter 3. For an LNA connected to a single antenna in a receiver chain, designing a suitable low-loss matching network between the antenna and the LNA ensures maximum SNR at the LNA output. Under such conditions, the only noise quantity of interest is the level of output noise. In certain other circumstances, however, the internally generated noise coming out of the LNA towards its input, back towards the antenna, may be of interest. This is of no consequence to the system just described, consisting of 1 antenna, as this noise is radiated away. However, in antenna array systems such as that proposed for the SKA project [4], where coupling between antennas can be a significant determinant of the overall system performance, it is very important to have knowledge of the levels of the noise coming from the input ports of the

LNAs. Some of this noise will couple to nearby antenna elements and contribute to the overall system noise. This chapter focuses on this aspect of system noise. Section 4.2 outlines the previous work by other researchers which inspected this aspect of system noise, and how the present work differs from those. Section 4.3 describes the theoretical principles that have been used to estimate the noise temperatures.

4.2 Previous work

Noise analysis of phased array feeds and dense aperture arrays is much less straightforward than the single-pixel feed case. The aspect of system noise for these arrays that has received much attention in recent years, in the SKA perspective, is the coupled noise between antenna elements: noise emanating from the input of a low noise amplifier that is coupled into adjacent antennas [29, 63, 64, 65]. An analysis technique has been developed by Maaskant *et al.* [66], and some results of this analysis suggest that surprisingly high levels of noise may be coupled between antenna elements, thus degrading their sensitivity. In the present work, an alternative approach to noise analysis of phased arrays has been presented. It looks at the coupled noise from the point of view of noise waves emanating from the input of each LNA, considering theory to evaluate these noise levels from the knowledge of the 4 noise parameters. It is based on the fundamental principles of noisy networks.

Some similar work has been previously described in radio astronomy [67], where the authors estimate the equivalent noise temperature in terms of the noise current flowing through the source impedance, when source inductive feedback is used in an LNA design to obtain a better VSWR. However, the derivation is valid only when the input side is matched for maximum gain. The theory used as part of the present work is more general in the sense that it is based on no assumptions about the technology of the amplifier, and is valid for any noisy 2-port.

Much work has previously been carried out to determine the noise levels emanating from the inputs of LNAs. Engen and Wait [68, 69] have published significant work in deriving a formula for the effective temperature at the input port of an LNA, T_{REV}. In their theoretical approach, they have expressed it in terms of both the amplifier's noise and S-parameters. They have also outlined a method to directly measure T_{REV} of an LNA. Wait, Randa and Walker [70, 71]

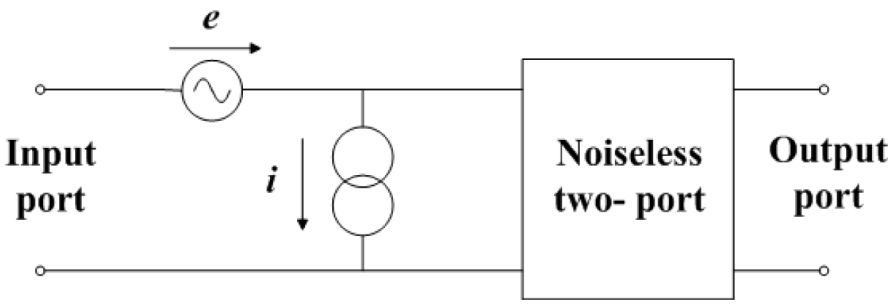

Figure 4.2: Rothe-Dahlke model of a linear noisy 2-port [44]

have carried out further measurements of the reverse temperature. Since T_{REV} is not normally used to determine the 4 noise parameters, Randa and Wait use the measurements as an independent check of the measured noise parameters. Weatherspoon and Dunleavy's [72] work provides equivalent results, but rely on extremely accurate measurements, which will be particularly difficult to achieve for the ultra low noise amplifiers required by the SKA. The present work differs in that rather than rely completely on measurements, well-established theoretical techniques have been used to determine the noise wave amplitudes.

4.3 Theory

The various representations of noise of a linear 2-port have been briefly discussed in section 2.6.2. The Rothe and Dahlke model [44] adopts the chain representation, shown in Figure 4.2, and is important because it facilitates the analysis of the circuit using the classical network theory approaches. Another important but rarely used representation is the wave representation. In this representation, a noisy 2-port is replaced by 2 noise wave sources in the forward and reverse direction. Such a representation of noise in linear 2-ports was originally proposed by Bauer and Rothe [73], and further work was done by Penfield [74]. Penfield's model simplifies this by considering that these 2 noise waves are uncorrelated. These are represented by a_n and b_n, respectively, at the input of the noise-free 2-port, as shown in Figure 4.3. These sources are related to the noise voltage and current sources, e and i, of the Rothe-Dahlke model [44], shown in Figure 4.2, through the relations:

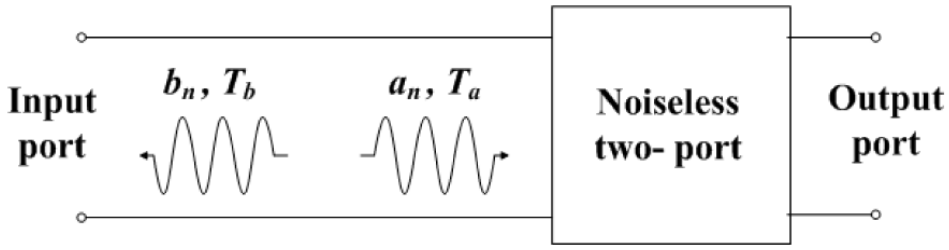

Figure 4.3: Penfield's wave representation of a linear noisy 2-port [74]

$$a_n = \frac{e + Z_\nu i}{2\sqrt{Re(Z_\nu)}} \tag{4.1}$$

$$b_n = \frac{e - Z_\nu i}{2\sqrt{Re(Z_\nu)}} \tag{4.2}$$

$$|a_n|^2 - |b_n|^2 = Re\{e_n i_n^*\} \tag{4.3}$$

where Z_ν is a normalizing impedance.

The noise wave sources a_n and b_n are associated with temperatures T_a and T_b defined by:

$$T_a = \frac{\overline{|a_n|^2}}{k\Delta f} \tag{4.4}$$

$$T_b = \frac{\overline{|b_n|^2}}{k\Delta f} \tag{4.5}$$

where k is the Boltzmann constant and Δf is the frequency interval. For the present scenario, the focus of interest lies in evaluating the equivalent temperature of the noise wave b_n travelling from the input of an LNA towards the antenna, plus any component of the equivalent temperature of the noise wave a_n reflected back from the input of the 2-port. Penfield has provided closed-form expressions of these temperatures in terms of the 4 noise parameters as well [74]:

$$T_a = T_{min} \tag{4.6}$$

$$T_b = \frac{4T_0 R_n}{Re(Z_{opt})} - T_{min} \tag{4.7}$$

where $T_0 = 290$ K and T_{min} is the minimum noise temperature.

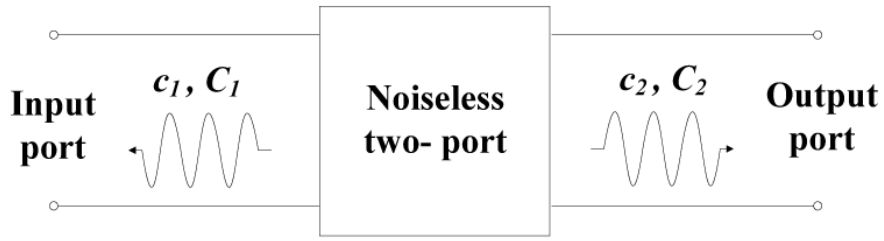

Figure 4.4: Wedge and Rutledge's representation of a linear noisy 2-port [75]

These equations are simple and straightforward to use. However, the simplification applied by Penfield, by disregarding the correlation effect, is valid only when the noise waves are normalized to the optimum source impedance of the 2-port. This is the ideal noise match condition, when the noisy 2-port is looking into an impedance of Z_{opt} at its input. Under this condition, the correlation component of noise generated by the correlation between the forward and the reverse wave becomes zero [74]. However, when this condition is not satisfied, the correlation component between the reverse and forward waves cannot be neglected any more, and must be taken into account in the relevant computations. The work done by Meys [76] and Wedge and Rutledge [75] are significant in this context. In these formulations, 2 correlated noise waves are used, the advantage being that the noise waves are normalized to an arbitrary real characteristic impedance of the surrounding transmission line or wave-guide elements.

Meys defines both the forward and reverse waves at the input, like Penfield, and additionally defines a temperature T_c associated with the correlated component $\overline{a_n^* b_n}$, the magnitude and angle of which are:

$$|T_c| = \frac{4T_0 R_n}{Z_0} |\Gamma_{opt}| \tag{4.8}$$

$$\phi_c = \pi - arg(\Gamma_{opt}) \tag{4.9}$$

Both the Penfield and the Meys models consider noise waves at the input of the 2-port. Wedge and Rutledge [75] outlined another approach to investigate the problem by considering noise waves c_1 and c_2 at the input and output of the noisy 2-port, respectively, as shown in Figure 4.4. If the 2-port is represented by the

S-parameter matrix S

$$\begin{pmatrix} b_1 \\ b_2 \end{pmatrix} = \begin{pmatrix} S_{11} & S_{12} \\ S_{21} & S_{22} \end{pmatrix} \begin{pmatrix} a_1 \\ a_2 \end{pmatrix} \tag{4.10}$$

then the waves in Meys' and Penfield's approach are incorporated as

$$\begin{pmatrix} b_1 - b_n \\ b_2 \end{pmatrix} = \begin{pmatrix} S_{11} & S_{12} \\ S_{21} & S_{22} \end{pmatrix} \begin{pmatrix} a_1 + a_n \\ a_2 \end{pmatrix} \tag{4.11}$$

whereas the waves in Wedge and Rutledge's approach are given by

$$\begin{pmatrix} b_1 - c_1 \\ b_2 - c_2 \end{pmatrix} = \begin{pmatrix} S_{11} & S_{12} \\ S_{21} & S_{22} \end{pmatrix} \begin{pmatrix} a_1 \\ a_2 \end{pmatrix} \tag{4.12}$$

The noise powers delivered to the terminations in a 1-Hz bandwidth, $\overline{|c_1|^2}$ and $\overline{|c_2|^2}$, and the correlation power $\overline{c_1 c_2^*}$ in terms of the noise and S-parameters of the 2-port are [75]:

$$\overline{|c_1|^2} = kT_{min}\left(|S_{11}|^2 - 1\right) + \frac{4kT_0R_n}{Z_0} \times \frac{|1 - S_{11}\Gamma_{opt}|^2}{|1 + \Gamma_{opt}|^2} \tag{4.13}$$

$$\overline{|c_2|^2} = |S_{21}|^2 \left(kT_{min} + \frac{4kT_0R_n}{Z_0} \times \frac{|\Gamma_{opt}|^2}{|1 + \Gamma_{opt}|^2}\right) \tag{4.14}$$

$$\overline{c_1 c_2^*} = \frac{4kT_0R_n}{Z_0} \times \frac{-S_{21}^*\Gamma_{opt}^*}{|1 + \Gamma_{opt}|^2} + \frac{S_{11}}{S_{21}} \times \overline{|c_2|^2} \tag{4.15}$$

where $\left(\overline{|c_2|^2}/k\right)$ is the noise temperature of the 2-port multiplied by the gain of the 2-port (considering a 1-Hz bandwidth).

Though both the Meys' and Wedge and Rutledge's representations consider the correlated noise, the latter representation has been preferred for the current evaluation process owing to the following reasons:

1. Expressions of the noise powers in equations (4.13) – (4.15) include the S-parameters making computations easier.

2. $\overline{|c_1|^2}$ is the deliverable noise power to the input termination (in this case an antenna element) in a 1-Hz bandwidth, which is the present quantity of interest. Let $C1$ be the temperature associated with this deliverable noise power

$\left(\overline{|c_1|^2}/k\right)$.

3. It may be of interest to know the noise temperatures of the 2-port at the output as well, provided by $\overline{|c_2|^2}$.

4. Circuit simulation softwares such as Advanced Design System (ADS) from Agilent Technologies [77] calculate noise powers based on this approach, thus verification by simulation, if required, becomes considerably easier.

It should be reiterated that any of the 3 approaches discussed above can be used for determination of the effective temperature of the reverse noise wave emanating from the input port of any noisy 2-port, each with its limitations. The Wedge and Rutledge's approach is selected here because of its completeness and the advantages discussed above.

4.4 Summary

This chapter described a theory to evaluate the effective noise temperature at the input port of an LNA, which provides useful information in in certain design scenarios such as the SKA antenna array environment. The theory has been implemented using MATLAB [30], and used to predict the noise levels emanating from the input ports of 2 COTS packaged amplifiers, after their noise parameters have been determined with appropriate tuner measurements. Measurements have then been performed to experimentally determine these levels, in terms of effective temperatures, for the 2 amplifiers. The measurement techniques used to verify the theory, and the experimental arrangement used are described in section 8.3. The results of noise measurements on the packaged amplifiers are presented in chapter 12. In the same chapter, the theoretical principle is used to estimate the amount of noise coupling between adjacent antennas in a low noise phased array system such as the SKA. The SKA plans to utilize phased arrays in at least 3 different forms: as sparse and dense aperture arrays on the ground, and as phased array feeds on dishes; therefore such a noise analysis is important.

Chapter 5

Essentials of microstrip patch antennas

5.1 Introduction

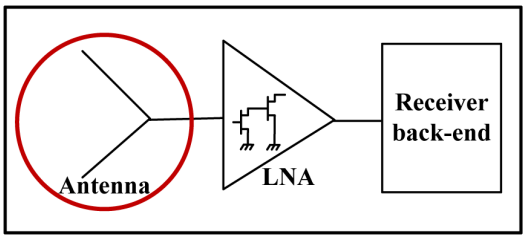

Figure 5.1: Focus of the chapter - overview of MPAs

MPAs and their variations have attracted considerable attention in the past few decades. They offer effective low-profile designs for a wide range of wireless applications. The antennas are compact and compatible with MICs for high frequency applications. It is also comparatively simpler to manufacture arrays utilising these structures. Unfortunately, they have some disadvantages, such as relatively low gain, narrow bandwidth and increased sensitivity to fabrication tolerances [31]. However, due to the rising demands for multi-band operation in wireless applications, requiring light-weight, inexpensive and compact antenna structures, research and development on MPAs continue to flourish [31, 78, 79]. This chapter presents an overview of the design principles of MPAs.

A brief discussion on some fundamental parameters of antennas in general,

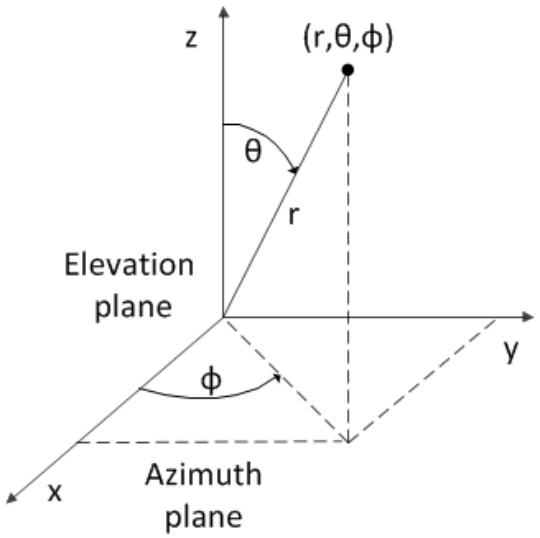

Figure 5.2: Spherical coordinate system generally used in antenna analysis [80]

in section 5.2, is followed by a discussion on the operating principle of MPAs in section 5.3. The various design parameters that determine the performance of MPAs are discussed in section 5.4. Finally the different methods to feed these antennas are outlined in section 5.5.

5.2 Fundamental parameters of antennas

Some of the useful parameters of antennas, that are relevant in context of the present work, are defined in this section. These are as follows [80]:

1. Far-field radiation pattern: The radiation pattern of an antenna is defined as a "graphical representation of the radiation properties of the antenna as a function of space coordinates" [81], where a convenient set of space coordinates is the spherical coordinate system shown in Figure 5.2. The far-field radiation pattern is then defined as "that region of the field pattern of an antenna where the angular field distribution is independent of the distance from the antenna" [80]. In Figure 5.2, the z plane is the azimuth or horizontal plane, and the y plane is the elevation plane.

2. Principal radiation planes: The radiation pattern is often described in terms of principal planes for linearly polarized antennas. There are two principal planes, the E-plane and the H-plane. The E-plane is defined as "the plane containing the electric-field vector and the direction of maximum radiation", and

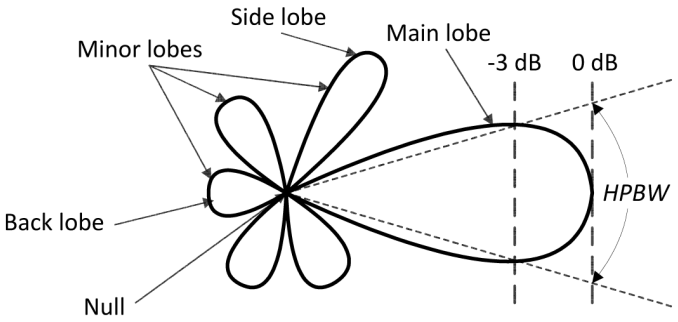

Figure 5.3: Major and minor lobes and $HPBW$ in the radiation pattern of a directional antenna [82]

the H-plane as "the plane containing the magnetic-field vector and the direction of maximum radiation" [80]. The E-plane and H-plane for a patch antenna are discussed in section 5.3. It is a general practice to orient antennas in a manner to coincide the geometrical planes with at least one principal plane.

3. Radiation pattern lobes: A radiation lobe is defined as a "portion of the radiation pattern bounded by regions of relatively weak radiation intensity" [80]. They are classified into major (or main), minor, side, and back lobes. The major lobe is the radiation lobe which contains the direction of maximum radiation, and is also called the main beam. All other lobes, like side lobe and back lobe, are classed as minor lobes. Side lobes are generally adjacent to the main lobe and occupy the same hemisphere in the direction of the main beam. Side lobes generally constitute the largest of the minor lobes. A minor lobe whose axis is directed exactly opposite to the main beam axis (at approximately 180 °) is called a back lobe. The minor lobe level is defined as the ratio of the power density in the minor lobe to that in the major lobe. This quantity is generally expressed in dB [80].

In general, the intention of any design is to reduce the minor lobes, as they represent radiation in undesired direction. In certain circumstances, however, when the radiation pattern needs to extend over most of the hemisphere, their existence may not be completely undesirable, provided the side lobe levels are not too small.

4. Radiation intensity and isotropic antenna: The radiation intensity in a specific direction is a far-field parameter and is defined as "the power radiated from an antenna per unit solid angle" [81].

An isotropic antenna is defined as "a hypothetical, lossless antenna having equal radiation intensity in all directions" [81]. Therefore, for an isotropic antenna, the radiation intensity U_0 in terms of the total power P_{rad} is:

$$U_0 = \frac{P_{rad}}{4\pi} \tag{5.1}$$

5. Directivity, gain and efficiency: The directivity of an antenna is defined as "the ratio of the radiation intensity in a given direction from the antenna to the radiation intensity averaged over all direction" [81]. When directions are not specified, the maximum radiation intensity U_{max} is implied. The average radiation intensity is equal to the total power radiated by the antenna divided by 4π. For an isotropic antenna, this is a constant quantity. As such, the directivity of an antenna can also be defined as the ratio of its radiation intensity in a given direction to that of an isotropic antenna. This is expressed as:

$$D_{max} = \frac{U_{max}}{U_0} = \frac{4\pi U_{max}}{P_{rad}} \tag{5.2}$$

The directivity does not include any dissipative losses. The measure of performance which takes these into account is the gain. It is defines as "the ratio of the radiation intensity, in a given direction, to the radiation intensity that would be obtained if the power accepted (P_{in}) by the antenna were radiated isotropically" [81]. In a mathematical format, this is expressed in equation 5.3.

$$G = \frac{4\pi U_{max}}{P_{in}} \tag{5.3}$$

Another frequently used term, the relative gain, is defined as "the ratio of the power gain in a given direction to the power gain of a reference antenna in its referenced direction" [81]. The power input must be the same for both antennas. The reference antenna is usually a dipole, horn, or any other antenna with calculable gain [80].

The radiation efficiency η of the antenna is defined as the ratio of the gain to the directivity, and mathematically expressed as:

$$\eta = \frac{gain}{directivity} = \frac{P_{rad}}{P_{in}} \tag{5.4}$$

In the context of discussion on MPAs, which tend to be of small dimensions in

some applications [83], it is important to note that there is a fundamental limit on the efficiency of electrically small antennas. In electrically small antennas, the sphere enclosing the antenna element is very small, and little propagation exist. The energy is contained primarily within the reactive near-field. Since little radiation is obtained in the far-field region of the antenna, the radiation efficiency decreases significantly [80]. In MPA design work, consideration of this effect is necessary when dimensions are reduced.

6. Beamwidth: The beamwidth of a radiation pattern is defined as "the angular separation between two identical points on opposite side of the radiation pattern maximum" [80]. "In a plane containing the direction of the maximum of a beam, the angle between the two directions in which the radiation intensity is one-half value of the beam" [81] is called the Half Power Beam Width ($HPBW$), and is most widely used. This is also referred to as the 3 dB beamwidth. The angular separation between the first nulls of the pattern is referred to as the First Null Beam Width ($FNBW$) [80]. Other beamwidths can be defined, however, in practice, the term beamwidth usually refers to the $HPBW$.

7. Input impedance: The input impedance of an antenna is defined as "the impedance presented by an antenna at its terminals" [81]. The input impedance need to be matched to the system impedance at least at the centre frequency (usually the resonance frequency f_r).

8. Bandwidth: The bandwidth of an antenna is defined as "the range of frequencies within which the performance of the antenna, with respect to some characteristic, conforms to a specified standard" [80]. This can be considered to be the range of frequencies on either side of f_r, where the antenna characteristics (such as input impedance, radiation pattern, beamwidth, side lobe level, gain, beam direction, radiation efficiency) are within an acceptable value of those at f_r.

For example, the variation of the input impedance with frequency implies that the frequency range over which the antenna impedance can be matched to the feed line is limited. For the present work, the 10 dB return loss bandwidth (a very common standard used in antenna design), where the return loss is greater than 10 dB, has been used.

For broadband antennas, the usual method of expressing bandwidth is the ratio of the upper-to-lower frequencies of acceptable operation. For example, a 10:1 bandwidth would indicate that the upper frequency is 10 times greater

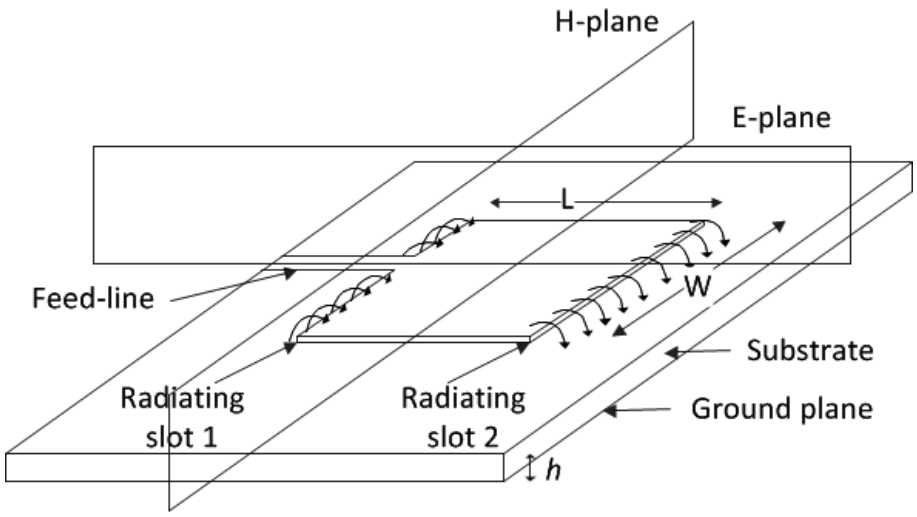

Figure 5.4: Rectangular microstrip patch antenna [84]

than the lower. For narrowband antennas, like microstrip patch antennas, the bandwidth is expressed as a percentage of the frequency difference (upper minus lower) over f_r. For example, a 10 % bandwidth indicates that the frequency difference of acceptable operation is 10 % of f_r.

5.3 Operating principle of MPAs

An MPA consists of a very thin metallic patch placed on a thin layer of dielectric sheet (substrate) above a ground plane [84]. Figure 5.4 illustrates the structure of a typical rectangular MPA. Electromagnetic energy is coupled to the antenna using a microstrip feed line. A coaxial cable can also be used; the central conductor of the coax serves as the feed probe [85]. L and W are the length and width of the radiating element. In the simplest configuration, the electrical length of a rectangular MPA is half wavelength at f_r. The substrate height is indicated by h in the figure.

The two radiating slots are shown in Figure 5.4. In the fundamental mode of operation, the electric field is zero at the centre of the MPA, maximum (positive) at one edge, and minimum (negative) on the opposite edge. The minimum and the maximum continuously change side according to the instantaneous phase of the applied signal. The electric field does not terminate abruptly at the MPA's periphery, but extends beyond the outer periphery to some degree. These field

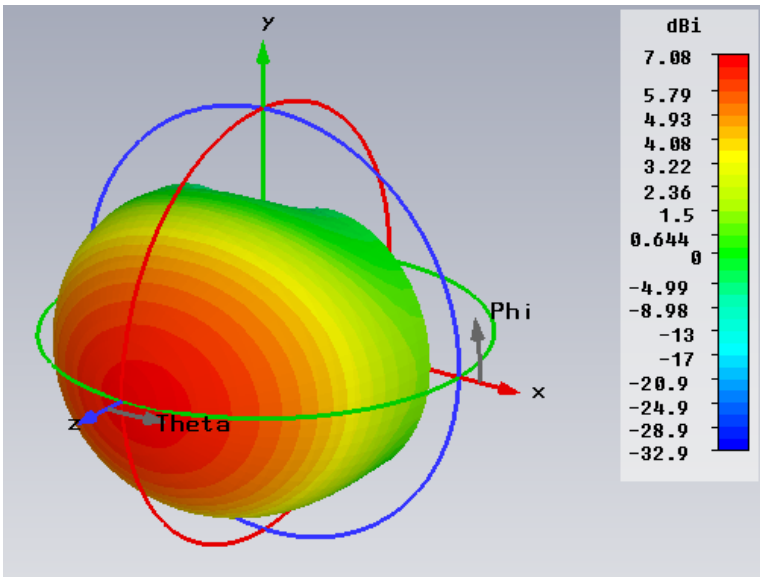

Figure 5.5: Typical 3D radiation pattern from a half-wavelength rectangular patch antenna

extensions are known as fringing fields and cause the MPA to radiate [84]. The radiating edges, and the electric field lines near these are indicated in Figure 5.4. Figure 5.4 also shows the E-plane and the H-plane.

A rectangular MPA excited in its fundamental mode has a maximum directivity in the direction perpendicular to the MPA (broadside), approximately 5 – 7 dB. The radiated field strength decreases when moving away from broadside direction. An example of the radiation pattern from a half-wavelength rectangular MPA placed in the z plane is shown in Figure 5.5. The beamwidth is similar in both the x and y planes, creating approximately a hemisphere of radiation outwards from the MPA. Typically, the 3 dB beamwidth is approximately 65°, or 32.5° either side of bore-sight.

Rectangular MPAs are extremely narrow-band, with the bandwidths being typically 2 – 5 % [84]. The essential parameters for the design of an MPA and how they affect performance are discussed in section 5.4.

5.4 Essential design parameters

An understanding of how the different design parameters of an MPA affect its performance and the various trade-offs in play is a pre-requisite for design. These

design parameters are discussed in brief below [31, 80]:

1. Patch length: The patch length L controls the resonant frequency f_r, and is inversely proportional to it. In the fundamental mode of operation, f_r is approximately given by:

$$f_r = \frac{c}{2L\sqrt{\epsilon_r}} \tag{5.5}$$

where c is the speed of light and ϵ_r is the relative permittivity of the substrate. However, in reality, due to the fringing fields around the antenna, the effective length of the patch is greater than its physical dimensions [31]. If the extension on each side is denoted by ΔL, a popular practical estimate of this quantity, normalised to the substrate height h, is given by [80, 86]:

$$\frac{\Delta L}{h} = 0.412\frac{(\epsilon_{eff} + 0.3)\left(\frac{W}{h} + 0.264\right)}{(\epsilon_{eff} - 0.258)\left(\frac{W}{h} + 0.8\right)} \tag{5.6}$$

where ϵ_{eff} is the effective permittivity, and W is the width of the patch. The effective patch length L_{eff} after extension is:

$$L_{eff} = L + 2\Delta L \tag{5.7}$$

This effective increase in patch length leads to a lower f_r than ideal. Hence, when designing a patch, the f_r in equation 5.5 should be modified to provide the effective f_r, $f_{r_{eff}}$:

$$f_{r_{eff}} = \frac{c}{2L_{eff}\sqrt{\epsilon_{eff}}} = \frac{c}{2\left(L + \Delta L\right)\sqrt{\epsilon_{eff}}} \tag{5.8}$$

where ϵ_{eff} is given by [31]:

$$\epsilon_{eff} = \frac{\epsilon_r + 1}{2} + \frac{\epsilon_r - 1}{2}\left[1 + 10\frac{h}{W}\right]^{0.555} \tag{5.9}$$

Once the width W is determined (from equations described later in this section), ϵ_{eff} can be evaluated from equation 5.9. ΔL, L_{eff} and $f_{r_{eff}}$ can subsequently be derived from equations 5.6, 5.7 and 5.8, respectively.

2. Patch width: The width W affects the bandwidth of the MPA. A practical initial value to start a design process is given as [87]:

$$W = \frac{c}{2f_r}\sqrt{\frac{2}{\epsilon_r + 1}} \tag{5.10}$$

This parameter is generally optimised using the design software to obtain the final W. It is an established design criterion that a patch with larger W has higher efficiency [31]. However, W should be restricted to a certain limit to prevent excitation of higher-order modes and associated field distortions [84]. Both L and W determine the far-field radiation properties of the MPA [31].

3. Relative permittivity of the substrate: The relative permittivity of the substrate, ϵ_r, is one of the most important design parameters. It controls the fringing fields, with lower ϵ_r resulting in wider fringes, better radiation and hence increased efficiency. A lower ϵ_r decreases the Q-factor, and as the bandwidth is inversely proportional to the Q-factor [31], the bandwidth increases. However, higher ϵ_r values allow "shrinking" of the patch antenna, as evident from equation 5.5. For a given f_r, if ϵ_r is increased by a factor of 4, L decreases by a factor of 2, resulting in reduced antenna dimensions.

4. Height of the substrate: The substrate height h controls the bandwidth, the latter being proportional to the former. However, increase in h also induces surface waves that travel within the substrate (which is undesired radiation and may couple to other components) [31].

5. Size of the ground plane: Radiation toward the back of the substrate is greatly reduced by the shielding effects of the ground plane. The amount of reduction depends on the extent to which the ground plane extends beyond the patch area [88]. The extension of the ground plane on each side of the patch should be minimum 6 times of h for efficient radiation [31].

6. Location of feed point: For use in a standard 50 Ω system, the feed point to the antenna must be located at that point on the patch, where the input impedance is closest to 50 Ω for a given f_r. Equations for determining an initial approximation of the impedance at the edge of the patch and at a certain length along the axis of the patch can be obtained from [31]. Often CAD optimisation tools are used to optimise the feed point location. A point exists along the patch length where the return loss RL is maximum, indicating the best match to the system impedance. The return losses obtained at various feed point locations can

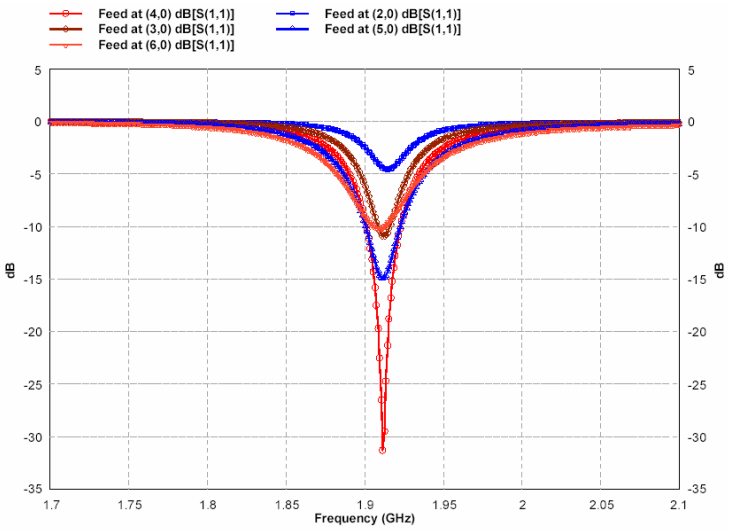

Figure 5.6: Variation in return loss with change in feed point [82]

be compared to locate the optimum feed point for a given system impedance [80].

The feed location has an effect on the resonant frequency, the return loss and the bandwidth. This is illustrated in Figure 5.6 for a reported work [82]. In Figure 5.6, the feed location for a patch with $L = 22$ mm ($f_r = 1.9$ GHz) has been varied along the patch length from the centre of the patch to its right edge. Thus, a feed at (x,0) represents a x mm shift from the centre towards the right. It is observed that the return losses vary between 5 and 32 dB even with very slight variations in feed location.

5.4.1 Factors affecting bandwidth and directivity

The bandwidth of a rectangular MPA is proportional to the patch width W and the substrate height h, and is also dependent on the relative permittivity ϵ_r. The plots in Figure 5.7 illustrate the significance of ϵ_r and h. These are results obtained for an antenna designed with Rogers RT/Duroid 5880 ($\epsilon_r = 2.2$, h= 0.76 mm), reported in [31]. As per observation, as h increases,

1. the bandwidth increases - the rate of increase is inversely proportional to the value of ϵ_r.

2. the directivity increases slightly - lower ϵ_r values are required to achieve higher directivity.

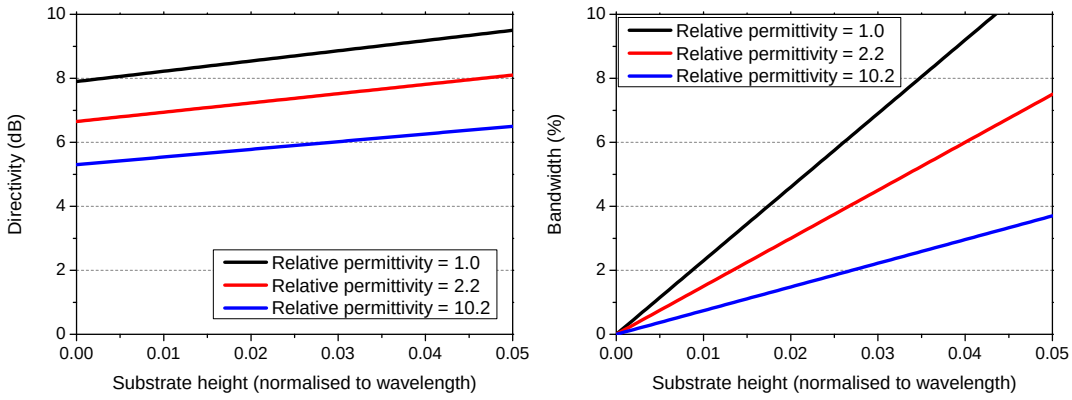

(a) Variation of directivity (b) Variation of bandwidth

Figure 5.7: Example plots showing variation of directivity and bandwidth with substrate height for different relative permittivities

The relevance of these inferences in the present design is discussed in chapter 7, where the detailed design and simulation are presented.

5.5 Feed considerations

Figures 5.8 (a)-(e) show some of the feed methods generally employed in MPA designs. The relatively simpler feed methods from the fabrication point of view are the coaxial probe feed and the microstrip feed. Although simple to fabricate, microstrip feed lines radiate, and hence alter the radiation pattern. Additionally, since the input impedance at the patch edge is very high, either an inset feed line or a quarter wavelength line is required to match to a 50 Ω system, as shown in Figures 5.8 (a) and (b). Coaxial probe feed, though comparatively difficult to fabricate, makes impedance matching easier. This also eliminates radiation losses from the feed structure.

5.6 Summary

In this chapter, the general parameters of antennas relevant to the present work has been discussed, followed by the fundamentals of MPAs and their operation. Variations of antenna response with respect to different design parameters for rectangular MPAs have been detailed. The performance depends significantly on

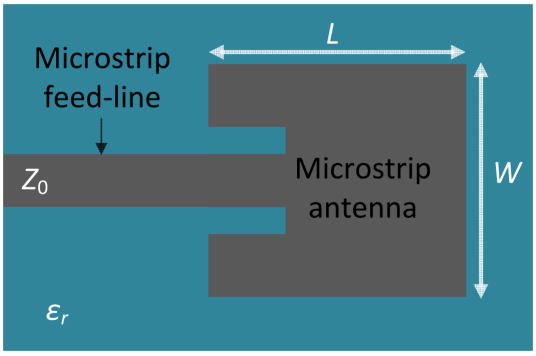

(a) MS line inset feed

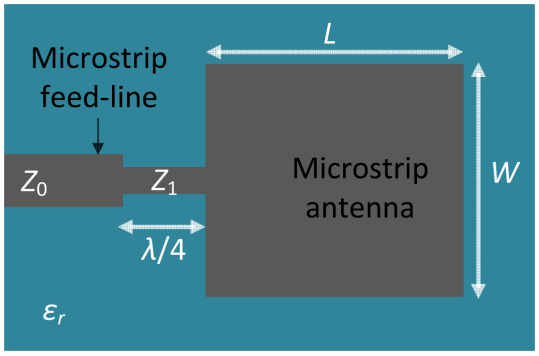

(b) MS line feed employing a quarter-wavelength matching section

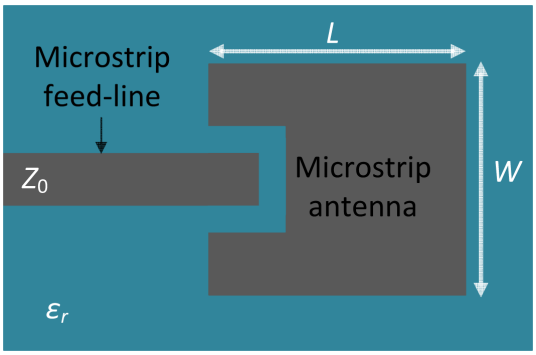

(c) MS line coupled (indirect) inset feed

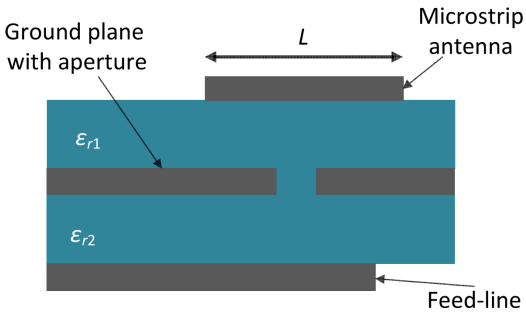

(d) MS line aperture coupled feed

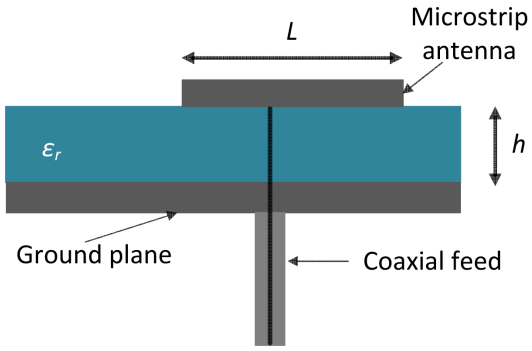

(e) Coaxial cable feed

Figure 5.8: Conventional feed methods employed in patch antennas [31]

the electrical and mechanical properties of the substrate, as well as the patch dimensions. Thus, a practical design would involve optimisation of all properties to attain the desired performance.

Some of the conventional feed mechanisms used to couple energy to patch antenna structures have also been highlighted. Chapter 7 elaborates the patch antenna design work. The observations made in the present chapter have been considered, and suitable modifications and trade-offs have been employed to produce an antenna structure which fulfils the design requirements.

Chapter 6

Transistor characterisation and LNA design

6.1 Introduction

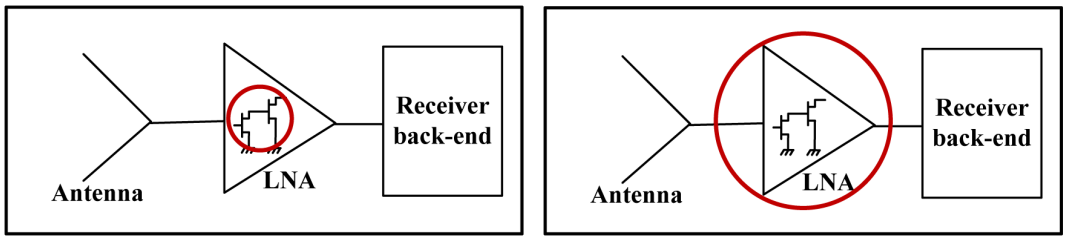

(a) (b)

Figure 6.1: Focus of the chapter - transistor characterisation and LNA design

This chapter focuses on the LNA block of the receiver front-end. The first step in LNA design comprises of selecting appropriate transistors from available low noise processes. Careful selection of the technology, topology and size of devices is necessary to obtain the desirable DC, RF and noise performances in the operating frequency band. This can be accomplished by characterisation of available transistors from low noise processes. Section 6.2 describes the transistor characterisation work that has been presently undertaken. Measurements have been performed on a wide variety of transistors in the Agilent Millimetre-wave Laboratory in the School of Electrical and Electronic Engineering at The University of Manchester.

The designs of 2 MMIC LNAs, based on 2 different processes, and operating in the C-band and the UHF-band, are presented in section 6.3. The working frequency of the C-band LNA is the entire C-band, 4 – 8 GHz, and that of the UHF-band LNA is 0.4 – 1 GHz.

6.2 Transistor characterisation

The current trends in the ever-emerging communications sector indicate that future communications receivers would continue to be increasingly diverse in nature. This would reflect in increasing diversity in LNA designs as well. For niche and/or one-time applications, the transistors for LNA development should provide the best noise and gain performances for the particular operation. Cost or power considerations may not be limiting factors in these one-off design scenarios. For example, in a satellite system, low cost may not be a limitation but the power considerations may still be a key driving factor.

Others applications may require more robust designs. For instance, mass production of mobile handsets necessitate that the transistor technologies used in LNA development are mature and robust ones. The pre-requisites are not only good performances in the operating bands, but also high repeatability, high reliability, high reproducibility and high yield in the fabrication process. Fulfilment of these requirements automatically reduces production costs, and expands the market to include a broader range of customers. Hence, in essence, as communication systems get increasingly diversified, the choice of the processes for LNA development becomes progressively crucial and challenging.

Subsection 6.2.1 outlines the importance of this characterisation work in multi-stage LNA design, with emphasis on the relevance to the SKA. Subsection 6.2.2 provides information about the DC, S-parameter and noise analysis.

6.2.1 Significance in multi-stage LNA designs

The various objectives of LNA design have been discussed in section 3.2. To achieve overall low NF values, the first stage transistor should have a low value of NF_{min}, with sufficient gain to overcome the noise contributions from subsequent stages. The transistors for the subsequent stages should have high gain. For broad band designs, low R_n values are required. Also, depending on the chip area, non-optimum alternatives may have to be considered.

Large antenna arrays used for radio astronomical observations, such as the SKA, provide excellent examples of applications which necessitate comprehensive transistor characterisation. Some of the aspects of the SKA project which have repercussions on device selection are highlighted here:

1. To render the telescope 50 times more sensitive than the present radio astronomical telescopes (at comparable frequencies), transistors with ultra low NF_{min} and high gain are required for the front-end LNAs.

2. Achievement of broadband designs necessitates low values of R_n. The noise analysis in section 11.3 will also show that low R_n is also essential to reduce the coupled noise between adjacent antenna elements.

3. It is estimated that more than 30 million LNAs would be required in the project. Hence, the processes need to have excellent repeatability, reliability and yield. Power efficiency also assumes a critical role and needs to be evaluated.

4. To facilitate continued observation for extended periods of time, a mature, robust and long-lasting technology is a pre-requisite.

5. The prospective sites of construction are either in Australia - New Zealand or Southern Africa, due to the privileges they offer in terms of low RFI levels. Both these sites experience a significant diurnal variation of temperature. The widely distributed architecture of the SKA also implies the possibility of having considerable difference in temperatures at separate locations at the same time. Therefore, an evaluation of the deviations from the desired performance with temperature fluctuations is important.

Considering these factors, it is not an overstatement that the best possible low noise processes and transistors to optimise performance can be selected for the SKA only after a comprehensive transistor characterisation.

Table 6.1 lists the HEMT transistors that have been characterised in the present work. These devices are of different topologies (pHEMTs or mHEMTS), based on different substrate technologies (GaAs and InP), with gate lengths ranging from 70 nm to 250 nm and a wide range of gate widths. In Table 6.1, 'M×N' indicates that N samples of M different sizes of transistors have been measured. Although S-parameters of all processes have been determined, the noise parameter characterisation has been limited to 6 of the promising processes. The measured or extracted parameters (from measurements) consist of the transconductance, drain and gate currents, gate voltages, power consumption, noise figure, minimum noise figure, noise measure, noise resistance and optimum

Table 6.1: List of Measured Samples

Process	Different sizes	DC, S-param samples	Noise samples	Details
1	8	8x2	7x2	150 nm GaAs pHEMT
2	9	9x2	-	150 nm GaAs mHEMT
3	4	4x2	4x2	130 nm GaAs pHEMT
4	7	7x2	4x2	100 nm InP pHEMT
5	8	8x2	-	150 nm GaAs mHEMT
6	6	6x2	3x2	70 nm GaAs mHEMT
7	1	1x2	-	150 nm GaAs pHEMT
8	1	1x2	-	100 nm InP pHEMT
9	4	4x2	4x2	100 nm GaAs pHEMT
10	5	5x2	5x2	250 nm GaAs pHEMT
Total	53	104	54	10 processes

noise impedance.

6.2.2 DC, *S*-parameter and noise characterisation

The important aspects and benefits of DC, *S*-parameter and noise characterisation in context of LNA design are highlighted in the following subsections.

DC characterisation

DC (or static) characterisation is an excellent starting point of transistor characterisation. The transconductance g_m determines the gain, the noise figure and the cut-off frequency of a transistor. DC characteristics also provide information on the power consumption at different biases, and a qualitative comparison of the power efficiency of different processes can be achieved. For applications where power efficiency is critical, detailed analysis of DC curves can provide information on the variation of g_m with variation in power consumption. Static characteristics can also provide clue to the optimum biases for minimum noise temperature, as proposed in [35].

The small-signal and noise responses of HEMTs are heavily dependent on the gate and drain biases. Determination of these parameters over an extensive bias space could therefore be extremely beneficial. In reality, conducting measurements over an exhaustive bias range is time-consuming, especially with

the wide range of device sizes available from the majority of advanced foundries. DC characteristics provide the foundation for selecting a suitable subset of bias points.

The present work encompasses DC characterisation of 10 low noise processes over a range of bias combinations. Issues arising from lack of repeatability of a process have been highlighted. Deviations in the g_m values with variations in the operating temperatures have also been studied.

S-parameter characterisation

The success of an LNA design work relies heavily of the accuracy of the process library. If the library models are not sufficiently accurate, complete reliance on these may lead to inconsistencies in the performances of the fabricated LNAs. For instance, the gain may be reduced or the LNAs may exhibit oscillatory behaviour. Furthermore, the majority of the process libraries are based on either linear small-signal models at specific bias combinations, or large-signal models. Libraries based on large-signal models may not provide the desired accuracy at all small-signal bias points. On the other hand, libraries based on small-signal models limit the choice of bias points for a designer.

Measurements of the S-parameters of the transistors in the desired frequency range at all bias points of interest provide an effective solution to these problems. They provide reliable indication of the performance of the transistors, and validate (or invalidate) the library models. Information on parameters like the maximum available gain, maximum stable gain and the stability factors can be derived from the S-parameters. Small-signal and noise models can also be developed based on these measurements [19]. In this work, S-parameters measurements of the 10 processes have been performed at room temperature. Comparisons between the measured and simulated S-parameters (based on library models) have also been performed for available libraries.

Noise characterisation

The noise figures NFs and the noise parameters of a device, especially NF_{min} and R_n, are strongly dependent on the bias voltages and currents. Hence, noise characterisation over the bias points of interest before commencement of LNA design is advantageous. Furthermore, if the noise models provided by the library are inaccurate, a perfect noise match condition may not be achieved, or the noise

match may change to an offset frequency range. This would defeat the primary application of the LNA. Noise characterisation of available transistor based on measurements, whenever feasible, is therefore beneficial in LNA design work.

Although at present, availability of high-precision network analyzers ensures precision S-parameter measurements, accomplishing accurate noise characterisation of low noise transistors is still a challenging task. Hence, in the present work, the noise characterisation of the transistors was performed using the state-of-the-art measurement system from Agilent, PNA-X. NF_{50} measurements were performed over a frequency range of 0.1 – 17 GHz. Complete extraction of the 4 noise parameters of the transistors have been performed using an automated tuner, at specific bias points of interest. The characterised HEMTs are state-of-the-art and exhibit extremely low NF and even lower NF_{min} values. Especially at low frequencies, these values are similar or lower than the instrument error ranges. The $\frac{1}{f}$ noise also dominates the spectrum and this further hinders accurate noise measurements. The interference from the GSM and UMTS bands also deteriorate the accuracies at frequencies below 3 GHz. Precision measurement of noise parameters in these frequency ranges is thus an extremely difficult task with known techniques, and reliability suffers. Therefore, the noise parameter extraction has been performed over 3 – 8 GHz.

6.3 C-band and UHF-band LNA designs

This section focuses on the designs of the C-band and the UHF-band MMIC LNAs. The design procedure followed in this work is described in subsection 6.3.1. Subsections 6.3.2 and 6.3.3 focuses on the 2 designs separately, and includes information on the circuit schematic, circuit layout and PCB layout development.

6.3.1 LNA Design Procedure

Both the C-band and the UHF-band LNAs are multi-stage LNAs. A step-by-step approach has been followed in the design work., and the circuits have been developed for each stage separately. An analysis has been performed at each stage before proceeding to subsequent stages. This leads to a systematic method, and troubleshooting is relatively easier. Furthermore, once a MMIC LNA is fabricated, it is impossible to test and modify each stage separately, unlike in a MIC LNA. Analysing the performance of each stage separately is therefore a good

design practice. The designs have been developed in Advanced Design System (ADS), a high-performance CAD software from Agilent Technologies [77].

The first step in the design process consisted of selecting appropriate device sizes for each stage of the LNA. To achieve this, the variations in parameters like NF_{min}, R_n and S_{21} with the bias conditions have been studied. This provides a) suitable transistors for each stage, and b) and the relevant bias points for the different stages. Measured data, if available, validates the library models, and provides an even better platform to initiate the design process.

In the second step, the design process has been initiated with available lumped components from ADS library. The noise matching in the first stage has been accomplished with lumped component matching networks. Design of inter-stage noise and power matching networks aim to: a) reduce the effect of these stages on the noise match b) obtain the required gain versus frequency response from the amplifier c) achieve a good roll-off in the gain outside the operating frequency band. A sharp gain roll-off minimises chances of out-of-band oscillations.

The networks required for noise or gain matching can be developed with the help of the Smith Chart – the values of the passive components required can be determined from this chart. This can be performed manually, or the Smith Chart matching tool provided by the ADS software can be used. In the latter case, the source and load terminations need to be specified correctly. The impedance presented at the LNA input is the impedance of the signal source, for example an antenna. Often this is nominally 50 Ω. The input impedance from the second stage (before inter-stage matching) is the complex output impedance of the first stage. The advantage of Smith Chart matching using the ADS tool is that the S-parameters of the matching network are highlighted over the desired frequency range, and can be easily monitored [19].

In the third step, the lumped components in the circuit have been replaced with passive components from the process library, which take into account the parasitics associated with the passive components. The fourth step comprised of designing biasing networks to provide the required gate and drain voltages to the transistors of the different stages. This generally affects the tuning, so the inter-stage matching may require re-optimisation. In the fifth step, transmission lines (TLs) from the library foundry have been used to connect the different passive elements in the design. This generally degrades the performance so further tuning of the passive components may be necessary.

Table 6.2: Table of Specifications of C-band LNA

Parameter	Specification
Frequency	4 – 8 GHz
Noise Figure in 50 Ω system	<1 dB
Gain	>25 dB
Gain variation	<3 dB pk-pk
Input return loss	<-10 dB
Output return loss	<-10 dB
Nominal input/output impedance	50 Ω

The sixth step relates specifically to MMIC LNA designs – layout generation. This has been accomplished using design rules specified by the foundry. These rules may relate to various aspects of fabrication, for example, the maximum die-size, the minimum dimensions of components, connectivity rules and the spacing between the different components. In the final step, a Design Rule Check (DRC) has been performed to determine whether all design criteria relevant to fabrication are satisfied. The DRC results may necessitate design modifications.

The later stages in an LNA design generally involve an iterative procedure of changing the schematic and the layout simultaneously to obtain the desirable performance within the layout restrictions imposed by the foundry.

6.3.2 C-band LNA design

The design requirements of the C-band MMIC LNA are specified in Table 6.2. To obtain the required broad band behaviour, a suitable transistor process had to be selected. At this stage, the usefulness of the transistor characterisation work can be appreciated. The results of this work indicated that the TQP13-N process from TriQuint Semiconductors showed promising performance in different aspects. This process has therefore been selected for the design of the C-band LNA.

The TQP13-N process is a 130 nm gate length low noise process based on GaAs substrate. The foundry specifies typical cut-off frequencies of 95 GHz, and typical NF<0.5 dB in the Ku-band. It is used for "V-band automotive radar and high frequency point-to-point radio applications, and converter blocks in consumer Direct Broadcast Satellite (DBS) dish systems" [89]. The process

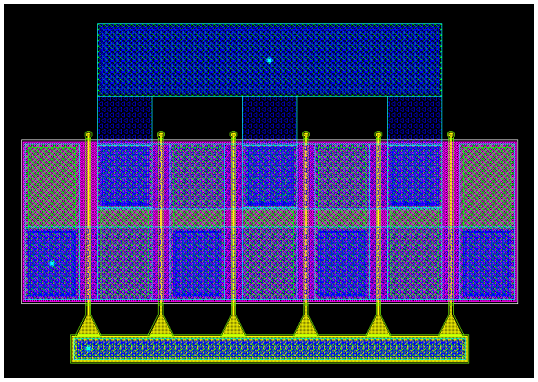

Figure 6.2: pHEMT layout of the TQP13-N process

offers several combinations of pHEMTs with various gate widths. An example of the layout of the 6×45 μm transistor is shown is Figure 6.2.

Circuit schematic development

The TQP13-N process library provides non-linear models of the process components. Using these, a study of the variation of the NF_{min}, R_n and S_{21} of the transistors, as a function of the frequency f, gate bias voltage V_{gs} and drain bias voltage V_{ds}, has been performed in ADS. Graphical representations of these have then been plotted using MATLAB [30]. Example plots for a typical 6 finger 45μm gate width device are shown in Figures 6.3 to 6.5.

Figure 6.3 shows the variations in the parameters when V_{gs} and V_{ds} are varied. The frequency f has been kept constant at 6 GHz, the C-band centre frequency. In Figure 6.5, f and V_{gs} have been varied, whilst V_{ds} is 1.5 V. For the other combination shown in Figure 6.5, V_{gs} is 0 V. The sweep ranges of the independent variables are as follows:

- Gate voltage sweep from -0.05 V to 0.5 V
- Drain voltage sweep from 0.5 V to 2.5 V
- Frequency sweep from 4 GHz to 12 GHz

The frequency sweep has been extended to 12 GHz to consider the possibility of developing a broad band LNA design operating in both the C and X bands, in subsequent wafer runs of the process. Observations from this study indicated the requirement of 3 stages to achieve the required gain in C-band, and the sizes of

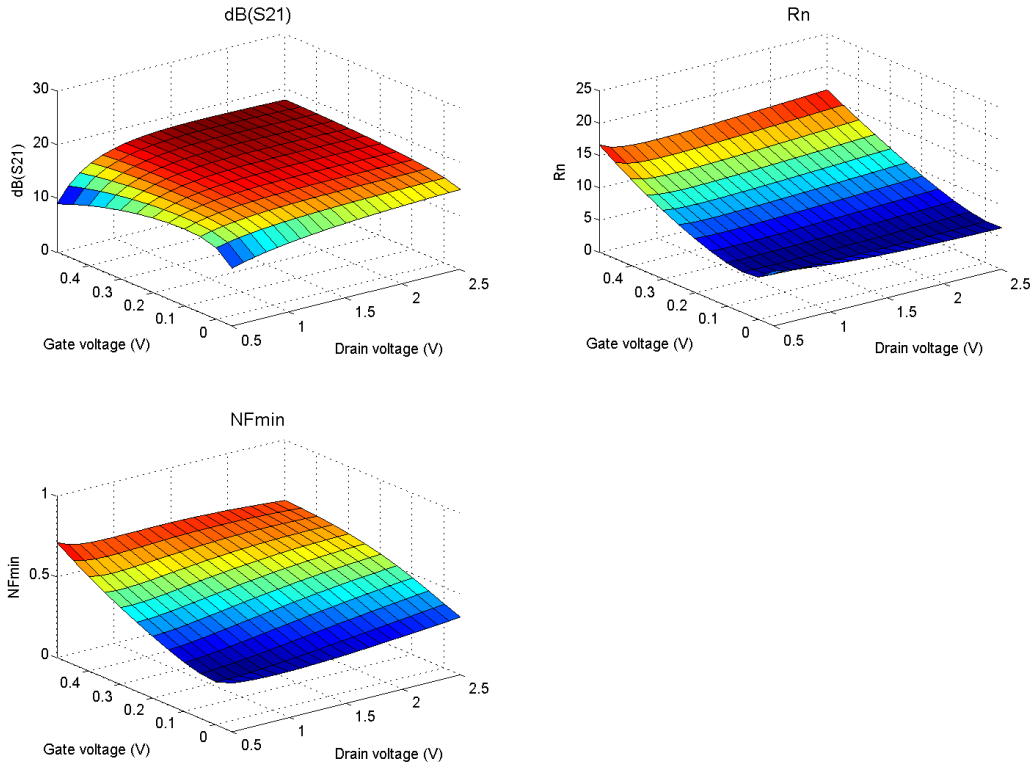

Figure 6.3: Plots of NF_{min}, R_n and forward gain of a 6×45 μm transistor at 6 GHz

the 3 transistors that should be selected for this purpose. Noise optimisation in the first stage has been achieved using the 6×45 μm device. The latter stages contribute to the gain and linearity of the LNA, and larger 8 and 10 finger devices have been selected for these.

The schematic of the designed LNA is shown in Figure 6.6. There is no on-chip noise matching network to match the optimum impedance Z_{opt} to the source impedance $Z_0 = 50\ \Omega$. This is because simulations have confirmed that the inductance (represented by L1=1.2nH) of a long gold bondwire required to bond to the MMIC input pad provides good noise matching. Since a bondwire is essential to connect the MMIC chip to external circuitry, incorporation of its inductance in the design serves 2 purposes. It minimises design space, and eliminates the noise contribution from the lossy MMIC inductor that is otherwise required. The bondwire at the RF output port helps in improving the output return loss and its inductance has also been considered in the design, with the

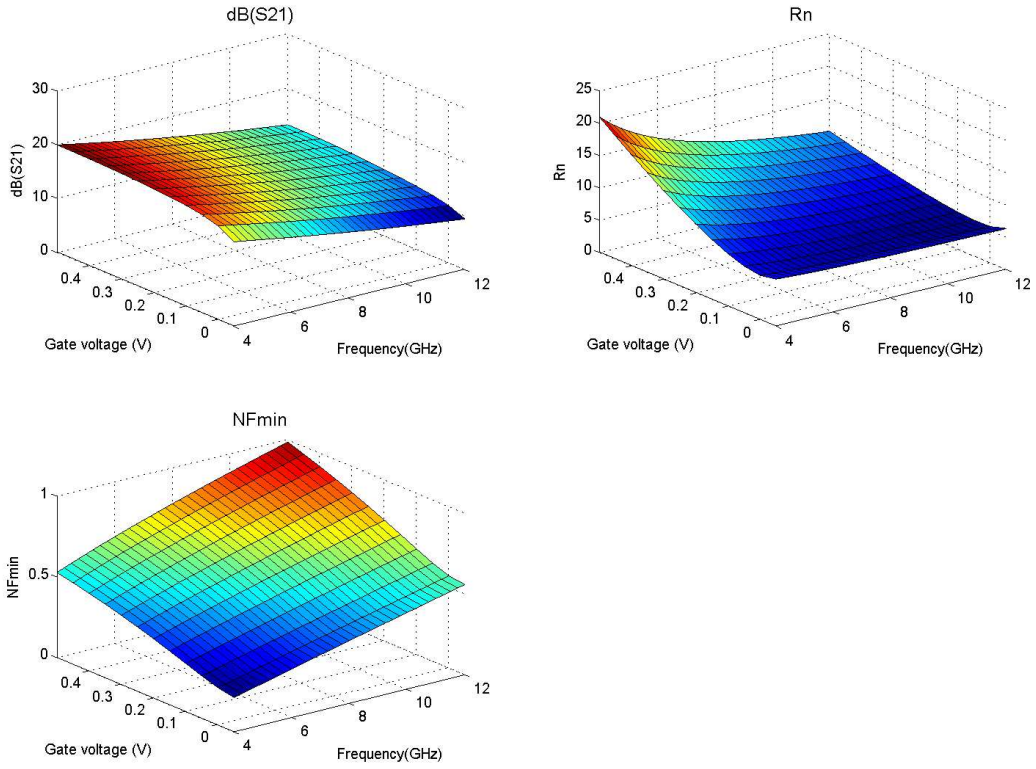

Figure 6.4: Plots of NF_{min}, R_n and forward gain of a 6×45 μm transistor at V_{ds} = 1.5 V

component L3.

The technique of source inductive feedback has been utilised in the first stage of this design, however this is not apparent from Figure 6.6. This is due to the fact that the length and width of the transmission line connecting the source terminal to the via-hole (ground) in the MMIC chip has been modified to attain the desired series source inductance. This serves to show how the design can be modified in the layout-generation stage to reduce the number of circuit components.

Inter-stage matching has also been implemented using the components R3, L2 and C4. The resistor R5 helps in enhancing the stability and improving the output return loss of the LNA. This helps in optimising the gain curve and in improving stability, but also results in a reduction of the gain. Coupling capacitors, which also act as DC blocks between the adjacent stages, have been incorporated. These are the components C2 and C3. These affect the matching circuitry and sometimes are a part of it, and hence have to be selected with care.

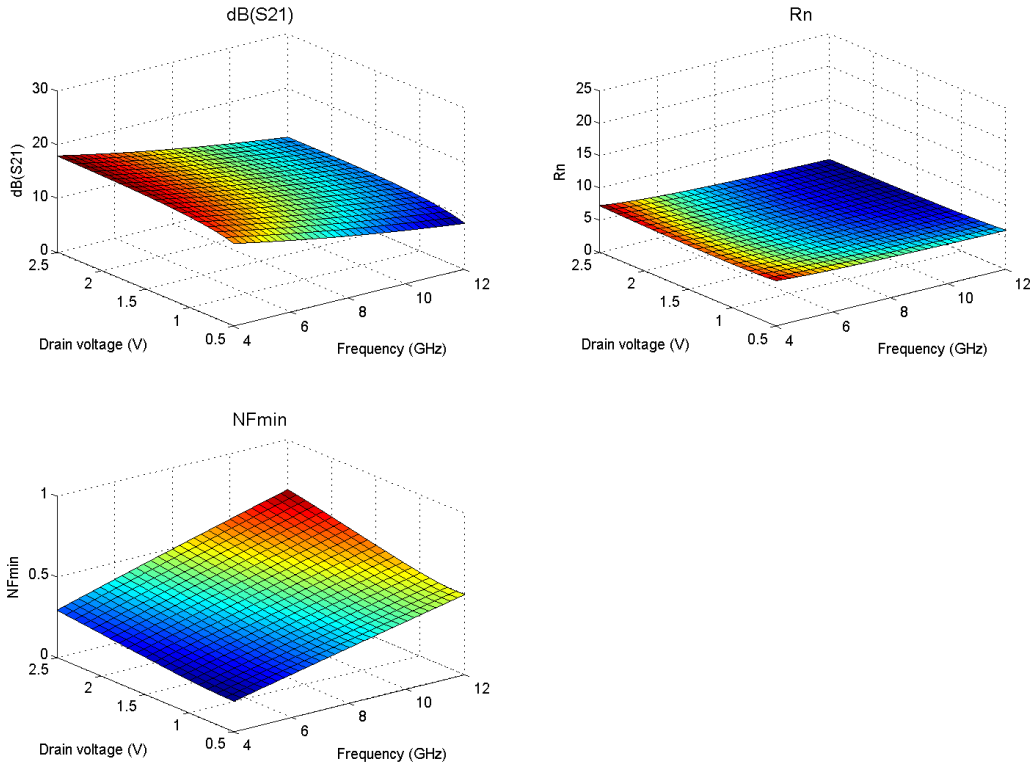

Figure 6.5: Plots of NF_{min}, R_n and forward gain of a 6×45 μm transistor at V_{gs} = 0 V

This applies to the DC blocking capacitors C1 and C5 at the input and output stages as well, which provide DC isolation of the MMIC.

The bias circuits have been designed with care to reduce the possibility of oscillations via feedback to previous stages. The different stages have been biased separately for the same reason. This separation of the bias paths, however, increases the power and space consumption of the MMIC. High values of the gate resistances R1, R2 and R4 have been selected (in the kΩ range) to provide the applied biases at the gate terminals, to reduce gate leakage currents and to protect the gate terminals.

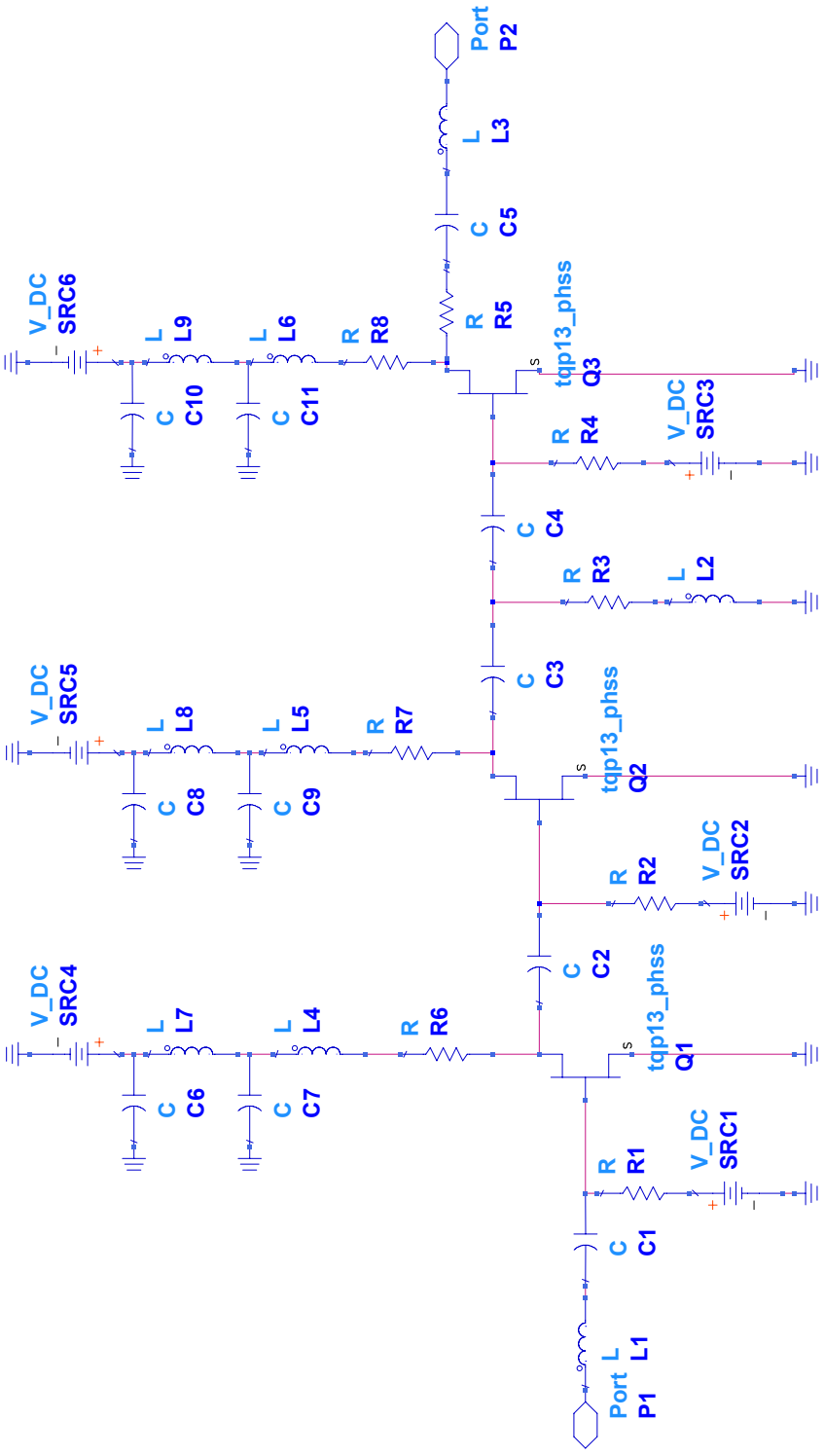

Figure 6.6: Schematic of the MMIC C-band LNA

Table 6.3: Components values for C-band LNA

L1	L2	L3	C1	C2	C3	C4	C5	R1	R2	R3	R4	R5
nH	nH	nH	pF	pF	pF	pF	pF	kΩ	kΩ	Ω	kΩ	Ω
1.2	0.5	0.5	3	3	3	1	3	3.5	4	3	4	9

The resistances in the drain circuitry R6, R7 and R8 have been selected such that they provide the proper biases at the drain terminals, do not significantly degrade the noise performance, enhance the bandwidth and improve the stability of the design. Bypass capacitors C6 – C11 have been included in each stage to ensure stable operation, and protect the MMIC from fluctuations arising from the DC power supply. These are only shown in Figure 6.6 for the drain circuits. The inductances of the bondwires required to connect the DC bias pads to external circuitry have also been taken into account to reduce chances of oscillations arising from their interaction with the off-chip bypass capacitors. Values of the some of these components are provided in Table 6.3.

The Rollet stability factor K of each stage has been checked to ensure stability of each individual stage. Finally, the performance of the LNA has been simulated over an extended frequency range to ensure that $K > 1$ across the entire frequency range in which the amplifier exhibits gain. This diminishes the chances of out-of-band oscillations. The generation of the schematic is followed by that of the layout, which is described next.

Circuit layout development

Figure 6.7 shows the layout of the 3-stage C-band MMIC. The dimensions of the MMIC chip are 1.5 mm × 1 mm. The RF signal path extends from the probe pad on the left side of the chip to the probe pad on the right hand side. The gate and drain biases are provided through the probe pads on the top and bottom of the circuit.

PCB development

Connections to the MMIC can be achieved by designing a suitable printed circuit board (PCB), which incorporates 50 Ω microstrip lines to provide the RF signals, and suitable DC biasing paths. In a microwave amplifier, although the primary

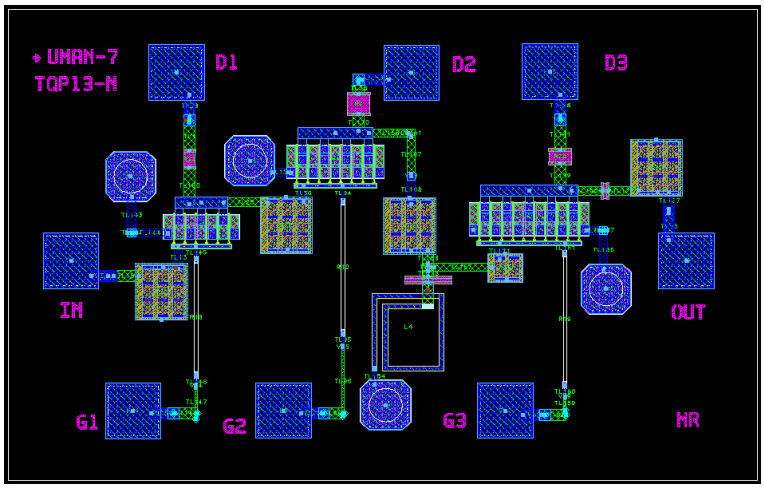

Figure 6.7: Layout of the MMIC C-band LNA

focus is on the RF response, a proper DC network design is also very important. The noise and S-parameter responses of a device are dependent on the bias settings. Hence, the DC bias network design plays an important role, ensuring that the desired bias voltages are reached at the gate and drain terminals, and the transistors draw the appropriate currents. A properly designed bias network also helps to eliminate oscillations. It filters and blocks any spurious RF noise or spikes from appearing at the gate and drain terminals of the transistors. This is important as spikes produced in power supplies can potentially damage the actual transistors.

A good design practice is to incorporate on-chip protection. However, a range of decoupling capacitors is required to ensure good decoupling across a wide frequency range, and accommodating these in the off-chip bias circuit in the PCB is comparatively easier. These off-chip bias components need to be selected carefully and simulated to inspect the effect on the overall MMIC performance, if any. In the present design, S-parameter files of the off-chip components provided by the manufacturers have been incorporated in the design stage to achieve this.

The PCB board for off-chip RF components, DC blocking capacitors and the DC biasing circuitry has been designed using Rogers RO4003 substrate material. This is a low-loss high frequency substrate, with a relative permittivity of 3.38, and is widely used for RF circuit designs.

Table 6.4: Table of Specifications of UHF-band LNA

Parameter	Specification
Frequency	0.4 – 1 GHz
Noise Figure	<0.5 dB
Gain	>30 dB
Gain variation	<3 dB pk-pk
Input return loss	<-10 dB
Output return loss	<-10 dB

6.3.3 UHF-band LNA design

The design requirements of the UHF-band MMIC LNA are listed in Table 6.4. This design has been based on the PD50-10 process of WIN Semiconductors. This is a 500 nm gate length power process based on GaAs substrate. Repeated DC and S-parameter measurements of devices from the WIN foundry have in general shown good agreement with the simulated responses. This implies an accurate process library, and a highly reliable and repeatable process. The WIN foundry is also one of the best choices in terms of cost-effectiveness. Moreover, an option of fabrication was available for the PD50-10 process. Based on these factors, this process has been selected for the UHF-band design.

The WIN PD50-10 pHEMT process provides both enhancement and depletion mode devices. The combinations of the gate fingers and the gate widths are however predetermined. The smallest device size available is 2×25 μm and the largest device size available is 8×200 μm. Non-linear models of all possible transistors are provided.

Circuit schematic development

A process similar to that described for the C-band design has been followed to develop a 2-stage LNA. Using the non-linear non-scalable models from the process library, plots similar to those presented in section 6.3.2 have been generated in ADS. Suitable transistors have then been selected for each stage and the complete schematic has been generated using design techniques discussed in section 6.3.1. A series inductor (L1) has been used in the input matching circuit. Source inductive feedback has been utilised in both stages using components L2 and L3.

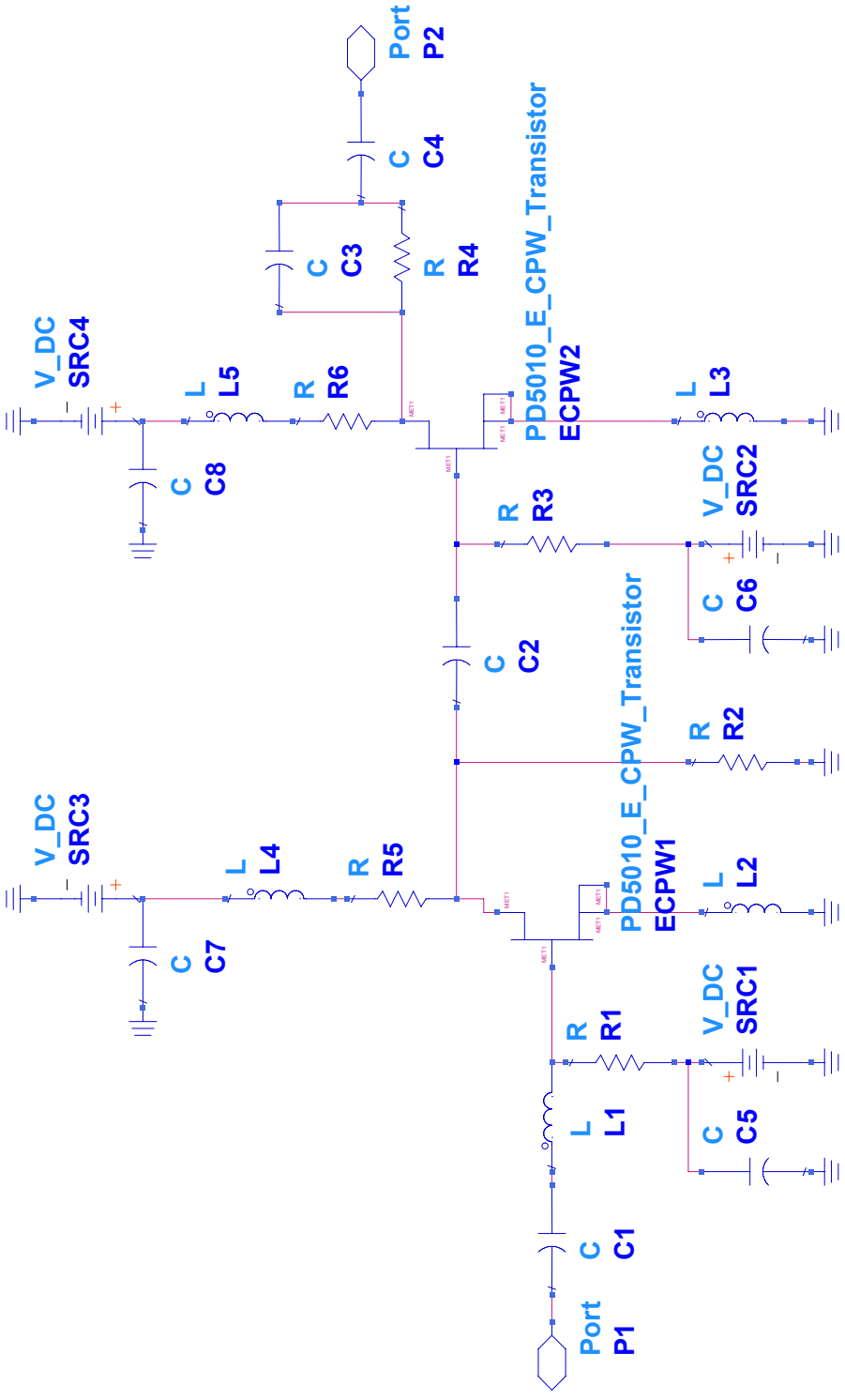

Figure 6.8: Schematic of the hybrid UHF-band LNA

Table 6.5: Components values for UHF-band LNA

L1	L2	L3	C1	C2	C3	C4	R1	R2	R3	R4
nH	nH	nH	pF	pF	pF	pF	kΩ	Ω	kΩ	Ω
6.2	0.8	0.8	20	5	1	20	5	75	5	100

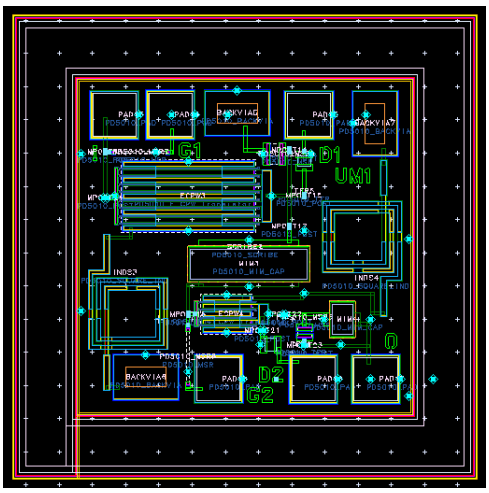

Figure 6.9: Layout of the MMIC component of the UHF-band LNA

The resistance R2 has been used to improve the stability, but it also decreases the gain. The matching circuit in the output, comprising of components R4 and C3 reduces the gain to a certain extent but improves the stability and the output return loss of the design. Capacitor C2 acts as the inter-stage coupling capacitor. Gate and drain resistances R1, R3, R5 and R6 have functionalities similar to discussed previously for the C-band design. Values of some of the components used in this design are provided in Table 6.5.

A restriction placed on this design was the available MMIC chip area for placing of components: 0.5 mm × 0.5 mm, with the die-size being 0.7 mm × 0.7 mm. The restrictions imposed by these dimensions are more pronounced in the UHF-band than they would be in a higher frequency band, due to the increased component sizes in this low frequency region. The size restriction severely limited the choice of components. Furthermore, some components like the series inductor in the noise matching circuitry (L1) and DC-blocking capacitors in the RF signal path (C1 and C4) could not be incorporated within the MMIC chip. In essence, the UHF-band design was therefore a hybrid design consisting both MMIC and

off-chip RF components.

Circuit layout development

Figure 6.9 shows the layout of the 2-stage UHF-band MMIC. In order to make the optimum use of the limited space, the RF signal path runs from the RF probe pad on the top left side of the chip to the probe pad on the bottom right side. The DC biasing is provided through the probe pads on the top and bottom of the circuit - the top and bottom pads are for the first and second stages, respectively.

PCB layout development

The PCB board for this LNA has been designed using Rogers RO4003 substrate material used for the C-band as well. Owing to the small chip dimensions, a substrate with the right combination of relative permittivity and small thickness had to be selected, to minimise the width of the 50 Ω TLs comprising the RF signal path. Also, the TLs of the bias circuitry had to be designed with care - close to the MMIC, but with sufficient separation to enable manufacturing.

6.4 Summary

This chapter has outlined the measurement and characterisation of low noise transistors and the development of 2 MMIC LNAs. The benefits of DC, *S*-parameter and noise characterisation of transistors, whenever possible, before commencement of an LNA design, have been highlighted. The performance of transistors from 10 low noise processes have been analysed to determine their credibility for state-of-the-art LNA development, especially for the SKA application. Results of all measurements, characterisations and analyses are presented in detail in chapter 10.

The designs of the C and UHF band MMIC LNAs have also been included in this chapter. The C-band MMIC chip has an area of 1.5 mm^2 whereas the UHF-band MMIC has a chip area of 0.25 mm^2. The complete LNA development cycle has been detailed, from choice of foundry and transistors, to development of the MMIC schematic and layout, to PCB fabrication. Both designs have been fabricated in wafer runs of the corresponding processes, and are presently in the assembly stage. The simulated performance of these MMIC LNAs has been discussed in chapter 10.

Chapter 7

Design of a multi-band microstrip patch antenna

7.1 Introduction

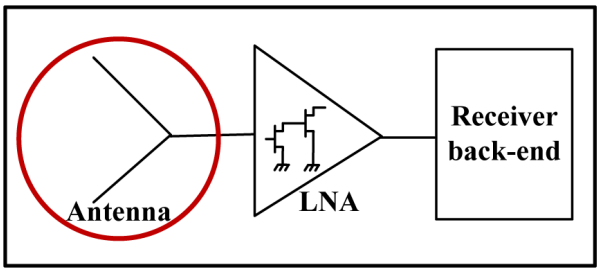

Figure 7.1: Focus of the chapter - design of multi-band MPA

The operation of MPAs and the various factors that determine their performance have been discussed in chapter 5. This chapter focuses on the design and simulation of a multi-band MPA. It has been stated in chapter 1 that the MPAs need to be operational in 3 extremely crowded frequency bands. Table 7.1 provides the details of the centre frequencies and the bandwidths of the 3 frequency bands of interest. The objective is to achieve diversity through the use of different frequency bands and services, by switching between bands or by weighting the QoS measures. This multi-band antenna structure is also required to be implemented in a process industry environment, which imposes stringent limitations on the size, orientation and placement of the antennas, and the environment in which they operate.

Table 7.1: Summary of frequency bands of interest

Band	Frequency Range (GHz)	Centre Frequency (GHz)
2.1 UMTS	2.100 – 2.170	2.140
2.4 ISM	2.400 – 2.500	2.450
5.8 ISM	5.725 – 5.875	5.800

These special requirements, which increase the challenges in this particular design task, are outlined in section 7.2. The selected design approaches which take into consideration all these factors are discussed in sections 7.3. Discussion on the design and simulation of the antennas in section 7.4 is followed by a highlight of the potential effects of the environment in section 7.5. Finally, in section 7.6, the various options considered for the antenna feed network are highlighted.

7.2 Design Requirements

This section describes the typical spatial, mechanical and environmental limitations of the process industry environment in which the multi-band antenna structure will be implemented. The diversity in the operating environment and the challenges it poses were discussed in chapter 1, and Figure 1.1 provided example scenarios. Typically, cylindrical or spherical metallic storage or process vessels of different diameters ranging 1 m to 20 m are surrounded by pipework and access platforms. Based on discussions with researchers who are deploying WSNs into process plants, a list of design constraints has been formulated. These represent the worst-case constraints, and have been selected to enhance the utility of the designed antenna in a broader range of applications. For brevity and ease of identification, these are denoted as 'Environmental Constraints and/or Requirements' (ECR) in the present thesis. These are outlined below:

ECR1: Reduced target area of specific orientation for placement of antennas

Due to severe limitations in available placement area, a limit has been set on the dimensions of this design - approximately 250 mm $\times$ 15 mm. This area is insufficient to create a standard size tri-band MPA design. The severe implications of

this constraint are discussed in subsequent sections. The antenna structure also needs to be oriented in a manner that the length is parallel to the ground.

ECR2: Capability of conformal attachment to a curved surface

The process industries are generally very reluctant to make modifications to the design of vessels, especially those already in service. Mounting brackets (for commercial MPA enclosures) therefore provide no solution in these scenarios. This leads to the requirement of low-profile antenna structures, which will need to be conformal with the curvatures of the cylindrical process vessels. In the first phase of this design, only larger process vessel diameters have been considered. A mimic curved metal frame structure has been created, which emulates part of the curved surface and can be measured in the laboratory as well. For simulation purposes, this mimic has been approximated by a flat surface. This approximation is valid only for large diameter vessels with low radii of curvatures.

The body of the cylindrical vessel with the antenna mounted on it is at the same potential as the antenna ground. Simulations have been performed to examine the effect of extension of the antenna ground plane in only one direction (when the antennas are attached to the lower edge of the vessels).

ECR3: Presence of the large metallic structures in close proximity

The favoured position for the placement of the antennas would be beneath the access platforms. The latter would therefore completely overshadow the antennas. The presence of these (electrically) large metallic structures in this close proximity to the antenna structure would definitely affect the radiation patterns. It is likely to affect the resonant frequencies as well. Pipework to the vessel on which the antenna is mounted may also affect the performance. Due consideration of these factors is required in the design phase. The access platforms are generally equipotentially bonded to the process vessels, and simulations need to reflect this as well.

ECR4: Different propagation paths for the signal

The access platforms are close to the ground, and this limits direct line-of-sight propagation paths between the antennas and the UMTS base station receivers, the 802.15.4 WSN gateways or the 802.11 WLAN access points. The signal

propagation would therefore rely significantly on reflection paths, for example, reflections from the ground.

ECR5: Environmental variations and possibility of contamination

The variations in environmental factors such as operating temperature and humidity levels in a process industry could be significant. Temperatures vary between 30°C and 70°C inside a single process plant, and over wider ranges in different process plants in different geographic locations. Seasonal variation in relative humidity levels may be between 30 % to 100 %. Other potential problems include contamination with oil or formation of a layer of frost over the antenna surface.

ECR6: Interference from other sources in a dynamic environment

The UMTS and ISM frequency bands are in reality either extremely congested or suffer from interference from other users (WLAN and Zigbee users in the ISM band for example). Leakage from other ISM band applications such as microwave ovens and ultrasonic equipment may also degrade performance [90]. Moreover, even though the antenna structure will be static, the environment will be essentially dynamic. Machines such as vibrator, motors and actuators in a factory environment can generate a significant amount of electromagnetic noise [14]. Changes in the RF propagation environment arising from these, or from movement of vehicles therefore require due consideration.

ECR7: Wide coverage in azimuth plane

A wide coverage in the azimuth (horizontal) plane is desirable to sustain the wireless link even if the locations of the UMTS base stations, the 802.11 WLAN access points or the 802.15.4 WSN gateways vary. The typical radiation from a rectangular MPA has been discussed in section 5.3. In the standard configuration, the radiation extends over one hemisphere only, and the back lobe levels are low. To obtain radiation in both hemispheres, more than one antenna structure can be used.

In addition to these design constraints, the antennas will be operational in both the transmit and receive mode in a system impedance of 50 Ω.

These environmental factors or design constraints affect different aspects of the design in various ways. The ECRs which have direct relevance to the design choices are ECR1, ECR2, ECR5 and ECR7; the available space, requirement of conformability and wide azimuth coverage, and possibility of contamination directly influence the choice of the antenna structure and the material used. These can be partially or completely considered in the design stage. The remaining ECRs, ECR3, ECR4 and ECR6, relate to the signal propagation conditions. These can be studied, even if only to a limited extent, by conducting measurements in the laboratory or in a typical application environment.

7.3 Choices in design approach

This section elaborates the design choices associated with the practical implementation of a multi-band antenna due to the constraints discussed in section 7.2.

7.3.1 Choice of materials

The influence of the various design parameters of a rectangular MPA, such as the length and width of the patch, the height and permittivity of the substrate, the size of the ground plane and the location of the feed point, on the antenna performance have been discussed in section 5.4. It has been established that

1. to reduce the antenna dimensions, higher substrate relative permittivity ϵ_r values are required.

2. larger bandwidth is achieved by increasing the width W and the height h of the substrate, and decreasing ϵ_r.

3. efficiency is increased by increasing the height h and decreasing ϵ_r.

4. the extension of the ground plane on each side of the patch should be at least 6 times the substrate thickness h.

A closer analysis of these observations indicates how the environmental factors affect this design:

1. Due to the severe lack of space, a high relative permittivity ϵ_r is required to reduce the antenna dimensions. This leads to compromises in the bandwidth and efficiency. Even if high permittivity (ϵ_r=10.2) substrates are used, the width of the space provided (15 mm) is smaller than that required for efficient radiation, especially for the lower frequency bands.

2. The requirement of the antennas to be conformal to a curved surface restricts the substrate height h (else fissures could appear in the structure, depending on the characteristics of the substrate used). This leads to further degradation in the bandwidth and the efficiency.

3. Condition 4 from the list above cannot be achieved in the reduced space - the ground plane extension cannot be 6 times the substrate height, at least not along the length of the antenna.

These observations emphasize the severity of the effects of the stringent design constraints, and the need for proper selection of the substrate ϵ_r and h.

The substrate materials have been selected from the wide range of RT/Duroid materials from Rogers Corporation [91]. These comprise an extensive selection of high frequency laminates for a wide range of applications, including MPAs. Among these are laminates with a range of dielectric constants, low dissipation factors, good outgassing properties, improved abilities to withstand temperature-variations and controlled mechanical properties, and some materials suitable for low-cost commercial applications. These laminates have certain standard thicknesses, and the present design has been based on these standard values.

7.3.2 Achieving multiband operation

There are techniques to obtain multi-band operation from a single MPA, 2 of the conventional ones being the use of reactive loading and stacked patch elements [31]. The design ideas investigated for the present work, including these two, are outlined below:

1. Stacked patch elements

In this configuration, patch elements of different lengths corresponding to the different f_r values are placed one above the other, with the coaxial feed location

being the same. The separation between the resonant frequencies can be controlled only to a certain extent and thus imposes a limitation. Additionally, only a compromise rather than the optimal match condition for the antennas can be obtained using just one feed. Loss of coupling between the patches can also result [92, 93]. The fabrication is complicated, especially for a 3-element stacked patch. Furthermore, the height of the antenna increases, and this is unacceptable here to achieve conformability to curved surfaces. Due to these reasons, this design concept is not suitable for the present situation.

2. Use of reactive loading

Use of one or more shorting pins or slots at various locations within a MPA are common ways to achieve multi-band operation [94]. These introduce reactive loading in various ways. Investigation of some of these methods has not yielded satisfactory results, potentially due to the space constraints which limits the radiating-edge size. Cutting out slots of different shapes and sizes or shorting the patch in the available area will also be extremely difficult to achieve in prototype fabrication.

3. Quarter-wave rectangular patches

A quarter-wave rectangular MPA resembles an inverted-F and is therefore also called PIFA (Planar Inverted-F Antenna). The patch is quarter wavelength long and shorted on one side with a shorting pin, and the feed is placed between the open and short ends [95, 96]. The increased compactness, the low profile and an omni-directional pattern have rendered PIFAs increasingly popular in the mobile phone industry and in the 2.4 GHz WSN applications. However, the bandwidth and efficiency are reduced by half in comparison to the corresponding half-wavelength antenna, and the reduction in size occurs in the length of the antenna and not the width. In the present design scenario, where the width of the design area is the limiting factor, the PIFA does not offer any benefit. This approach has therefore been discarded in this instance.

4. Microstrip dipoles

Considering the strip-like shape of the design space, using single microstrip flat dipoles [97, 98] fed by coaxial feeds and placed side by side would have been

a very good design approach. However, the direction of the radiation from the dipoles would not be suitable. They would be omni-directional patterns, but in the elevation plane - not in the azimuth plane as required. Since the antenna needs to be oriented in the horizontal plane, this approach would offer no benefit in the present environment.

6. Adjacent placement of rectangular half-wavelength patches

In this case, the patches would radiate at the different resonant frequencies. This is naturally the simplest of the approaches considered, and has been considered to be the best choice to concentrate on.

The justification behind this choice is as follows: The primary driving force for designing a single MPA structure for dual-band or tri-band operation is compactness. As circuit dimensions get reduced, the compactness of the radiating element becomes increasingly crucial if the RFIC and antenna are to be in the same enclosure. Miniature MPAs therefore find widespread application in mobile handsets. Process industries also impose spatial constraints. The compact structures of these antennas, however, affect the performance (as observed in section 7.3.1):

1. The bandwidth is compromised
2. The radiation patterns are modified
3. The frequency ratio between the upper and lower resonant frequencies is difficult to control, and only a range of frequency ratios can be achieved for different structures. Control of frequency ratios between tri-band structures is more difficult.
4. Impedance matching becomes difficult because sensitivity to the feed location increases, necessitating precision engineering.
5. Fabrication complexity and cost increase significantly.

It is evident that the performance can be significantly compromised only to obtain the added compactness. The present design constraints already lead to severe compromises due to the reasons detailed in sections 7.2 and 7.3.1. Also, when the width of the radiating element is severely restricted, the actual radiating edge of the patch is considerably lower than the theoretically predicted width for

proper operation (both for single and dual-band designs). This makes dual or tri-band designs with a single patch almost impossible to obtain. Furthermore, the curvature of the surface (for antenna placement) will affect complex multi-band antennas (with slotted patterns for instance) more than it will affect a single rectangular antenna.

These observations underpin the decision to implement individual patches and aim to maintain the radiation patterns rather than design multi-band patches, especially because there is sufficient space for adjacent placement of 3 patches. The simplicity of the feeding structure and fabrication is also an added advantage. However, with this approach the following factors need consideration:

1. Coupling to the neighbouring patches
2. Use of a duplexer/triplexer/power divider or any other suitable feeding network

This design approach has been investigated, and section 7.4 details the simulation results.

7.3.3 Choice of antenna feed

The feeding requirements of the antennas will be application specific. In some transceiver designs, the individual patches will be connected to individual wireless modems. There will also be applications where a single feed would be desirable.

The various methods of feeding a MPA have been discussed in section 5.5. The microstrip line and coaxial feed types have been considered in this design. The simplicity in fabrication associated with these feeds is attractive in a design scenario with spatial and mechanical constraints. In the first phase of design work, coaxial feed method has been selected due to the following reasons:

1. Microstrip feed lines radiate as well as the actual antenna.
2. The feed-line modification required to match to the 50 Ω system impedance would require etching of slots in the reduced width dimension for inset feed or implementing a quarter-wave line (thereby requiring more space).

7.3.4 Modelling software

The electromagnetic simulation tool that has been used for the design is the Microwave Studio suite within the Computer Simulation Technology software (CST MWS) [99]. This software is extensively used by passive component designers because of its accuracy and the ease of designing components. CST MWS offers solution capability in both time and frequency domains. The mesh structures can easily be modified for complex structures as well. Typical applications include design of antennas, filters, connectors, to name but a few. A screen-shot of the CST design environment is included in Appendix A.

7.4 Design and simulation of patches

In section 5.4, it has been pointed out that an MPA design process can be initiated by calculating the required patch width W from the desired resonant frequency and the dielectric constant of the substrate (equation 5.10). Calculation of this ideal width W_{ideal} with the commercially available RT/Duroid substrate materials has confirmed that, for all frequencies of interest, W_{ideal} values are more than can be contained within the provided design space. As such, a compromise in the patch widths for all the 3 MPAs is inevitable in the present design work. This problem has been addressed through a 3-step approach for each individual antenna design:

Step 1. Design and simulation of the antenna with dimensions determined using design formulas (W_{ideal}).

Step 2. Reduction of the width from W_{ideal} to contain the antenna within the provided space (15 mm width), and observation of the effects on the resonant frequency and bandwidth.

Step 3. Modification to the feed location to obtain resonance at the desired centre frequency. Specifically, this implies determination of the optimal feed point to match to the 50 Ω system impedance.

7.4.1 Simulation of individual patches

Figures 7.2 (a)-(c) show the front, side and back views of an example design in the 2.1 GHz band. '{u,v,w}' represent the local coordinates associated with the global

coordinates '{x,y,z}', not displayed in the figures. The patch is positioned in the w-plane. Initial values of the patch length L obtained from design formulas can be optimized to obtain resonance at 2.14 GHz, the centre frequency of the UMTS band. The width W has been kept constant at W=13 mm, allowing 1 mm on each side in the 15 mm available width. The coaxial feed structure and the signal port (with impedance 50 Ω) are shown in Figures 7.2 (b) and (c), respectively. Coaxial feeds can be simulated in CST using waveguide ports. Hence, 3 waveguide ports have been used to launch the signals into the 3 antennas.

The dimensions of the ports have been calculated to provide a 50 Ω impedance at these ports, using values of the diameters of the inner and outer conductors of a 50 Ω coaxial cable and the dielectric constant of the PTFE core. The restricted space limits the outer conductor diameter, whereas reduced inner conductor (feed) diameters increase the fabrication complexity. Considering these trade-offs, an optimised value has been selected for this design. Hexahedral meshing has been used in CST to produce the solution set over an extended frequency range of 1.9 GHz - 6.5 GHz. Adaptive mesh refinement technique has been used to obtain the desired accuracy in the simulated S-parameters. Specifically, the criterion $\Delta S = 0.02$ has been set, implying that the adaptive mesh refinement stops only when the differences in S-parameters between consecutive iterations reach below 2%. A similar design procedure has been followed for the other 2 frequency bands.

Design of the lower band 2.1 GHz UMTS and 2.4 GHz ISM antennas has been initiated with RT/Duroid RT6006 substrate material from Rogers Corporation with a high substrate relative permittivity ϵ_r of 6.15 (to reduce the patch sizes) and a substrate thickness (h) of 1.9 mm. The lengths of the patches which provide resonance at the centre frequencies 2.14 GHz and 2.45 GHz are approximately 29 mm and 24 mm, respectively.

For the 5.8 GHz ISM antenna, simulation results with the same substrate have yielded unsatisfactory results - the radiation pattern is modified, and the directivity is significantly reduced. This is due to the fact that, with $\epsilon_r = 6.15$ at this frequency, the patch length is reduced to such an extent that the probe feed starts interfering with the radiation pattern significantly. Using a lower permittivity substrate (RT/Duroid RT5870, $\epsilon_r = 2.33$, $h = 1.575$ mm) solves this problem, and the radiation pattern improves significantly. This highlights another important advantage of placing the separate patch elements side by side; the designs can be modified independently to achieve best performance without

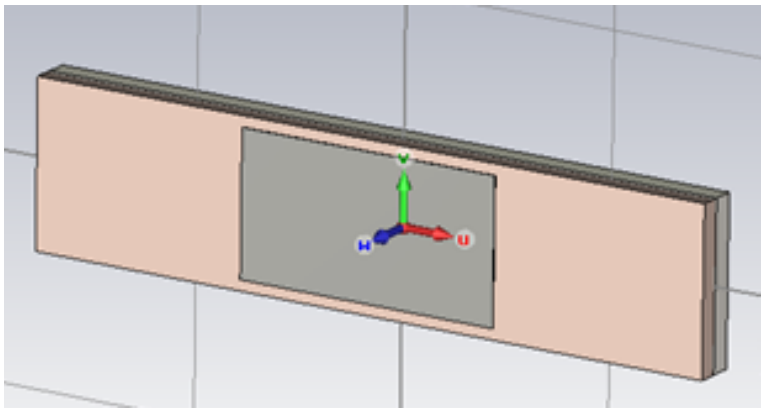

(a) Front view of an individual antenna

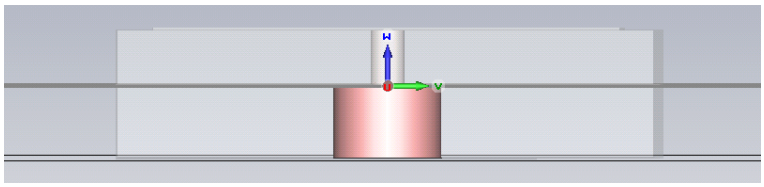

(b) Side view of the probe feed

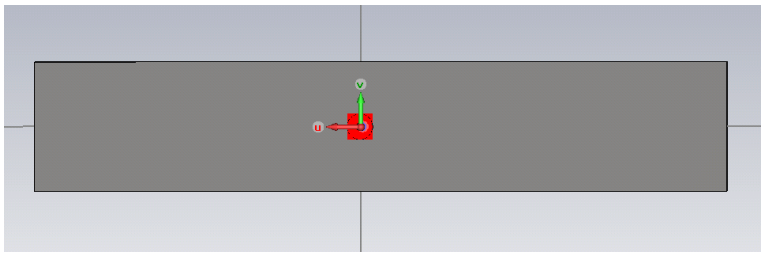

(c) Back view showing the signal port

Figure 7.2: Rectangular patch at 2.1 GHz which fits in the design space

affecting other frequency bands, provided that the coupling levels are not significant (< 30 dB).

7.4.2 Study of the effect of placing patches side-by-side

Based on the deductions in subsection 7.4.1, in the second step, the performance of the complete antenna structure has been simulated using different substrates for different bands - RT/Duroid 6006 ($\epsilon_r = 6.15$) for 2.1 GHz and 2.4 GHz, RT/Duroid 5870 ($\epsilon_r = 2.33$) for 5.8 GHz. Figure 7.3 shows the placement of the 3 patches. Patches P1, P2 and P3 operate in the 2.1 GHz, 2.4 GHz and 5.8 GHz bands, respectively. This structure looks like an 'antenna strip', and this

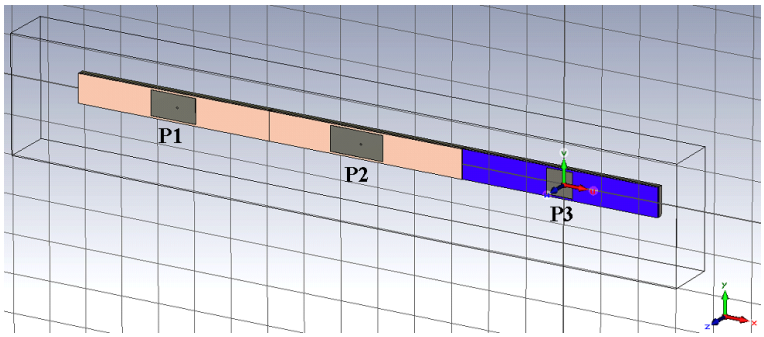

Figure 7.3: Placement of the 3 patches side by side - on different substrates

nomenclature is followed henceforth.

The patches are designed to operate at different resonant frequencies, and none of these are harmonically related to each other. As such, ideally, a particular patch should not have significant radiation levels at the other resonant frequencies. In other words, the total radiation efficiencies at the other frequencies are low, implying that the coupling levels should be sufficiently low. Simulations have been performed over an extended frequency range to investigate the coupling levels and deviations in the resonant frequencies, if any. In these simulations, the antenna strip acts like a 3-port system and the transmission parameters S_{12}, S_{21}, S_{13}, S_{31}, S_{23} and S_{32} provide the information on coupling levels. It is observed that adjacent placement of the antennas deviates the resonant frequencies by less than 1%. The resonant frequencies can be readjusted by tuning the probe feed locations. The coupling levels are plotted in chapter 12.

7.4.3 Modifications based on measurements and observations

Based on the design approach outlined in subsection 7.4.2, antenna strips using different substrates have been fabricated. Initial measurements of these antenna strips have reaffirmed observations from simulations - even though use of $\epsilon_r = 6.15$ in the lower bands reduces patch sizes, the performance is not satisfactory. The 10 dB return loss bandwidths are significantly smaller than that of the 5.8 GHz WLAN band antenna (with $\epsilon_r = 2.33$). Following this observation, the RT/Duroid RT6006 substrate for the lower bands has been replaced with the RT/Duroid RT5870 used for the 5.8 GHz antenna. This also simplifies the design

procedure, reduces costs of procurement and enables fabrication of all 3 patches in one step (thereby decreasing the fabrication and assembly complexities and times). Furthermore, this particular material, RT/Duroid RT5870, has been widely used in recent years in a wide variety of high-reliability applications. This material is one of the better choices to prevent performance degradation under the extreme environmental conditions relevant to the present design problem, because of its relatively high temperature tolerance and low outgassing characteristics.

7.5 Study of the effects of the environment

It is important to simulate the performances of the antenna structures in the actual environment in which they are supposed to be operational. Complete emulation of the actual operating environment with large metal structures (access platforms) in the vicinity of the antennas is not possible, because of the computation problems associated with large structures. However, simulation with smaller dimensions can be used to determine, partially if not completely, how these structures may affect the performance of the antennas. It determines whether the resonant frequency may change, and also how the radiation pattern may be affected.

Figure 7.4 shows the simulated structure used for this study. The antenna strip is positioned in the w-plane, and a large metal surface representing an access platform is placed above the strip in the v-plane. The dimensions of this sheet are selected to be at least 10 wavelengths at the lowest resonant frequency. Although simulations provide some idea of the effect on performance, these effects are better studied by performing actual measurements, either in the laboratory

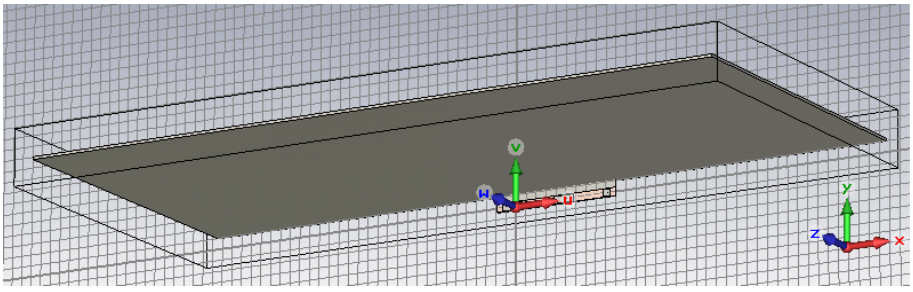

Figure 7.4: Simulated structure with a large metal surface above the antenna strip

or more appropriately in an actual operating environment. Both simulation and laboratory measurement results are presented in chapter 12.

7.6 Feed network design

The approaches considered for the antenna feed network design are as follows:

1. Using 3 separate feeds for the 3 separate antennas, and using a COTS multiplexer/switch to route the signals through to the various antennas.

2. Using only one feed to the complete structure.

The first option entails the use of 3 coaxial feed cables. The second option provides more retrofit capability by enabling a single signal path from the receiver/transmitter to the antenna structure. However, both are equally useful depending on specific project requirements. The second option has been considered initially.

A single feed structure can be created based on 2 separate functionalities:

1. As a power splitter/combiner - In this case, a power divider having 3 branches in total is required. A 4-way splitter/combiner can be used, but the fourth branch needs to be terminated with a matched 50 Ω termination. This can be achieved by using a commercial splitter or designing a similar power divider in a microstrip (MS) circuit.

2. As a custom-designed passive tri-plexer - This can be realised by designing suitable matching circuits so that only the resonant frequencies are passed to each antenna respectively, and the other frequencies are eliminated. A customised feed circuit can be implemented using a MS design.

Both these options have been considered. In the first instance, the second option has been considered since it promised a better (more customised) response. A matching circuit with 3 output branches has been designed. These branches have been terminated with 1-port S-parameter files containing simulated or measured antenna impedance pattern data for the 3 individual antennas. The matching circuit presents an open circuit condition to out-of-band signals in any particular branch. However, simulations have confirmed that this design procedure needs precise information about the complex impedance pattern of each

antenna in the Smith Chart, and over the entire frequency range. This severely restricts the functionality of such a design - variations between the simulated and measured impedance patterns arising from fabrication uncertainties renders the matching circuit ineffective. The open circuit condition for out-of-band signals is not achieved and this results in loss of signal power. Furthermore, fabrication errors also leads to different impedance patterns for the same antenna fabricated in separate batches. Therefore, using measured impedance pattern instead of simulated data also fails to provide an effective solution to this problem. Due consideration to these factors through extensive simulations has resulted in discarding this MS tri-plexer design approach, and in the decision to concentrate on the MS power divider network design. The design approach is discussed next.

7.6.1 Power splitter/combiner

A commercial or a MS network power splitter/combiner can be used to feed the MPAs only if it is a 4–way splitter operating over the relatively large bandwidth of 2.100 GHz – 5.875 GHz. Two such COTS power dividers have been procured from Minicircuits. Their stand-alone performances have been measured to determine their applicability. The results are presented in section 12.5.

For the MS network power splitter/combiner circuit, if the feed network could be designed in an area slightly less than that of the antenna strip, then attaching this to the back of the antenna strip can result in a very compact structure. Pins are then required to feed the antennas from the MS lines. This design based on the Wilkinson power divider [100] principle has been implemented in the Agilent ADS software [77], and Figure 7.5 shows the design schematic.

The operating principle of the Wilkinson power divider is provided in [100]. In general, these dividers are narrowband in nature. However, the bandwidth can be increased by adding more stages to the circuit. This requires modifications to the impedances of the quarter-wavelength lines and also the resistor values at each stage. In the present design, the first divider stage is centred at the centre frequency of the complete band that needs to be covered. After some consideration of the performance and the space limitations, a 2-stage design has been implemented for the first divider. One output signal path has then been divided using another 1-stage Wilkinson power divider to split power between the 2.1 GHz UMTS and 2.4 GHz ISM antennas. The second output signal is fed straight to the 5.8 GHz ISM antenna.

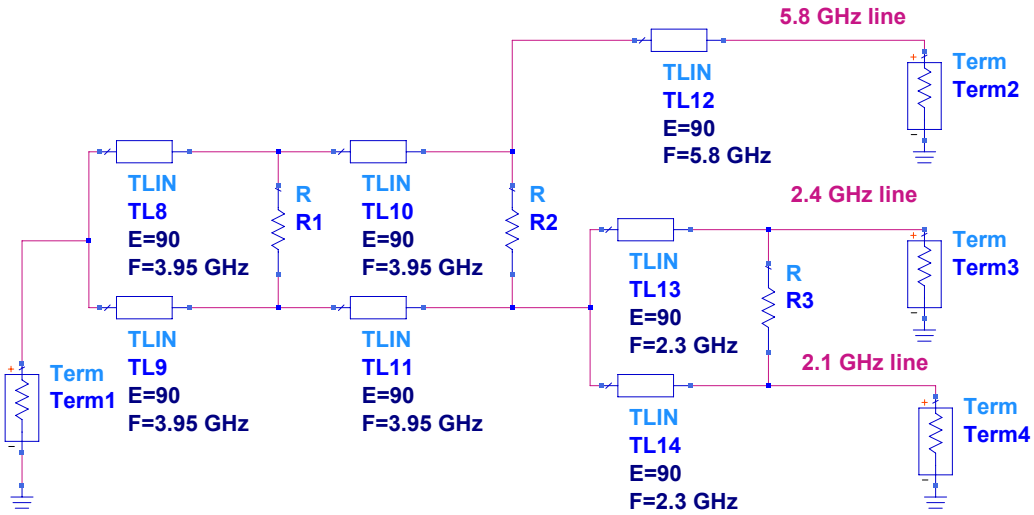

Figure 7.5: Schematic of the power splitter/combiner network

Figure 7.6 shows the MS feed network designed and fabricated to fit to the back of the antenna strips. The 3 output signal paths are positioned such that they lead up to the 3 antennas, which are lined up along the centre of the strip. Measurement results of antennas using these feed circuits are provided in section 12.5.

Use of a MS feed network provides a compact solution to the feeding problem. Nonetheless, the fabrication can be very complicated, especially lining up the antenna strip and the feed network strip correctly (so that the pins can be inserted in the correct positions to feed the antennas). Furthermore, there is always the possibility of the feed network itself affecting the radiation patterns. This cannot be corrected for once the board is in place. However, in this instance, as the ground plane lies in between the 2 strips, it should provide some amount of shielding.

7.7 Summary

In this chapter, the complete design of an antenna system operational in 3 frequency bands has been described. The severe spatial, mechanical and environmental restrictions that make this particular design work extremely challenging have been discussed. Choices adopted in the design approach, with considerations of their feasibility in the operating environment, and their effect on the

(a) Front

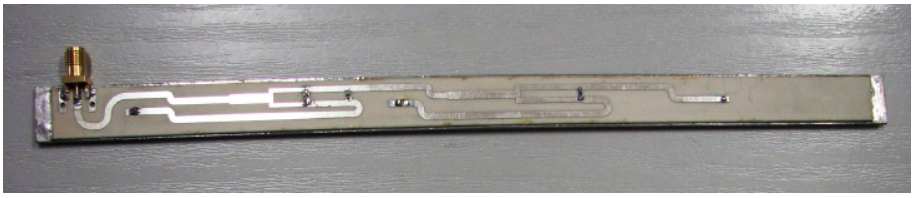

(b) Back

Figure 7.6: The antenna strip with the microstrip feed structure at the back

performance, have been outlined with appropriate justifications. A discussion of how the design and simulation have taken into consideration the effects of the environment is presented. The different possible feeding options for the antenna structure have been discussed as well. Chapter 12 presents the results of the simulations and laboratory measurements.

Chapter 8

Experimental arrangements

8.1 Introduction

This chapter describes the different experimental arrangements that have been used in this work. Measurement procedures for DC, S-parameter and noise characterisation of on-wafer transistors are discussed in section 8.2. These include information on the calibration principles. A brief description of MMIC LNA measurements is also presented. The experimental arrangement to measure the reverse noise emanating from the input port of an LNA (used in phased array noise analysis) is presented in section 8.3. Finally, the antenna experimental arrangement used to measure the fabricated multi-band patch antennas is described in section 8.4.

8.2 On-wafer transistor and LNA measurement

This section describes on-wafer transistor and MMIC LNA measurement techniques. Sections 8.2.1, 8.2.2 and 8.2.3 relate to DC and S-parameter, noise figure and noise parameter measurements of on-wafer transistors, respectively. In section 8.2.1, an overview of DC and S-parameter measurements of MMIC LNAs has been presented.

8.2.1 DC and S-parameter experimental arrangement

The on-wafer transistor characterisation process starts with DC and S-parameter measurements. Figure 8.1 depicts the experimental arrangement. Figure 8.2

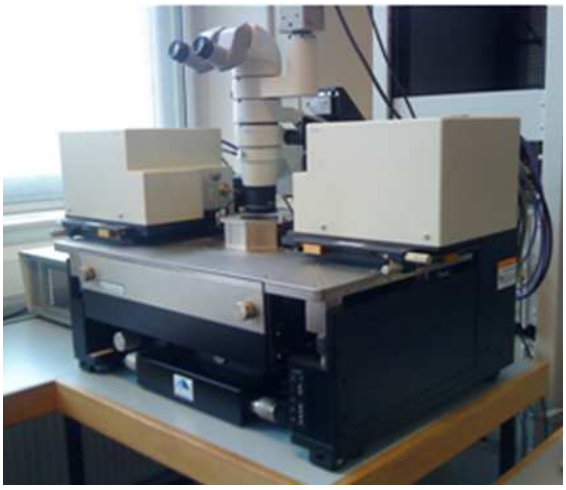

(a) Probe station

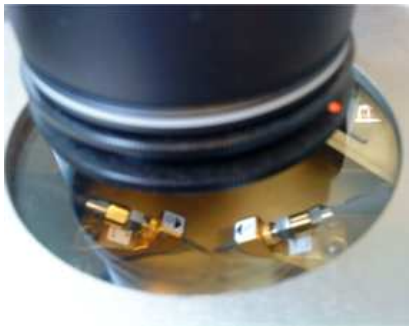

(b) Probes inside micro-chamber

Figure 8.1: On-wafer transistor measurement apparatus at the University of Manchester

(a) shows the block diagram of the experimental arrangement. The mounted transistors are placed on a chuck inside a micro-chamber from Cascade Microtech. The ambient temperature of the chuck and the moisture content of the air inside the chamber can be controlled by an external computer. A sensor on the chuck monitors the chuck temperature [19]. This experimental arrangement is required to perform measurements over an extended temperature range.

The gate and drain biases V_{gs} and V_{ds} are provided with Agilent Technologies's 4142B, a sophisticated Power Supply Unit (PSU) with the capability of supplying and measuring currents in the range of nA simultaneously. These voltages are fed through the bias-Ts of the Vector Network Analyzer (VNA) to the RF input and output probes. The RF probes have the signal probe in the middle with the ground probes on either side, as depicted in magnified scale in Figure 8.2 (b).

All measurements are performed in a computer-controlled environment using the Integrated Circuit Characterization and Analysis Program (IC-CAP) software [101]. The IC-CAP software is used to set the range of bias levels. It is important to limit the current levels to ensure the safety of the devices and measurement components. The captured data can be used to generate the I-V characteristics in IC-CAP.

For S-parameter measurements using the 110 GHz HP8510C VNA, the experimental arrangement remains the same, however, complete calibration of the

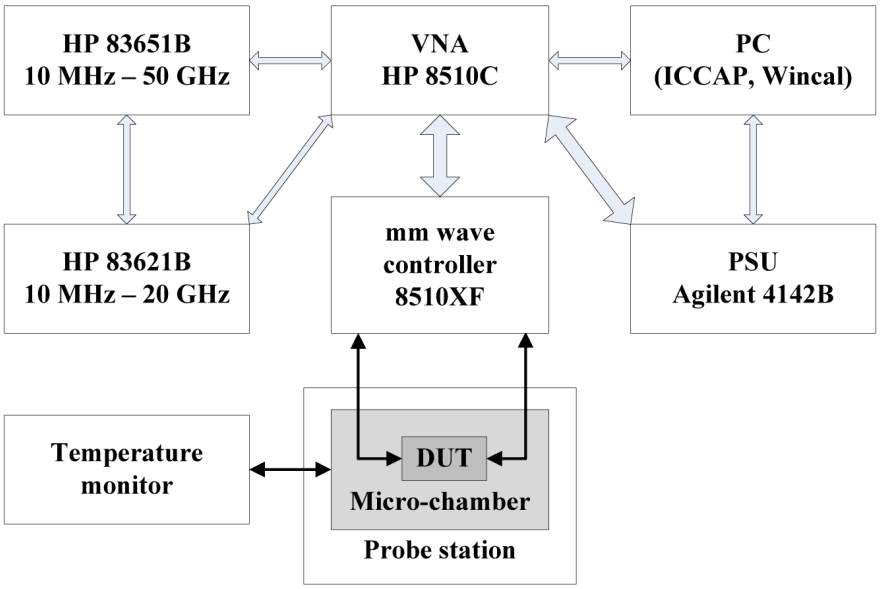

(a) Block diagram representation

(b) Magnified view of an on-wafer transistor

Figure 8.2: On-wafer transistor DC and S-parameter measurements

VNA and the RF cables and probes is required. Calibration is performed using standard LRRM techniques in Cascade Microtech's WinCal software environment [102].

Figure 8.3 shows the experimental arrangement for the DC and S-parameter measurements of MMIC LNAs. This is very similar to the experimental arrangement for on-wafer measurements. The differences are highlighted here:

- Separate DC bias cards, and not the internal bias-Ts of the VNA, are used to supply the gate and drain biases. The PSU supplies the DC biases straight to the MMIC via the bias cards.
- A different Cascade Microtech probe station, which can accommodate DC cards for biasing the LNA, is used. The absence of a micro-chamber in this particular probe station implies that temperature-variation is not possible.

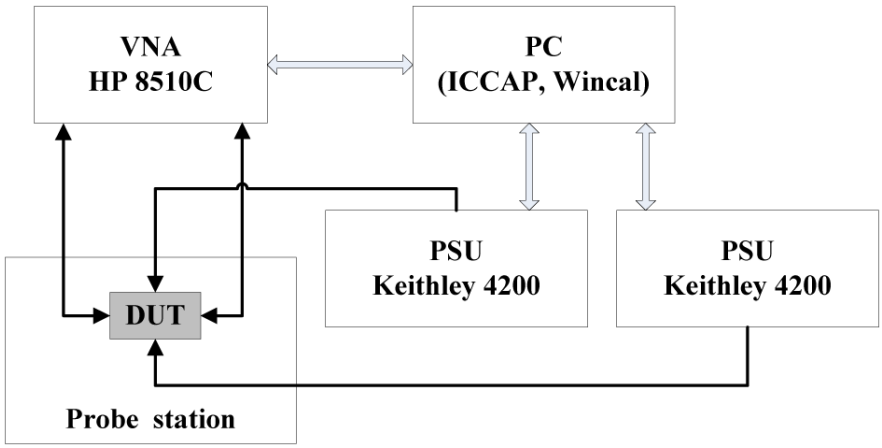

(a) Block diagram representation

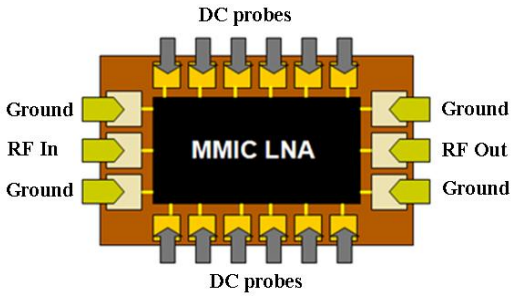

(b) Magnified view of an on-wafer MMIC LNA

Figure 8.3: On-wafer MMIC LNA DC and S-parameter measurements

- The 4142B PSU is replaced with 2 Keithley 4200 PSUs with a larger number of power supply ports. This is required to provide the gate and drain biases for all stages of the LNA.

The DC bias cards have 6 bias probes each, with the 2 outer-edge probes for ground potentials. The top and bottom arrows in the magnified view of the MMIC in Figure 8.3 (b) represent these probes.

8.2.2 Overview of Noise Figure measurements

This subsection describes the measurement principles of the noise figure in a 50 Ω system, NF_{50}. The 2 principal methods of NF_{50} measurements are the Y-factor(or hot/cold-source) method [103] and the cold source method [47]. These

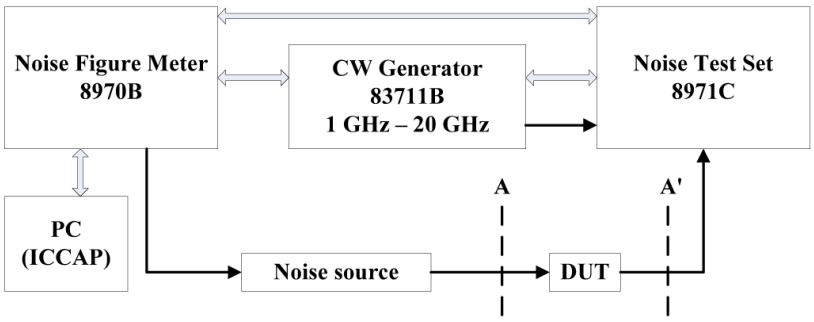

Figure 8.4: NF_{50} measurement using Y-factor method

methods, and their relevance to on-wafer transistor measurements, are discussed in the following subsections.

Y-factor method

The majority of modern day Noise Figure Meters (NFMs), Noise Figure Analyzers (NFAs), and spectrum analyzer-based solutions are based on this traditional method of measuring NF_{50}. Detailed information on this method can be obtained from [103].

Figure 8.4 shows the experimental arrangement to measure NF_{50} using the HP 8970B NFM, which implements the Y-factor method. The HP 8970 NFM operates up to 1.8 GHz but the frequency range can be extended up to 20 GHz with an external signal generator and a mixer. The calibrated noise source is either the Agilent 346A with a 6 dB Excess Noise Ratio (ENR) or the Agilent 346B with a 15 dB ENR. The calibration planes AA$'$ are marked in dashed lines. Noise calibration and measurements are performed using second-stage noise correction technique, detailed in [103].

The Y-factor method has several inherent disadvantages, arising from the following assumptions [104]:

1. The noise source presents a good 50 Ω match to the Device Under Test (DUT). Deviations from this lead to the following errors:

   (a) The reflected noise power from the DUT input is not fully absorbed but re-reflected back towards the DUT, thus creating a ripple pattern.

   (b) The DUT NF is a function of the source impedance. Non-ideal source

match therefore leads to another ripple pattern, which is indistinguishable from the ripple in 1(a).

2. The output match of the noise source remains the same in the hot and cold states.

3. The NF of the NFM's receiver remains the same when connected to the noise source and to the DUT.

4. The gain measured using the Y-factor is close to the available gain of the DUT even when its input and output match are not close to 50 Ω.

The mismatch errors outlined in 1 and 2 are magnified when components are added between the noise source and the DUT, even when loss compensation is used [104]. With these measurement uncertainties leading to typical error margins of 0.5 dB, this technique is unsuitable for on-wafer low noise transistor measurements. The NF_{50} measurements in the present work have been performed using the state-of-the-art instrument from Agilent Technologies, the PNA-X N5242A, which operates over 10 MHz – 26.5 GHz.

Cold source method used by PNA-X

The PNA-X implements the cold source method of NF_{50} measurement, also called the direct-noise method. This was first proposed by Adamian and Uhlir [50, 105]. A single direct measurement of the DUT noise with a cold (room temperature) termination at its input is performed and the gain of the DUT is measured independently with a VNA. Since the PNA-X has an in-built noise receiver along with the network analyzer functionality, multiple S-parameters and NF_{50} measurements can be performed with a single set of connections [47]. The measurement uncertainty decreases to 0.2 dB with a PNA-X [104].

Source-corrected measurements are achieved by using an Agilent Ecal module as an impedance tuner. The Ecal module presents a set of source impedances to the DUT, which are approximately but not exactly 50 Ω, and are determined during calibration. At each impedance state, the noise power is measured. This provides the solution of the noise parameter equation, thus providing a very accurate NF_{50}. This is called source-correction. Only 4 impedance states are required to calculate the noise parameters of the DUT during the measurement

process, however, 7 impedance states have been used in the present work to achieve higher accuracy [104].

PNA-X Calibration procedure:

Calibration of the PNA-X for NF_{50} measurements is a complex and intricate process, and needs to be performed with extreme care. The steps for the calibration for a connectorised DUT are as follows [104]:

1. The noise source is connected to port 2. This accomplishes
   - measurement of the hot and cold match of the noise source
   - measurement of the hot and cold noise power
2. Port 1 is connected straight to port 2. With this thru connection, the following are measured
   - load match of noise receivers
   - gain differences between the 0, 15, 30 dB settings of the LNA within the receiver
   - source impedance Γ_s values of the Ecal used as impedance tuner
3. The Ecal module is connected between ports 1 and 2, and
   - the S-parameters are measured
   - the receiver noise power with different Γ_s values of the Ecal is measured

The noise source is still used for characterising the noise figure and gain of the noise receiver in Step 1 (as in the Y-factor method), during calibration, but not used during measurements.

For on-wafer calibration, the coaxial connector of the noise source cannot be interfaced with the wafer probe tip. This implies that the noise source cannot be at the same measurement plane as the DUT, and increases the complexity of the calibration. An Adapter Characterization Macro is used to characterise the probes, and a fixturing tool is used to enable NF_{50} measurements at the probe tips [104]. This is detailed in Appendix A.

The noise calibration and measurement procedures using a PNA-X, although complicated, reduce the error in NF_{50} measurements to 0.2 dB.

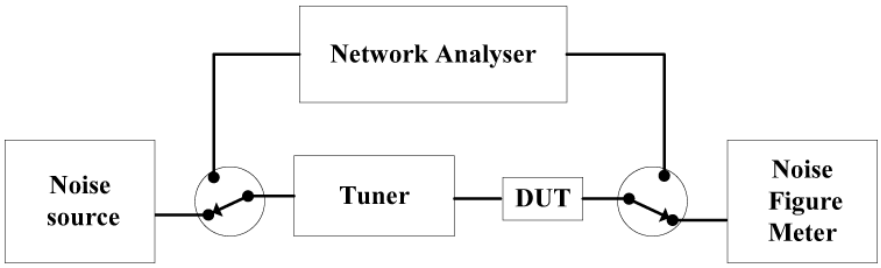

Figure 8.5: Traditional tuner measurements using separate NFM and VNA [108]

8.2.3 Noise parameter characterisation

The principle of noise parameter extraction using a tuner has been discussed in section 2.6.4. The experimental arrangement using the PNA-X and the automated tuner from Maury, MT982EU (operating from 3 – 8 GHz) and its benefits over the traditional arrangement are discussed here.

A traditional noise parameter measurement system using an automated tuner consists of a VNA and a separate NFM, as shown in the block diagram in Figure 8.5. Once the tuner sets a source impedance, the switches connect the DUT to the VNA for S-parameter measurements. For noise power measurements, the switches connect the noise source to the DUT input and the NFM to the DUT output.

Figure 8.6 shows the block diagram of the same system when a PNA-X is used. An integrated interactive program provided by Maury Microwave Corporation, called SNPW [106], is used to control the measurements. It utilises the network analyzer within PNA-X to measure S-parameters, the noise receiver within PNA-X to measure the noise power levels, and the Maury Automated Tuner System (ATS) software [107] to extract the noise parameters. This simplifies the system considerably, reduces the number of cables and connections, improves the stability and integrity of the system and makes it less prone to human errors [108].

Tuner calibration process

The noise parameter measurement system can be calibrated in 2 ways: 1) pre-characterization of all system blocks separately, and 2) in-situ calibration. The former method enables blocks to be switched in and out without re-calibration. The in-situ calibration (called SNP Cal) requires the PNA-X to be permanently

connected to the system. It allows the entire system to be calibrated without breaking any critical connections, which leaves fewer possibilities for connection error or changes caused by cable bending [108]. This procedure has been followed in the present work. The complete calibration sequence consists of 2 steps:

1. **In-situ S-parameter calibration of the system:** This comprises of 3 steps:

   (a) **2-port calibration at DUT reference planes AA′:** Figure 8.6 shows the AA′ plane. An on-wafer SOLT calibration kit was used. This calibration enables direct measurements of the DUT S-parameters.

   (b) **1-port S_{22} calibration at the noise source reference plane B:** Performed with the previous 2-port calibration in place (by inserting a thru at the AA′ plane), this 1-port calibration enables determination of the reflection coefficients of the noise source under hot and cold conditions. The 2-port S-parameters from the noise source to the DUT are processed by subtracting error terms from the above measurements.

   (c) **Tuner characterisation:** The complete 2-port S-parameters, at different tuner positions, are directly measured.

2. **Noise receiver calibration:** A thru is placed between AA′ and the noise and gain parameters of the receiver are measured as a function of frequency and source impedance state. The noise averaging can be set to a high value of 32 to improve data smoothness. The ambient temperature can also be set during the noise calibration to accurately model the noise contribution of the passive components of the system.

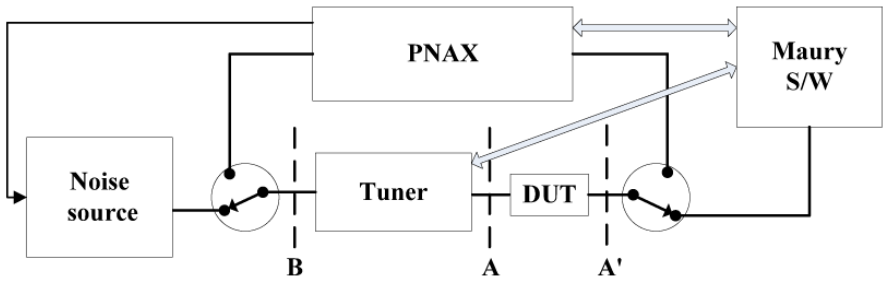

Figure 8.6: Tuner measurements using PNA-X [108]

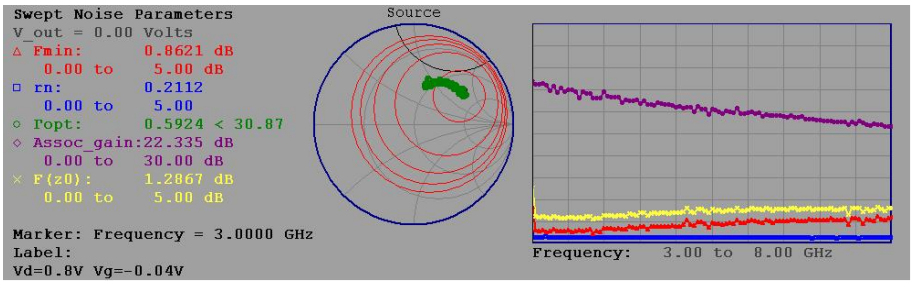

Figure 8.7: An example output from the Maury software

Measurement

The measurements can be performed over the entire frequency range that tuner has been characterised over, or over a subset of this. The tuner moves to a particular position and the S-parameters and noise powers are acquired for the entire frequency range before the tuner moves to a different position. After complete data acquisition, the program uses the selected solution method to extract the noise parameters. The gain parameters are calculated using the device S-parameters. The noise and gain parameters are displayed in both graphical and tabular form; an example graphical representation is shown in the screen-shot in Figure 8.7.

8.3 Reverse noise experimental arrangement

This section encompasses the measurement techniques utilised to validate the principles of LNA reverse noise measurement, described in chapter 4. As discussed in section 4.3, $C1$ is the temperature associated with the deliverable noise power $\left(\overline{|c_1|^2}/k\right)$ (in a 1-Hz bandwidth) to the input termination at the input port of an LNA. This termination is an antenna element in a single receiver chain. To verify that the noise coming out from the LNA input port is equal to the theoretically calculated value of $C1$, an experimental arrangement has been designed. This is described in detail here.

8.3.1 Measurement of noise coming out from an LNA input port

Figure 8.8 shows the reverse noise experimental arrangement. It is very similar in principle to the experimental arrangement used in [70] and [71]. In [70], a standard radiometer has been used, whereas in this case the HP 8970B NFM has been used as the noise power receiver. The NFM is set to display the relative noise power in the logarithmic scale, with respect to the noise power of a standard 290 K termination. The power displayed in the NFM is given by

$$\text{Power displayed} = 10\log\frac{T_d}{290}\ \text{dB} \tag{8.1}$$

where T_d is the temperature associated with the unknown power spectral density and is expressed in K. Since the DUT is connected in a reverse manner, this is also the effective reverse noise temperature, the quantity of interest. Addition of a low noise pre-amplifier improves the accuracy of the measurements.

An isolator is connected before the pre-amplifier, as shown in Figure 8.8. Calibration is performed with the 346B noise source (with 15 dB ENR) connected to the isolator port 1. Inclusion of the isolator in the experimental arrangement, between the DUT and pre-amplifier, is important because it removes the following sources of errors:

i) The noise wave emanating from the input of the pre-amplifier, reflected by the input of the DUT and sent back to the measurement system. This contribution would be small in the case of low input reflection coefficient of the DUT and/or a very low noise pre-amplifier. This effect could also be theoretically corrected for, but then the noise parameters of the pre-amplifier have to be known. The use of an isolator previous to the pre-amplifier effectively eliminated this source of error. Any noise coming out of the pre-amplifier input is absorbed by the matched termination (50 Ω) at port 3 of the isolator. For an isolator the noise parameters are well determined and it is necessary only to know the magnitude of the reflection coefficient of the DUT.

ii) The portion of the noise wave emanating from the input of the DUT which is reflected back by mismatch at the input of the pre-amplifier.

Together, the above effects can generate a standing wave pattern. Even with the

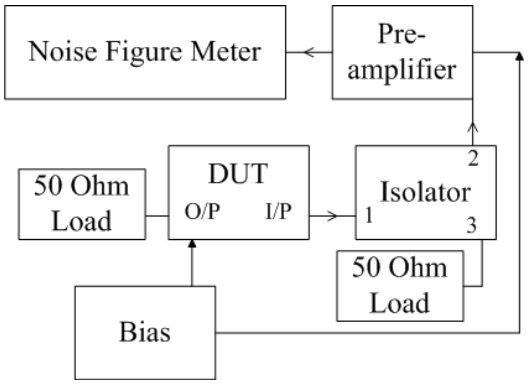

Figure 8.8: Experimental arrangement for determination of the effective temperature of the reverse noise wave emanating from the DUT

use of an isolator, however, the following noise components remain:

i) **Component 1:** Noise generated by the matched termination (50 Ω) at port 3 of the isolator, reflected by the input of the DUT, and incident on the measurement system.

ii) **Component 2:** Noise generated by the matched termination (50 Ω) at the output of the DUT transmitted to the input. In case of an amplifier with negligible reverse transmission, this can be neglected.

The total noise incident on port 1 of the isolator is given by the sum of the noise from the DUT input, Component 1 and Component 2. The input mismatch of the isolator Γ_{iso} is another potential source of measurement error and has to be accounted for in the calculations. The expressions in equation 8.2 are therefore defined:

$$\begin{aligned} C1' &= C1 \times \left(1 - |\Gamma_{iso}|^2\right) \\ E1' &= \text{Component 1} \times \left(1 - |\Gamma_{iso}|^2\right) \\ E2' &= \text{Component 2} \times \left(1 - |\Gamma_{iso}|^2\right) \\ \text{Total} &= C1' + E1' + E2' \end{aligned} \tag{8.2}$$

where Γ_{iso} is the input reflection coefficient of the isolator. A comparison of the calculated ('Total') and measured values of the effective temperature of the reverse noise wave thereby provides validation of the theoretical predictions. In summary, the experimental arrangement to evaluate $C1$ has intentionally been designed in a manner that all potential sources of error have either been eliminated or accounted for in the calculations. To determine the value of $C1$ theoretically, knowledge of the S-parameters and noise parameters of the DUTs is required.

The tuner measurements required to obtain these have already been discussed in section 8.2.3.

8.4 Antenna measurements

This section presents an overview on antenna measurements in the laboratory environment. Ideally, antenna measurements need to be performed with the Antenna Under Test (AUT) so far removed from any objects causing environmental effects that an open space approximation is valid [109]. Professional laboratories use indoor RF anechoic chambers which facilitate secure measurements in a controlled environment. The chambers are designed to minimise electromagnetic interference and prevent reflections of the radiation emanating from the antennas [80]; the chamber walls are covered with commercial RF absorbing material. The present measurements were performed inside such an anechoic chamber.

Anechoic chambers are limited by space restrictions. As the frequency of the operation decreases, far-field measurement capability is reduced. The size of the RF absorber also limits the lower frequency measurement limits. Measurements would then require large anechoic chambers. These are generally very expensive, and hence sometimes measurements are conducted in a roof, a terrace or an open field. The location should be as far as possible from power lines, aerials and microwave radio transmitters and without any metallic structure or conductive surface, concrete walls, buildings and trees [109]. This is very often difficult to achieve.

In the present work, the 5071B Electronic Network Analyzer (ENA) from Agilent Technologies, operating over 300 KHz – 8.5 GHz has been used for the antenna measurements. The resonant frequencies of the antennas have been determined by standard 1-port measurements, and the coupling levels between the 3 separate patches in the antenna strip have been determined by 3-port measurements. Due to the impracticalities associated with direct measurements of the 3-dimensional radiation patterns of the antenna, a number of 2-dimensional patterns are measured in practice, in the horizontal or vertical planes. A 2-dimensional pattern is referred to as a pattern cut. Pattern cuts can be obtained by keeping the azimuth angle constant and varying the elevation angle to record the received power levels, and vice versa.

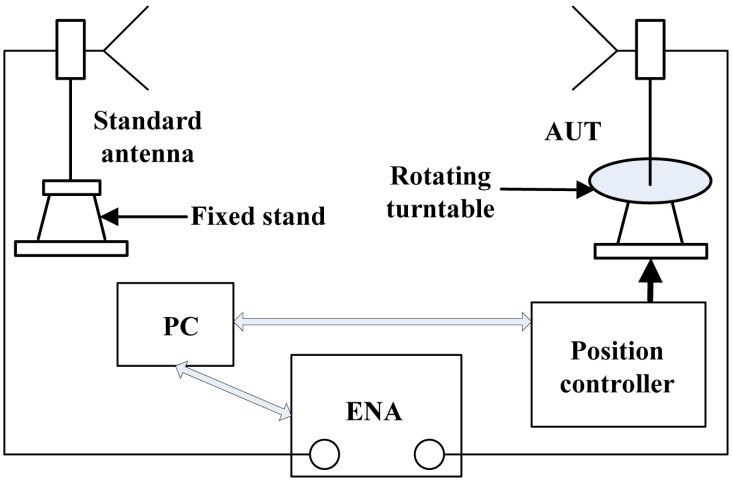

Figure 8.9: Experimental arrangement used in anechoic chamber to measure radiation patterns [110]

Figure 8.9 shows a picture of the present experimental arrangement. A standard horn antenna is attached to the fixed stand, and the AUT is attached to a rotating turntable. The standard antenna is used as the transmitting antenna and the AUT as the receiving antenna. A desktop computer controls both the ENA and the position controller (which rotates the turntable). The DAMS Antenna Measurement Studio software [111] is used to capture and process the data. Polar plots of the radiation patterns can be obtained at any desired frequency, in both linear and logarithmic scales. A screen-shot of the DAMS software environment is presented in Appendix A.

8.5 Summary

In this chapter details of the various experimental arrangements that have been used in the present research work are presented. The different intricacies relevant to the different measurements have been discussed. These include measurements with state-of-the-art instruments such as the PNA-X, those implementing modifications to standard noise measurements to measure a particular parameter of interest (the reverse noise from an LNA), and standard antenna measurements in anechoic chambers. The range of measurements performed encompasses both active and passive components. The results obtained from measurements based on the principles outlined in this chapter are discussed in chapters 9 to 12.

Chapter 9

Results and analysis - transistor characterisation

9.1 Introduction

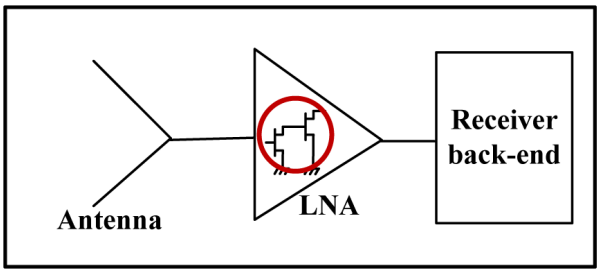

Figure 9.1: Focus of the chapter - results of transistor characterisation

This chapter focuses on the results and analysis of the transistor characterisation work. The measurements have been conducted using the measurement principles and set-ups discussed in section 8.2. The results of the DC and S-parameter measurements are presented in sections 9.2 and 9.3, respectively. Section 9.4 presents the results of the NF_{50} and the tuner based noise parameter extraction measurements.

9.2 DC characterisation

This section presents the results of the DC measurements performed on the 10 different processes, which had been listed in Table 9.1 in section 6.2.1. For each

Table 9.1: Complete range of bias variations

Process	Drain bias voltage (V_{ds}) (V)	Gate bias voltage (V_{gs}) (V)
1	0 to 1.5	-0.7 to 0.1
2	0 to 1.5	-0.9 to 0.2
3	0 to 2	-0.4 to 0.6
4	0 to 1	-0.4 to 0.4
5	0 to 2	-0.6 to 0.3
6	0 to 0.7	-0.4 to 0.3
7	0 to 1	-0.84 to 0
8	0 to 1.2	-0.6 to 0
9	0 to 2	-0.9 to 0
10	0 to 2	-0.9 to 0

of the processes, a variety of devices have been measured, characterised and compared. Table 9.1 summarises the range of gate and drain bias voltages, V_{gs} and V_{ds}, respectively, that have been applied to the different transistor processes. Decision on the bias ranges has been based on the following criteria:

- V_{ds} has been varied from 0 V to the voltage at which the saturation region is reached or the breakdown region is approached, in intervals of 0.05 V.
- V_{gs} has been varied from the pinch-off voltage to the voltage where the transconductance g_m starts decreasing after reaching the peak ($g_{m(peak)}$), in intervals of 0.02 V.

Subsections 9.2.1, 9.2.2 and 9.2.3 present comparative analyses of the current-voltage (I_{ds}-V_{ds}) characteristics, the derived transconductances and the variation of the gate current I_{gs} with the gate voltage V_{gs}. The 4 finger 50 μm (4×50 μm) gate width transistor from each process has been selected for this purpose to maintain uniformity. This particular gate width device was unavailable for processes 7, 8 and 10, and hence the comparisons do not include these processes. In the following discussion, the 'total gate width' has sometimes been referred to as the device 'size', a terminology frequently used by designers.

Issues arising from lack of repeatability in wafer runs are discussed in subsection 9.2.4. Subsection 9.2.5 presents the variations of the transconductance of the processes over an extended temperature range.

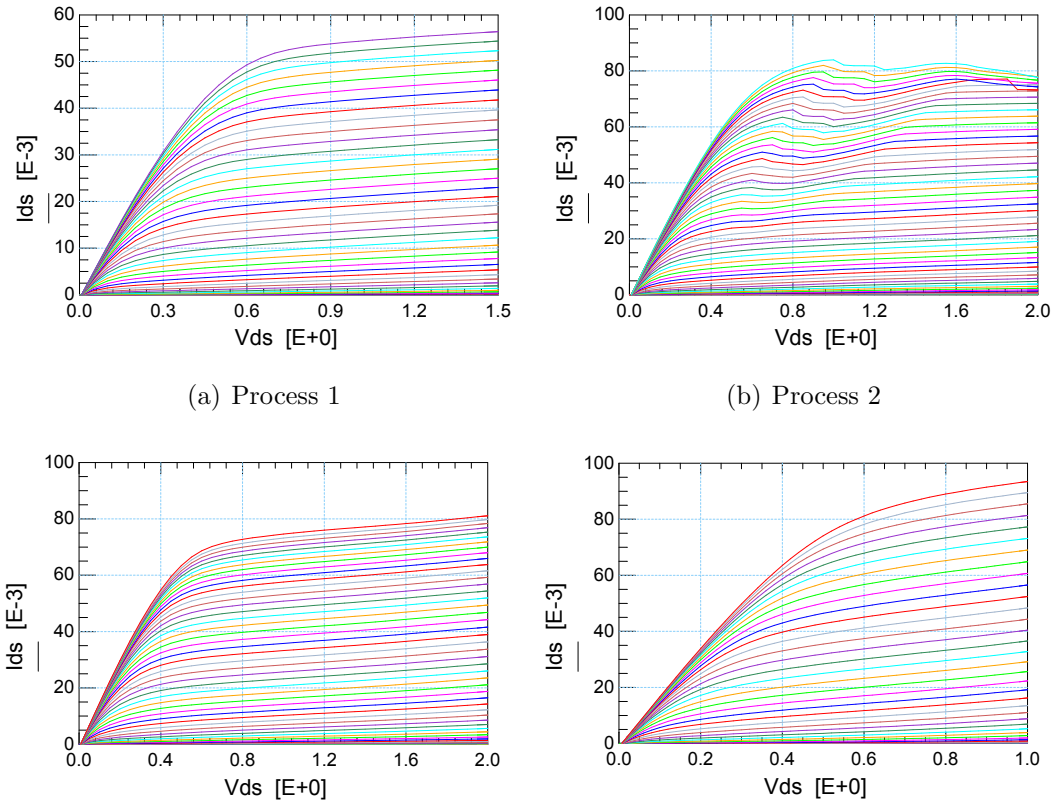

(a) Process 1

(b) Process 2

(c) Process 3

(d) Process 4

Figure 9.2: Comparison of I_{ds} – V_{ds} characteristics of a 4×50 μm transistor (Process 1 – 4)

9.2.1 Current-voltage characteristics

This subsection presents a comparative analysis of the I_{ds}–V_{ds} characteristics for the 4×50 μm transistors. A similar comparison between a 4×25 μm gate width device has been made for processes 1 – 8 in [19].

Figures 9.2 and 9.3 show the plots of the I_{ds}–V_{ds} curves. It is observed that the transition from the linear to the saturation region occurs at different V_{ds} levels for different processes. In most cases, the currents do not appear to saturate completely, but there is a finite slope in the saturation region.

Other interesting aspects can be observed from the plots. Process 2, the 150 nm GaAs mHEMT process, shows oscillatory behaviour in higher V_{gs} levels. The 70 nm GaAs mHEMT process, process 6, exhibits high current levels even at comparatively low values of V_{ds}. Due to this reason, this process has been

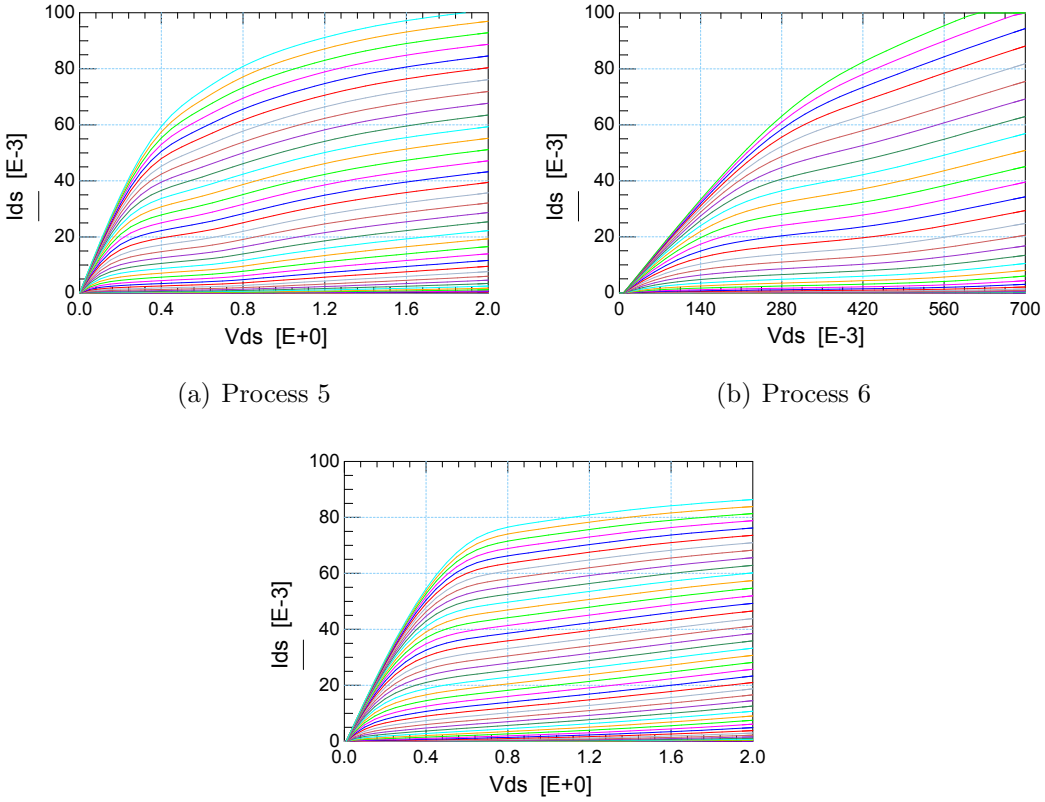

(a) Process 5

(b) Process 6

(c) Process 9

Figure 9.3: Comparison of I_{ds} – V_{ds} characteristics of a 4×50 μm transistor (Process 5, 6 and 9)

observed to have good power efficiency. One wafer run of this process, however, shows breakdown symptoms above V_{ds} levels of 0.9 V, and hence the process is not reliable. The repeatability of process 6 has been examined in subsection 9.2.4.

Process 6 also generally exhibits the worst pinch-off properties. Process 3 exhibits the best pinch-off properties, and processes 1 and 9 also show comparatively better trends. A good pinch-off is required to achieve better noise performance at cryogenic temperatures [112].

9.2.2 Transconductance curves

A comparative analysis of the transconductance plots, calculated from the variation of I_{ds} with V_{gs}, is presented here. Figures 9.4 and 9.5 show these plots for the 4×50 μm devices of the 7 processes. The various parameters discussed

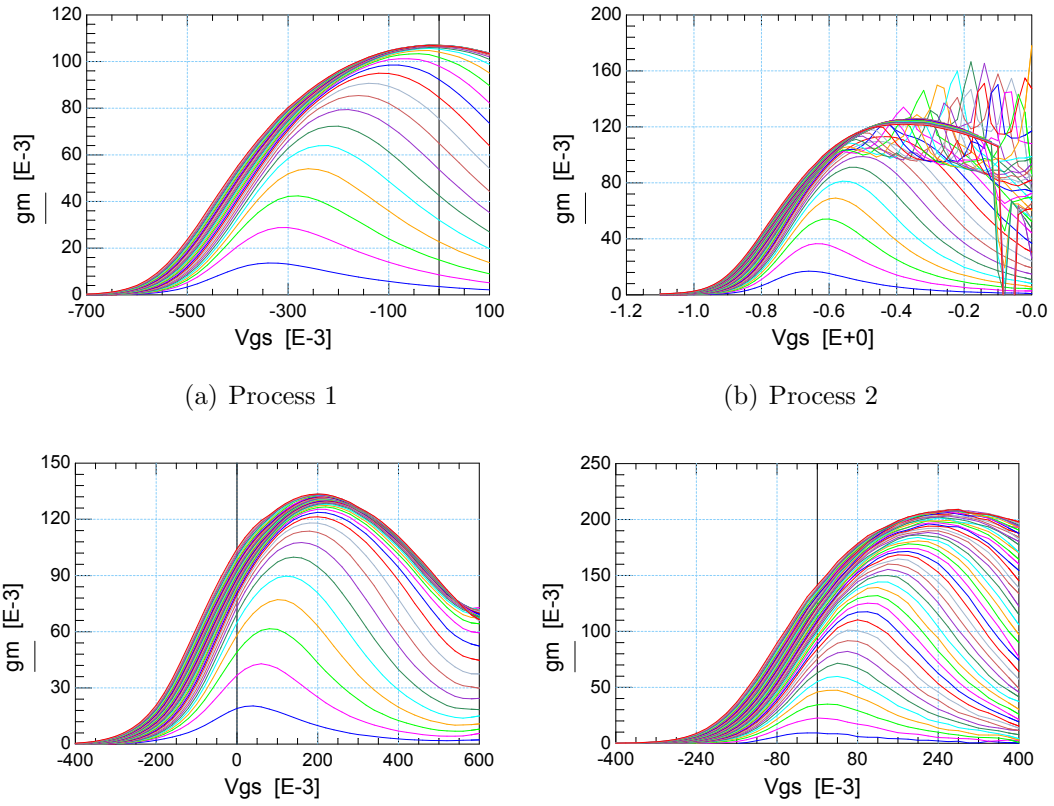

(a) Process 1

(b) Process 2

(c) Process 3

(d) Process 4

Figure 9.4: Comparison of transconductance curves of a 4×50 μm transistor (Process 1 – 4)

in this subsection have been tabulated in Table 9.2. To maintain uniformity in comparison, the peak g_m point, $g_{m(peak)}$, the point at which $(\Delta g_m/g_m) < 1\%$ has been selected. Noise measurements, described later in section 9.4, have been conducted at the same bias point. This particular bias point is henceforth referred to as 'Bias 1'.

The plots in Figures 9.4 and 9.5 show that process 6 exhibits the highest $g_{m(peak)}$ values rising above 300 mS, and at much lower values of V_{ds} compared to the other processes. Process 1 has the lowest values of 105 mS $g_{m(peak)}$. A higher $g_{m(peak)}$ value indicates higher gain and higher cut-off frequencies, and a higher slope of the g_m curve implies better control of the gate over the conducting channel.

Process 2 exhibits an oscillatory behaviour; a breakdown of the g_m curves is observed at V_{ds} levels above 0.5 V. This has been observed consistently for all

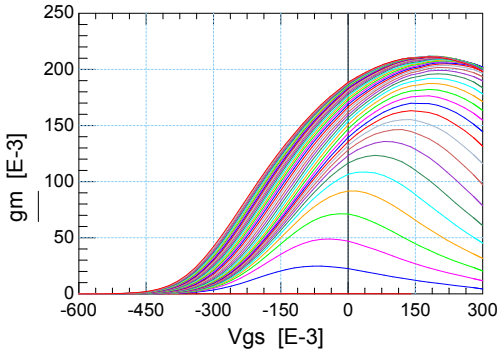

(a) Process 5

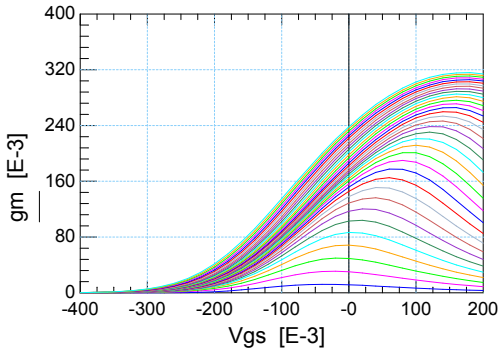

(b) Process 6

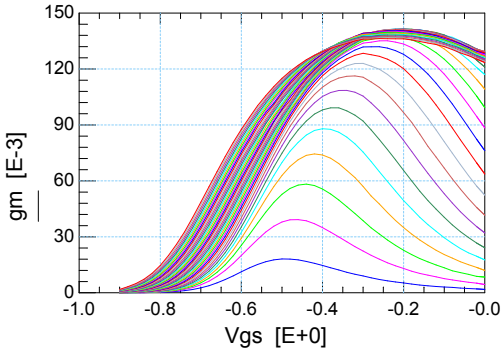

(c) Process 9

Figure 9.5: Comparison of transconductance curves of a 4×50 μm transistor (Process 5, 6 and 9)

Table 9.2: Comparison of the DC performance of 4 × 50 μm device from the different processes

Process	Pinch-off voltage (V)	V_{gs} at $g_{m(peak)}$ (V)	$g_{m(peak)}$ (mS)	Power consumed at peak g_m (mW)
1	-0.7	-0.02	105	27
2	-1.2	-0.4	120	26
3	-0.5	0.2	130	20
4	-0.35	0.3	200	33
5	-0.5	0.2	205	71
6	-0.35	0.18	315	57
9	-1.0	-0.25	137	28

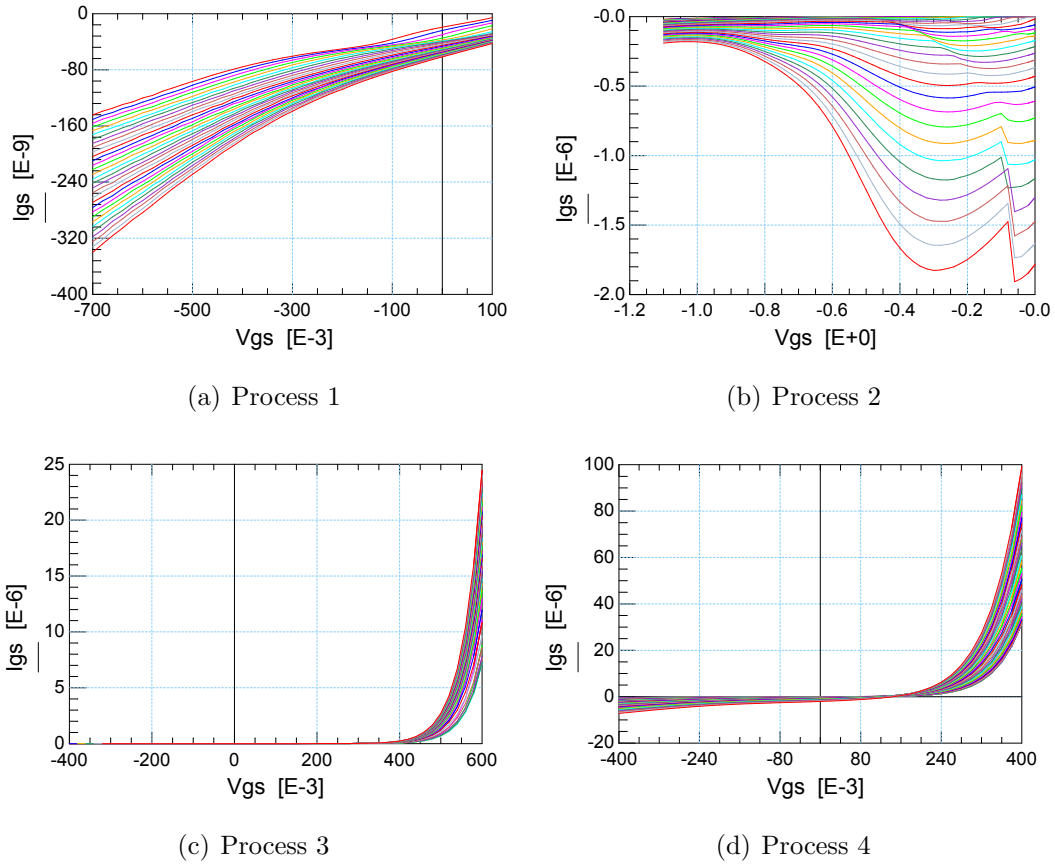

(a) Process 1

(b) Process 2

(c) Process 3

(d) Process 4

Figure 9.6: Comparison of I_{gs} – V_{gs} variation of a 4×50 μm transistor (Process 1 – 4)

devices of this process. The gate bias $V_{gs(g_{m(peak)})}$ at which $g_{m(peak)}$ is reached is of interest to a design engineer. It is observed that the $V_{gs(g_{m(peak)})}$ values are negative for processes 1, 2 and 9, and positive for processes 3 to 6.

The g_m curves also indicate the pinch-off voltages for the various processes. These values vary between -0.35 V V_{gs} (for porcesses 4 and 6) and -1.2 V V_{gs} (for process 2). The lowest swing of V_{gs} between pinch-off and the peak g_m point is observed for process 6 at 0.525 V. As stated earlier, this indicates the control of the gate over the channel.

9.2.3 Gate leakage current levels

This subsection presents a comparison of the gate leakage current levels. Ideally a HEMT transistor should have no gate leakage current I_{gs}. High levels of I_{gs}

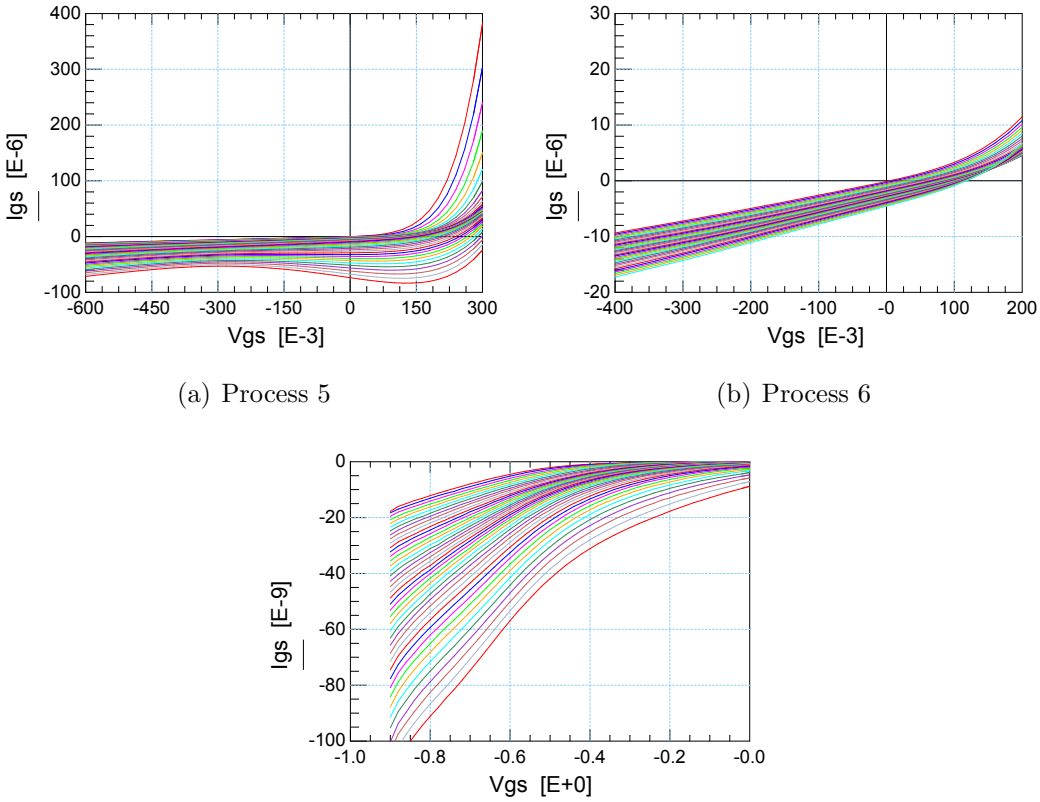

(a) Process 5

(b) Process 6

(c) Process 9

Figure 9.7: Comparison of I_{gs} – V_{gs} variation of a 4×50 μm transistor (Process 5, 6 and 9)

indicate static power consumption as well as increases noise [113]. It also generates shot noise at low frequencies [114]. The plots of the gate current levels are depicted in Figures 9.6 and 9.7.

The plots depict that magnitudes of I_{gs} increases with increasing magnitudes of V_{gs} for all processes except process 2, but the rate of increase varies. Process 2 exhibits negative resistance behaviour up to -0.3 V V_{gs}. This is observed for all devices of this process. Similar behaviour is exhibited, to a certain extent, by process 5 as well, but not as significantly. This negative resistance behaviour can lead to oscillation issues, as has been observed for process 2.

9.2.4 Repeatability and reliability concerns

The repeatability and reliability of a process is an important criterion for LNA design. A study of this has been conducted on the transistors of 2 different wafer runs for process 3 and 5. Although process 3 exhibits identical behaviour in both wafer runs, transistors of process 5 exhibit significant deviations, raising concerns about the repeatability of the process. This section outlines these results (for process 5) in brief. Figures 9.8 (a) - (e) show the I_{ds}–V_{ds}, g_m and I_{gs} – V_{gs} plots for the 4×15 μm device fabricated in 2 wafer runs, over the same bias voltage ranges.

Figures 9.8 (a) and (b) indicate significantly higher (sometimes 100 %) I_{ds} levels for wafer run 1, at same V_{ds} levels. Wafer run 2 indicates a lower level of breakdown voltage. Another significant fact is that the peak g_m values reached at constant V_{ds} levels are significantly lower for wafer run 1 $g_{m(peak)}$ values are obtained at lower V_{gs} in wafer run 1, especially at higher V_{ds}. Deviations in the gate leakage currents and the pinch-off voltages are also observed. I_g levels are considerably lower ($\approx$ 40 - 50 times) in wafer run 1 in comparison to wafer run 2. The difference in pinch-off voltage is a significant 0.3 V.

In summary, under similar bias conditions, the transistors in wafer run 1 exhibit higher I_{ds} and lower I_{gs} levels, lower $V_{gs(g_{m(peak)})}$, and achieve lower g_m and $g_{m(peak)}$ values at identical V_{ds}. Since the performance of an LNA designed with this process would be essentially based on these factors, these deviations in the process could severely affect the efficiency and reliability of the LNA.

9.2.5 DC measurements across temperature

In addition to the room-temperature measurements described in subsections 9.2.1 to 9.2.3, the variations in the DC behaviours of 6 processes, as a function of the ambient temperature, have also been studied. Processes 1 to 6 have been characterised over the temperature range of 60°C to -55°C, and an analysis of the variation of the peak g_m values has been performed.

Figures 9.9 (a)-(d) show the variation of the g_m curves with ambient temperature for the 4×50 μm transistor of processes 1, 4 and 6 (for both wafer runs). The drain voltage V_{ds} has been kept constant at 0.4 V. The plots shown here represent the different behaviours observed for the different processes. It is noted

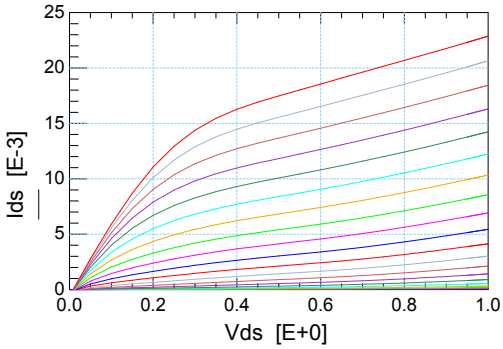

(a) Wafer run 1

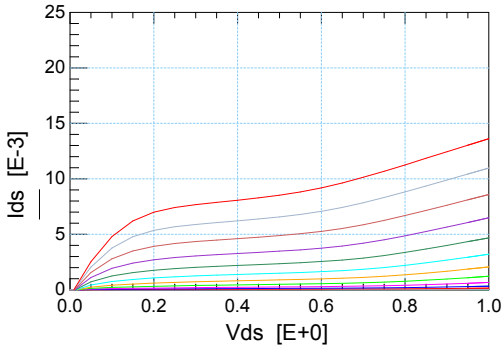

(b) Wafer run 2

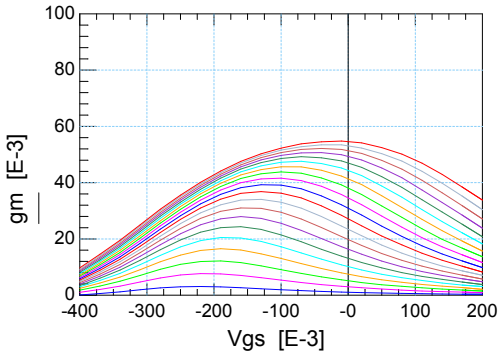

(c) Wafer run 1

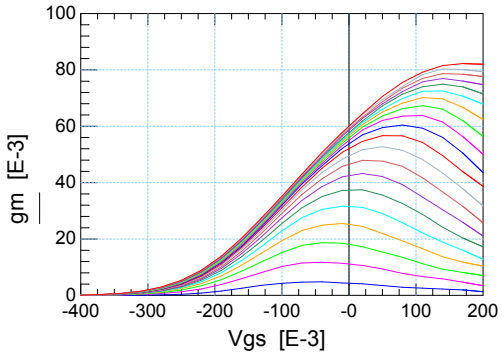

(d) Wafer run 2

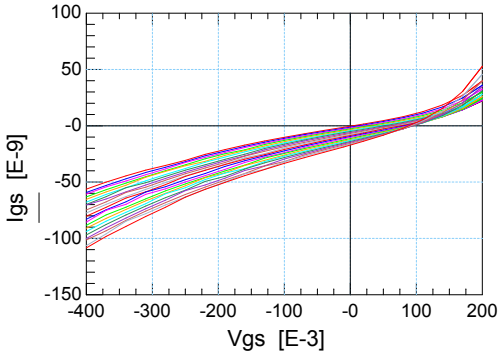

(e) Wafer run 1

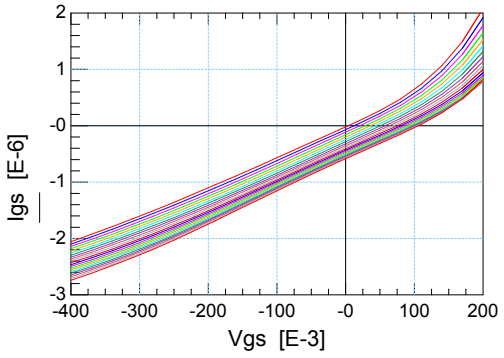

(f) Wafer run 2

Figure 9.8: Comparison of I_{gs} – V_{ds}, g_m and I_{gs} – V_{gs} curves of 4×15 μm device of process 6 for 2 wafer runs

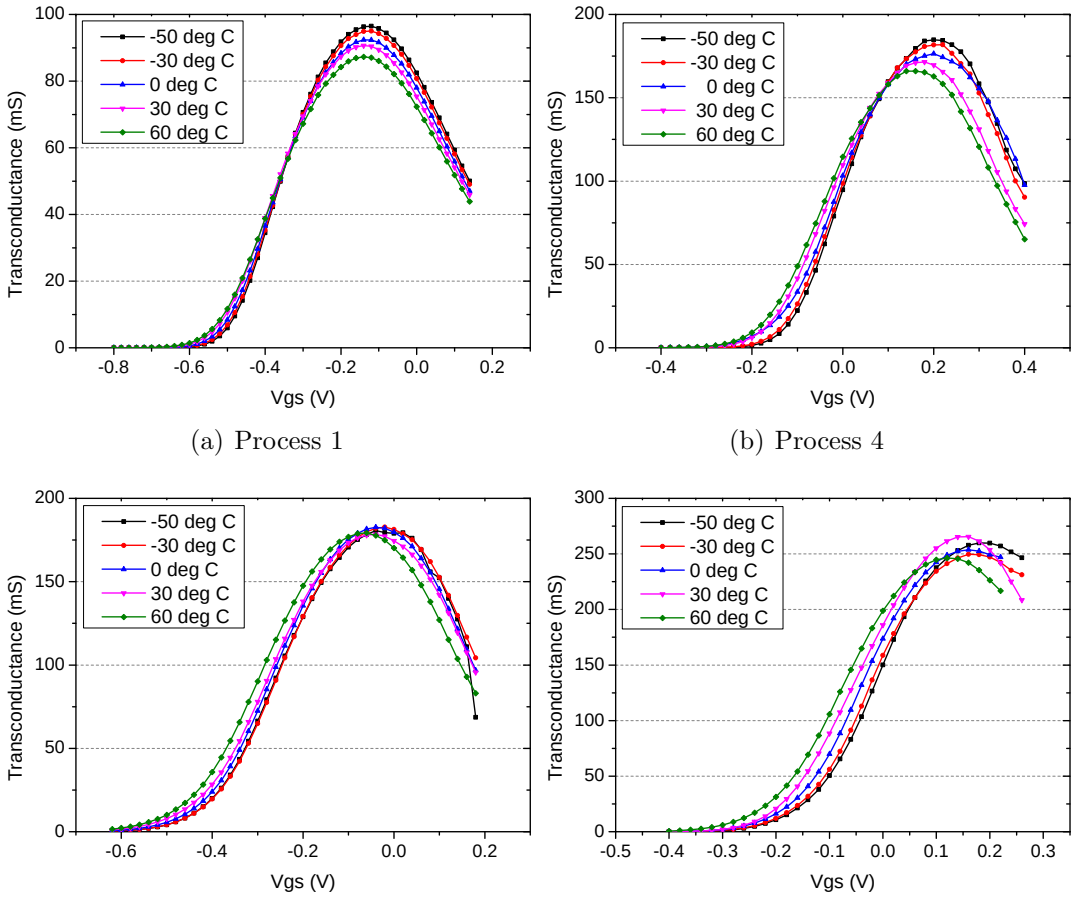

(a) Process 1

(b) Process 4

(c) Process 6 wafer run 1

(d) Process 6 wafer run 2

Figure 9.9: Variation of g_m curves of 4×50 μm transistor across temperature at V_{ds}=0.4 V

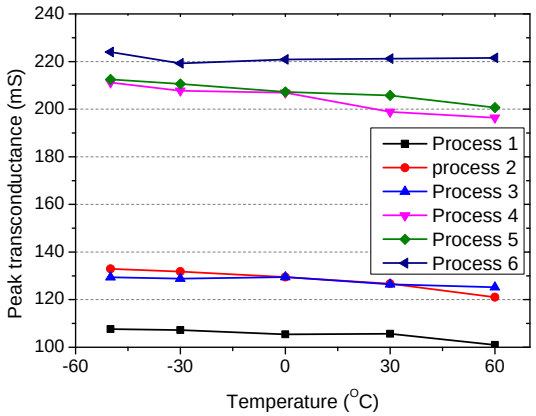

Figure 9.10: Variation of $g_{m(peak)}$ values with ambient temperature for the different processes

that at constant V_{ds}, the $g_{m(peak)}$ for both processes 1 and 4 increases with decreasing temperatures. However, while there is no shift in $V_{gs(g_{m(peak)})}$ for process 1, process 4 shows a shift towards more positive voltages. This is an important observation because in situations where there is significant diurnal and annual variations in temperature, V_{gs} levels may need to be varied in order to meet the required performance. Figures 9.9 (c) and (d) depict that transistors of wafer run 1 for process 6 show no variation in the $g_{m(peak)}$ values with temperature, and those of wafer run 2 show a random variation.

Figure 9.10 shows the variation of $g_{m(peak)}$ values with ambient temperature for the 4×50 μm devices of processes 1 to 6. The values have been extracted at 'Bias 1', mentioned earlier in subsection 9.2.2, at which $(\Delta g_m/g_m) < 1\%$. Processes 1, 2 and 3 have significantly lower values of $g_{m(peak)}$ in comparison to processes 4, 5 and 6. This was evident in Figures 9.4 and 9.5 in subsection 9.2.2 as well. The additional information conveyed in Figure 9.10 is that $g_{m(peak)}$ increases with decrease in ambient temperature for all processes except for process 6.

The extensive study of the DC performance of the various transistors indicates that different trends are observed for different processes. Some exhibit higher transconductance values or higher power efficiency. The majority of the processes show better performance at lower temperatures. Some processes have higher gate currents than others. The repeatability of some processes can cause serious concerns, while others show excellent agreement between the various wafer runs. This study of the DC characteristics has therefore provided an indication of the expected performance from the various processes.

9.3 S-parameter characterisation

The experimental arrangement described in section 8.2.1 has been used to measure the S-parameters of the transistors of the 10 different processes. The data has been used to predict the gain performance with variations in the bias settings and validate the library models of available process libraries. For example, Figures 9.11 (a) and (b) show the measured and simulated $|S_{21}|$ and $|S_{12}|$ for the 4×25 μm device of process 1, in 50 MHz – 45 GHz frequency range. The bias conditions are V_{gs} = -0.1 V, and V_{ds} = 1 V. The plots indicate that the predictions from the process library (simulated performance) up to approximately 10 GHz are reasonably good for $|S_{21}|$, and very good for $|S_{12}|$. It can be concluded that

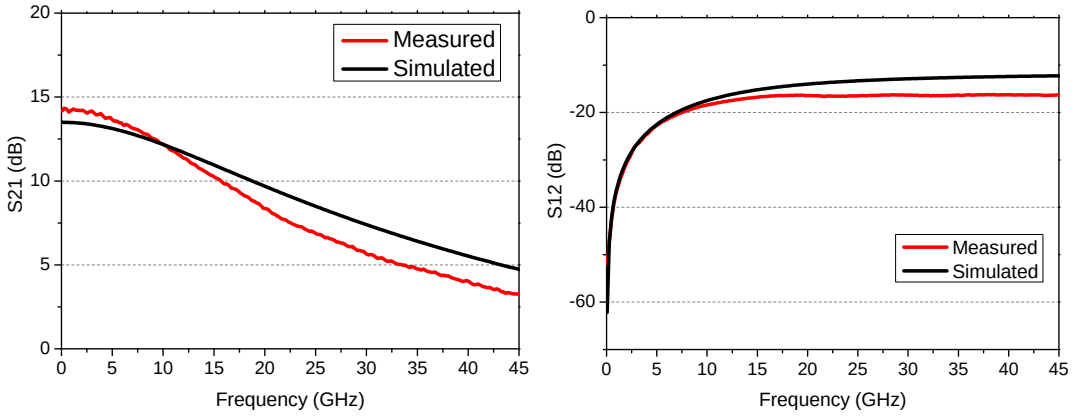

(a) Measured (b) Simulation

Figure 9.11: Comparison of simulated and measured $|S_{21}|$ and $|S_{12}|$ of a 4×25 μm transistor of process 1

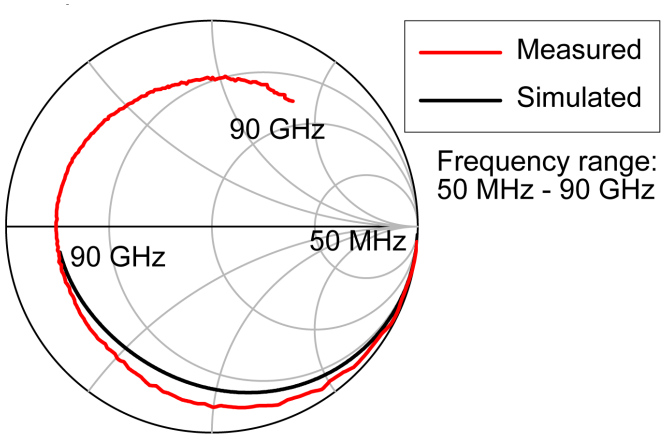

Figure 9.12: Comparison of simulated and measured S_{11} of a 4×25 μm transistor of process 9

the process library for process 1 is reasonably good.

The Smith Chart plot in Figure 9.12, on the other hand, brings out the deviations between measured and simulated performance of S_{11} for a 4×25 μm device of process 9, in 50 MHz – 90 GHz frequency range. The difference is significant at high frequencies, and indicates that matching at high frequencies based on the library models would be completely useless.

From the above examples, it is evident that direct S-parameter measurements serve as a highly effective way of validating the library models before initiating

LNA design work. S-parameter measurements also constitute an important step in both NF_{50} and noise parameter measurements, discussed next in section 9.4. Noise measurements are comparatively more complicated than S-parameter measurements. The results of the direct S-parameter measurements have been used as a validation during noise measurements.

9.4 Noise characterisation

This section focuses on the transistor noise characterisation work performed using the PNAX and Maury automated tuner. The measurement principles and set-ups were outlined in sections 8.2.2 and 8.2.3. Results of DC measurements in section 9.2 indicated that the mHEMT processes 2 and 5 do not exhibit reliable DC behaviour. Processes 7 and 8 are limited to transistors of only one size. These processes (2, 5, 7 and 8) have therefore been excluded, and noise measurements have been performed only on the remaining 6 processes.

In addition to 'Bias 1', a second bias point ('Bias 2')has been selected based on the criterion originally proposed in [35] - a lower NF_{min} can be obtained at the bias point where the quantity $\sqrt{I_{ds}}/g_m$ reaches a minimum value. These minima can be conveniently extracted from the DC curves.

Two distinct categories of data are generated by the Maury SNPW software used in automated tuner measurements:

- Data obtained directly from measurements - the S-parameters, the maximum available gain MAG, the gain in 50 Ω system G_{50} and the Rollet stability factor k.

- Data extracted from noise power measurements - the minimum noise figure NF_{min}, the noise resistance R_n, the optimum noise reflection coefficient Γ_{opt}, the noise figure in 50 Ω system NF_{50} and the associated gain (which is the gain at Γ_{opt}).

In addition to the S-parameter validation (as mentioned in section 9.3), comparison of the extracted NF_{50} values with directly measured values (using the measurement technique described in section 8.2.2) provides the second method of validation. Subsection 9.4.1 presents a comparison of the measured noise parameters. Subsection 9.4.2 presents the noise parameters of all measured devices at a spot frequency, to analyse their behaviour with variation in device size.

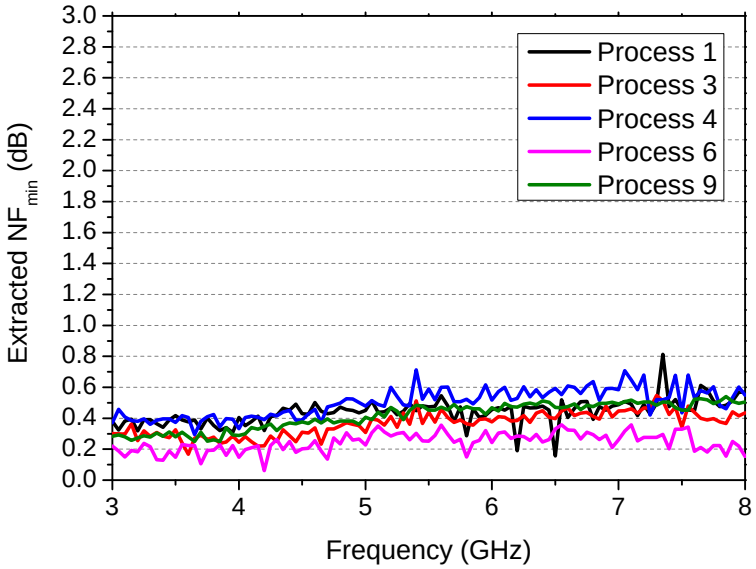

Figure 9.13: Comparison of extracted NF_{min} for 4×50 μm transistors at Bias 1

9.4.1 Comparison of noise parameters across frequency

A comparative analysis of the extracted noise parameters from the tuner measurements over a frequency range of 3 – 8 GHz is presented here, for the 4×50 μm devices of the 5 characterised processes. As in the DC analysis, process 10 has been omitted in this particular comparison due to unavailability of a device of this size.

Bias 1

Figures 9.13 and 9.14 show the plots of the extracted NF_{min} and normalised noise resistance r_n (normalised to 50 Ω). The major division in the y-axis is 0.2 dB in Figure 9.13, the error margin of the PNA-X. Process 6 shows the best performance in terms of both NF_{min} and r_n. The performance is closely matched by process 3, with maximum 0.2 dB increase in NF_{min}, and 2 Ω increase in R_n in a 50 Ω system. These parameters for process 1, 4 and 5 are in the similar range.

It is observed that the slope of NF_{min} with frequency is different for different processes. A definite increase in NF_{min} slope for process 6 is not evident. The reason for this is determined from a study of the NF_{50} plot, discussed later in this section. Figure 9.14 indicates that the values of r_n decrease with increasing frequency in this range for all processes.

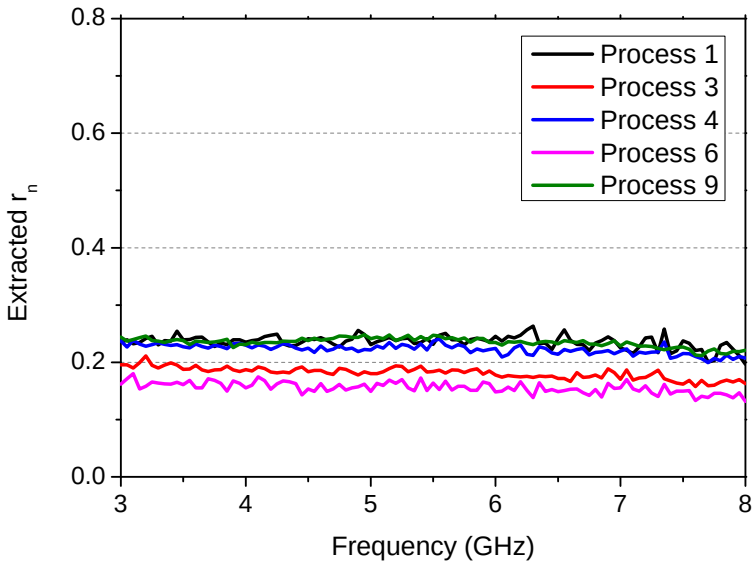

Figure 9.14: Comparison of extracted r_n for 4×50 μm transistors at Bias 1

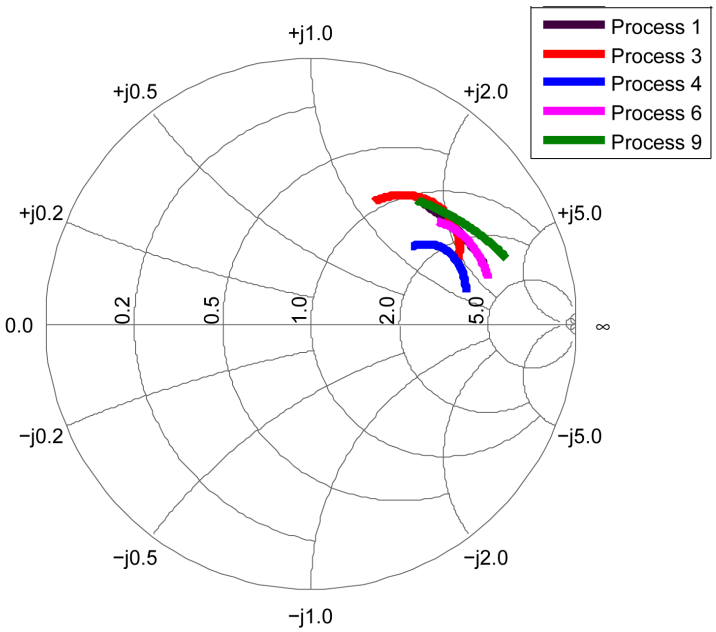

Figure 9.15: Comparison of extracted Γ_{opt} for 4×50 μm transistors at Bias 1

Figure 9.15 shows the locations of the extracted optimum noise reflection coefficients Γ_{opt} in the Smith Chart. They lie in different positions and the curvatures of the loci differ. The locus for process 3 signifies ease of matching in 50 Ω system at higher frequencies. This implies that the losses associated with the matching

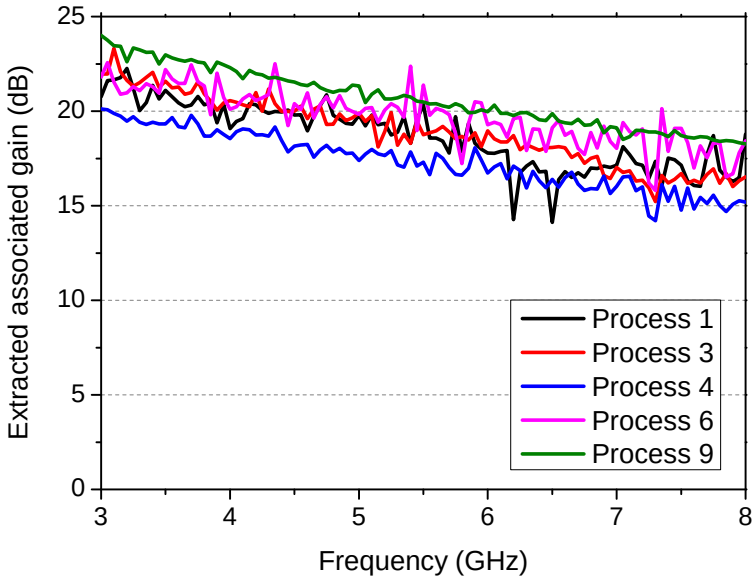

Figure 9.16: Comparison of extracted associated gain for 4×50 μm transistors at Bias 1

network would also be less. The spread of the loci over the Smith Chart also indicates that processes 4 and 6 would provide better broad band response than the other processes.

The extracted associated gain, which is the gain at NF_{min}, is plotted in Figure 9.16. It is seen that process 9 exhibits the highest associated gain, while process 4 shows the lowest. This parameter is important because it provides the designer an idea of the expected gain at the optimum noise match condition.

Figure 9.17 shows the plots of the extracted NF_{50} for all 6 processes. Process 6 exhibits the lowest NF_{50} of approximately 0.6 dB. Analysis of the behaviours of processes 1 and 4 leads to an interesting observation. In Figures 9.13 and 9.14, process 1 showed slightly less NF_{min} (<0.1 dB) in comparison to process 4, but slightly higher ($\approx 2\ \Omega$) R_n. This may be the reason why the NF_{50} values show the opposite - process 1 NF_{50} values are higher by ≈ 0.1 dB than process 4 NF_{50} in Figure 9.17. This signifies the important role the transistor R_n plays in determining the NF_{50} values.

The measured gains in a 50 Ω system, indicated as G_{50}, are plotted in Figure 9.18. It is observed that the G_{50} values for corresponding processes are lower than the associated gains, and the highest gain is exhibited by process 9.

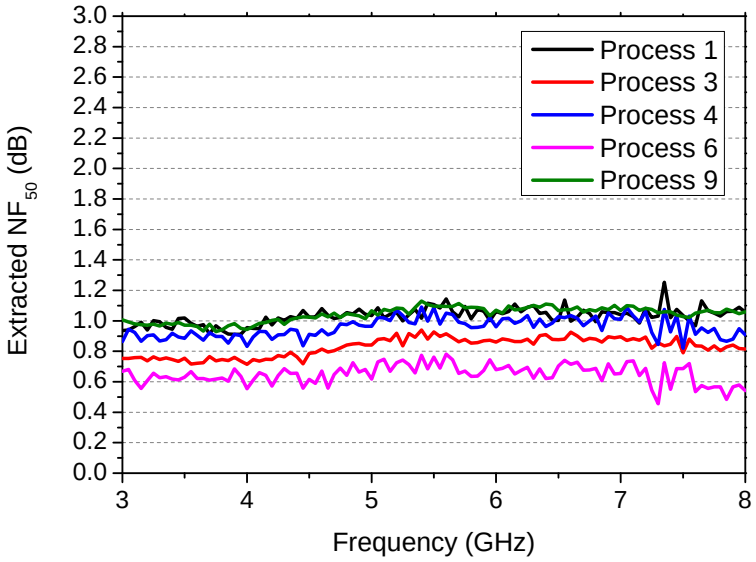

Figure 9.17: Comparison of extracted NF_{50} for 4×50 μm transistors at Bias 1

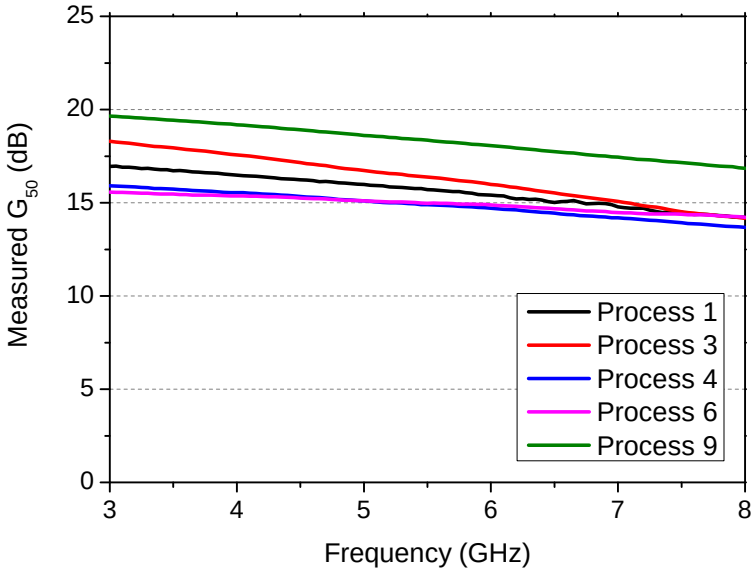

Figure 9.18: Comparison of measured G_{50} for 4×50 μm transistors at Bias 1

The accuracy of these results have been determined by comparing the extracted NF_{50} values (obtained from these tuner measurements) with those obtained from direct measurements. These are different set-ups and the calibration procedures are completely different, hence these comparisons provide a good validation. Figure 9.19 shows the results of the direct measurement of NF_{50} for

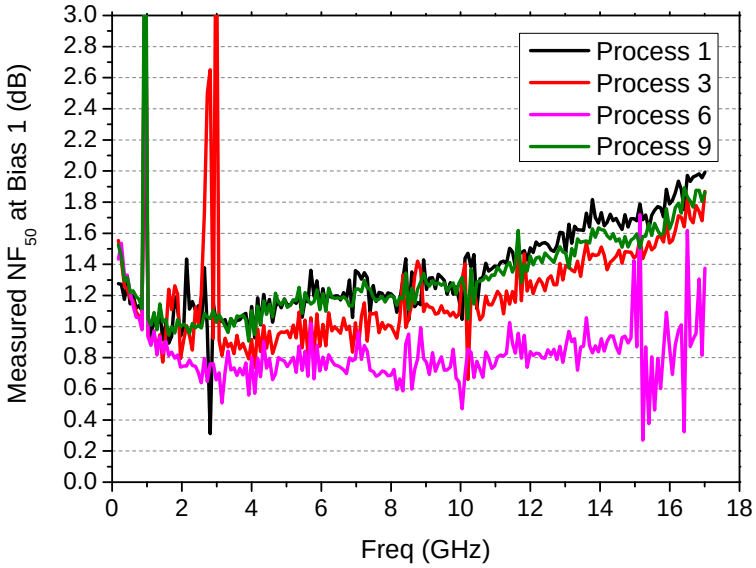

Figure 9.19: Measured NF_{50} for 4 × 50 μm transistors obtained from direct measurements

the 4×50 μm device of all processes (except process 4) over 10 MHz – 17 GHz. Process 4 results could not be presented here due to a corrupt file. Close comparisons between Figure 9.17 and Figure 9.19 (over the 3 – 8 GHz segment) for corresponding processes reveal the excellent match in both the values and the slope of NF_{50}. Any deviations lie within the measurement error range of 0.2 dB. This provides validation to the noise parameter measurements.

Process 6 shows the lowest NF_{50} values. Process 1 and 9 have the highest (and similar) NF_{50}. The apparent decrease in both extracted NF_{min} and NF_{50} for process 6 observed earlier can be justified by scrutiny of the relevant plot in Figure 9.19. It shows that the NF_{50} for process 6 remains almost flat over a much wider frequency range as compared to the other processes, as expected from the shape of the Γ_{opt} locus in Figure 9.15. A similar behaviour for the NF_{min} values should be observed as well. The observed anomaly in slope for process 6 therefore represents the local variation in the noise levels around 6 – 8 GHz.

From this analysis of the noise performance of 6 low noise processes, it can be concluded that the low values of NF_{min}, r_n and NF_{50}, and the wide noise bandwidth renders process 6 very suitable for broad band low noise applications. Its performance is closely matched by process 3.

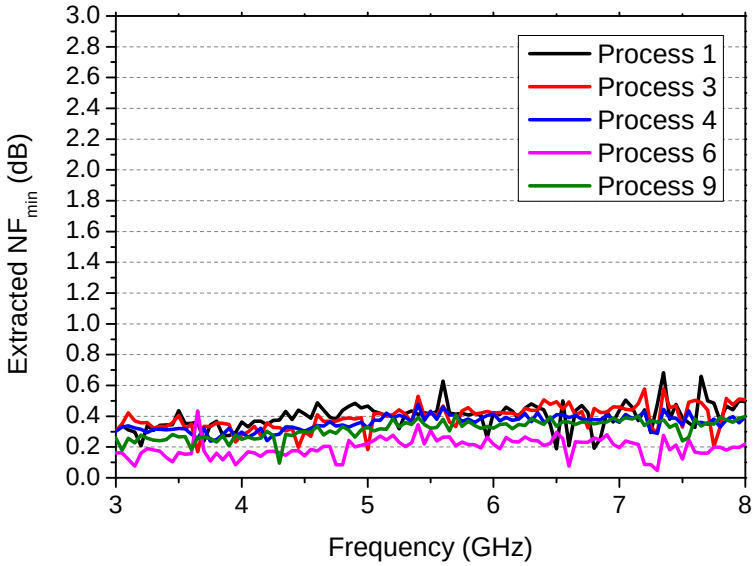

Figure 9.20: Comparison of extracted NF_{min} for 4×50 μm transistors at Bias 2

Bias 2

An analysis of the extracted noise parameters of the transistors at the second bias point, 'Bias 2' (which is where $\sqrt{I_{ds}}/g_m$ reaches a minimum value) reveals that some processes show improvements in performance, whereas others exhibit no significant difference. Figures 9.20 and 9.21 illustrate this for NF_{min} and r_n. A comparison with Figure 9.13 for Bias 1 reveals that process 4 exhibits 0.2 dB lower NF_{min} values at Bias 2, whereas process 1 NF_{min} values remain unaffected. The R_n values also decrease by 2 Ω for process 4 at Bias 2 whereas no difference is observed for process 6. It is also noticed that the overall performances of processes 1 and 3 degrades at Bias 2, for example the R_n of process 3 increases by 4 Ω in a 50 Ω system. Further investigation is required to characterise these trends.

The detailed plots of the noise parameters for the 4×50 μm device are presented in Appendix B. Comparisons between extracted and measured NF_{50} have shown agreement for this bias as well, any deviations being within the instrument error range. The NF_{50} plots of all devices across all processes at both bias points have been presented in Appendix B as well.

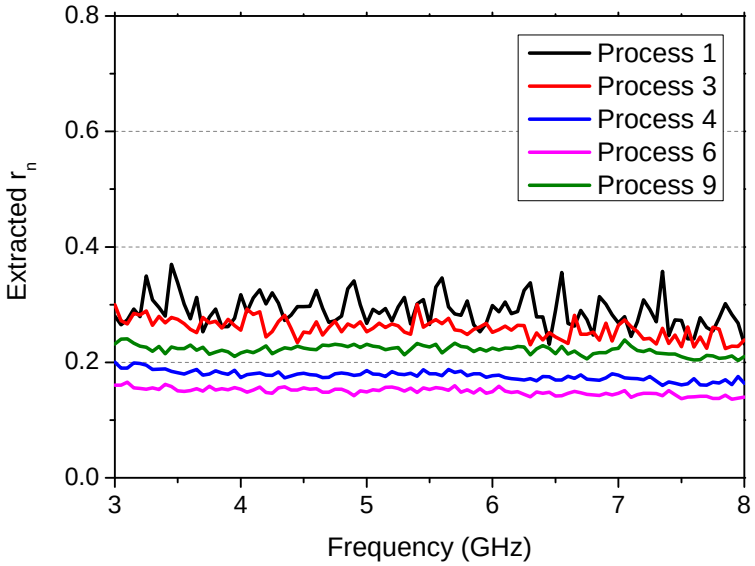

Figure 9.21: Comparison of extracted NF_{min} and r_n for the 4×50 μm transistor at Bias 2

9.4.2 Comparison of noise parameters across device size

This section presents an analysis of the variation of the noise parameters with device size (or total gate width W_g) at Bias 1, at a spot frequency of 6 GHz. Figures 9.22, 9.23 and 9.24 show the variation of the NF_{min}, the associated gain and the noise measure M (calculated from these two parameters), respectively. These relate to the noise match impedance Z_{opt}, associated with Γ_{opt}.

Figure 9.22 shows that NF_{min} values for different processes generally decreases with increasing W_g up to a certain point beyond which they start increasing again, that is, there appears to be a value of W_g that minimizes NF_{min}. The gate widths at which the minimum values are reached would be different for a different spot frequency. Owing to the larger gate widths of process 10, the NF_{min} minimum is not apparent.

Figure 9.23 indicates that the associated gains for processes 1, 4 (up to a certain W_g) and 9 remain almost constant. The associated gains of the larger gate width devices of process 10 decrease with increasing W_g. The shape of the calculated noise measure curves follow trends similar to NF_{min} for all processes.

Figures 9.25 and 9.26 present the measured NF_{50}, G_{50} and calculated noise measure from these two values. The curves of NF_{50} in Figure 9.25 show a sharp decrease with increasing W_g up to a certain size and then starts to increase. The

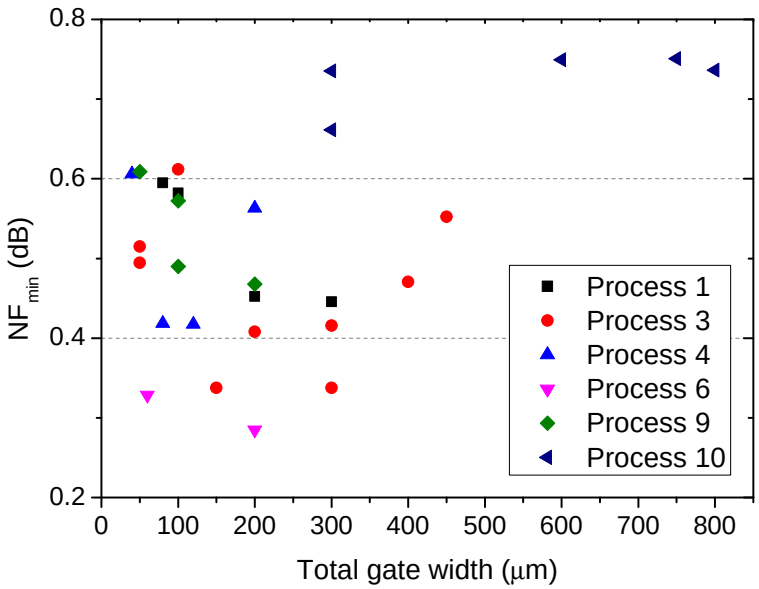

Figure 9.22: Variation of NF_{min} at Z_{opt} with increasing gate width

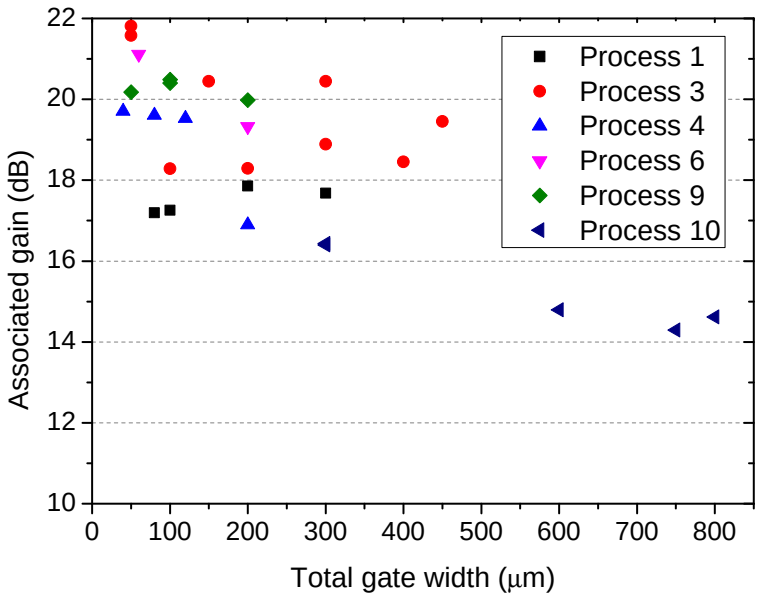

Figure 9.23: Variation of associated gain at Z_{opt} with increasing gate width

overall estimate suggests that at 6 GHz, it should be easier to match to 50 Ω with W_g in the range of 150 to 300 μm. This observation corroborates with the fact the size of transistor selected for the author's C-band design is a 270 μm W_g device (in section 6.3.2). This range of W_g suitable for LNA design would be

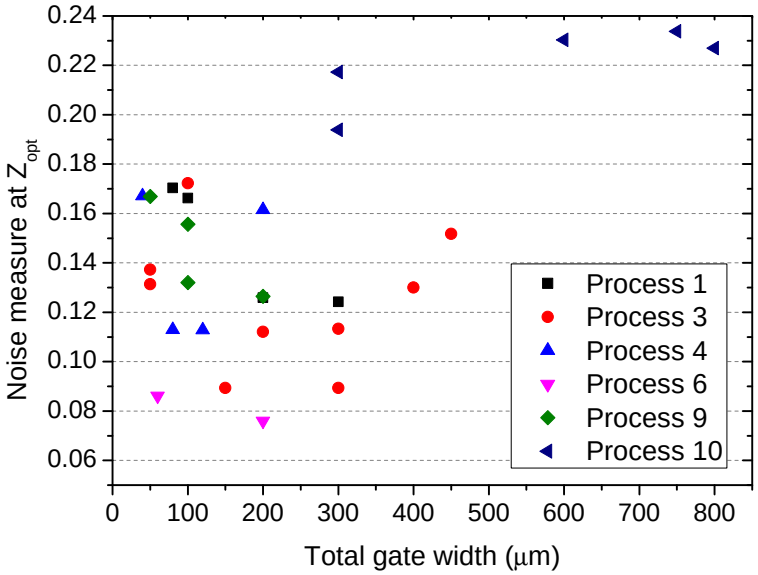

Figure 9.24: Variation of M at Z_{opt} with increasing gate width

different for a different spot frequency.

The plot of the gain in 50 Ω system, G_{50}, in Figure 9.26, indicates an increase in the gain with increasing W_g up to a certain point. It then remains almost constant up to a specific range, and subsequently starts to fall. For processes 6 and 9, this optimum range of W_g which provides highest G_{50} cannot be predicted because of unavailability of larger size transistors. Overall, the plot suggests that the best performance in a 50 Ω system may be achieved with 150 to 300 μm W_g values. The noise measure, calculated from the NF_{50} and G_{50} and shown in Figure 9.27, follows a similar trend to NF_{50}.

Figure 9.28 shows the variation of the r_n with increasing gate width. It is observed that the r_n decreases for larger devices, and an approximately hyperbolic trend is observed for all processes. There exists a threshold W_g above which r_n drops to a value suitable for efficient broadband designs. This trend has also been observed at other frequencies. It is evident from Figures 9.22 and 9.28 that there is a distinct trade-off in the optimum W_g when broad-band designs are required. At 6 GHz spot frequency, the optimum W_g required to achieve NF_{min} do not necessarily exhibit lowest R_n values. This analysis therefore has a direct implication on the choice of transistors for broadband LNA designs.

The plots of the parameters discussed in this subsection have been generated for Bias 2 as well. It is noticed that even if the absolute values may be different,

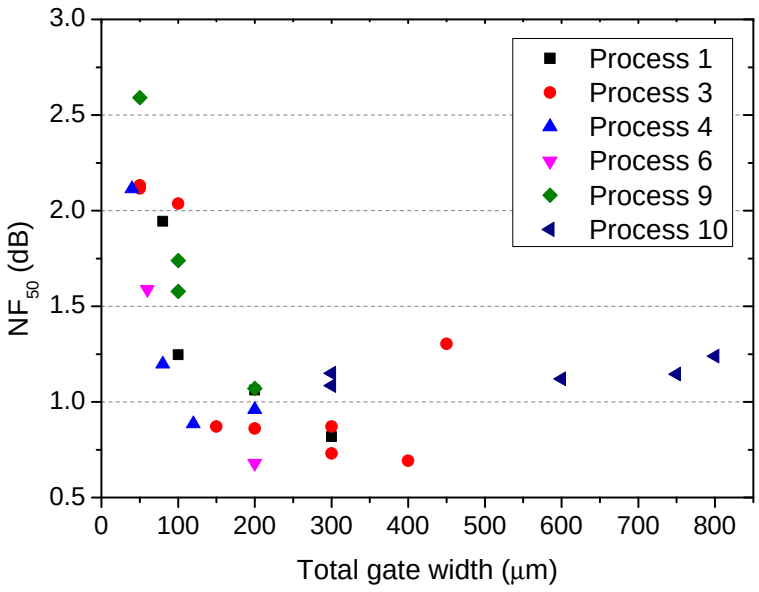

Figure 9.25: Variation of NF_{50} with increasing gate width

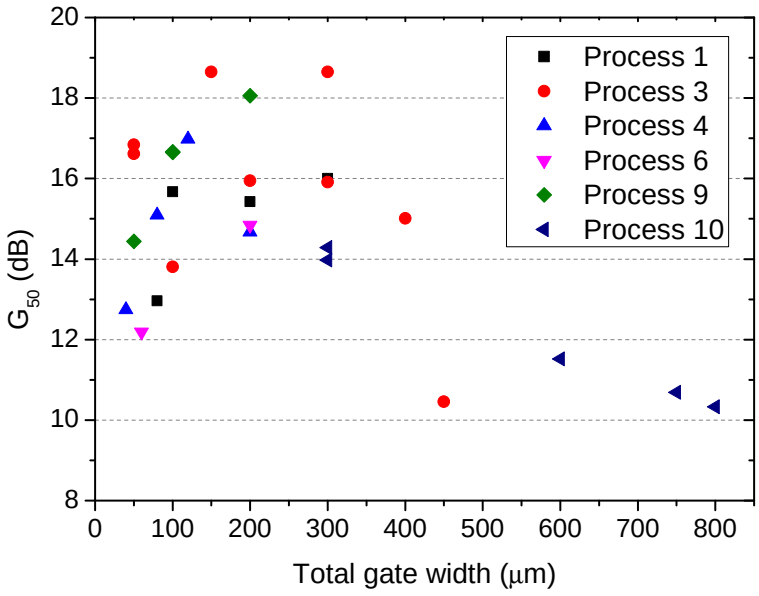

Figure 9.26: Variation of G_{50} with increasing gate width

the trends in the performance remain the same. These plots are presented in Appendix B.

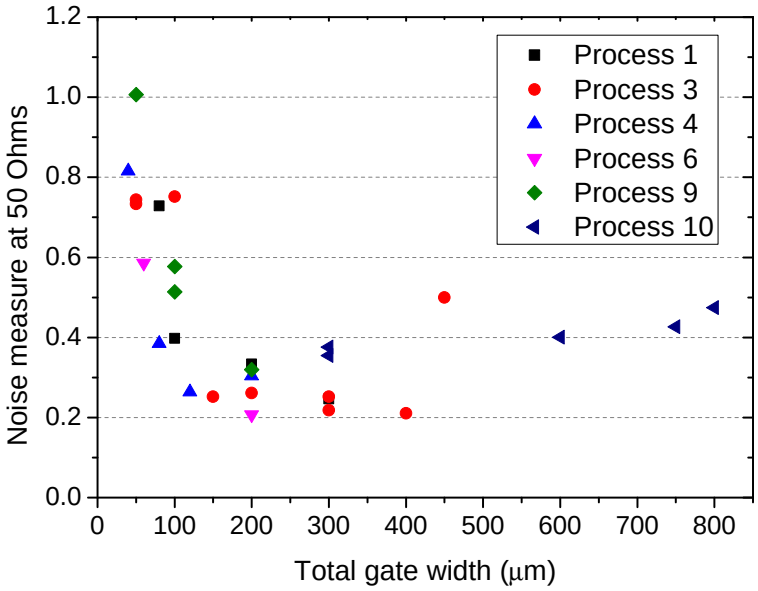

Figure 9.27: Variation of M_{50} at 50 Ω with increasing gate width

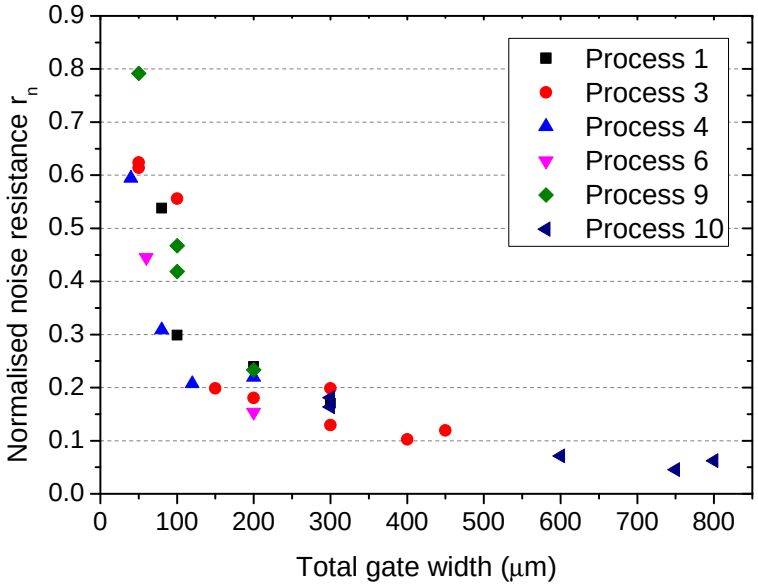

Figure 9.28: Variation of normalised noise resistance with increasing gate width

9.5 Summary

In this chapter, results of the transistor characterisation work have been presented. Results of DC analysis, including variations of DC performance with temperature have shown that some processes exhibit better performance than

others. The transconductance of all processes except process 6, a 70 nm mHEMT process, have shown an increase with decreasing temperatures. Repeatability concerns have also arisen for process 6, which pose a severe hindrance in developing reliable designs, especially for mass-scale production. In general, the mHEMT processes tend to show unreliable or oscillatory tendencies. The pHEMT processes show more stable and reliable behaviour.

The S-parameter measurements have been used to study the influence of the bias levels on the small-signal behaviour, and also to validate the library data provided by the foundries. The noise figure and noise parameter extraction measurements have brought forth the similarities and dissimilarities between the different processes. Process 6 has exhibited the best noise behaviour, and the performance of process 3 closely matches this at the measured peak g_m bias points. Unlike process 6, there are no repeatability issues arising for process 3, implying that it emerges as the best low noise processes in these bias ranges. Interesting variations with the gate width at a spot frequency have also been observed in this study. This analysis can provide an LNA design engineer with an initial guide to device selection in multi-stage LNA designs.

Chapter 10

Results and analysis - LNA design

10.1 Introduction

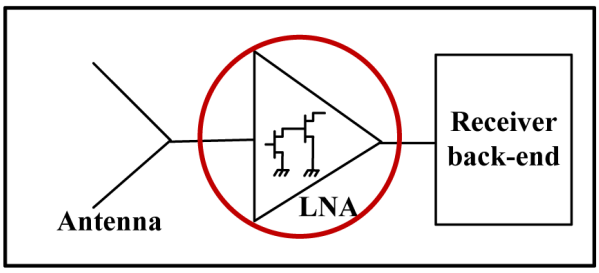

Figure 10.1: Focus of the chapter - results of LNA design

The development of a C-band and a UHF-band MMIC LNA has been discussed in chapter 6. In this chapter, the simulated results of these LNAs are presented, in sections 10.2 and 10.3, respectively. In addition to these, measured results of previously-designed MMICs (designed by the author's supervisor) are presented in section 10.4. The primary objective for performing measurements on already existing MMIC LNAs were as follows:

- establishing measurement techniques to completely characterise fabricated LNAs
- obtaining an understanding of how biasing in multi-stage LNAs influence performance

- investigating the application of genetic algorithm in generating optimised bias condition (as part of a separate program) [115]

These measurements also provide better insights into the aspects of amplifier stability, and bias ranges or frequency ranges where oscillations could potentially occur. Previously designed MMIC LNAs operating in 3 different frequency bands have been measured and characterised, using the measurement set-up described in section 8.2.1.

10.2 C-band LNA simulated results

The simulated results of the designed C-band MMC LNA are displayed in Figure 10.2. The left and right hand columns show the results in the operating band and an extended frequency band, respectively. Simulations over an extended frequency range help in detecting the potential for out-of-band oscillations. Figures 10.2 (a)-(b) show the noise figures at the system impedance of 50 Ω (NF_{50}), Figures 10.2 (c)-(d) display the Rollet stability factor K, and Figures 10.2 (e)-(f) depicts the S-parameters.

Figure 10.2 (a) indicates that the NF_{50} at the centre frequency 6 GHz is 0.62 dB. The variation in NF_{50} over the operating frequency range is less than 0.1 dB, implying a 4 GHz 0.1 dB noise bandwidth. Figure 10.2 (b) shows that the NF_{50} remains reasonably flat up to approximately 10 GHz and then starts increasing. From Figures 10.2 (c) and (d), the Rollet stability factor $K > 10$ in the C-band. Out-of-band, it drops to 7.4 and then continues to increase. Since $K > 1$ ensures unconditional stability, these values predict significantly reduced potentials of both in-band and out-of-band oscillations.

The S-parameter plots in Figure 10.2 (e) and (f) depict that the within the operating frequency range, the gain peaks at 30.4 dB, and the variation in gain remains within 1 dB for the operating band. The gain rolls off beyond the edge of the band, which is desirable to minimise the chances of oscillations. The input return loss obtained at 6 GHz is -23 dB, and is less than -8 dB for the complete band. The output return loss is uniform over this range at approximately -11 dB. The reverse gain increases with frequency but is below -55 dB for the entire band.

Overall, the simulated results indicate that all requirement specifications detailed in Table 6.2 have been successfully met (and in some cases exceeded) for

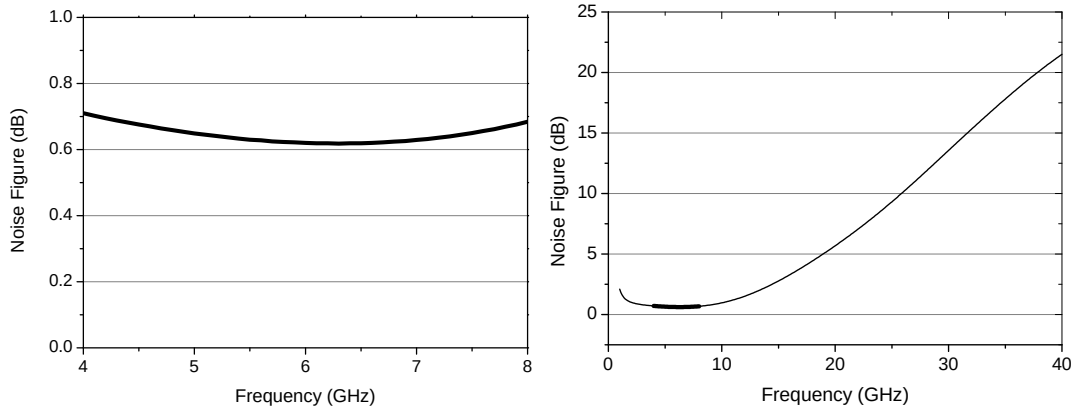

(a) Noise figure in 50 Ω - $NF50$

(b) Noise figure in 50 Ω - $NF50$

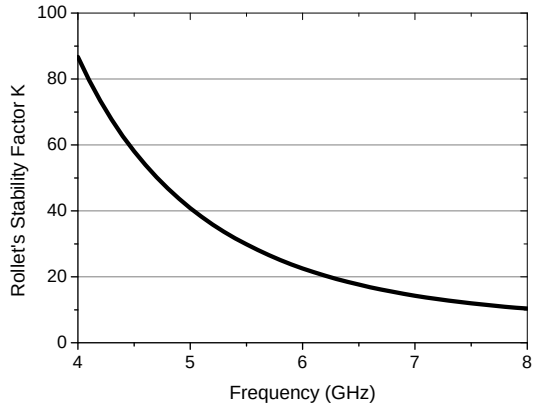

(c) Rollet's stability factor (K)

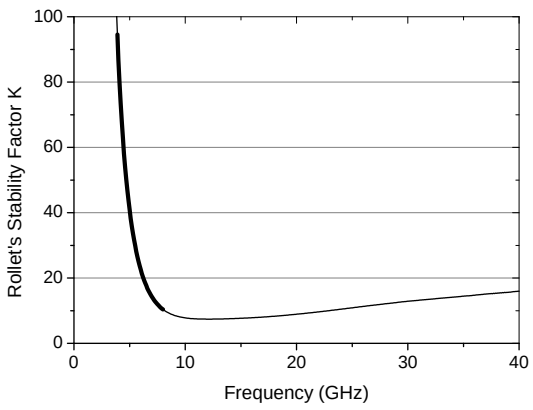

(d) Rollet's stability factor (K)

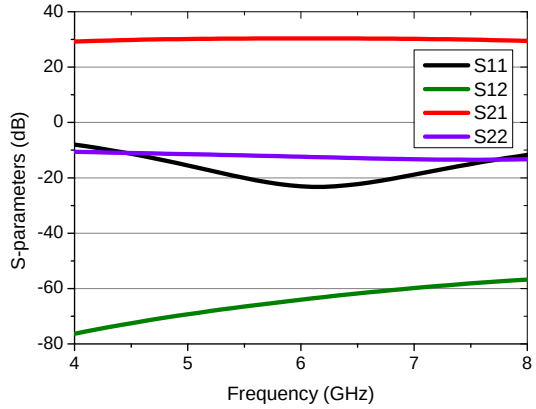

(e) S-parameters

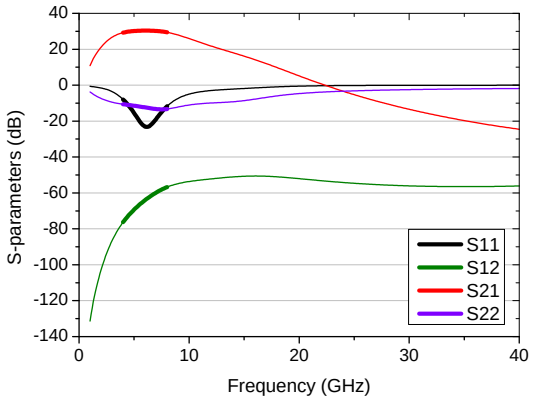

(f) S-parameters

Figure 10.2: Simulated results for the C-band LNA in the operating range and in an extended frequency range

Table 10.1: DC bias conditions of C-band LNA and power consumption

Stage	V_{DD} (V)	V_{GG} (V)	I_{ds} (mA)	Power Dissipation (mW)
1	1.5	0	9	14
2	1.5	0	16	24
3	1.5	0	21	32
Total				70

this design except for the input return loss. This is less than -10 dB from 4.3 – 8 GHz, and hence the slight degradation observed in the 4 – 4.3 GHz range is acceptable. The gain and the flatness obtained are better than the requirements specified: 30 dB instead of 25 dB, and 1 dB instead of 3 dB pk-pk variation in operating band. A lower pk-pk ripple is desirable in some applications, particularly in receivers which digitise with restricted number of bits.

The expected noise and gain bandwidths from this design are superior to existing C-band designs. Most designs in this band either exhibit comparable noise figures but over a much smaller bandwidth [116], higher noise figures in a narrow bandwidth [10] or higher noise figures in an enhanced bandwidth [11, 117]. This designs attains the objective of a low noise figure in the entire frequency range.

Table 10.1 presents the details of the supplied drain and gate voltages, the drain currents, and the power dissipation for all three stages. The drain and gate voltages are 1.5 V and 0 V for all stages, respectively. The total power dissipation is 70 mW, which is reasonable for a 3-stage LNA.

10.3 UHF-band LNA simulated results

This section presents the results of the UHF-band hybrid LNA design. Figure 10.3 shows the parameters in the 0.4 – 1 GHz range in the left column and over an extended range in the right column. The noise figure increases from 0.34 dB to 0.45 dB from 0.4 GHz to 1 GHz. The 0.1 dB noise bandwidth is approximately 450 MHz. The Rollet stability factor $K > 8$ in the entire band.

Overall, the results satisfy most of the design requirements. The noise figure $NF_{50} < 0.5$ dB specified in the requirements. The forward gain reaches its peak

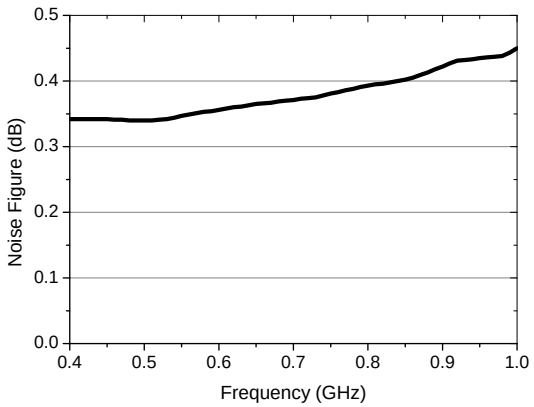

(a) Noise figure in 50 Ω - $NF50$

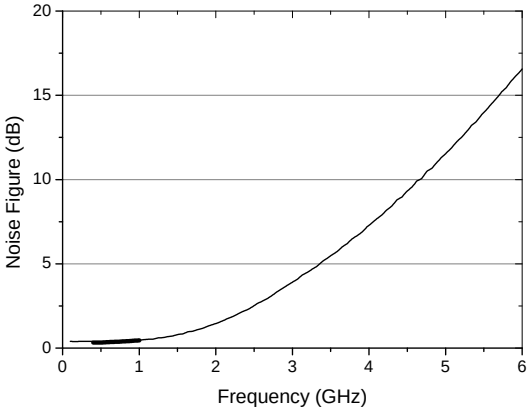

(b) Noise figure in 50 Ω - $NF50$

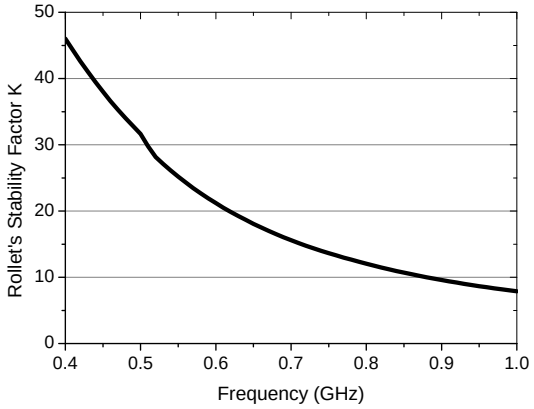

(c) Rollet's stability factor (K)

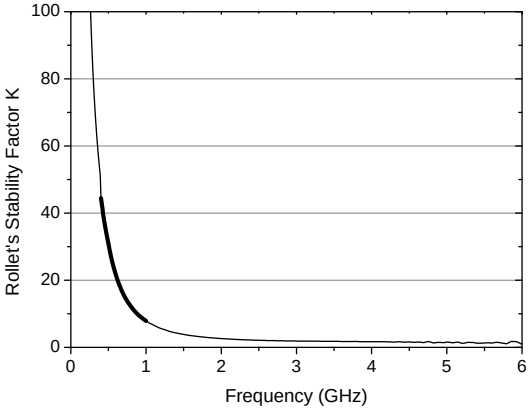

(d) Rollet's stability factor (K)

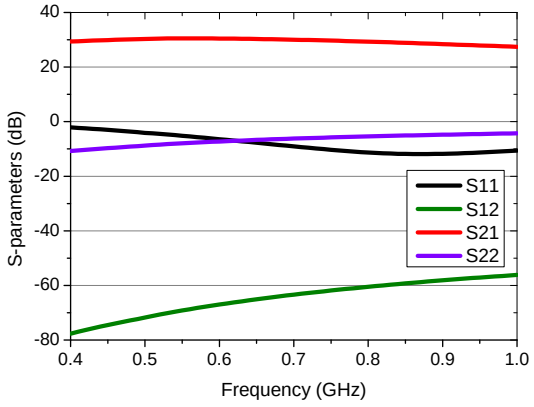

(e) S-parameters

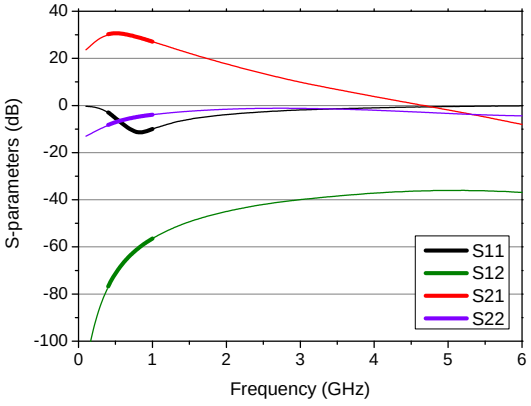

(f) S-parameters

Figure 10.3: Simulated results for the UHF-band LNA in the operating range and in an extended frequency range

Table 10.2: DC bias conditions of UHF-band LNA and power consumption

Stage	V_{DD} (V)	V_{GG} (V)	I_{ds} (mA)	Power Dissipation (mW)
1	3	0.45	3	9
2	2	0.80	29	58
Total				67

at 30.5 dB between 0.5 and 0.6 GHz and drops to a minimum 27.4 dB at 1 GHz, producing a 3 dB gain bandwidth of 600 MHz. The input return loss reaches -12 dB between 0.8 and 0.9 GHz, but is below -10 dB only from 0.72 GHz onwards. The output return loss increases from -11 dB to -4 dB from 0.4 GHz to 1 GHz, and hence is not satisfactory. The reverse gain is below -55 dB over the entire band. The performance of this LNA is comparable to other available LNAs in this band [118]. In Table 10.2, the supplied drain and gate voltages, the drain currents, and the power dissipation for the two stages of the LNA are listed.

10.4 On-wafer MMIC measurements

This section presents results of on-wafer measurements on previously designed MMIC LNAs. The justification of performing these measurements has been highlighted in section 10.1. Table 10.3 lists the LNAs, their operating frequency bands, the number of stages and the extended frequency bands over which they have been measured to evaluate their out-of-band performance. These multi-stage LNAs have been designed to operate at particular DC bias levels for the different stages. It has been observed, however, that their performance can be improved by sweeping the different stages with a range of bias settings, observing the performance and selecting the optimum bias points.

The C-band MMIC LNA shown in Figure 10.4. The $I_{ds} - V_{ds}$ curves of the 3 stages of the C-band LNA are displayed in Figure 10.5. To generate these curves, V_{ds} has been varied from 0 V to 1.3 V and V_{gs} from -0.5 V to 0.1 V for each stage. The currents in the 3 stages are in similar ranges, presumably because the different stage transistors are of similar sizes. The currents do not appear to reach saturation in any of the stages. Based on these DC curves, an extensive sweep of

Table 10.3: List of measured MMIC LNAs

MMIC LNA	Operating band	Number of stages	Measured frequency range (GHz)
CLNA_01A	C	3	2 – 10
22LNA_85A	K	3	5 – 25
30LNA-B	Ka	4	20 – 40
31LNA-02A	Ka	4	20 – 40

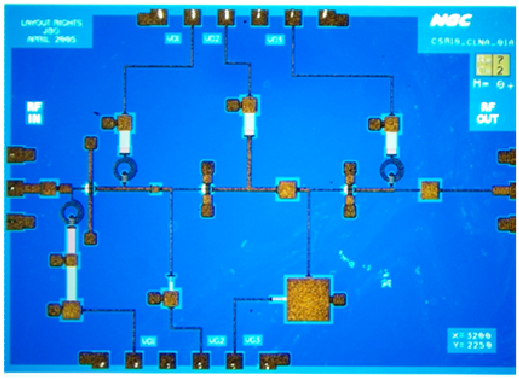

Figure 10.4: Measured C-band LNA CLNA_01A [119]

V_{ds} and V_{gs} has been performed to generate the S-parameters. Results of these measurements are shown in Figure 10.6. V_{ds} has been varied from 1 V to 1.6 V in steps of 0.1 V, and V_{gs} from 0 V to 0.16 V in steps of 0.02 V. S-parameters are thereby generated for the 63 combinations.

Figure 10.6 depicts that the forward gain S_{21} continues to increase even outside the band of interest at all bias points. This implies a probability of interference or oscillations. Within the band, a positive slope of 8 dB over 4 GHz is noticed in the gain curve. As expected, the S_{21} is proportional to the applied V_{ds}. The gain at 6 GHz, for example, varies between 13 dB to 26 dB.

The input match S_{11} is higher than -5 dB over most of the frequency range, and remains unaffected by bias variations. This is attributed to the fact that the matching circuitry of this MMIC had been designed by incorporating the effect of the bondwire required to connect the MMIC to the off-chip RF path. Simulations have confirmed that placing an inductor (representing the electrical behaviour of a bondwire) before that MMIC improves the input match of this LNA.

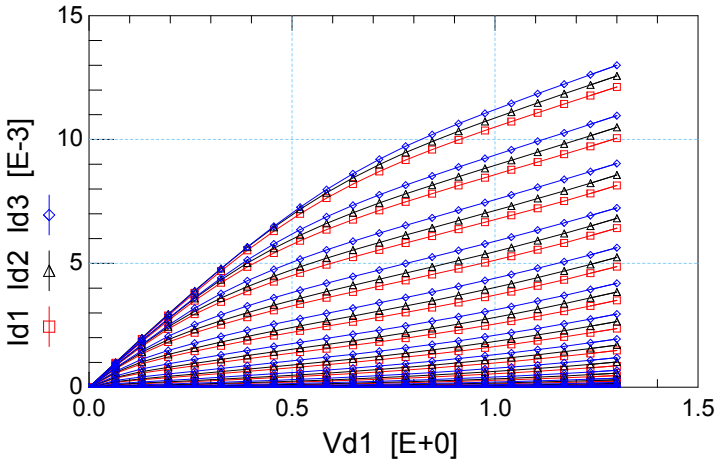

Figure 10.5: Measured $I_{ds} - V_{ds}$ curves of the three stages of the CLNA_01A LNA

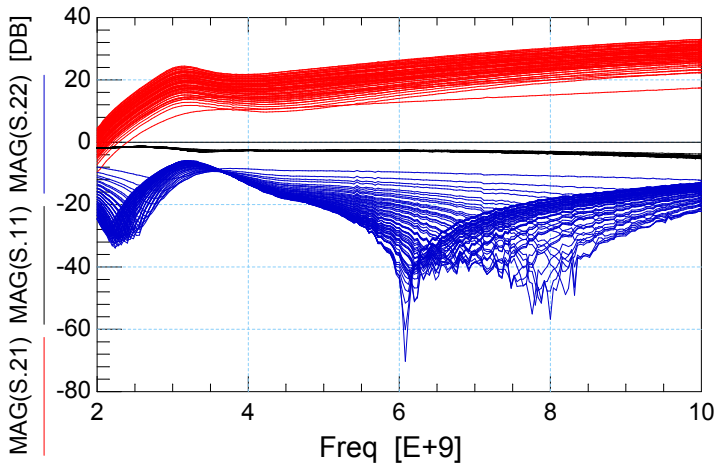

Figure 10.6: Measured S-parameters plots over a range of bias sweeps for the CLNA_01A LNA

The output match S_{22} is better than -10 dB over most of the measured frequency range at the bias level specified in [119]. The variations observed in S_{22} with changing bias conditions is significant. Tuning the bias settings helps optimise the best output match significantly between 6 – 8 GHz. Characterisation of the remaining MMIC LNAs in this manner provides a very good idea of how their performances vary with the bias settings applied to the various stages.

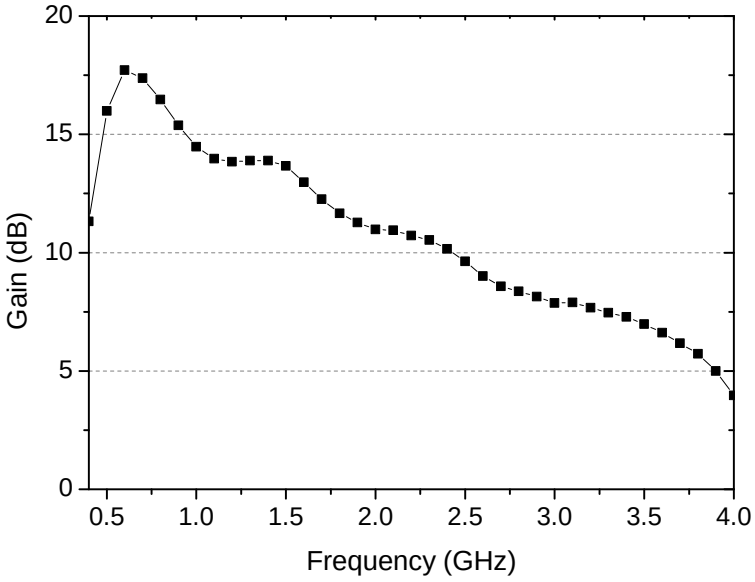

(a) G_{50}

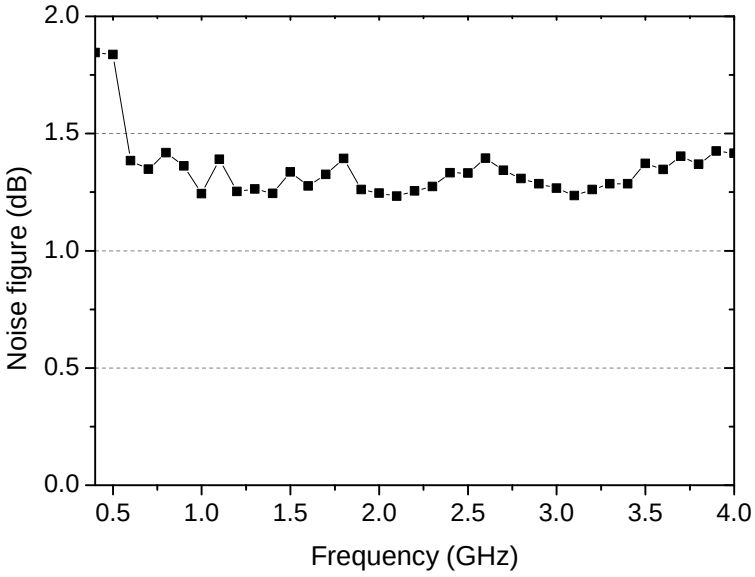

(b) NF_{50}

Figure 10.7: Measured on-wafer gain and noise performance of ASTRON MMIC LNA

Besides the DC and S-parameter measurements, noise measurements have been performed on on-wafer MMIC LNAs as well, using principles outlined in section 8.2.2. Figure 10.7 shows the results of the noise and gain measurements of an MMIC LNA designed in ASTRON, using the HP8970 NFM. The gain shows a huge fluctuation between 25 dB and 12 dB, but the noise figure remains between 1.3 dB and 1.45 dB for most of the band.

10.5 Summary

This chapter presents the results of the C and UHF band LNA designs produced by the author. Simulated results of NF_{50}, S-parameters, and stability factors have been presented, along with comparisons with the design specifications outlined in chapter 6. Most of the specifications for the C-band design has been met, and in some instances exceeded. For the UHF-band design, some of the more crucial requirements (in terms of achieving low noise and gain) have been met. The noise and gain bandwidths that have been achieved for both designs are superior to existing designs in these bands.

Measured results of previously designed MMIC LNAs have also been presented. These LNAs have been measured to obtain familiarity with MMIC measurements techniques, observing the changes in performance with different bias settings, and investigating the application of genetic algorithm to optimise LNA design (as part of a different project). This work would serve as a background for future MMIC measurements on the fabricated C-band and UHF-band LNAs.

Chapter 11

Results and analysis - reverse noise in phased array systems

11.1 Introduction

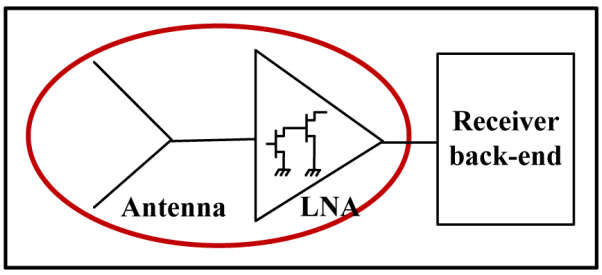

Figure 11.1: Focus of the chapter - results of noise analysis in phased arrays

The theory to estimate the reverse noise from an LNA has been outlined in chapter 4. Using the measurement principles described in section 8.3, 2 readily available COTS packaged amplifiers have been measured to validate the theory. This chapter presents the results. Since the main purpose of this work is to estimate levels of noise emanating from a single receiver chain in a phased-array environment such as the SKA, an ideal test amplifier would be one specifically designed for the SKA application. LNAs to be used in the SKA, however, have very low noise temperatures, typically of the order of 35 K in the L-band. In the present context, this is the contribution of the forward noise wave. The noise sources in an LNA which contribute to both the forward and the reverse waves would, in reality, have a certain amount of correlation between them. It can

therefore be assumed that for the SKA LNAs, the reverse noise temperatures would also be very low. Measurement of such low noise powers in a laboratory environment was not feasible in the present laboratory set-up. Hence, COTS packaged amplifiers with higher noise temperatures have been used here. Section 11.2 presents the results and application of this theory to the SKA environment is discussed in section 11.3.

11.2 Results of packaged LNA measurements

Tuner measurements and S-parameter measurements of 2 packaged amplifiers ZX60-2522M [120] and ZX60-3018G [121] from Mini Circuits have been performed, at DC biases of 5 V and 12 V, respectively.

Figures 11.2 to 11.6 display the measured S-parameters and the noise parameters. These have been used to calculate the values of the effective temperature of the reverse noise wave $C1$ theoretically. Although the amplifiers operate over a larger frequency range, all measurements have been restricted to the 1 - 2 GHz range. The reason is that the isolator used in the reverse noise measurement set-up only operates over 1 - 2 GHz. For better comparison purposes, data points have been taken at 100 MHz intervals. For the reverse measurements, the amplifiers have been connected reversely, and the effective temperatures at the inputs have been measured. Suitable pre-amplifiers have been used when necessary. The components $C1'$, $E1'$, $E2'$ and 'Total' as defined in section 8.3 have been calculated. The results of the measurements and calculations are tabulated in Table 11.1 and Table 11.2, respectively.

A comparison of the calculated ('Total') and measured values of the effective temperature of the reverse noise wave from Tables 11.1 and 11.2 shows that they are in good agreement for both the ZX60-2522M and ZX60-3018G amplifiers. This proves the validity of the theoretical approach.

Figures 11.7 and 11.8 show plots of these effective reverse noise wave temperatures. It is observed that, for both the amplifiers, these temperatures are significantly less compared to the noise temperatures of the amplifiers, displayed in Figure 11.9. Also, the component E1′ and E2′ are negligible in comparison to C1′.

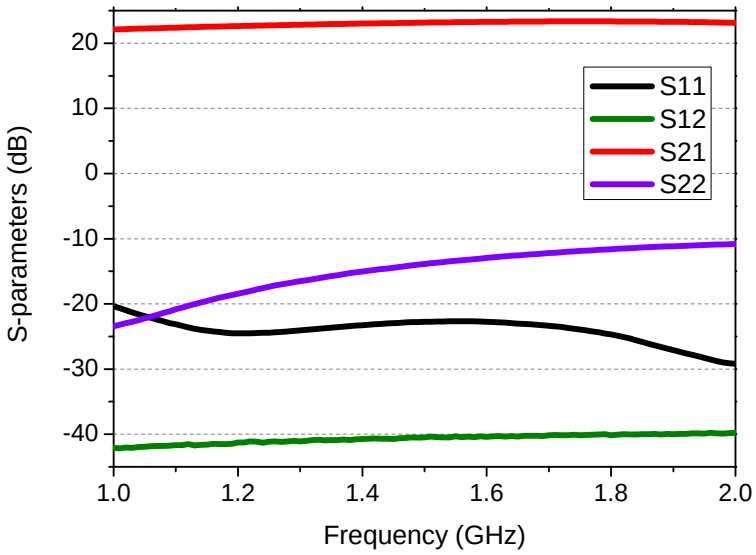

Figure 11.2: Measured S-parameters of ZX60-2522M amplifier

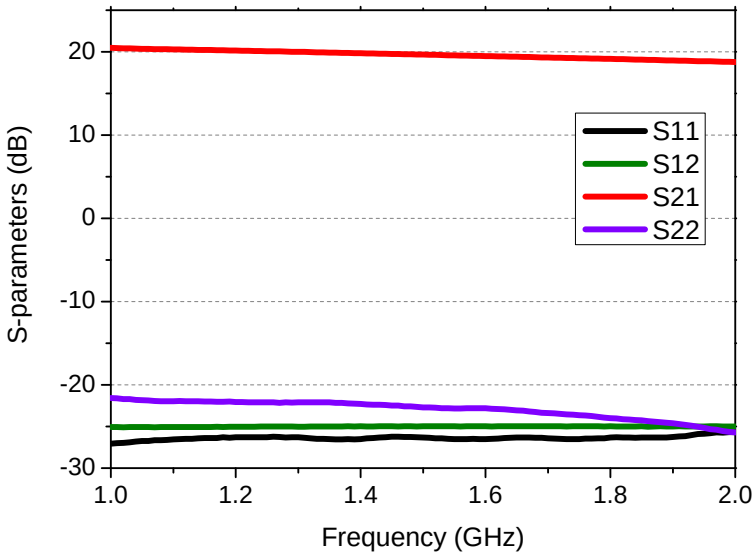

Figure 11.3: Measured S-parameters of ZX60-3018G amplifier

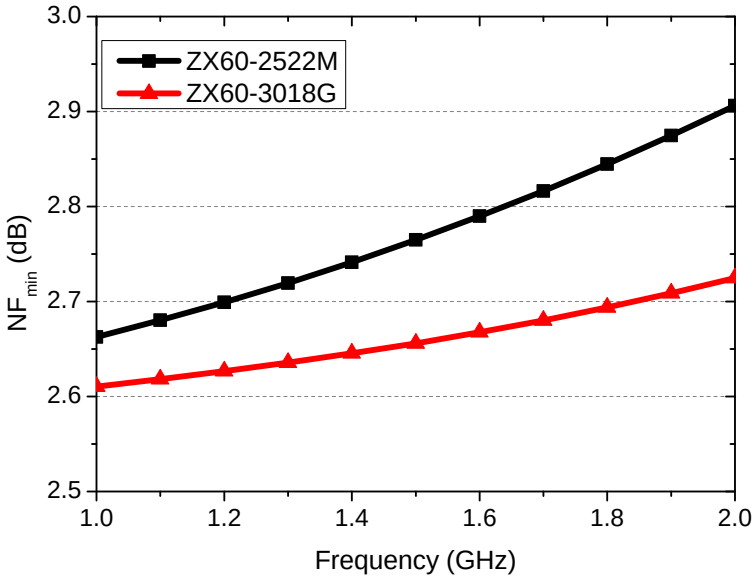

Figure 11.4: Measured NF_{min} of ZX60-2522M and ZX60-3018G amplifiers

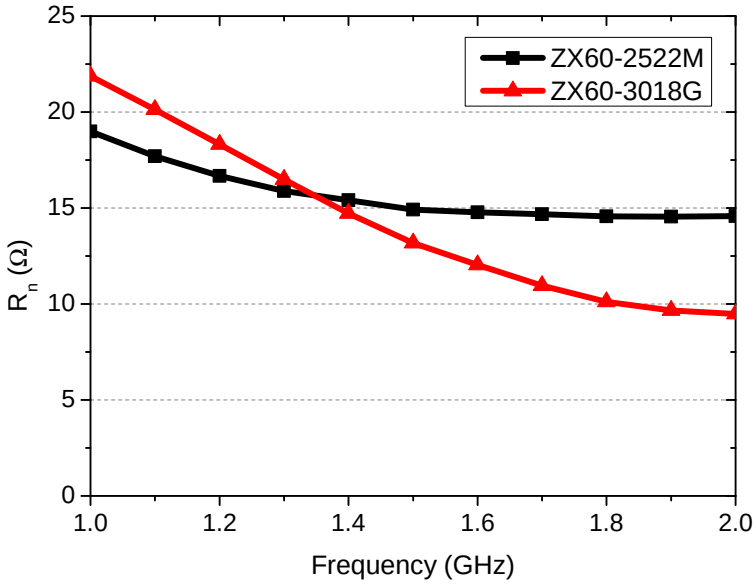

Figure 11.5: Measured R_n of ZX60-2522M and ZX60-3018G amplifiers

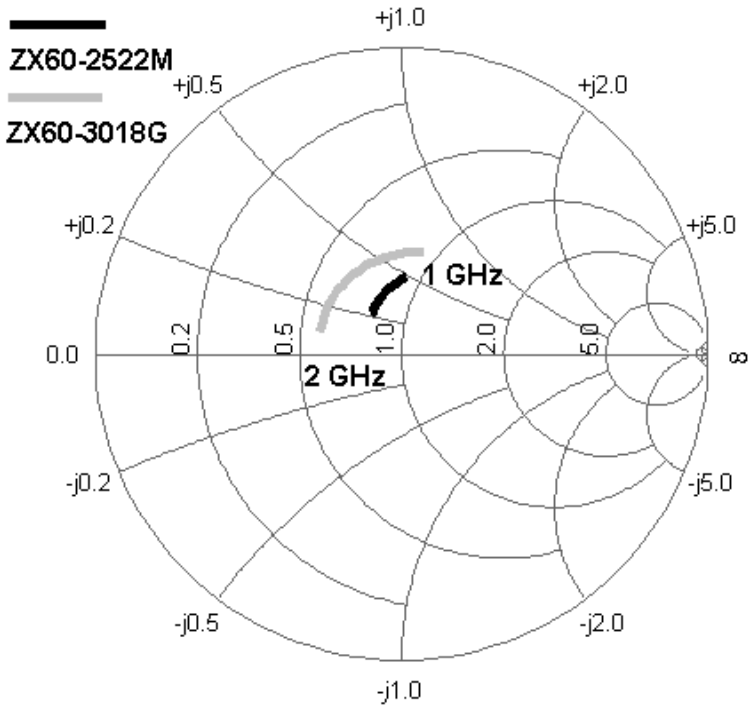

Figure 11.6: Measured Γ_{opt} for ZX60-2522M and ZX60-3018G amplifiers

Table 11.1: Calculated and Measured Effective Temperatures of the Reverse Noise Wave for ZX60-2522M

Freq (GHz)	Calculated (K)				Measured (K)
	$C1'$	$E1'$	$E2'$	Total	
1.0	156.0	2.74	0.02	157.3	143.7
1.1	147.7	1.45	0.02	148.5	138.8
1.2	140.9	1.06	0.02	141.5	133.5
1.3	136.0	1.17	0.02	136.6	131.3
1.4	135.5	1.41	0.03	136.3	130.1
1.5	131.6	1.59	0.03	132.5	128.9
1.6	134.2	1.59	0.03	135.1	129.8
1.7	135.3	1.38	0.03	136.1	131.0
1.8	134.7	1.02	0.03	135.3	133.8
1.9	134.8	0.58	0.03	135.1	135.6
2.0	136.3	0.36	0.03	136.5	140.7

Table 11.2: Calculated and Measured Effective Temperatures of the Reverse Noise Wave for ZX60-3018G

Freq (GHz)	Calculated (K)				Measured (K)
	$C1'$	$E1'$	$E2'$	Total	
1.0	168.7	0.59	0.94	169.9	170.4
1.1	175.7	0.66	0.93	176.9	173.1
1.2	179.3	0.70	0.94	180.5	172.7
1.3	179.4	0.70	0.94	180.6	171.2
1.4	176.1	0.67	0.95	177.3	168.4
1.5	170.5	0.70	0.95	171.8	168.4
1.6	163.3	0.67	0.95	164.5	166.9
1.7	156.9	0.68	0.95	158.1	165.7
1.8	153.8	0.70	0.95	155.1	163.8
1.9	157.6	0.71	0.95	158.9	165.0
2.0	171.6	0.81	0.95	172.9	167.3

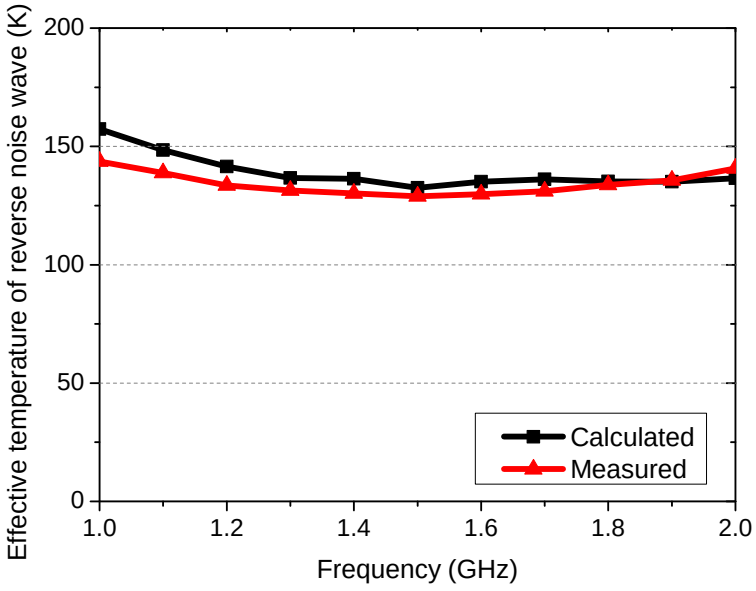

Figure 11.7: Comparison of calculated and measured effective temperatures of the reverse noise waves for the ZX60-2522M amplifier

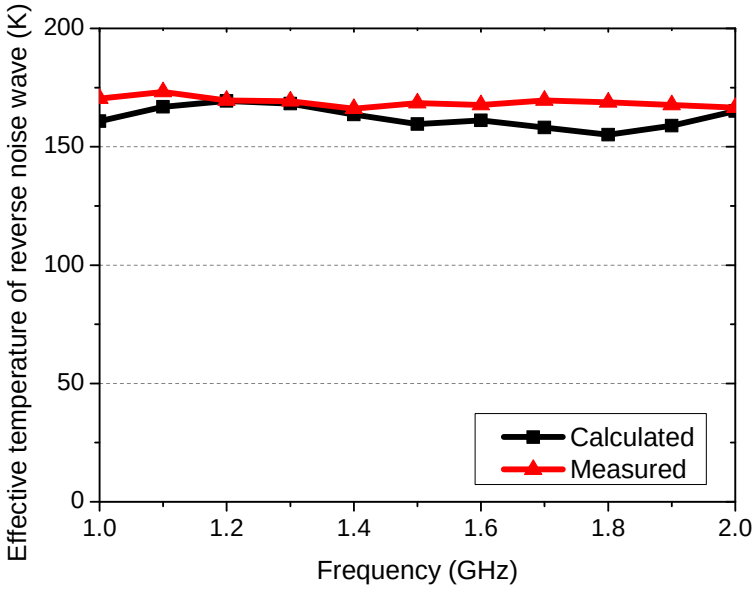

Figure 11.8: Comparison of calculated and measured effective temperatures of the reverse noise waves for the ZX60-3018G amplifier

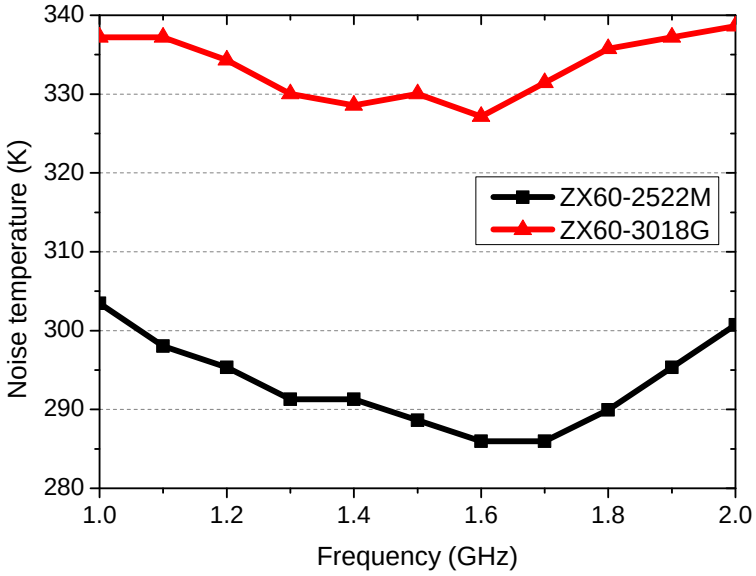

Figure 11.9: Measured noise temperatures of ZX60-2522M and ZX60-3018G amplifiers

11.3 Application of the theory to SKA

An excellent agreement has been observed in subsection 11.2 between the predicted and measured effective temperatures of the noise waves emanating from the input of 2 commercially available amplifiers. Based on this premise, it can be concluded that the theoretical approach is valid, and can be utilised to determine the level of noise emanating from the input of any noisy 2-port, if the 4 noise parameters and the input reflection coefficient are known. This approach can hence find significant application in the SKA project which would have thousands of individual receiver chains to comprise a phased array system.

As mentioned in section 4.2, the coupled noise between antenna elements has been one aspect of the system noise for these phased arrays that has received much attention [66]. This is the noise emanating from the input of an LNA in one receiver chain which couples into an adjacent antenna and passes through their associated LNAs into the beam-former. The present theory can be used to calculate the noise emanating from the input of the LNA and the levels of the coupled noise. The following information is needed: a) the noise parameters and the input reflection coefficient of the LNA in a single receiver chain, and b) the coupling between 2 adjacent elements. To elucidate this, a step-by-step approach has been taken, outlined below:

Step 1: First, an LNA designed specifically for the SKA application, with available noise parameter data, has been considered.

Step 2: Next, the temperature $C1$ associated with the reverse noise wave c_1 has been calculated for this LNA.

Step 3: Finally, a previously-used antenna S-parameter dataset has been used to determine the maximum amount of noise that will be coupled into an adjacent antenna in an example 2 element array system.

Subsection 11.3.1 describes steps 1 and 2, and subsection 11.3.2 discusses the final step. It is important to note that for the SKA phased array applications the main concern is to determine 'estimates' of the maximum noise that can be coupled between the antennas in the array. Any assumption or generalisation that has been made is based on this criterion.

Table 11.3: Measured Noise Parameters of ASTRON LNA obtained from [122]

Frequency (GHz)	NF_{min} (dB)	R_n (Ω)	Γ_{opt} Mag.	Γ_{opt} Phase(°)	S_{11} (dB)
1.0	0.52	3	0.0978	-7.3361	-11
1.2	0.52	3	0.1230	62.4014	-12
1.4	0.5	2.5	0.1372	122.7336	-8
1.6	0.52	3	0.18636	158.6415	-8

11.3.1 Calculation of noise emanating from a single chain towards the antenna

The study done by Bhaumik and George [118, 122] summarises the reported measured data from different LNA teams involved in SKA. It reports the noise parameters and input reflection coefficient of an L-band LNA designed by the SKA team at ASTRON, over a frequency range of 1 – 1.6 GHz. This particular LNA has been chosen here due to the following reasons:

1. The design of this LNA has been based on Avago Technologys GaAs pHEMT device, ATF54143, and these pHEMT devices (ATF54143, ATF35143) from Avago have been popular choices for LNA designs in the SKA frequency range in the recent years [118].

2. A noise temperature value of 35 K has been achieved by this LNA over the frequency range of 1 - 1.6 GHz in the least. The study in [118] also shows that noise temperature levels of 35 - 40 K at room temperature have been achieved by more than 1 team in the SKA frequency range.

This particular LNA designed by ASTRON is therefore a very good representative of the typical LNAs being designed by different teams across the world for the SKA application. It can hence serve as a good representative example for the present purpose.

The measured noise parameters and the input reflection coefficient for this LNA, as reported in [122], are tabulated in Table 11.3 over 1 – 1.6 GHz. The approximate values of the input reflection coefficient have been obtained from a plot presented in [122]. Using equation 11.1, the noise power associated with the reverse noise waves emanating from the input ports of this LNA can be

Table 11.4: Calculated Noise Wave for the ASTRON LNA and the corresponding Coupled Noise

Frequency (GHz)	Temperature of the reverse noise (K)	Coupled noise temperature (K)
1.0	32.9	4.2
1.2	32.9	4.2
1.4	23.5	2.9
1.6	10.4	1.3

calculated. Division of the value of $\overline{|c_1|^2}$ by the Boltzmanns constant k would provide the associated noise temperature $C1$ in an 1 Hz bandwidth.

$$\overline{|c_1|^2} = kT_{min}\left(|S_{11}|^2 - 1\right) + \frac{4kT_0R_n}{Z_0} \times \frac{|1 - S_{11}\Gamma_{opt}|^2}{|1 + \Gamma_{opt}|^2} \tag{11.1}$$

From equation 11.1, it is seen that all information needed to calculate the power associated with the reverse noise is available except the phase of S_{11}. Since the magnitudes of both S_{11} (assuming a value of -10 dB from Table 11.3) and Γ_{opt} are in the range of 0.1, the component $S_{11}\Gamma_{opt}$ is in the order of 0.01. For simplicity, $S_{11}\Gamma_{opt}$ can be approximated by $|S_{11}|\,\Gamma_{opt}$.

Column 2 in Table 11.4 summarizes the effective temperature values of the reverse noise wave for the L-band LNA, and the black curve in Figure 11.10 shows the plot of this temperature with respect to frequency. It can be observed that levels of reverse noise are below 33 K. It is certain that in the final stage, LNAs in the SKA will have similar or improved noise and S-parameters. This indicates that the levels of noise will be similar to the present estimation, or lower.

An important point to note is that, in these calculations, it has been assumed that the LNAs are unilateral. This assumption should be quite valid for amplifiers which will actually be used in the SKA. In circumstances where a very accurate estimate of the reverse noise is required, or the reverse gain cannot be neglected, the process outlined in [72] can be used. This of course adds to the complexity of the measurements, which can be particularly difficult when ultra LNAs are used, such as in SKA.

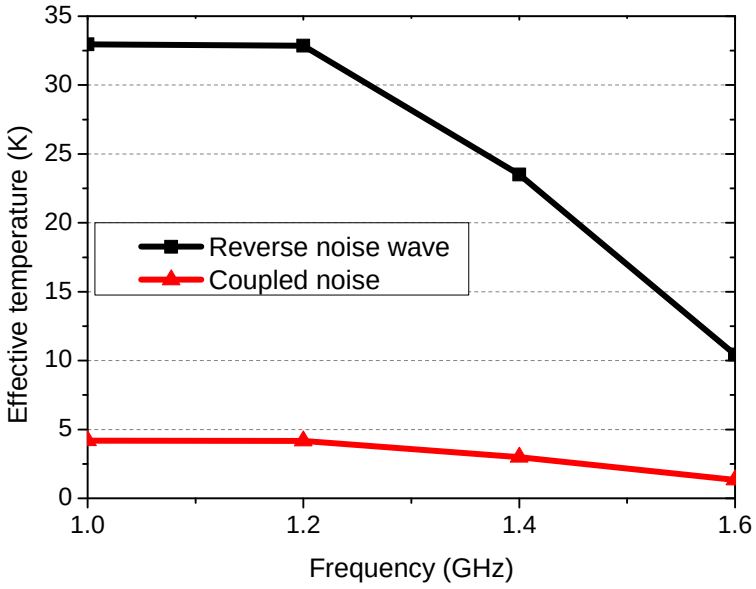

Figure 11.10: Effective temperatures of the reverse noise wave and the coupled noise

11.3.2 Estimation of coupled noise to an adjacent receiver chain

For a phased array system, if the coupling between adjacent antennas is known, the portion of the reverse noise from a single chain which gets coupled back into the receiver system through an adjacent antenna can also be determined, provided the coupling coefficients are known. Figure 11.11 illustrates this concept for a simple 2-element array, which has also been used previously in [66]. Noise waves $C1_{(LNA1)}$ and $C2_{(LNA1)}$ correspond to LNA1 in a receiver chain, and noise wave $C1_{(LNA2)}$ and $C2_{(LNA2)}$ correspond to LNA2 in an adjacent receiver channel. If the S-parameters of the coupled antenna system $[S]_{ant}$ are known, the part of $C1_{(LNA1)}$ coupled to receiver 2, denoted here by $C12_{(LNA1)}$, can be determined. To illustrate this with the example LNA discussed earlier, it is considered that both receiver chains use the same LNA, implying $C1_{(LNA1)} = C1_{(LNA2)}$. The same S-parameters (normalized to 50 Ω) for the antenna system as specified in [66] are used. These are as follows:

$$[S]_{ant} = \begin{bmatrix} 0.166 - 0.123i & 0.272 + 0.219i \\ 0.272 + 0.219i & 0.166 - 0.123i \end{bmatrix} \tag{11.2}$$

From this set of S-parameters, the calculated value of coupling between adjacent

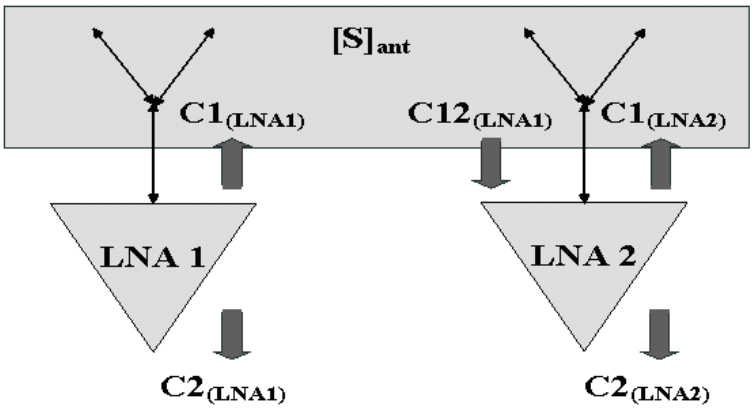

Figure 11.11: A 2-element array to illustrate the noise coupling

channels is 12.7 %. This can be used to calculate the maximum values of the coupled noise from one receiver channel to the adjacent channel $C12_{(LNA1)}$ can be calculated. Column 3 in Table 11.4 summarizes these results, and the red curve in Figure 11.10 shows the plot of this coupled noise temperature. It is observed that the maximum coupled noise $C12_{(LNA1)}$ is very small and in the order of a few Kelvin for LNAs of the type to be used in the SKA.

Important to note in this context is that to be of practical use in SKA, the antennas need good radiation efficiencies. From the principle of reciprocity, most of the noise coming out from the input port of the LNA in a receiver chain towards the antenna should therefore be radiated into space, rather than be coupled to adjacent antennas.

This analysis suggests that for the ultra LNAs that will be used for the SKA, the amount of noise coupled between antennas will be relatively small, generally a few K at most. There is another important observation that surfaces from the present work. It has been observed that the effective temperature of the reverse noise wave depends heavily on the value of the noise resistance R_n. This is evident from closer analysis of equation 11.1, in which the second component is directly proportional to R_n. The noise parameter of the utmost importance in LNA design specifications is generally the minimum noise figure NF_{min}, and is frequently the only parameter specified by designers. The importance of the noise resistance R_n as a significant determinant of performance is highlighted through this analysis. Lower R_n values are crucial in achieving broadband designs, as discussed in section 3.2.1. This study points out that it is also very beneficial in a phased array system where noise coupling effects can be significant and

hence need to be considered. The SKA project requirements encompass both these criteria; broadband LNAs are required, and the noise coupling between the phased array antennas needs to be considered as well. Hence, the importance of low noise resistance values for the SKA LNA designs cannot be overemphasized.

In this analysis, a simple 2-element antenna array model has been considered. The noise analysis could be extended to an n-element antenna array model. Determining estimates of the noise coupling between the n antenna elements would require knowledge of (a) the S-parameters and noise parameters of the LNAs in individual receiver chains (b) the complete n-port S-parameter dataset of the n-element model. In the case where the LNAs in different chains are identical, and the antenna S-parameters are identical for each combination of 2 antennas (A_i, A_j), the solution set of noise coupling values is reduced from ${}^nP_2$ to ${}^nC_2$, where P and C are the permutation and combination operators, respectively. Important to note in this context, however, is the fact that the total amount of deliverable noise power to a matched termination $\left(\overline{|c_1|^2}/k\right)$ at the LNA input port is determined only by the noise and S-parameters of the LNAs in individual receiver chains.

11.4 Summary

This chapter summarises the results of the measurements on 2 COTS packaged amplifiers to validate the theory outlined in chapter 4. Measurements show excellent agreement with estimated values of the effective temperatures of the reverse noise waves. Using this theory, a noise wave analysis has been performed to estimate the levels of noise that may be coupled between antenna elements in the SKA phased array receivers, with reported measured values of an LNA designed for SKA. This analysis indicates that the coupled noise contribution to system noise temperature should be quite small, especially since the LNAs which will be finally used in the SKA applications will have either similar or improved noise parameters than those presently analysed. The importance of the noise resistance parameter has also been established, and this aspect cannot be overemphasized for SKA LNA designs.

The importance of this work is that although the analysis has been limited to an example SKA LNA, the theoretical principle can be applied to a broader range

of phased array systems. It provides a simple and effective tool to effectively determine if the coupled noise is potentially detrimental to the overall performance of the system significantly. As such, it can be utilised by both LNA designers and phased array system designers to estimate the noise coupling effects, from the perspective of the noise contribution of the LNA. An exhaustive analysis of the effect of this coupling on the beam former in a phased-array system would provide better insights into the effect of the correlation components of the forward and reverse noise powers. This analysis also establishes the potential application of the wave representation of noise in linear 2-ports, which is a powerful technique of noise analysis.

Chapter 12

Results and analysis - multi-band MPA design

12.1 Introduction

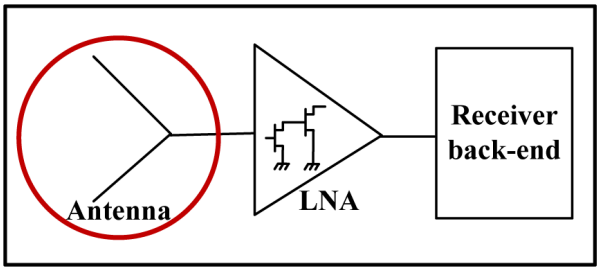

Figure 12.1: Focus of the chapter - results of multi-band MPA design

In chapter 7, a step-by-step approach to designing a multi-band MPA structure suitable for operation in 3 frequency bands of interest, the 2.1 GHz UMTS, the 2.4 GHz ISM and the 5.8 GHz ISM bands, have been thoroughly discussed. This structure consists of a single strip of patch antennas placed side-by-side. This chapter presents the results of the simulation and measurement of the patch antenna structures.

The limited availability of space in the present design prohibits use of COTS single-band rectangular MPAs. Despite this, 3 COTS single band and multi-band antennas have been measured. This serves to determine their performance, acquire an understanding of antenna measurements and primarily to determine

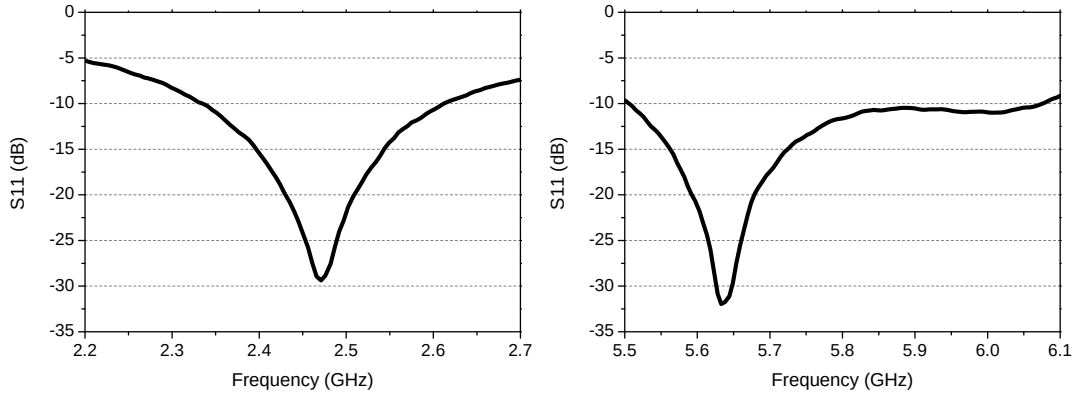

(a) 2.4 GHz antenna from Panorama - W24-CP-9

(b) 5.8 GHz antenna from Stella Doradus (product ID - 584040)

Figure 12.2: Measured input reflection coefficient of COTS single-band MPAs

an acceptable benchmark for the performance of the present designs. The results of these measurements are detailed in section 12.2.

The results of simulations to account for the effects of the mimic metal frame to emulate the surface of a vessel and a large metallic surface in close proximity to the antenna structure (representing an access platform) are detailed in a step-by-step approach in section 12.3. Measurements performed in the laboratory environment are discussed in section 12.4. Section 12.5 presents the analysis of the suitability of the COTS 4-way broad-band splitter and a MS-line based power divider to implement the feeding network.

12.2 Measurement of COTS antennas

This section presents plots of the return loss and radiation patterns of the 3 COTS MPAs. The single-band MPAs measured are the W24-CP-9 2.4 GHz antenna from Panorama [123] and a 5.8 GHz planar antenna from Stella Doradus [124]. Their dimensions are 93 mm $\times$ 93 mm and 120 mm $\times$ 110 mm, respectively, and hence cannot be contained within the design space.

Figures 12.2 (a) and (b) show the plots of the input reflection coefficient S_{11} for the 2 antennas, from which the return losses can be determined. Table 12.1 lists the various parameters - measured resonant frequency f_r, % deviation from the ideal f_r, the return loss (denoted as RL), the 10 dB return loss bandwidth (denoted as 10 dB RL BW), also expressed in % values.

Table 12.1: Performance of COTS single-band MPAs

Antenna	f_r (GHz)	% deviation from ideal F_R	RL (dB)	10 dB RL BW (MHz)
2.4 GHz ISM	2.471	0.86	29	276 (11.2 %)
5.8 GHz ISM	5.633	2.88	32	564 (10.0 %)

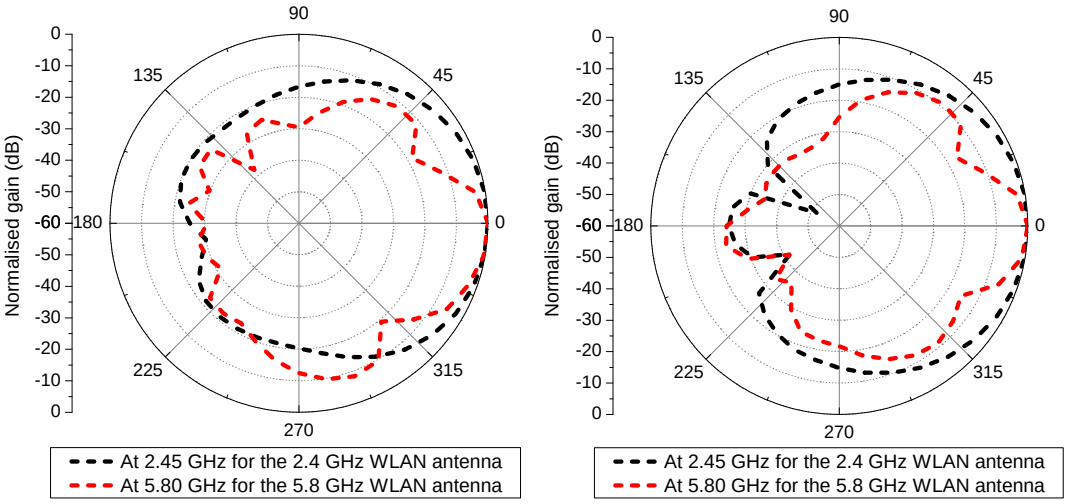

(a) In the azimuth plane

(b) In the elevation plane

Figure 12.3: Measured radiation patterns of the COTS single-band MPAs

The radiation patterns measurements have been performed in the azimuth and the elevation planes. Patterns typical of standard single-band rectangular MPAs designed with no space constraints are observed. Figures 12.3 (a) and (b) show the azimuth and elevation plane patterns. Table 12.2 summarises the various performance parameters obtained from the radiation plots – the direction of maximum directivity in the 2 planes (the direction of the main lobe), the $HPBW$, and the side-lobe levels where applicable.

A COTS multi-band MPA from Panorama, EFC3G-3F, has been measured as well. It operates over the 0.8 GHz, 0.9 GHz, 1.8 GHz and 1.9 GHz GSM bands and 3G frequency bands [125]. The dimensions of this MPA, 130 mm × 17 mm, indicate a possibility that this can be contained within the design space with some adjustments. However, this particular antenna does not operate at all the frequency bands of interest.

Figure 12.4 shows the measured S_{11} of the EFC3G-3F multi-band MPA. The

Table 12.2: Measured radiation parameters of the COTS single-band antennas

Plane	Azimuth		Elevation	
Frequency (GHz)	2.45	5.80	2.45	5.80
Main lobe direction (°)	0	0	0	0
$HPBW$ (°)	64	31	65	15
Side-lobe level (dB)	-20	-8.5	-25	-23

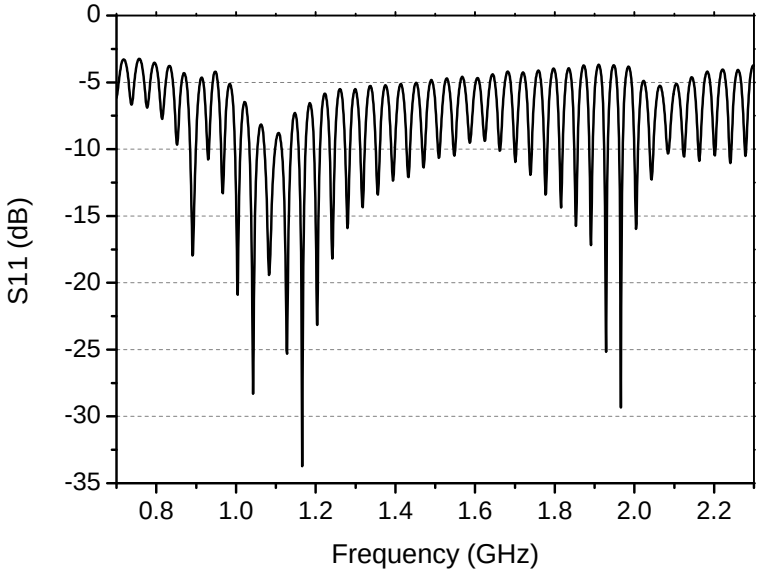

Figure 12.4: Measured S_{11} of EFC3G-3F, the COTS multi-band MPA from Panorama

performance is unsatisfactory - the resonant frequencies are hardly distinguishable. One potential reason may be the standing wave in the feed cable that connects to the antenna. Since this cable is part of the COTS MPA structure, its effects cannot be calibrated out.

In summary, it can be concluded that none of the measured COTS MPAs, representatives of the typically available COTS MPAs, satisfy the current design criterion. The single-band MPAs, despite having standard performance, cannot be contained within the provided design space. The multi-band MPA which can be contained in the design space has an inferior performance. A search for COTS MPAs that operate at the 3 frequency bands of interest and are of suitable dimensions has yielded no results. These comprise the reasons for eliminating these types of COTS MPAs as potential solutions to the present design problem.

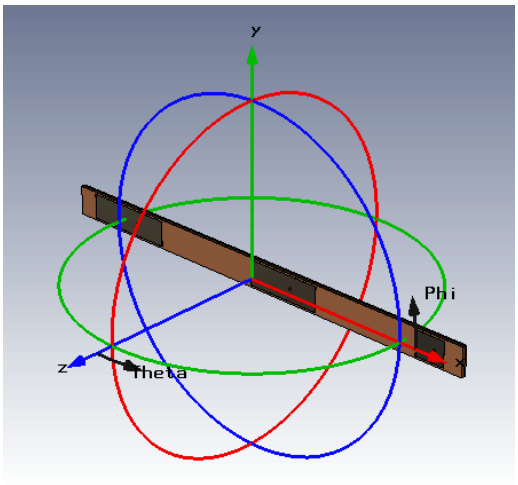

Figure 12.5: The simulated structure of the stand-alone antenna strip also showing the co-ordinate system

12.3 Simulation results

The simulation results of 3 progressively complicated simulations are presented in this section - stand-alone antenna strips, antenna strips with the extended ground plane the metal frame in effect provides, antenna strips in close proximity to a large metallic surface. These are referred to as case 1, 2 and 3, respectively. In each case, figures showing the simulated structure have been included in the discussion to provide references for the radiation patterns. For case 3, the computational capability of the simulation software restricts the dimensions of the metal structure.

12.3.1 Stand-alone antenna strip

The stand-alone antenna strip is displayed in Figure 12.5, and the simulated S-parameters of 3-port antenna system are depicted in Figure 12.6, over 1.9 – 6.5 GHz. Ports 1, 2 and 3 have been used to stimulate the 2.1 GHz UMTS (extreme left), the 2.4 GHz ISM (centre) and the 5.8 GHz ISM (extreme right) antennas, respectively. Table 12.3 lists the various parameters.

Figure 12.6 shows that the antennas resonate at the ideal resonant frequencies with return loss $>$ 10 dB, and the bandwidth improves with increasing frequency. Table 12.3 lists the results. The reduction in antenna widths affect the lower frequency bands (with comparatively higher wavelengths) more than the higher

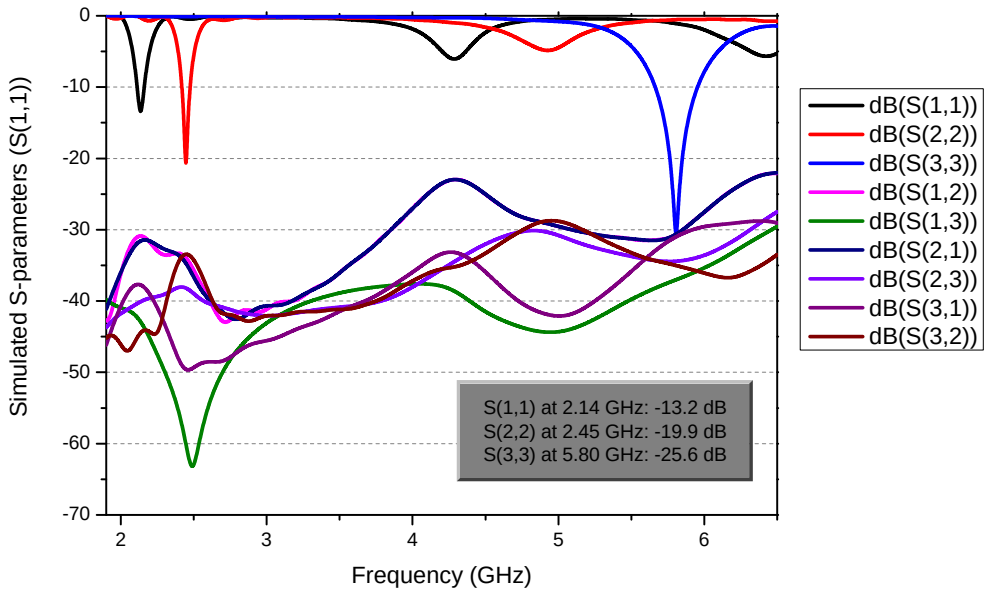

Figure 12.6: Simulated S-parameter plots showing the input reflection coefficients and the coupling levels between the patches

frequency band, leading to a better overall performance in the 5.8 GHz ISM band. However, the small patch length at 5.8 GHz makes it difficult to obtain the ideal f_r. It is expected that this problem will manifests itself during fabrication as well.

The troughs in the S_{11} curve at 4.3 GHz and 6.4 GHz, and in the S_{22} curve at 4.9 GHz, respectively, are expected. Being resonating structures, MPAs also radiate at frequencies which are multiples of the resonant frequencies. The radiation patterns at these frequencies are however different, because the patch length at these frequencies is not half-wavelength but multiples. These resonant troughs in the response can be eliminated by incorporating suitable filtering circuitry within the receiver.

The coupling between the 3 patches, both indicated by S_{12}, S_{13}, S_{21}, S_{23}, S_{31} and S_{32} in Figure 12.6 and tabulated in Table 12.3 are very low across a wide band of frequency.

Figure 12.5 provided the direction of the axes, as well as those of the azimuth angle θ, and the angle ϕ, respectively. 3D plots of the simulated radiation patterns of the 3 antennas at the respective resonant frequencies are presented in Figures 12.7 (a)-(c). These plots indicate the values and directions of the maximum directivities, the radiation efficiencies and the total efficiencies.

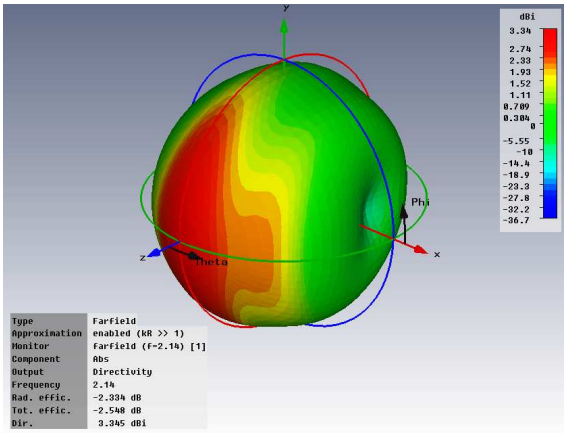

(a) At 2.14 GHz

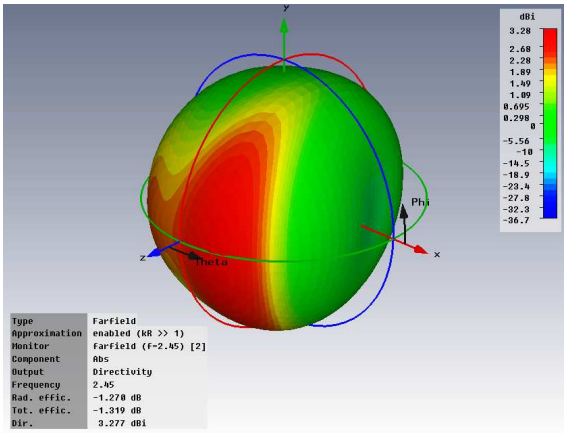

(b) At 2.45 GHz

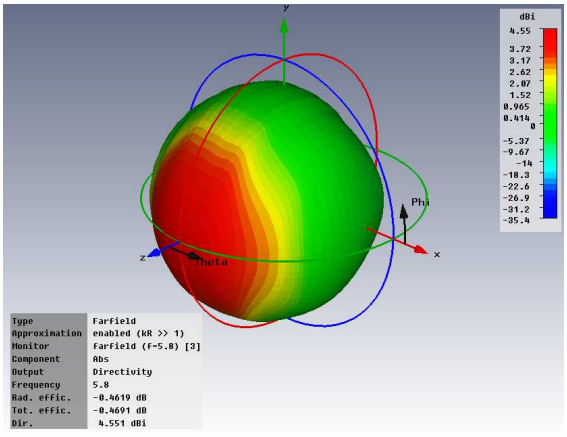

(c) At 5.80 GHz

Figure 12.7: 3D plots of simulated radiation patterns of the stand-alone antenna strip

Table 12.3: Simulated performance parameters of the 3 stand-alone antennas

Antenna	f_r (GHz)	RL (dB)	10 dB RL BW (MHz)	Max. coupling in bands (dB)	Max. coupling 1.5 – 6.5 GHz (dB)
2.1 UMTS	2.14	13	49 (2.3 %)	<-30	<-23
2.4 ISM	2.45	20	58 (2.4 %)		
5.8 ISM	5.8	30	291 (5.0 %)		

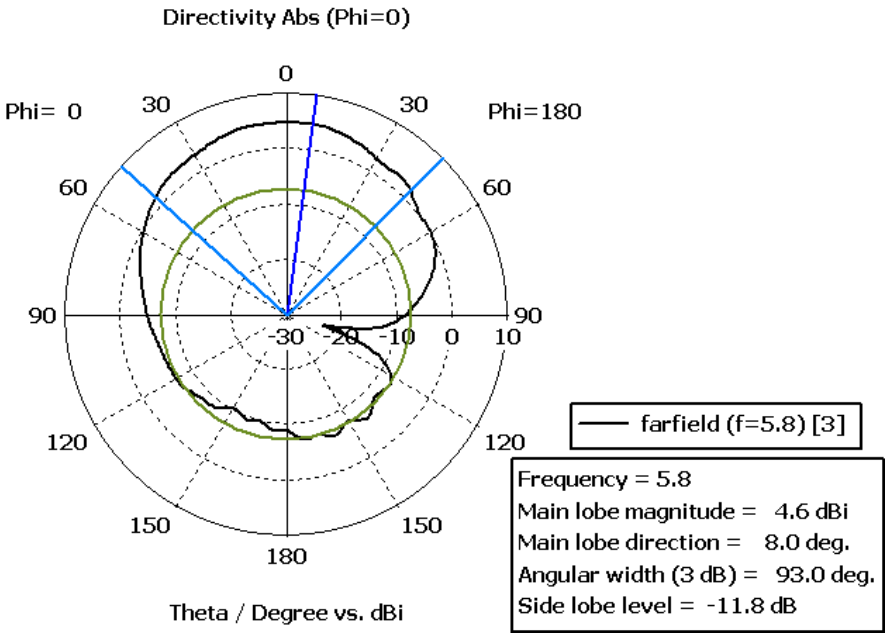

Figure 12.8: Polar plot of simulated azimuth radiation pattern at 5.8 GHz

The change in the main lobe with the angular direction can also be noted. It is observed that the radiation properties of the 5.8 GHz antenna is superior to the others; the beam pattern, directivity and the efficiency are improved, due to the reasons discussed earlier.

Polar plots showing the variations in the relative gains in the azimuth plane (y-plane in Figure 12.5) are included in Appendix C. One plot has been shown here in Figure 12.8, for the 5.8 GHz antenna. The radiation parameters indicated by the plots are tabulated in Table 12.4.

Table 12.4: Simulated radiation parameters of the stand-alone antenna strip

Plane	Azimuth		
Frequency (GHz)	2.14	2.45	5.80
Relative gain (dBi)	3.3	3.3	4.6
Main lobe direction (°)	1.0	18.0	8.0
HPBW (°)	92.3	95.3	93.0
Side-lobe level (dB)	-2.8	-3.1	-11.8

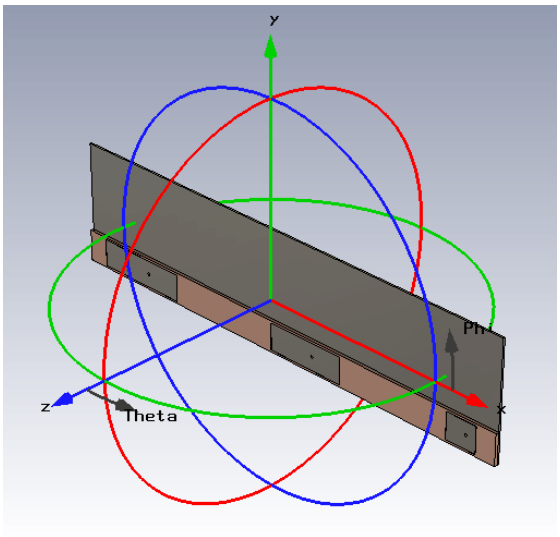

Figure 12.9: The simulated structure of the antenna strip with an extended ground plane

12.3.2 Antenna strip with an extended ground plane provided by the metal frame

The simulated structure of the antenna strip attached to the metal frame is shown in Figure 12.9. The extension of the ground plane alters the resonant frequencies slightly, but the designs can be modified to counteract this.

Plots of S-parameters similar to the previous case have been simulated. The parameters are tabulated in Table 12.7. Similar to case 1, the performance of the 5.8 GHz ISM antenna is significantly superior to the lower frequency antennas.

Figures 12.10 (a)-(c) present the 3D plots of the simulated radiation patterns of the complete structure at the resonant frequencies, and Table 12.6 lists the important parameters. The radiation pattern is superior at 5.8 GHz both in

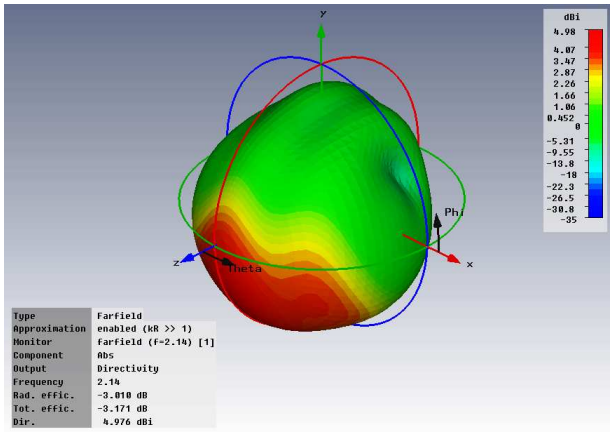

(a) At 2.14 GHz

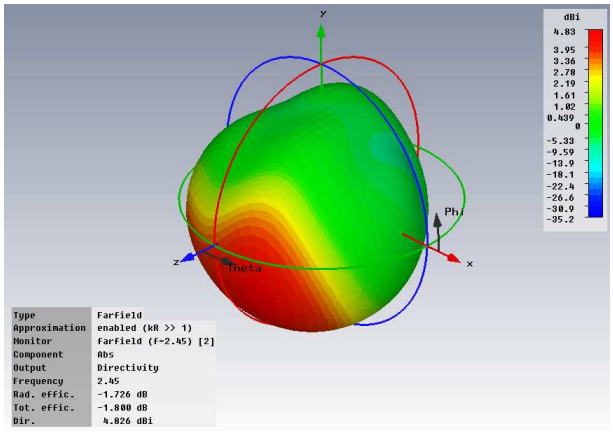

(b) At 2.45 GHz

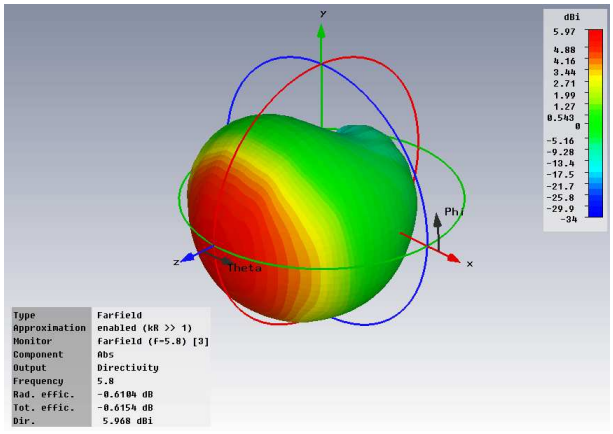

(c) At 5.80 GHz

Figure 12.10: 3D plots of simulated radiation patterns of the antenna strip with an extended ground plane

Table 12.5: Simulated performance parameters of the antenna strip with an extended ground plane

Antenna	f_r (GHz)	RL (dB)	10 dB RL BW (MHz)	Max. coupling in bands (dB)	Max. coupling 1.5 – 6.5 GHz (dB)
2.1 UMTS	2.14	14	39 (1.8 %)	<-35	<-25
2.4 ISM	2.45	18	43 (1.8 %)		
5.8 ISM	5.8	30	275 (4.7 %)		

Table 12.6: Simulated radiation parameters of the antenna strip with an extended ground plane

Plane	Azimuth		
Frequency (GHz)	2.14	2.45	5.80
Relative gain (dBi)	4.1	4.4	6.0
Main lobe direction (°)	3.0	19.0	0.0
$HPBW$ (°)	99.1	101.5	92.2
Side-lobe level (dB)	-8.2	-8.2	-14.4

terms of maximum directivity and efficiency. The direction of the main beam is also not altered significantly, unlike in the lower frequency bands. In these cases, the main beam directions are modified - they are oriented towards the lower hemisphere. The observed angular tilt is also more at 2.14 GHz than at 2.45 GHz. Polar plot of the radiation pattern are presented in Appendix C.

12.3.3 Antenna strip with a metal surface in close proximity

The simulated structure for this particular scenario is shown in Figure 12.11, in a different orientation to that depicted earlier in Figure 7.4. The orientation of the coordinate axes in Figure 12.11 is to provide a better visualisation of the 3D radiation patterns shown in Figures 12.12 (a)-(c). These results are valid when the metal surface is at the same potential as the antenna ground.

The results of the S-parameter simulations are provided in Table 12.7, and Figure 12.12 show the 3D plots of the simulated radiation patterns. The various simulated performance parameters are listed in Table 12.8. Polar plots of the

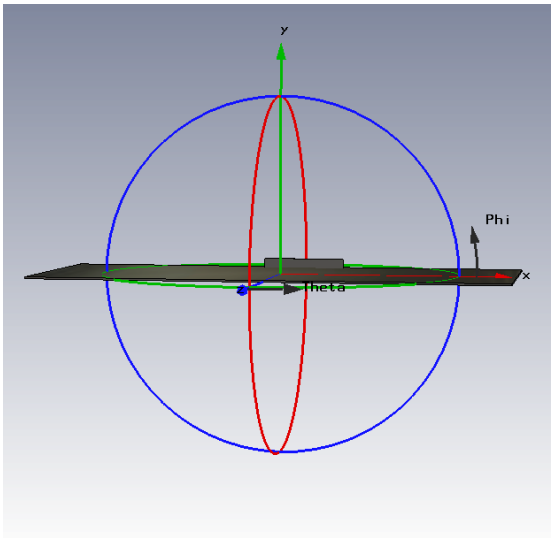

Figure 12.11: The simulated structure of the antenna strip in close proximity to a metal surface

Table 12.7: Simulated performance parameters of the 3 antennas

Antenna	f_r (GHz)	RL (dB)	10 dB RL BW (MHz)	Max. coupling in bands (dB)	Max. coupling 1.5 – 6.5 GHz (dB)
2.1 UMTS	2.14	17	35 (1.6 %)	<-30	<-24
2.4 ISM	2.45	12	28 (1.1 %)		
5.8 ISM	5.8	23	239 (4.1 %)		

Table 12.8: Simulated radiation parameters of the antenna strip in close proximity to a metal surface

Plane	Azimuth			Antenna		
Frequency (GHz)	2.14	2.45	5.80	2.14	2.45	5.80
Maximum directivity (dBi)	0.9	-0.5	-1.5	5.5	5.8	2.5
Main lobe direction (°)	70.0	70.0	120.0	305.0	290.0	195.0
$HPBW$ (°)	92.6	86.7	63.5	105.9	125.0	34.8
Side-lobe level (dB)	-4.2	-2.0	-2.9	-16.5	-13.1	-2.1

radiation patterns are presented in Appendix C.

The 3D plots indicate that the maximum directivities and 3 dB beamwidths ($HPBW$) increase at each f_r, the large metal surface orients the main lobes at a

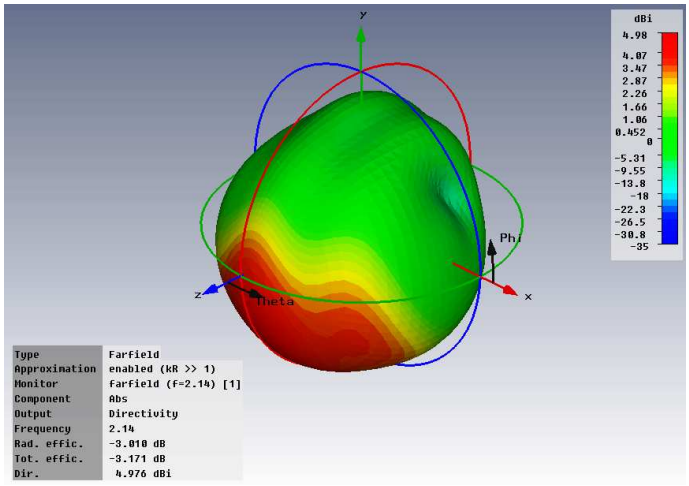

(a) At 2.14 GHz

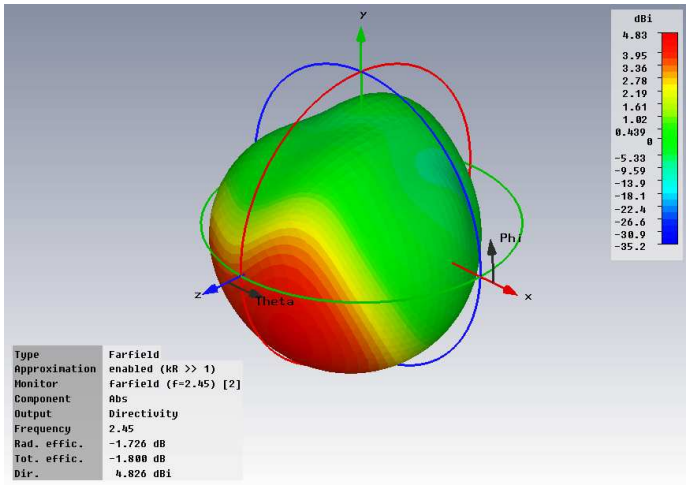

(b) At 2.45 GHz

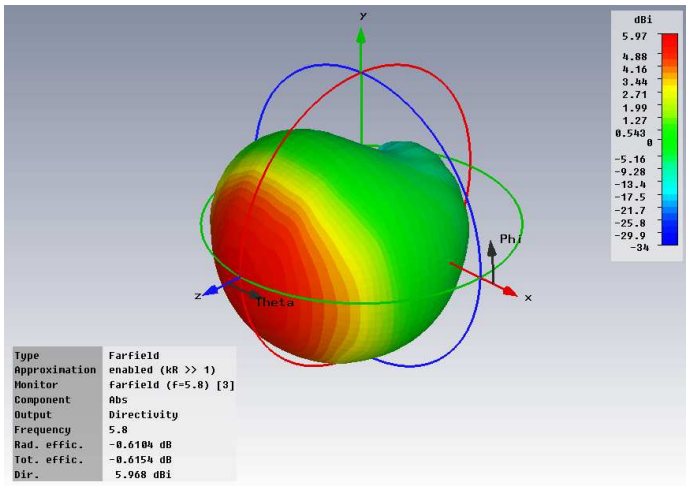

(c) At 5.80 GHz

Figure 12.12: 3D plots of simulated radiation patterns of the antenna with a metal surface in close proximity

greater angle to the y-plane than in case 2. Side lobes become more prominent. This is not undesirable in the present scenario since it also results in a better spread of the radiated power in the azimuth plane. This indicates that the presence of a metallic surface lead to better performance in applications where a wide beamwidth is required in the azimuth plane.

12.4 Laboratory measurements

The observations made in the simulation phase indicate the suitability of the design approach. Four antenna strips have been fabricated in the PCB fabrication facility and mechanical workshop of the University of Manchester. This section presents the results of the laboratory measurement conducted on these structures, and a comparison with the results of the COTS antennas discussed in section 12.2.

12.4.1 Stand-alone antenna strips

The measurement results of the 4 fabricated antenna strips are presented here. However, initial measurements were conducted on the separate single-band patches, and a brief discussion follows.

Figure 12.13 depicts the measured radiation patterns of the fabricated single-band 5.8 GHz ISM antenna, and Table 12.9 lists the radiation parameters. Comparisons with the COTS antenna results (in section 12.2) show that the $HPBW$ values are enhanced in the azimuth and elevation planes by 92° and 140°, respectively.

The measurements of the 4 fabricated antenna strips, each of which comprises of 3 patch antennas, are presented next. The repeatability provides an indication of the tolerances introduced by the fabrication process. Figure 12.14 shows the measured S_{11} of the 2.1 GHz UMTS antennas in the different strips, over 1.90 – 2.40 GHz, and Table 12.10 lists the calculated performance parameters. The maximum observed deviation in f_r is 0.65 %. The return losses remain between 17 and 19 dB, however the 10 dB return loss bandwidth value varies between 43 MHz to 79 MHz.

Table 12.10 also shows the measured results of all the antennas in the 4 strips. It can be observed that the maximum deviation in the f_r for the 2.45 GHz antenna is 0.94 %. The return loss value increases to 23 dB for 1 antenna, however this

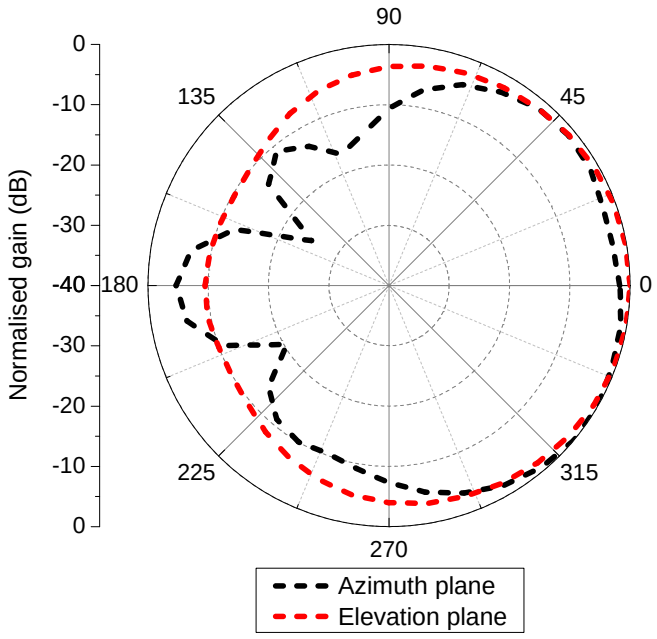

Figure 12.13: Polar plots of the measured radiation pattern of a fabricated 5.8 GHz ISM antenna

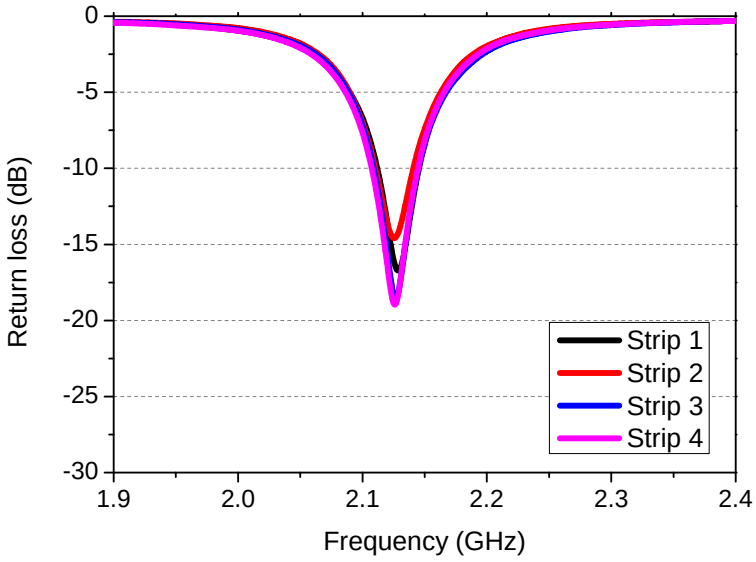

Figure 12.14: Measured input reflection coefficients of the 2.1 GHz UMTS antennas in the different strips

comes at the cost of reduced bandwidth – the 10 dB return loss bandwidth drops to 29 MHz from 105 MHz.

For the 5.8 GHz antenna, the deviations remain within 1 %, except for one

Table 12.9: Measured radiation parameters of the single-band 5.8 GHz antennas

Plane	Azimuth	Elevation
Main lobe direction (°)	330	0
$HPBW$ (°)	123	155
Side-lobe level (dB)	-5	–

Table 12.10: Measured performance parameters of the 3 antennas in the different strips

Antenna	Strip	f_r (GHz)	% deviation from ideal f_r	RL (dB)	10 dB RL BW (MHz)
2.1 UMTS	1	2.128	0.56	17	56 (2.6 %)
	2	2.126	0.65	15	79 (3.7 %)
	3	2.127	0.61	19	45 (2.1 %)
	4	2.126	0.65	19	43 (2.0 %)
2.4 ISM	1	2.438	0.49	23	29 (1.2 %)
	2	2.438	0.49	16	100 (4.1 %)
	3	2.441	0.37	18	60 (2.4 %)
	4	2.427	0.94	15	105 (4.3 %)
5.8 ISM	1	5.763	0.64	18	246 (4.2 %)
	2	5.756	0.76	17	293 (5.1 %)
	3	5.731	1.19	16	381 (6.6 %)
	4	5.757	0.74	18	262 (4.5 %)

antenna showing 1.19 % deviation. This is superior to the COTS antenna exhibiting a deviation of 2.88 % (in Table 12.1). The measured return losses are inferior compared to the simulated results, potentially due to fabrication uncertainties.

These observations validate the predictions from simulations. Obtaining the ideal f_r for the 5.8 GHz antenna is comparatively more difficult since the patch length is significantly reduced. This implies that the fabrication errors (involving cutting the patch length and inserting the feed at the precise location) manifest as larger errors in the 5.8 GHz band. The bandwidth is however improved since the reduction in width has less effect at higher frequencies, and the grounding obtained with the smaller dimensions is much better. Measurements of the coupling levels between the various patches in different strips indicate that they remain below -30 dB for the frequency bands of interest, as shown in Figure 12.15.

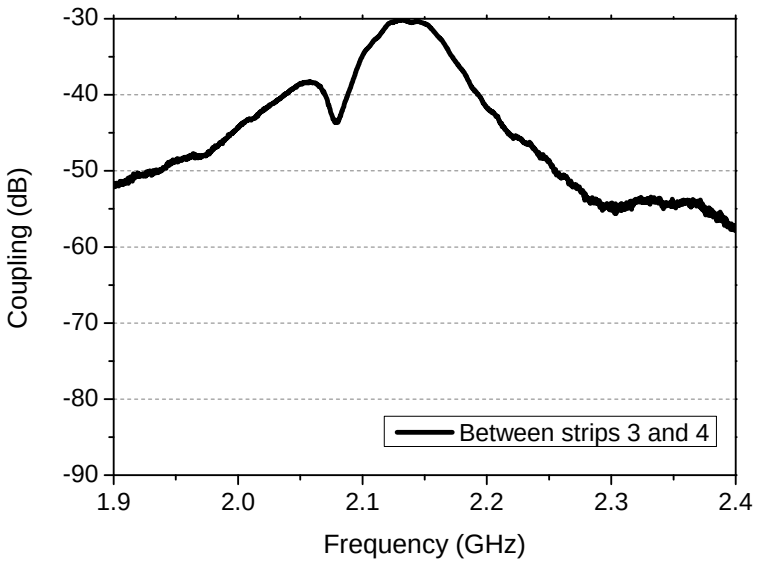

Figure 12.15: Measured coupling levels between the 2.1 GHz UMTS antennas

12.4.2 Antenna strip with an extended ground plane provided by the metal frame

In the next phase of measurements, 4 curved metal frames have been produced to mimic the vessel surface, and each antenna strip has been attached to a curved metal frame. Measurements similar to those on the stand-alone antennas have been repeated for these structures, and no significant deviations have been observed.

In addition, measurements have been performed to determine the coupling levels in the same frequency band if 2 antenna strips are positioned in close proximity to each other. For this purpose, two of the curved metal frames have been attached to each other along their outer edges. The antenna strips now face opposite directions. This leads to a free-space distance of approximately 4 cm between the 2.1 GHz antennas, and approximately 2 cm between the 2.4 GHz and 5.8 GHz antennas in the 2 strips. Under such measurement conditions, the coupling levels determined from 2–port measurements remain below -30 dB for all bands. Figure 12.15 shows the coupling for the 2.1 GHz antennas.

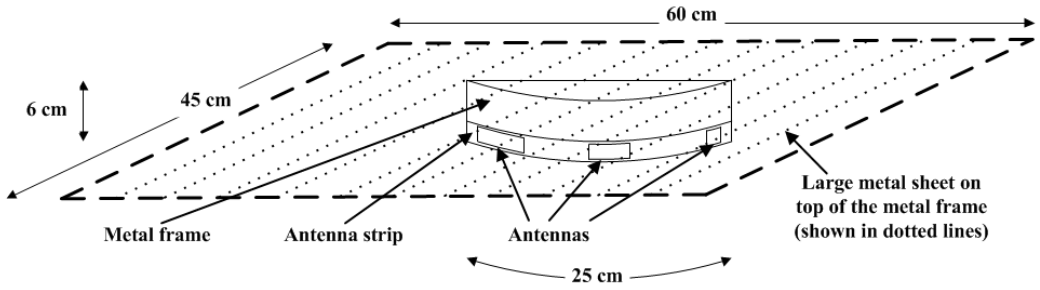

Figure 12.16: Diagram showing the placement of a large metal sheet on top of the metal frame to partially emulate the effect of the access platform

12.4.3 Antenna strip with a metal surface in close proximity

In the next phase of the measurements, a thick and sturdy structure covered with an aluminium foil has been designed to mimic a large metal sheet. This has been placed on top of the antenna strips to emulate the effect of the access platform overshadowing the antenna structures. Figure 12.16 shows this arrangement. The antenna strip containing the 3 antennas is attached to the metal frame of dimensions 25 cm $\times$ 6 cm, towards the bottom half of the structure. An extension of the frame on the backside provides mechanical support to the metal sheet on top. The dimensions of the metal sheet are specified in Figure 12.16. The extension of the metal frame towards the forward direction, looking from the antennas, is minimum $2.5\lambda_0$ at the lowest resonant frequency of 2.14 GHz and reaches up to $6\lambda_0$ at the highest resonant frequency of 5.8 GHz, where λ_0 is the free-space wavelength. Connections with copper strips ensure that this structure is at the same potential as the antenna ground. The size of such a metal structure that can be measured in a laboratory environment, especially within an anechoic chamber, is restricted. However, this provides some indication of the potential effect of the access platform on the performance.

Measurements of S_{11} indicate no significant difference than in the previous 2 cases, implying that the resonance patterns of these antenna structures are relatively insensitive to the environment. It is observed that the achieved bandwidths of the antennas are sufficient that the slight deviations in the resonant frequencies ($< 1\%$) do not affect the usability of the antennas. It can also be predicted that the shapes of the metal structures around the antenna may not affect the

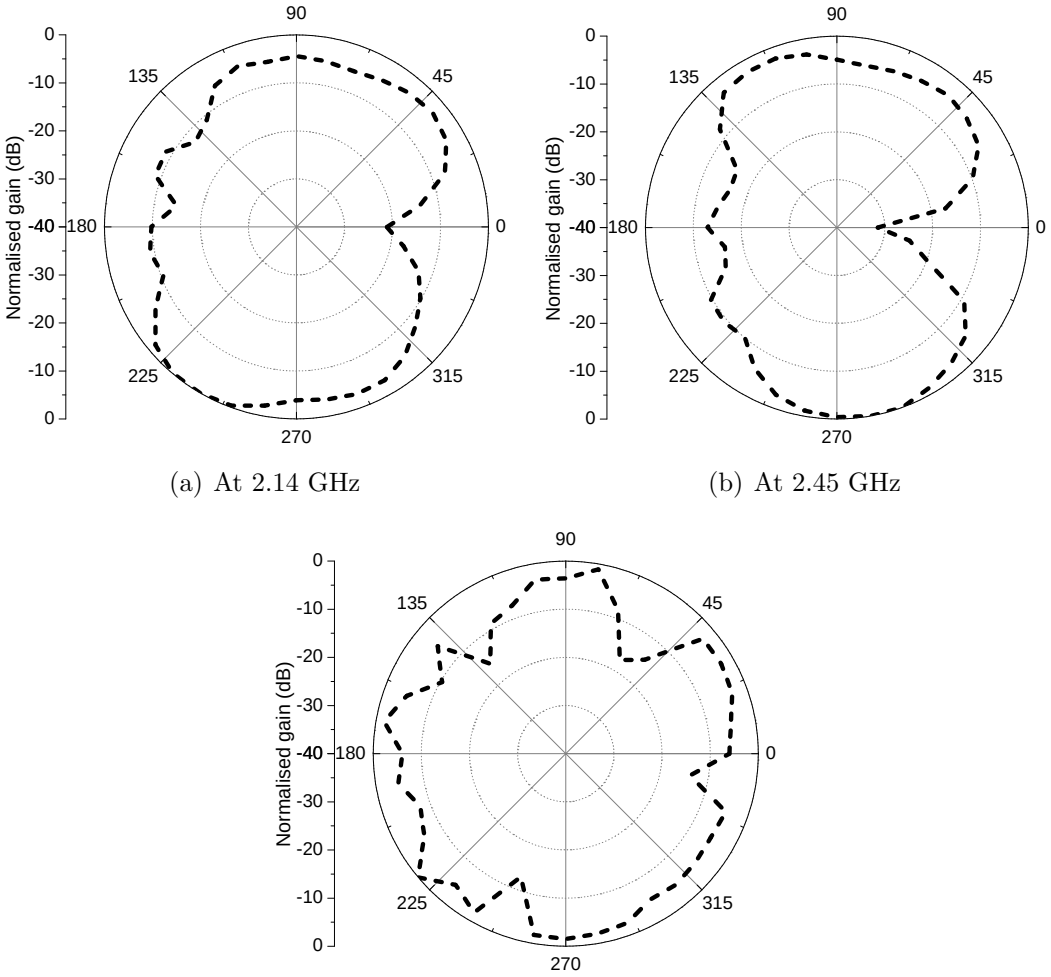

(a) At 2.14 GHz

(b) At 2.45 GHz

(c) At 5.80 GHz

Figure 12.17: Polar plots of measured radiation patterns in the azimuth plane for antenna strips in close proximity to a metal surface

resonance patterns. This needs further investigation.

Figures 12.17 (a)-(c) show the polar plots of the measured azimuth radiation patterns at the 3 resonant frequencies. Table 12.11 lists the radiation parameters. The $HPBW$ values do not provide an indication of the improved radiation patterns in this case. The reason is that there is an increase in the number and level of minor lobes, which leads to a wider azimuthal radiation pattern. This is especially valid for the 5.8 GHz antenna, for which an approximately omni-directional pattern is observed. The presence of a metallic sheet overshadowing the antennas

Table 12.11: Measured azimuth radiation parameters of the antenna strips overshadowed by a large metal surface

Antenna	2.1 GHz	2.4 GHz	5.8 GHz
Main lobe direction (°)	240	280-290	220
$HPBW$ (°)	80	60	10
Levels of minor lobes (dB)	-2.9, -2.9	-2.4, -3.8	-1.1, -1.5, -1.7, -2.7

therefore improves the azimuthal coverage. Hence, from the laboratory measurements, it can be concluded that the designed MPA structures should perform well in the real application environment within the process industry, even when overshadowed by large metallic access platforms.

12.5 Measurements of the feed networks

This subsection concentrates on the results of measurements performed on the proposed feeding networks for the separate patches - the COTS wideband power splitter and the designed MS splitter network.

COTS splitter

Two COTS wideband 4-way splitters have been procured from Minicircuits, ZN4PD1-63+ (2 – 6 GHz) [126] and ZN4PD1-63W+ (0.25 – 6 GHz) [127]. These are henceforth referred to as 'SC1' and 'SC2', respectively. Figures 12.18(a)–(d) and Figures 12.19 (a)–(d) display the results of 5-port S-parameter measurements for SC1 and SC2, respectively, over 2 – 6 GHz.

The insertion losses are higher than 6 dB (ideal value for a 4-way splitter) for both splitters. The return loss and the coupling plots show there is wide variation in these values for SC2 in comparison to SC1. Overall, the performance of SC1 is definitely better in comparison to SC2.

The effectiveness of using these splitters in the present design has been verified next. The 3 antennas in each strip have been connected to output ports of the splitter through RF cables, with a 50 Ω termination in the fourth output port. 1-port S-parameter measurements have then been performed on the splitter input port, over 1.5 GHz – 6.5 GHz. The results are shown in Figures 12.20 (a) and (b), for the 2 splitters, respectively.

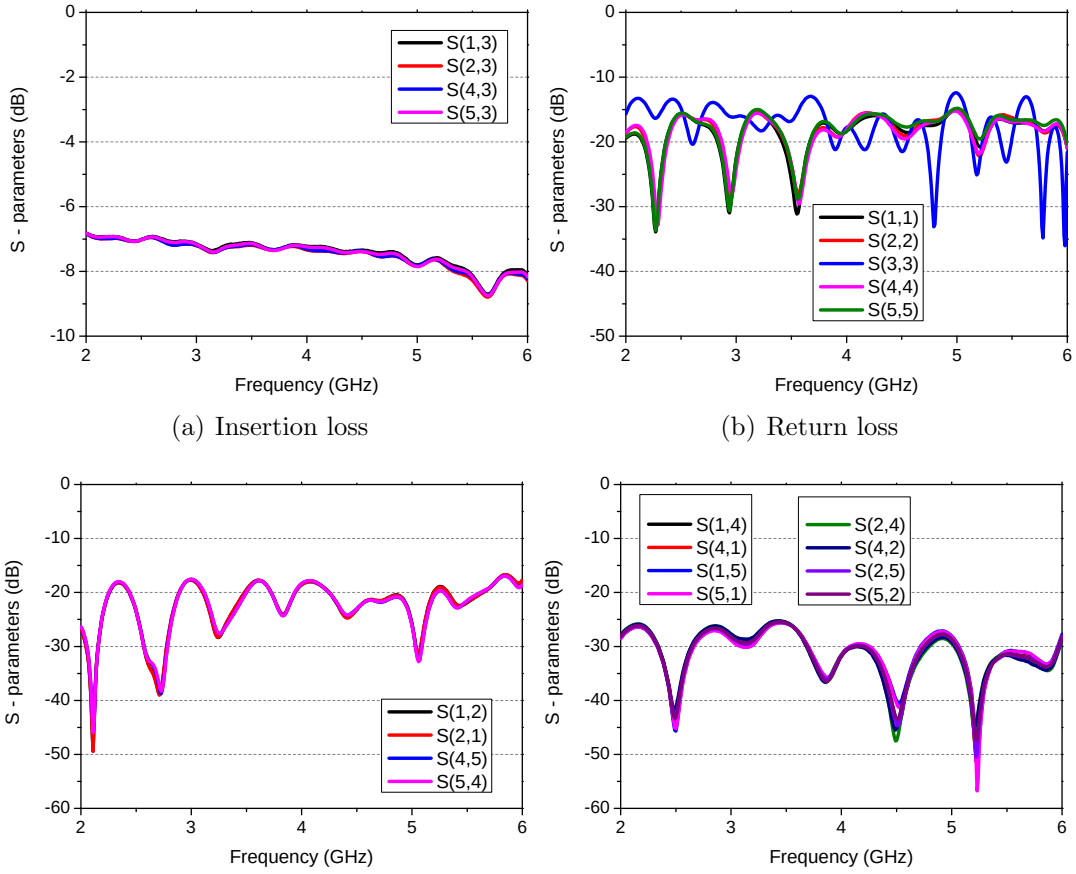

(a) Insertion loss

(b) Return loss

(c) Coupling between adjacent arms

(d) Coupling between non-adjacent arms

Figure 12.18: S-parameters of the ZN4PD1-63+ splitter

The return loss values obtained are not satisfactory, especially when the return loss values of the individual antennas are higher than 15 dB for all the antennas. The ripple pattern observed in Figure 12.20 (b) can be attributed to the fact that the reflection coefficient of SC2 (which is relatively poor) is going in and out of phase with the reflection coefficients of the antennas.

Microstrip splitter

The results of measurements with the fabricated MS power splitter network are discussed next. The plot of S_{11} in Figure 12.21 depicts that the performance in this case is unsatisfactory as well. The ripple and spikes are due to reflection coefficients of the splitter and antennas being in and out of phase. Furthermore, use of the MS splitter network involves potential fabrication and assembly errors,

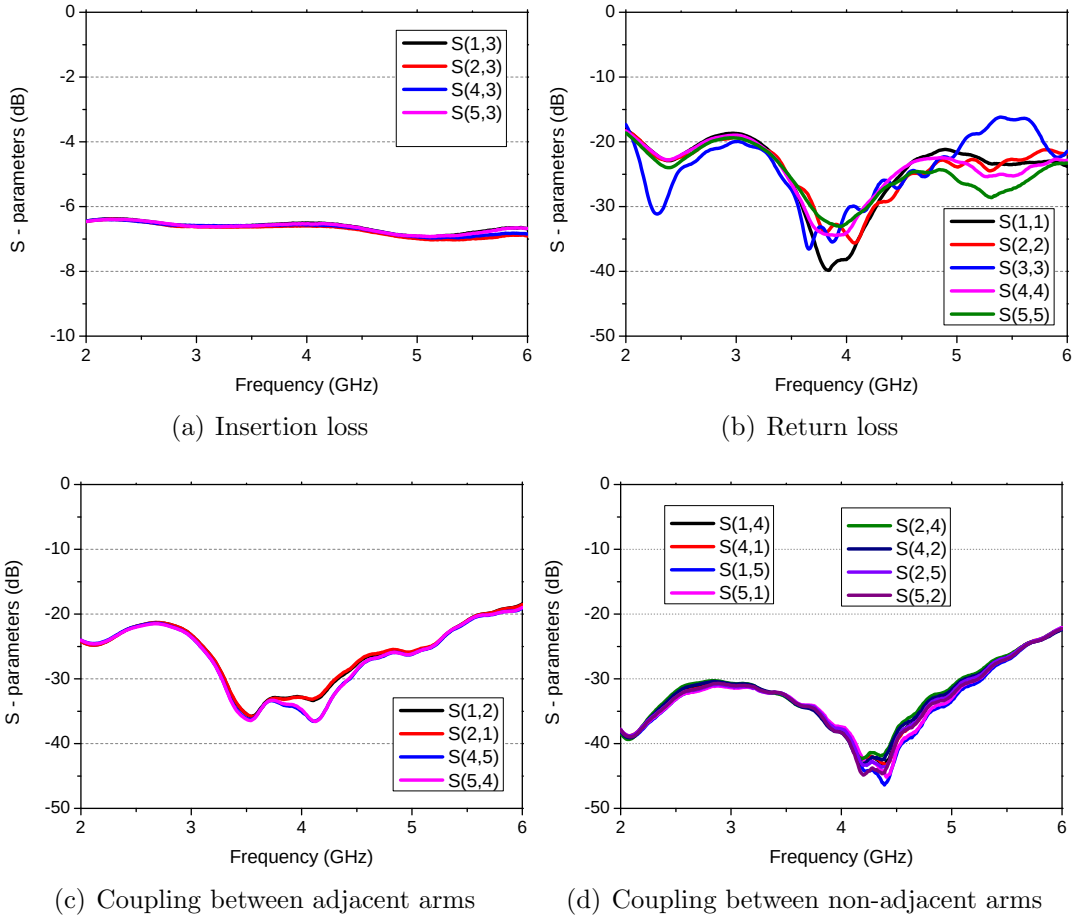

(a) Insertion loss

(b) Return loss

(c) Coupling between adjacent arms

(d) Coupling between non-adjacent arms

Figure 12.19: *S*-parameters of the ZN4PD1-63W+ splitter

and this could degrade the performance in a random manner. This approach of implementing a MS power splitter network thus offers no benefit.

Final choice of feeding mechanism

Based on the above observations, it has been decided that the best feeding mechanism in the present design scenario would be to use separate feeds for the separate patches, even though this would increase the number of cables. A separation of the feeds also has some inherent advantages which are as follows:

i. Better isolation between the antennas is achievable.

ii. Power handling is improved because optimised return loss values can be achieved for all the 3 antennas.

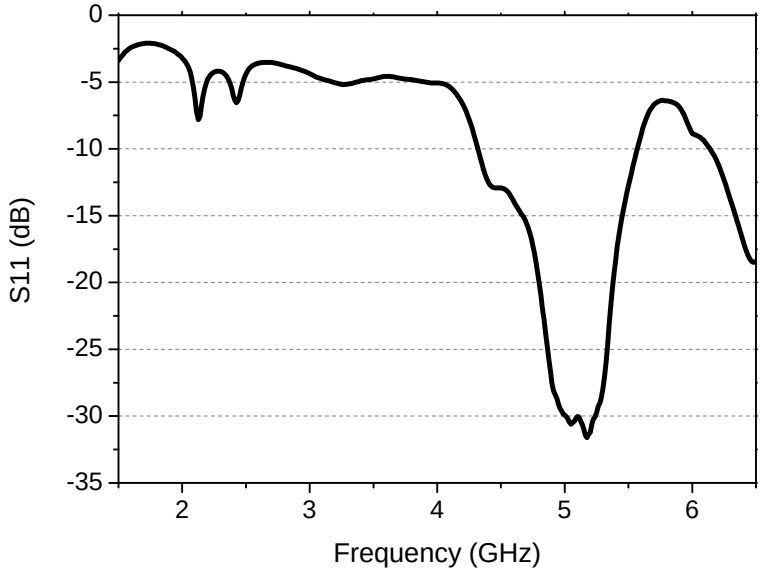

(a) SC1: ZN4PD1-63+

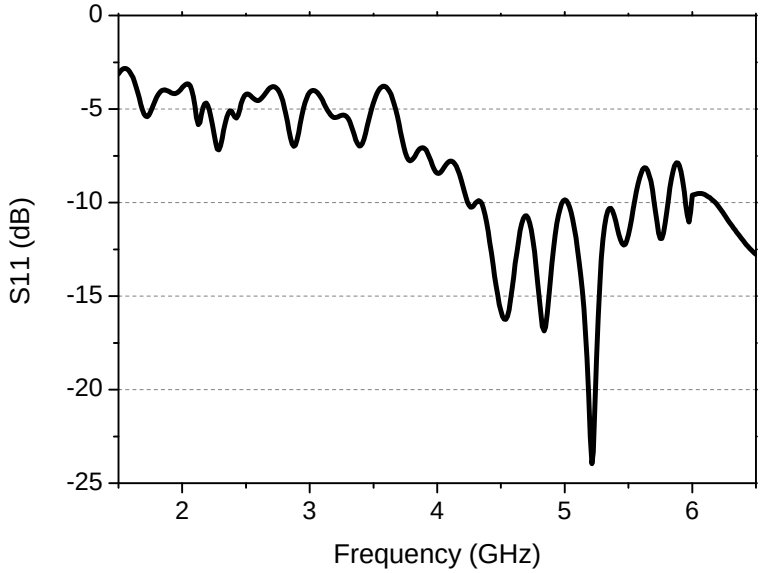

(b) SC2: ZN4PD1-63W+

Figure 12.20: Return loss at the splitter input port with the antennas attached to their output ports

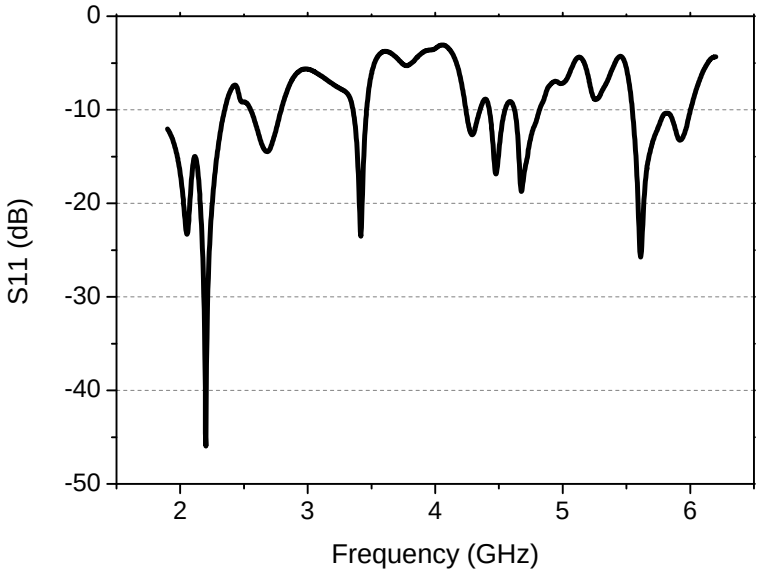

Figure 12.21: Return loss at the input of the MS splitter network which feeds the patch antennas

iii. It improves redundancy. If one antenna or its cable feed is damaged for any reason, operation in the other frequency bands is not hampered.

iv. The power amplifiers in the transceiver can be tuned separately, which means that a broadband design is not required, thereby improving their performances.

The advantages outweigh the disadvantages and as such, providing separate feeds to the antennas has been considered to be the best option for the present design.

12.6 Summary

In this chapter, the simulated and measured results of the designed patch antenna structures have been presented. The most crucial aspect of the work was to determine whether a reasonable bandwidth could be achieved such that slight deviations in the resonant frequency due to the surrounding metallic objects do not affect the usability of the antennas. The present work suggests that this is indeed achievable. It is observed that the extension of the ground plane of the antenna and the presence of the metal surface in close proximity do not lead to significant deviations in the resonant frequency. This indicates that the resonance patterns of these antenna structures are not too sensitive to the environment.

However, the extent of the grounded metal sheet that could be incorporated into the present measurements was limited by the available space within the anechoic chamber; the extent in the forward direction was $2.5\lambda_0$ and $6\lambda_0$ at 2.14 GHz and 5.8 GHz, respectively. An anechoic chamber of larger dimensions could be sued to validate the measurement results further.

Some interesting observations regarding the antenna radiation patterns have been made. It is seen that the extension of the ground plane in one direction tilts the main beam towards the opposite side. The inclusion of a large metallic surface further tilts the radiation pattern, and the beamwidth is enhanced. Laboratory measurements have shown a very wide coverage in the azimuth plane. Lower frequency antennas are affected more by these environmental changes. These observations strongly indicate the capability of achieving wireless operation inside process industry environments. The surrounding structures could also be potentially utilised - modifications to the radiation patterns could be obtained by suitable placement of the antennas. Further investigation is required to reach definite conclusions in this regard.

Chapter 13

Conclusions and future work

The final chapter of the thesis consolidates the observations and outcomes from the receiver front-end research work that has been detailed in the previous chapters. Section 13.1 presents these conclusions, and includes evaluations of the accomplishments and limitations of this research. Section 13.2 brings forth the diverse scope of the future work which could be based on the foundations of the present work.

13.1 Conclusions

The objectives of this research work were highlighted in chapter 1. The focus of the research was to investigate specific aspects of receiver front-ends applicable to next generation receiver systems, extending from those in ultra-sensitive radio receivers detecting minute signals to wireless systems operating in harsh conditions. These objectives were segregated into 4 major categories. These are reiterated here:

- Characterisation of low noise transistors of different technologies and topologies and of widely varying sizes, in an effort to determine their suitability in various applications, especially the SKA.
- Development of 2 MMIC LNAs operational in the C and UHF bands.
- Estimation of the noise coupling levels between adjacent antenna elements in low noise phased array systems such as those currently being developed for radio astronomy.

- Development of a multi-band MPA structure which would be operational under the severe environmental constraints imposed by process industry environments.

With respect to the first objective, the on-wafer transistor characterisation work was performed on 10 different low noise processes, both pHEMTs and mHEMTs, with gate lengths ranging from 70 nm to 250 nm, and gate widths ranging from 40 μm to 800 μm. It provided some very interesting insights into the behaviours of these transistors. Comparisons of the DC characteristics of identical gate width devices under uniform conditions indicated significant variations in drain currents, transconductance, power consumption, pinch-off conditions and gate leakage current levels. DC measurements with temperature variations verified that the transconductances generally increased with decreasing temperatures. Another significant observation was that the measured mHEMT processes suffered from reliability or oscillation issues, or exhibited unacceptably high power consumption levels. S-parameter measurements were used to validate the available library models.

Measurements of NF_{50} and noise parameters were performed using the state-of-the-art PNA-X instrument from Agilent Technologies. Comparisons of NF_{50} and noise parameters of identical gate width transistors and subsequent validations with measurements from a different experimental arrangement helped in identifying the lowest-noise processes. It was observed that devices from process 6, the 70 nm gate length GaAs mHEMT process, showed the lowest noise performance. However, there are severe reliability issues associated with this process that significantly restrict its usability. Process 3, a 130 nm gate length pHEMT process, offered good reliability, had good stability and exhibited good low noise and gain performance, with 0.3 – 0.4 dB NF_{min}, 8 – 10 Ω R_n and 130 mS peak g_m values. These observations indicated it would be one of the best processes for room temperature LNA designs in 3 – 8 GHz. Analysis of the variations of the noise parameters with increasing gate width indicated an optimum range of gate widths to achieve best performance at a spot frequency. For example, it was determined that the optimum device gate width for an LNA at 6 GHz was 150 – 300 μm. It was also observed that the noise resistance R_n decreased with increasing gate width for all processes, and overall exhibited approximately hyperbolic trends. These analyses serve as a useful guidelines for LNA design engineers. The characterisation work presented here was commenced as part of research to

determine suitable low noise processes at room temperature for the SKA project. However, the results would be equally useful in determining the best low noise HEMT processes for other applications in the 3 – 8 GHz band.

The MMIC LNA development work, which constituted the second research objective, was based on the more promising processes (or foundries) as determined from the transistor characterisation work. Simulated results of the C-band LNA indicated peak NF_{50} of 0.62 dB and peak gain of 30.4 dB. Both the 0.1 dB noise bandwidth and the 1 dB gain bandwidth are 4 GHz. Maximum input and output return loss values of -23 dB and -11 dB, respectively, were achieved. The input return loss was higher than -10 dB for 93 % of the operating range. For the UHF-band LNA, the NF_{50} peaked at 0.45 dB, and the 0.1 dB noise bandwidth was 450 MHz. The gain peaked at 30.5 dB, and the 3 dB gain bandwidth was 600 MHz. The input return loss satisfied the design specifications of -10 dB only in part of the band. The output return loss, varying between -4 dB and -11 dB was also unsatisfactory. The novelty of these designs was that broad bandwidth noise and gain performance can be expected, as compared to currently available LNAs in these frequency bands. This is especially true for the C-band MMIC LNA in which simulations indicate a 4 GHz bandwidth. The noise performance and bandwidth is expected to be superior compared to other broadband designs and comparable to narrowband designs. The noise, gain and bandwidth performance in the UHF band MMIC LNA are also comparable to designs produced in recent years in this band by SKA LNA designers.

Partially to facilitate ease of measurements when the fabricated LNAs are ready to be measured, on-wafer DC, S-parameter and NF_{50} measurements of previously-designed MMIC LNAs were performed. Various biasing options were investigated. Observations indicated that certain parameters in a particular design could be relatively insensitive to bias settings, whereas the performances of other parameters could be optimised by varying the bias settings (as observed for the C-band LNA S_{11} and S_{12}, respectively). This work also proved beneficial in investigating the application of genetic algorithm to LNA design, as part of another project.

The third objective of the work was to determine how the noise coupling between front-ends could affect, if at all, the performance in low noise phased array systems with closely coupled antennas. A theory to evaluate the level of noise emanating from the input of any linear noisy 2–port based on the fundamental

principles of noisy networks was described. The powerful technique of noise wave representation for noisy networks was used for this. This was used to estimate the noise that may be coupled between antenna elements in low noise phased array receivers of the type expected to be implemented in the SKA. Measurements performed on 2 COTS packaged amplifiers showed good agreement with the theoretically predicted values of the reverse noise levels from the LNA input ports, and hence validated the theoretical approach. The theory was applied to an example 2-antenna array system, using reported measured values of noise parameters of an SKA LNA designed in ASTRON. Results from this noise wave analysis suggested that the coupled noise contribution to system noise temperature in SKA phased array receivers should be quite small, especially since the LNAs which will finally be used in the SKA will have either similar or improved noise parameters than those analysed in this work.

The work also resulted in highlighting the importance of the noise resistance R_n. The importance of low R_n in achieving broadband LNA designs is well established. It has been observed that the reverse noise emanating from an LNA input port depends heavily on R_n as well, in comparison to the other noise parameters. In general, the interest of system designers may sometimes be limited to only the minimum noise figure NF_{min}, since this is the value achievable through efficient LNA designs. However, this work points out that for phased array systems, where coupling effects need to be considered, the noise resistance assumes a critical role. Though the focus of this work was to apply the theory to the SKA, the principles outlined could be very effectively used by array design engineers to evaluate whether the coupled noise is likely to be high enough to affect the overall system noise temperature significantly. This analysis therefore provides a simple but effective tool for LNA and phased array systems designers to obtain an estimate of the noise coupling in phased array systems from knowledge of the LNA S-parameters and noise parameters. If the noise coupling is found to be significant enough to deteriorate performance, the LNA and antenna designs could be optimised to achieve lower levels of coupling.

The final aspect of the research focused on the complete design, simulation, fabrication and measurement of a multi-band MPA structure designed to operate in a harsh environment in the following frequency bands - 2.1 GHz UMTS, 2.4 GHz ISM and 5.8 GHz ISM. Decisions of the design choices were based on the typical constraints of process industry environments. These include severely limited

space, near-ground operation in close proximity to large metallic structures like access platforms and conformability to curved surfaces of process vessels, among other restraints. The primary aim of the work was to determine if sufficient bandwidths and wide angular coverages could be achieved such that the effects of these environmental factors did not limit the functionalities of the antennas. The simulations indicated that this was potentially achievable.

The MPAs were then fabricated and laboratory based measurements were conducted to validate the concept. The deviations in the measured resonant frequencies (from ideal) of 4 such antenna structures were less than 1 % in all the frequency bands, except in one instance when it increased to 1.6 %. The achieved return loss values varied between 15 dB and 23 dB. Maximum 10 dB return loss bandwidths of 79 MHz (3.7 %), 105 MHz (4.3 %) and 381 MHz (6.6 %) were achieved in the 2.1 GHz, 2.4 GHz and 5.8 GHz bands, respectively, with standalone antennas. The fabricated MPAs achieved wider coverages in the azimuth plane than typically obtained from commercial MPAs aimed at similar applications. It was also observed that the extension of the antenna ground plane in one direction or the presence of large metallic structures in close proximity to the MPAs had no significant effect on the resonant frequencies of the antennas, but modified the radiation patterns. Presence of a metallic structure enhanced the radiation in all directions in the azimuth plane significantly. This would be advantageous in the intended application in the process industry, where an omnidirectional azimuth radiation pattern is desirable. It was also observed that, as expected, the environmental factors and the reductions in the MPA dimensions affected the lower frequency bands (2.1 and 2.4 GHz) more than they affected the higher frequency band (5.8 GHz). The limitations of this research were that complete emulation of a process industry environment was not achievable and only a specific range of conditions were considered (for example, only larger diameters were considered). The significance of this research lies in the fact that with the ever-increasing demands of implementing wireless communications inside process industry environments, these multi-band antenna structures could be very effectively used to provide wireless solutions in a customised manner.

The following paragraphs reflect on the author's experiences of carrying out this research.

The research has provided the author with an opportunity to gain theoretical knowledge and practical experience of how the active and passive components in

receivers interact and affect system performance. The principal challenges in this research were concerned with practical implementation and performance characterisation. The author offers the following observations as a guide to researchers interested in this field of work.

The author has observed that compared to noise figure measurement of standard coaxial components, noise figure measurement of on-wafer transistors is considerably more challenging. The intricacies associated with both the calibration procedure and the actual measurements increase significantly. For noise parameter measurements, the challenges increase manifold. Selection of proper parameters in the SNPW software as well as in the PNA-X is important to increase the accuracy of the measurements. Measurements should also be performed in a screened room to eliminate interference effects. In both transistor and MMIC LNA measurements, good probing skills are extremely essential. The author also found that achieving good calibration to 110 GHz is also a significant challenge. However, use of LRRM techniques in calibration and good probing practices can help overcome this problem. In context of the LNA design work, the author found the incorporation an UHF-band design in a 0.25 mm^2 space extremely challenging. In relation to the antenna design work, the difficulty of designing an antenna structure which satisfied all the stringent design criteria proved to be a challenging task. However, accomplishment of the objectives by overcoming these challenges also provided excellent motivation for this research.

The principal theoretical and practical skills gained during the project are listed below:

- On-wafer measurement techniques to characterise transistors and MMIC LNAs,
- DC, S-parameter and noise measurement techniques using high quality instruments such as the PNA-X,
- Antenna measurement techniques,
- Practical considerations in setting up experimental arrangements,
- Design theory and intricacies of narrowband and broadband LNAs,
- Practical issues in producing LNA designs, from schematic and layout generation to final assembly and testing,

- Noise contribution of LNAs in a phased array system,
- Interaction between the active and passive components of a receiver front-end,
- Design of passive components such as antennas, tri-plexers and splitters,
- Challenges associated with achieving efficient antenna structures for operation in harsh environments with constraints on both the design and the signal propagation conditions,
- Other essential skills in doctoral research, such as time and resource management, project planning (especially with deadlines), ability to critically analyse an article, academic writing, presentation skills and liaising effectively with industrial partners.

This research project has involved: system, circuit and antenna design; active and passive component simulation; circuit and antenna fabrication; and system performance characterisation. As such, it has encompassed the entire engineering design cycle. The project was enhanced through interactions with a number of industries and international research groups.

13.2 Future work

Based on the observations and conclusions of the present research work, some areas of future work have been identified. A synopsis of these ideas is presented here.

The transistor characterisation work has the scope of being extended to other foundry processes and other device sizes. This is required to obtain a better understanding of the manner in which the performances change with varying gate lengths and gate widths. Since the measurements in the present work extend only from 3 – 8 GHz, extrapolation of these results to both higher and lower frequency ranges will also be beneficial. This will facilitate determination of suitable transistors for low noise applications outside the 3 – 8 GHz band. The optimum device sizes at 6 GHz spot frequency were determined in the present research. This could be extended to other frequencies. Noise figure and noise parameter measurements of ultra low noise transistors in lower frequency ranges

(<3 GHz) are extremely difficult due to increased interference levels and tolerances of measurement equipments. Hence, an investigation of suitable techniques to extrapolate the measured data to these frequencies is required.

The MMIC LNAs designed by the author are presently in the assembly stage. The next phase in this design work will comprise of laboratory measurements. The techniques adopted while performing the on-wafer measurements of previously-designed MMICs (as discussed in section 10.4) could be applied here. For example, the variations in the performance trends with changing bias conditions could be studied, and optimal bias points could be determined. Based on the success of these measurements, the existing C-band design could be utilised to generate a complete WLAN receiver front-end, in conjunction with the designed 5.8 GHz ISM antenna. Simulations of the C-band LNA also indicated a relatively wide noise bandwidth extending up to 12 GHz. Therefore, the author also proposes development of a broadband LNA for simultaneous operation in both the C and X bands. Modifications to the existing design may be sufficient for this purpose, or initiation of the design work from the first step of transistor characterisation may be required. Further investigation into broadband design techniques is required to determine this.

Presently, the noise analysis for low noise phased arrays is limited to estimating coupling levels between adjacent antenna elements. The next step in this analysis will cover evaluation of the effect of this coupling on the total received signal. It is expected that the correlation between the forward and reverse noise waves will be critical in this analysis. This work could also be extended to a multiple-antenna system, provided suitable antenna S-parameter datasets are available. The complexity of the analysis will naturally increase.

In context of the antenna design work, the laboratory measurements have shown promising results. However, measurements in the laboratory environment can never completely replicate a real application environment. Therefore, the next step in the antenna design work will comprise measurements inside process industry premises. The robustness of the antennas could be evaluated by performing measurements inside different industry environments. The achievable data rates in the different bands need to be determined as well. In this first phase of work presented in this thesis, only larger process vessel diameters have been considered. Smaller diameter vessels need consideration in the next phase of work. It can be speculated that the increased curvatures will restrict the height of the

MPA substrate even further. Potential development of fissures in the structure arising from high curvatures will require investigation as well.

In chapter 1, the increasing need for LNAs in WSNs had been highlighted. The final scope of the future work will be to investigate the applicability of the present C-band design in WSNs employed in process industry environments, and development of receiver front-end components for such applications. The objective will be to use the multi-band antenna structure designed in this research work in conjunction with LNAs in the different bands (which need to be designed) to achieve reliable communication in such harsh environments. This work will bring together 3 aspects of the present research work - transistor characterisation, LNA design and antenna design.

From this discussion, it is evident that the research work presented in this thesis has not only contributed to a better understanding of receiver front-end components but has also provided the foundations for a broad and varied range of future work.

Bibliography

[1] IEEE 802.11 WIRELESS LOCAL AREA NETWORKS. [Online]. Available: http://www.ieee802.org/11/

[2] IEEE 802.15: WIRELESS PERSONAL AREA NETWORKs (PANs). [Online]. Available: http://standards.ieee.org/about/get/802/802.15.html

[3] D. A. Kettle, "Characterisation of low noise devices for radio astronomy applications," *PhD Thesis submitted to the University of Manchester*, 2006.

[4] R. T. Schilizzi *et al.* (Dec. 2007) Preliminary Specifications for the Square Kilometre Array. [Online]. Available: http://www.skatelescope.org/PDF/memos/100_Memo_Schilizzi.pdf

[5] G. Hampson, B. Smolders, and A. Joseph, "One Square Metre of a Million," in *29th European Microwave Conf.*, vol. 1, Oct. 1999, pp. 111 –114.

[6] A. Van Ardenne, "Concepts of the Square Kilometre Array; toward the new generation radio telescopes," in *IEEE Int. Symp. Antennas and Propagation Soc.*, vol. 1, Jul. 2000, pp. 158 –161 vol.1.

[7] A. Faulkner *et al.* (2010) Aperture Arrays for the SKA: the SKADS White Paper. [Online]. Available: http://www.skatelescope.org

[8] B. Gaensler, "The Square Kilometre Array: An international radio telescope for the 21st century," in *IEEE Int. Frequency Control Symp., Joint with the 22nd European Frequency and Time forum*, Apr. 2009.

[9] J. D. Kraus, *Radio Astronomy.* Cygnus-Quasar.

[10] J. S. Yuk, B. G. Choi, Y. S. Lee, C. S. Park, and S. Kang, "Low-power PHEMT MMIC LNA for C-band applications," *Microwave and Optical*

Technology Letters, vol. 48, no. 2, pp. 253–255, 2006. [Online]. Available: http://dx.doi.org/10.1002/mop.21320

[11] W. Ciccognani, E. Limiti, P. Longhi, and M. Renvoise, "MMIC LNAs for Radioastronomy Applications Using Advanced Industrial 70 nm Metamorphic Technology," in *Annual IEEE Compound Semiconductor Integrated Circuit Sym. (CISC)*, Oct. 2009, pp. 1 –2.

[12] N. Wang, N. Zhang, and M. Wang, "Wireless sensors in agriculture and food industry Recent development and future perspective," *Computers and Electronics in Agriculture*, vol. 50, no. 1, pp. 1 – 14, 2006. [Online]. Available: http://www.sciencedirect.com/science/article/pii/S0168169905001572

[13] Cisco Secure Wireless Plant Solution: Wireless Sensor Networking for Industrial Environments. [Online]. Available: http://www.cisco.com/web/strategy/docs/manufacturing/secure$_$wireless$_$plant$_$solution.pdf

[14] G. Zhao, "Wireless Sensor Networks for Industrial Process Monitoring and Control: A Survey," *Network Protocols and Algorithms Journal*, vol. 3, no. 1, 2011.

[15] ZigBee Specification Overview. [Online]. Available: http://www.zigbee.org/Specifications/ZigBee/Overview.aspx

[16] CC2590 2.4-GHz RF Front End Datasheet. Texas Instruments. [Online]. Available: http://www.ti.com/product/cc2590

[17] Process Vessels and Storage Tanks. [Online]. Available: http://www.tetrapakcps.com/index.php?pagecode=process_vessels

[18] Food Industry Storage tanks and process vessels. [Online]. Available: http://www.packo.com/en/7016

[19] S. Bhaumik, "MMIC Design of Ultra Low Noise Amplifiers," *PhD Thesis submitted to the University of Manchester*, 2010.

[20] M. Pospieszalski, "Extremely low-noise amplification with cryogenic FETs and HFETs: 1970-2004," *IEEE Microwave*, vol. 6, no. 3, pp. 62 – 75, Sep. 2005.

[21] S. Okwit, "An Historical View of the Evolution of Low-Noise Concepts and Techniques," *IEEE Trans. Microw. Theory Tech.*, vol. 32, no. 9, pp. 1068 – 1082, Sep. 1984.

[22] I. D. Robertson, *MMIC Design*. London: The Institute of Electrical Engineers, 1995.

[23] W. van Cappellen, L. Bakker, and T. Oosterloo, "Experimental results of a 112 element phased array feed for the Westerbork Synthesis Radio Telescope," in *IEEE Int. Symp. Antennas and Propagation Soc. (APSURSI '09)*, Jun. 2009, pp. 1 –4.

[24] Australian Square Kilometer Array Pathfinder. [Online]. Available: http://www.atnf.csiro.au/SKA/

[25] (2009) Phased Array Demonstrator. [Online]. Available: http://www.nrc-cnrc.gc.ca/eng/projects/hia/phased-array.html

[26] Low Frequency Array. [Online]. Available: http://www.lofar.org/

[27] Murchison Widefield Array. [Online]. Available: http://www.haystack.mit.edu/ast/arrays/mwa/

[28] R. Aaron *et al.*, "The Precision Array for Probing the Epoch of Reionization: Eight Station Results," *IEEE Trans. The Astronomical Journal*, vol. 139, p. 1468, Apr. 2010.

[29] M. Ivashina, M. Kehn, P. Kildal, and R. Maaskant, "Control of reflection and mutual coupling losses in maximizing efficiency of dense focal plane arrays," in *1st European Conf. on Antennas and Propagation (EuCAP)*, Nov. 2006, pp. 1 –6.

[30] Matrix Laboratory (Version R2006b). The Mathworks. [Online]. Available: http://www.mathworks.co.uk/

[31] P. S. Hall and J. R. James, *Handbook of Microstrip Antennas*. Peter Peregrinus Ltd., 1989.

[32] S. Bhaumik, M. Roy, and D. George, "Comparative study of HEMTs for LNAs in Square Kilometre Array telescope," in *IEEE MTT-S Int. Microwave Symp. Digest (MTT)*, Jun. 2011, pp. 1 –4.

[33] M. Roy and D. George, "Estimation of coupled noise in low noise phased array antennas," *IEEE Trans. Antennas Propag.*, vol. 59, no. 6, pp. 1846 –1854, Jun. 2011.

[34] S. F. T. Mimura, T. Hiyamizu and K. Nanbu, "A new field-effect transistor with selectively doped GaAs/n-$Al_xGa_{1-x}As$ heterojunctions," *Japanese Journal of Applied Physics*, vol. 19, no. 5, pp. 225 – 227, May 1980.

[35] M. Pospieszalski, "Modeling of noise parameters of MESFETs and MODFETs and their frequency and temperature dependence," *IEEE Trans. Microw. Theory Tech.*, vol. 37, no. 9, pp. 1340 –1350, Sep. 1989.

[36] R. S. Pengelly, *Microwave Field-Effect Transistors-Theory, Design and Application.* Research Studies Press, 1984.

[37] D. Kettle and N. Roddis, "Cryogenic Performance of a Very Low Noise MMIC Ka-Band Radiometer Front-End," in *IEEE MTT-S Int. Microwave Symp.*, Jun. 2007, pp. 2087 –2090.

[38] S. Marsh, *Practical MMIC Design.* Artech House, 2006.

[39] J. M. Golio, *Microwave MESFETs and HEMTs.* Norwood, MA: Artech House, 1970.

[40] G. A. Ali, F, *HEMTs and HBTs: Devices, Fabrication, and Circuits.* London: Artech House, 1991.

[41] G. Dambrine, A. Cappy, F. Heliodore, and E. Playez, "A new method for determining the FET small-signal equivalent circuit," *IEEE Trans. Microw. Theory Tech.*, vol. 36, no. 7, pp. 1151 –1159, Jul. 1988.

[42] G. Gonzalez, *Microwave Transistor Amplifiers Analysis and Design.* Prentice Hall, 1997.

[43] A. van der Ziel, *Noise: Sources, Characterisation, Measurement.* Prentice-Hall, Inc., 1970.

[44] H. Rothe and W. Dahlke, "Theory of Noisy Fourpoles," *IRE Proc.*, vol. 44, no. 6, pp. 811 –818, Jun. 1956.

[45] G. Vasilescu, G. Alquie, and M. Krim, "Exact computation of two-port noise parameters," *Electronics Lett.*, vol. 25, no. 4, pp. 292 –293, Feb. 1989.

[46] H. Haus, W. Atkinson, G. Branch, W. Davenport, W. Fonger, W. Harris, S. Harrison, W. McLeod, E. Stodola, and T. Talpey, "Representation of noise in linear two ports," *IRE Proc.*, vol. 48, no. 1, pp. 69 –74, Jan. 1960.

[47] D. Ballo and G. Simpson. (2009) New Ultra-Fast Noise Parameter System - Opening A New Realm of Possibilities in Noise Characterization. [Online]. Available: http://www.home.agilent.com/agilent/eventDetail.jspx?ckey=1630447-1&pid=null&nid=-35211.934429.08&lc=eng&cc=SG

[48] R. Lane, "The determination of device noise parameters," *Proc. IEEE*, vol. 57, no. 8, pp. 1461 – 1462, Aug. 1969.

[49] G. Caruso and M. Sannino, "Computer-Aided Determination of Microwave Two-Port Noise Parameters," *IEEE Trans. Microw. Theory Tech.*, vol. 26, no. 9, pp. 639 – 642, Sep. 1978.

[50] A. Davidson, B. Leake, and E. Strid, "Accuracy improvements in microwave noise parameter measurements," *IEEE Trans. Microw. Theory Tech.*, vol. 37, no. 12, pp. 1973 –1978, Dec. 1989.

[51] M. Mitama and H. Katoh, "An Improved Computational Method for Noise Parameter Measurement," *IEEE Trans. Microw. Theory Tech.*, vol. 27, no. 6, pp. 612 – 615, Jun. 1979.

[52] L. Escotte, R. Plana, and J. Graffeuil, "Evaluation of noise parameter extraction methods," *IEEE Trans. Microw. Theory Tech.*, vol. 41, no. 3, pp. 382 –387, Mar. 1993.

[53] S. Van den Bosch and L. Martens, "Improved impedance-pattern generation for automatic noise-parameter determination," *IEEE Trans. Microw. Theory Tech.*, vol. 46, no. 11, pp. 1673 –1678, Nov. 1998.

[54] A. Boudiaf and M. Laporte, "An accurate and repeatable technique for noise parameter measurements," *IEEE Trans. Instrum. Meas.*, vol. 42, no. 2, pp. 532 –537, Apr. 1993.

[55] M. Gupta, "Determination of the noise parameters of a linear 2-port," *Electronics Lett.*, vol. 6, no. 17, pp. 543 –544, Aug. 1970.

[56] M. Murphy, "Applying the Series Feedback Technique to LNA Design," *Microwave Journal*, Nov. 1989.

[57] D. Henkes, "LNA Design Uses Series Feedback to Achieve Simultaneous Low Input VSWR and Low Noise," *Applied Microwave & Wireless*, Oct. 1998.

[58] H. Friis, "Noise Figures of Radio Receivers," *IRE Proc.*, vol. 32, no. 7, pp. 419 – 422, Jul. 1944.

[59] S. Mao, S. Jones, and G. Vendelin, "Millimeter-Wave Integrated Circuits," *IEEE J. Solid-State Circuits*, vol. 3, no. 2, pp. 117 – 123, Jun. 1968.

[60] E. Mehal and R. Wacker, "GaAs Integrated Microwave Circuits," *IEEE J. Solid-State Circuits*, vol. 3, no. 2, pp. 113 – 116, Jun. 1968.

[61] R. Pengelly and J. Turner, "Monolithic broadband GaAs f.e.t. amplifiers," *Electronics Lett.*, vol. 12, no. 10, pp. 251 –252, May 1976.

[62] E. Bayar and A. Aghvami, "Miniaturised L-band MIC LNA design," *Electronics Letters*, vol. 29, no. 19, pp. 1698 –1699, Sep. 1993.

[63] K. Warnick, "Optimal noise matching for a phased array feed," in *IEEE Antennas and Propagation Soc. Int. Symp. (APSURSI '09)*, Jun. 2009, pp. 1 –4.

[64] K. Warnick and M. Jensen, "Optimal noise matching condition for mutually-coupled antenna arrays," in *IEEE Antennas and Propagation Soc. Int. Symp.*, Jun. 2007, pp. 2953 –2956.

[65] K. Warnick, B. Woestenburg, L. Belostotski, and P. Russer, "Minimizing the noise penalty due to mutual coupling for a receiving array," *Antennas and Propagation, IEEE Transactions on*, vol. 57, no. 6, pp. 1634 –1644, june 2009.

[66] R. Maaskant and E. Woestenburg, "Applying the active antenna impedance to achieve noise match in receiving array antennas," in *IEEE Int. Symp. Antennas and Propagation Soc.*, Jun. 2007, pp. 5889 –5892.

[67] R. Frater and D. Williams, "An Active "Cold" Noise Source," *IEEE Trans. Microw. Theory Tech.*, vol. 29, no. 4, pp. 344 – 347, Apr. 1981.

[68] G. F. Engen, "A New Method of Characterizing Amplifier Noise Performance," *IEEE Trans. Instrum. Meas.*, vol. 19, no. 4, pp. 344 –349, Nov. 1970.

[69] D. Wait and G. Engen, "Application of Radiometry to the accurate measurement of amplifier noise," *IEEE Trans. Instrum. Meas.*, vol. 40, no. 2, pp. 433 – 437, Apr. 1991.

[70] D. Wait and J. Randa, "Amplifier noise measurements at NIST," *IEEE Trans. Instrum. Meas.*, vol. 46, no. 2, pp. 482 –485, Apr. 1997.

[71] J. Randa and D. Walker, "Amplifier noise-parameter measurement checks and verification," in *63rd ARFTG Conf. Digest Spring*, Nov. 2004, pp. 41 – 46.

[72] M. Weatherspoon and L. Dunleavy, "Experimental validation of generalized equations for FET cold noise source design," *IEEE Trans. Microw. Theory Tech.*, vol. 54, no. 2, pp. 608 – 614, Feb. 2006.

[73] H. Bauer and H. Rothe, "Der aquivalente rauschvierpol als wellenvierpol," *Archiv der elektrischen Uetertragung*, vol. 10, pp. 241 – 252, Jun. 1956.

[74] J. Penfield, P., "Wave Representation of Amplifier Noise," *IRE Trans. Circuit Theory*, vol. 9, no. 1, pp. 84 – 86, Mar. 1962.

[75] S. Wedge and D. Rutledge, "Wave techniques for noise modeling and measurement," *IEEE Trans. Microw. Theory Tech.*, vol. 40, no. 11, pp. 2004 –2012, Nov. 1992.

[76] R. Meys, "A Wave Approach to the Noise Properties of Linear Microwave Devices," *IEEE Trans. Microw. Theory Tech.*, vol. 26, no. 1, pp. 34 – 37, Jan. 1978.

[77] Advanced Design System (Version 2009). Agilent Technologies. [Online]. Available: http://www.home.agilent.com/agilent/product.jspx?nid=-34346.0.00&lc=eng&cc=GB&pselect=SR.Looking

[78] N. Bayatmaku, P. Lotfi, M. Azarmanesh, and S. Soltani, "Design of simple multiband patch antenna for mobile communication applications using new e-shape fractal," *Antennas and Wireless Propagation Letters, IEEE*, vol. 10, pp. 873 –875, 2011.

[79] H. Zhou, N. Sutton, and D. Filipovic, "Wideband w-band patch antenna," in *Antennas and Propagation (EUCAP), Proceedings of the 5th European Conference on*, april 2011, pp. 1518 –1521.

[80] C. A. Balanis, *Antenna Theory: Analysis and Design.* Wiley., 1997.

[81] "IEEE Standard Definitions of Terms for Antennas," *IEEE Std 145-1993*, p. i, Aug. 1993.

[82] P. S. Nakar, "Design of a compact microstrip patch antenna for use in wireless/cellular devices," *MSc Thesis submitted to Florida State University*, 2004.

[83] M. Liang, Y. Chen, C. Huang, and W. Chen, "An electrically small impedance-matched microstrip antenna design," in *Antennas and Propagation Society International Symposium, 2002. IEEE*, vol. 4, 2002, pp. 38 – 41 vol.4.

[84] N. U. Lau, "Broadband suspended patch antennas with low loss feed networks," *PhD Thesis submitted to UMIST*, 2003.

[85] D. Orban. The basics of patch antennas. [Online]. Available: www.orbanmicrowave.com/The_Basics_Of_Patch_Antennas.pdf

[86] E. O. Hammerstad, "Equations for microstrip circuit design," in *5th European Microwave Conf.*, Sep. 1975, pp. 268 –272.

[87] I. Bahl and P. Bhartia, *Microstrip Antennas.* Artech House., 1980.

[88] G. Breed. The Fundamentals of Patch Antenna Design and Performance. [Online]. Available: http://www.highfrequencyelectronics.com/Archives/Mar09/HFE0309_Tutorial.pdf

[89] 0.13 um D pHEMT Foundry Service. [Online]. Available: http://www.triquint.com/prodserv/foundry/docs/TQP13-N.pdf

[90] S. Unawong, S. Miyamoto, and N. Morinaga, "Techniques to improve the performance of wireless lan under ism interference environments," in *5th Asia-Pacific Conf. on Communiations and 4th Optoelectronics and Communications Conf. (APCC/OECC '99)*, vol. 1, Oct. 1999, pp. 802 –805 vol.1.

[91] RT/Duroid laminates Datasheet. Rogers Corporation. [Online]. Available: http://www.rogerscorp.com/acm/producttypes/2/Rogers-High-Frequency-Laminates.aspx

[92] D. Mirshekar-Syahkal and H. Hassani, "Characteristics of stacked rectangular and triangular patch antennas for dual band applications," in *8th Int.Conf. on Antennas and Propagation*, Mar. 1993, pp. 728 –731 vol.2.

[93] M. Shakib, M. Islam, and N. Misran, "Stacked patch antenna with folded patch feed for ultra-wideband application," *Microwaves, Antennas Propagation, IET*, vol. 4, no. 10, pp. 1456 –1461, october 2010.

[94] J. Anguera, C. Puente, C. Borja, and J. Soler, "Dual-frequency broadband-stacked microstrip antenna using a reactive loading and a fractal-shaped radiating edge," *Antennas and Wireless Propagation Letters, IEEE*, vol. 6, pp. 309 –312, 2007.

[95] Z. D. Liu, P. Hall, and D. Wake, "Dual-frequency planar inverted-f antenna," *IEEE Trans. Antennas Propag.*, vol. 45, no. 10, pp. 1451 –1458, Oct. 1997.

[96] L. Low, J. Batchelor, R. Heaton, and N. Chen, "Dual patches microstrip fed antenna with wide bandwidth," in *Antennas Propagation Conference, 2009. LAPC 2009. Loughborough*, nov. 2009, pp. 429 –432.

[97] Y.-H. Suh and K. Chang, "Low cost microstrip-fed dual frequency printed dipole antenna for wireless communications," *Electron. Lett.*, vol. 36, no. 14, pp. 1177 –1179, Jul. 2000.

[98] W. K. Toh, X. Qing, and Z. N. Chen, "A planar uwb patch-dipole antenna," *Antennas and Propagation, IEEE Transactions on*, vol. 59, no. 9, pp. 3441 –3444, sept. 2011.

[99] Computer Simulation Technology (Version 2010). CST. [Online]. Available: http://www.cst.com/

[100] E. Wilkinson, "An n-way hybrid power divider," *IRE Trans. Microw. Theory Tech.*, vol. 8, no. 1, pp. 116 –118, Jan. 1960.

[101] Integrated Circuit Characterization and Analysis Program (Version 2009). Agilent Technologies. [Online]. Available: http://www.home.agilent.com/agilent/product.jspx?cc=GB&lc=eng&ckey=1297149&nid=-34268.0.00&id=1297149

[102] Wincal. Cascade Microtech. [Online]. Available: http://www.cmicro.com/products/probes/wincal-xe

[103] (2004) Noise figure measurement accuracy The Y-factor method. [Online]. Available: http://cp.literature.agilent.com/litweb/pdf/5952-3706E.pdf

[104] (2010) High-accuracy Noise Figure Measurements Using the PNA-X Series Network Analyzer. White Paper. [Online]. Available: http://cp.literature.agilent.com/litweb/pdf/5990-5800EN.pdf

[105] V. Adamian and A. Uhlir, "A Novel Procedure for Receiver Noise Characterization," *IEEE Trans. Instrum. Meas.*, vol. 22, no. 2, pp. 181 –182, Jun. 1973.

[106] SNPW. Maury Microwave Corporation.

[107] Automated Tuner System (Version 5). Maury Microwave Corporation. [Online]. Available: http://www.maurymw.com/MW_RF/ATS_Automated_Tuner_Software.php

[108] Operating Manual, Automated Tuner System. Document no. MT993-2.

[109] Antenna measurements. [Online]. Available: http://wireless.ictp.it/handbook/C6.pdf

[110] (2007) Antenna Measurement Theory. Agilent Technologies. Santa Clara, CA. [Online]. Available: http://www.home.agilent.com/upload/cmc_upload/All/ORFR-Theory.pdf?&cc=GB&lc=eng

[111] DAMS Antenna Measurement Studio (Version 5.5). Diamond Engineering. [Online]. Available: http://www.diamondeng.net/dams-software-studio

[112] J. J. Bautista, "Cryogenic, Low-Noise High Electron Mobility Transistor Amplifiers for the Deep Space Network," in *The Telecommunications and Data Acquisition Progress Report 42-115*, Nov. 1993, p. 6580.

[113] S. Hong, K. Shim, and J. Yang, "Reduced gate leakage current in AlGaN/GaN HEMT by oxygen passivation of AlGaN surface," *Electronics Lett.*, vol. 44, no. 18, pp. 1091 –1092, Aug. 2008.

[114] D.-S. Shin, J. Lee, H. S. Min, J.-E. Oh, Y. J. Park, W. Jung, and D. S. Ma, "Analytical noise model with the influence of shot noise induced by the gate leakage current for submicrometer gate-length high-electron-mobility transistors," *IEEE Trans. Electron Devices*, vol. 44, no. 11, pp. 1883 –1887, Nov. 1997.

[115] A. Prasad, M. Roy, A. Biswas, and D. George, "Application of Genetic Algorithm to multi-objective optimization in LNA design," in *Asia-Pacific Microwave Conf. Proc. (APMC)*, Dec. 2010, pp. 362 –365.

[116] M. Bergano, A. Rocha, L. Cupido, and D. Barbosa, "A 5 GHz LNA for a radio-astronomy experiment," in *EUROCON - International Conference on Computer as a Tool (EUROCON), 2011 IEEE*, Apr. 2011, pp. 1 –4.

[117] K. Benboudjema, A. Swarup, and K. Ali, "A C-band low noise amplifier for satellite communications," in *Technologies for Wireless Applications, 1999. Digest. 1999 IEEE MTT-S Symposium on*, Feb. 1999, pp. 157 –160.

[118] S. Bhaumik and D. George, "Review of Square Kilometer Array LNA technologies and topologies," in *Wide Field Astronomy and Technology for the Square Kilometre Array*, Nov. 2009, pp. 279 – 284.

[119] D. Kettle, "FARADAY Technical Peformance Document," *Internal Project Report, FARADAY Project*, 2007.

[120] Connectorized Amplifier ZX60-2522M+ Datasheet. Minicircuits. [Online]. Available: http://www.minicircuits.com/pdfs/ZX60-2522M+.pdf

[121] Connectorized Amplifier ZX60-3018G+ Datasheet. Minicircuits. [Online]. Available: http://www.minicircuits.com/pdfs/ZX60-3018G+.pdf

[122] S. Bhaumik and D. George, "SKA LNA Technologies and Topologies," in *Wide Field Astronomy and Technology for the Square Kilometre Array*, Nov. 2009, pp. 279 –284.

[123] 9dBi Client Patch Wireless LAN Antenna Datasheet. Panorama Antennas. [Online]. Available: http://www.panorama.co.uk/datasheets/w24-cp-9.pdf

[124] 5.8GHz Planar Antenna Datasheet. Stella Doradus Ireland Ltd. [Online]. Available: http://www.stelladoradus.com/pdfs/5.8/Planars/58.4040.(27-11-08).pdf

[125] Flexi-strip multi band 800MHz + 900MHz +1800MHz 1900MHz + 3G Antenna Datasheet. Panorama Antennas. [Online]. Available: http://www.panorama.co.uk/datasheets/efc3g.pdf

[126] ZN4PD1-63+ Coaxial Power Splitter/Combiner Datasheet. Minicircuits. [Online]. Available: http://www.minicircuits.com/pdfs/ZN4PD1-63+.pdf

[127] ZN4PD1-63W+ Coaxial Power Splitter/Combiner Datasheet. Minicircuits. [Online]. Available: http://www.minicircuits.com/pdfs/ZN4PD1-63W+.pdf